Magnetic Properties of $\mathrm{SmCrO_3}$ and $\mathrm{GdCrO_3}$ Based Bulk Orthochromites

A Thesis Submitted

By

Bibhuti Bhusan Dash

Roll No: 126121010

In Partial Fulfillment of the Requirements for the Award of the Degree of

Doctor of Philosophy in Physics

Department of Physics
Indian Institute of Technology Guwahati
Guwahati-781039, India

January, 2019

भारतीय प्रौद्योगिकी संस्थान गुवाहाटी
Indian Institute of Technology Guwahati

Statement

The work contained in the thesis entitled **“Magnetic Properties of $SmCrO_3$ and $GdCrO_3$ Based Bulk Orthochromites”** has been carried out by me under the supervision of Prof. S. Ravi, Department of Physics, Indian Institute of Technology Guwahati. This work has not been submitted elsewhere for the award of any degree.

January, 2019

(Bibhuti Bhusan Dash)
Department of Physics
Indian Institute of Technology Guwahati
Guwahati – 781039, India

Certificate

It is certified that the work contained in the thesis entitled "**Magnetic Properties of $SmCrO_3$ and $GdCrO_3$ Based Bulk Orthochromites**" by Mr. Bibhuti Bhusan Dash, a Ph. D. student of the Department of Physics, Indian Institute of Technology Guwahati, for the award of the degree of *Doctor of Philosophy* has been carried out under my supervision. This work has not been submitted elsewhere for the award of any degree.

January 2019

(S. Ravi)
Professor, Department of Physics
Indian Institute of Technology Guwahati
Guwahati – 781 039, India

Dedicated

to

My Family

Acknowledgments

First and foremost I would like to express my sincere gratitude to my research supervisor Prof. S. Ravi, Department of Physics, Indian Institute of Technology Guwahati (IITG) for giving me an opportunity to work under him. His resourceful guidance and encouragement were the driving forces that helped me to complete my research work. It's been a great journey of learning the beautiful area of condensed matter of Physics especially magnetism under him. I shall remain grateful to him for the rest of my life.

I am thankful to my Doctoral Committee members, Prof. A. Srinivasan (Chairman), Dr. D. Pamu, and Prof. Roy P. Paily for reviewing my research work regularly and their valuable suggestions for improvement of the quality of my research work.

I would like to thank Prof. K. Sethupathi, IIT Madras for kindly extending their PPMS-VSM facility for high field magnetization measurements.

I am thankful to the current HoD, Department of Physics, Prof. Subhradip Ghosh and the former HoDs, Prof. P. Poulose and Prof. S. Basu for their immense support. I am also thankful to all the faculty members of Physics department, for their help in various ways during my research work in IIT Guwahati.

I sincerely thanks to Dr. Sidananda Saharma, scientific officer in the Department of Physics for his help and guidance to handle various instruments of the department. I am also thankful to all the scientific officers and technical officers of the central instrumental facilities of IITG for giving me access to various sophisticated instruments to carry out my research work.

I travelled the journey of my PhD with the help from my seniors and my lab mates. So, I take this opportunity to thank, in no particular order, my seniors Dr. Sunita Mohanty, Dr. Tribedi Bora, Dr. Padam, Dr. Bipul Deka and Dr. Ranganadha. I offer my special thanks to my lab mates Dr. Junmoni Barman, Pratap Behera, Aakansha, Mahananda Bramha, Ritupon Borah, Dr Vishwajit and Pushpanjali Patra for their support and cooperation and also for providing a great working environment.

My special thanks to all my batchmates for all the good times we have spent together (especially the coursework days). I express a special thanks to my senior, Mr Omkar Tripathy from Sambalpur University as he played a significant role behind the joining of my PhD at IIT Guwahati. Dr. Akhilesh Singh, Dr. P. C. Shyni, Dr. Bhargab, Dr. Santosh, Dr, Batakrushna, Dr. Ranjan Bhuyan, Dr. Bhagaban Kishan, Dr. Mahesh, Dr. Arnab, Dr. Anabil, Dr. Ravi Patta, Dr. Gyan, Aneeta, Camelia, Dolly, Rajkumar, Srinivas, Arnab, Sushmita, Shibananda and all other research scholars of department of Physics will always be remembered for their support during my PhD. Also, my sincere thanks to all those who helped me in whatever manner and I inadvertently forgot to mention their names here.

I gratefully thanks to my parents, my sister Lippsa and other family relatives for being a source of constant support and inspiration. I owe this PhD to my parents as I strongly believe that without their love and support I couldn't have completed the journey of my Phd.

I am also thankful to Ministry of Human resource and Development (MHRD) and Indian Institute of Technology, Guwahati for the financial assistantship during my PhD tenure. Department of Science and Technology, New Delhi is also acknowledged for providing financial support for various experimental facilities.

Finally, I thank the almighty God for giving me the strengths to face all the difficulties that I came across and also giving me the abilities to keep moving in this great journey called “Life”.

Bibhuti Bhusan Dash

IIT Guwahati

Abstract

In today's technologically driven world, magnetism and magnetic materials play an important role in shaping the size and efficiency of modern electronic devices. Magnetism is a broad research area in condensed matter physics which deals with several important sub areas such as giant magneto resistance, colossal-magnetoresistance, magnetic refrigeration, spintronics, exchange bias effect, magnetization reversal, *etc*. In recent years, negative magnetization or magnetization reversal (MR) and exchange bias (EB) have drawn significant interest due to their wide applications in switching devices, magnetic random access memories and spintronic devices. MR and EB have been reported in various magnetic materials like spinel chromites, molecular magnets, intermetallic alloys, garnets, *etc*. Several researchers continue to work on various magnetic materials to understand the MR and EB behaviours and to tune them for device applications. The focus of the thesis is to study the magnetization reversal and exchange bias behaviour in rare earth orthochromites.

The rare earth orthochromites $RCrO_3$ (R = Y or rare earth ions), crystallize in orthorhombically distorted perovskite structure (*Pbnm* space group). It exhibits a G type canted antiferromagnetic spin structure with a weak ferromagnetic behaviour below their Neel temperature (T_N) due to Dzyaloshinskii-Moriya interaction. The antiferromagnetic ordering temperature due to superexchange interaction in Cr^{3+} - O^{2-}- Cr^{3+} networks is found to be quite sensitive to the radius of R^{3+} ions. The T_N value is known to increase with the increase in ionic size of the R^{3+} ion *i.e.* from 135 K for $ErCrO_3$ to 289 K for $LaCrO_3$. The temperature and magnetic field dependence of magnetic moment of R^{3+} and Cr^{3+} ions often leads to interesting behaviours such as spin reorientation, magnetization reversal, exchange bias, *etc.* Moreover, $RCrO_3$ compounds are also known to show magnetically driven ferroelectric behaviour with relatively large ferroelectric ordering temperature compared to rare earth manganites.

The present thesis work is mainly focused on the study of magnetic properties of two orthochromites, $SmCrO_3$ and $GdCrO_3$. Both of them exhibit a distorted perovskite structure with orthorhombic symmetry with a Neel temperature of T_N = 197 K and 170 K respectively. $SmCrO_3$ is one of the emerging multifunctional materials due to its novel magnetic and

dielectric properties. It is known to undergo a spin reorientation transition (SR) below 40 K, where the magnetic spin configuration changes from a high temperature $\Gamma_4(G_x, A_y, F_z)$ to low temperature $\Gamma_1(A_x, G_y, C_z)$ configuration. Negative magnetization, exchange bias behaviour and multiferroic responses have been recently reported in $SmCrO_3$. In addition, the temperature dependent isotropic, antisymmetric, and anisotropic exchange interactions among the Cr^{3+} - Cr^{3+}, Cr^{3+} - Sm^{3+} and Sm^{3+} - Sm^{3+} pairs leads to various interesting magnetic behaviours such as magnetization reversal and spin reorientation transition. Similar to $SmCrO_3$, $GdCrO_3$ also exhibits the spin reorientation transition at T_{SR} = 7 K. Interesting temperature induced magnetization reversal behaviour is observed in polycrystalline $GdCrO_3$ at T_{comp} = 130 K. $GdCrO_3$ is also one of the promising materials for magnetic refrigeration applications due to its large magneto-caloric effect. The magnetic properties of $RCrO_3$ compounds are greatly affected by the substitution of other rare earth or transition elements at R and Cr site respectively. Substitution of Bi for Sm in $SmCrO_3$ induces magnetization reversal whereas zero field cooled exchange bias has been reported in $Sm_{1-x}La_xCrO_3$. However, a systematic study about the effect of substitution at the Sm^{3+}/Gd^{3+} site and Cr^{3+} site on the magnetic properties of the above two orthochromites is lacking. Thus, we have taken up the study of structural and magnetic properties of transition elements (Fe and Mn) substituted $SmCrO_3$ and $GdCrO_3$ along with Y doped $GdCrO_3$ compounds for the present thesis work. The main objective of the thesis work is to look for the possible presence of magnetization reversal and exchange bias behavior in these compounds.

Following five series of bulk samples were prepared.

i. $SmCr_{1-x}Mn_xO_3$ (x = 0.0 to 0.50)
ii. $SmCr_{1-x}Fe_xO_3$ (x = 0.0 to 0.50)
iii. $GdCr_{1-x}Mn_xO_3$ (x = 0.0 to 0.50)
iv. $GdCr_{1-x}Fe_xO_3$ (x = 0.0 to 0.50)
v. $Gd_{1-x}Y_xCrO_3$ (x = 0.0 to 1.0)

The above samples were characterized by using X-ray diffractometer (XRD), field scanning electron microscope (FESEM), Raman spectrometer and Vibrating sample magnetometer (VSM). The crystal structure was determined by recording the room temperature XRD patterns of all the samples using the Rigaku made TTRAX III difractometer. Lakeshore make vibrating sample magnetometer of model no. 7410 has been used to measure the DC magnetization as a function of temperature and field.

The thesis contains six chapters:

1. Introduction
2. *E*xperimental Techniques
3. Magnetization Reversal and Exchange Bias in Sm(Cr,Mn)O_3 and Sm(Cr,Fe)O_3 Compounds.
4. Magnetic Properties of Mn and Fe substituted $GdCrO_3$
5. Magnetic Properties of (Gd,Y)CrO_3 Compounds
6. Conclusions

Chapter 1 provides a brief introduction to the basic aspects of magnetism along with a special emphasis on the structural and magnetic properties of rare earth orthochromites. A detailed review of magnetization reversal and exchange bias behaviour observed in various layered, nanocrystalline and bulk form of different types of magnetic materials is presented. The literature on Sm and Gd based orthochromites with a special focus on their structural and magnetic properties is given. A brief outline of motivation of the present thesis work is also provided.

Chapter 2 describes the different e*x*perimental techniques used in the present thesis work, which includes the methodology of sample preparation and their characterization by employing different techniques. In addition, working principles of the sophisticated instruments like X-ray diffractometer, Raman spectrometer and vibrating sample magnetometer, *etc.,* are discussed briefly.

Chapter 3 presents the sample preparation, characterization and detailed analysis of structural and magnetic properties of Mn and Fe substituted $SmCrO_3$ compounds.

Samples of $SmCr_{1-x}Mn_xO_3$ series with x = 0 to 0.50 were prepared in single phase form by the standard citrate based sol-gel method. The lattice parameters obtained from the Rietveld refinement of the XRD patterns are found to increase with increase in Mn concentration. Temperature dependence of magnetization reveals that the samples x = 0 – 0.40 exhibit antiferromagnetic ordering. However, x = 0.50 sample shows ferromagnetic behaviour due to possible double exchange interaction in Mn^{3+} - O^{2-} - Mn^{4+} networks in the samples. The AFM transition temperature (T_N) is found to decrease with increase in Mn concentration. The parent compound ($x = 0$) and $x = 0.05$ samples show spin reorientation transition at $T_{SR} = 35$ K due to the change in the magnetic spin structure of Cr^{3+} ions. Interesting reversal in the sign of magnetization is observed as the temperature is reduced under field cooled condition for $x = 0.10$, 0.15, 0.20, and 0.30 samples. The magnetic compensation temperature (T_{comp}) increases from 51 K for $x = 0.10$ to 126 K for $x = 0.30$ samples as a result of suppression of the weak ferromagnetic component of spin canted Cr^{3+} ions. Exchange bias behaviour is observed in $x = 0.10$ sample which changes its sign across the T_{comp}. The origin of magnetization reversal is explained by considering the competition between the weak ferromagnetic component of canted Cr^{3+} ions and the paramagnetic moment of Sm^{3+} ions and Mn^{3+} ions under the influence of negative internal field arising from AFM ordered Cr^{3+} ions.

Single phase samples of $SmCr_{1-x}Fe_xO_3$ with $x = 0 – 0.50$ were prepared by sol-gel method and the prepared samples are found to crystallize in orthorhombic structure. All samples show AFM ordering. The magnetization reversal with $T_{comp} = 75$ K and 148 K is observed in $x = 0.10$ and 0.15 samples respectively along with a low temperature spin reorientation. The $x = 0.10$ sample exhibits tunable exchange bias behaviour. For $T < T_{comp}$, bipolar switching of magnetization is demonstrated. The origin of magnetization reversal and tunable exchange bias is attributed to the competition between the canted ferromagnetic component of the Cr^{3+} ions and the paramagnetic moment of Sm^{3+} and Fe^{3+} ions under the influence negative internal field due to the AFM ordered Cr^{3+} ions.

Chapter 4 provides a detailed study of structural and magnetic properties of $GdCrO_3$ based samples by substituting Mn and Fe ions at Cr site.

Samples of $GdCr_{1-x}Mn_xO_3$ ($x = 0 – 0.50$) were prepared by sol-gel method and the prepared samples are found to crystallize in orthorhombic structure with *Pbnm* space group. The lattice parameters are found to increase with increase in Mn concentration. The Neel temperature, T_N is found to decrease from $T_N = 174$ K for $x = 0$ to 91 K for $x = 0.50$. Magnetization as a function of temperature shows the presence of magnetization reversal in $x = 0$ and $x = 0.05$ samples with T_{comp} values of 136 K and 139 K respectively. No magnetization reversal is observed in $x = 0.10 – 0.30$ samples. However, the MR reappears in

$x = 0.40$ and $x = 0.50$ samples at low temperatures around 30 K. The origin of magnetization reversal in $x = 0$ and 0.05 samples is explained by considering the Gd^{3+} and Mn^{3+} ions as paramagnetic entities under the influence of internal magnetic field from AFM ordered Cr^{3+} ions, whereas for $x = 0.40$ and $x = 0.50$ samples it is attributed to the spin reorientation transition from Γ_4 to Γ_1 phase. Switching of the polarity of magnetization is demonstrated for $x = 0$ and 0.05 samples below their T_{comp} just by changing the magnitude of external magnetic field by keeping its direction fixed. Tunable exchange bias is observed in samples showing the magnetization reversal.

Samples of $GdCr_{1-x}Fe_xO_3$ ($x = 0 – 0.50$) were prepared in single phase form. Raman spectroscopic measurement shows the presence of an oxygen breathing mode due to the transfer of electron between Fe^{3+} and Cr^{3+} ions. All samples show AFM transitions. The T_N value is found to decrease with increase in Fe concentration upto $x = 0.20$ and beyond that it is found to increase due to the considerable concentration of Fe^{3+} - O^{2-} - Fe^{3+} networks having superexchange interactions. MR is observed only in the parent compound ($x = 0$) whereas it disappears in the Fe substituted samples. However, for $x = 0.40$ sample, magnetic compensation without any negative magnetization is observed at $T_{comp} = 125$ K. The impedance spectrum and, AC conductivity data were measured at different temperature over a wide range of frequency. The impedance spectra measured at different temperature reveal the presence of a thermally activated relaxation process in the samples. The Nyquist plots (Z'' vs. Z') show two semicircular arcs which indicate the contribution of two electroactive regions towards the relaxation dynamics. The real part (σ') of ac conductivity data of the Fe substituted samples are found to be lower than that of the parent compound and it is attributed to the increase in the average bond length of Cr/Fe – O bonds which results in a weaker overlap between the *p* orbitals of oxygen and *d* orbitals of Cr^{3+} cations.

Chapter 5 discusses the effect of nonmagnetic Y substitution on the structural and magnetic properties of $GdCrO_3$. Samples of $Gd_{1-x}Y_xCrO_3$ ($x = 0 - 1.0$) were prepared in single phase from by solgel method. The samples are found to crystallize in orthorhombic structure with *Pbnm* space group. Lattice parameters increase systematically with increase in Y concentration. The Raman spectra recorded at room temperature reveal the presence of structural distortion in the lattice which increases upon Y substitution. The temperature dependence of magnetization reveals a systematic fall in the antiferromagnetic transition temperature (T_N) from $T_N = 174$ K ($x = 0$) to 142 K ($x = 1.0$). Magnetization measured as a function of temperature in the field cooled mode shows magnetization reversal behaviour which is observed upto $x = 0.70$ samples. The field variation of magnetization (M-H) measured in the field cooled mode for $x = 0 – 0.50$ samples indicates the presence of tunable exchange bias in the system which changes its sign across the compensation temperature. The exchange bias behaviour is explained by considering the anisotropic exchange interaction between the ferromagnetic component of canted Cr^{3+} ions and the paramagnetic moment of Gd^{3+} ions under the influence of negative internal field.

Chapter 6 provides an overall brief summary of results obtained from the study of above five series of Sm-Cr-O and Gd-Cr-O based bulk samples. Both Mn and Fe substitution at Cr site of $SmCrO_3$ gives rise to magnetization reversal behaviour which is absent in the parent compound $SmCrO_3$. The MR behaviour is observed over wide range of Mn concentration i.e. for $x = 0.10 – 0.30$, whereas in the case of Fe substitution, it is observed only for $x = 0.10$ and $x = 0.15$ samples. The compensation temperature and exchange bias field observed for 10 at% Fe substitution is found to be higher than that of 10 at% Mn substituted sample. In Mn substituted $GdCrO_3$ samples, magnetic compensation is observed for $x = 0.05$, 0.40 and 0.50 samples whereas, the magnetization reversal is found to be suppressed upon Fe substitution. However, for $x = 0.40$ sample, magnetic compensation without any negative magnetization is observed. Complex impedance spectroscopic studies of Fe substituted $GdCrO_3$ reveal the presence of non-Debye type thermally activated dielectric relaxation process in the samples. In $Gd_{1-x}Y_xCrO_3$ series, magnetization reversal is observed for $x = 0$ - 0.70 samples and the compensation temperature is found to decrease as a result of the substitution of nonmagnetic Y ions. This chapter also discuss briefly about some of the future scopes of research in this area.

List of Abbreviations used in this Thesis

AFM Antiferromagnetic

BSE Back scattered electrons

CEP Conduction electron polarization

CW Curie-Weiss

CN Co-ordination number

DM Dzyaloshinskii-Moriya

EB Exchange Bias

EDS Energy dispersive X-ray spectroscopy

FC Field cooled

FE Field emission

FESEM Field emission scanning electron microscope

FM Ferromagnetic

GMR Giant magnetoresistance

JPL Jonscher's Power Law

MR Magnetization Reversal

NM Negative Magnetization

PM Paramagnetic

RKKY Ruderman, Kittel, Kasuya and Yosida

SG Space group

SR Spin reorientation

TAMRAM Thermally assisted magnetoresistive random access memory

VSM Vibrating sample magnetometer

XRD X-ray diffraction

ZFC Zero field cooled


भारतीय प्रौद्योगिकी संस्थान गुवाहाटी
Indian Institute of Technology Guwahati

Table of Contents

Contents **Page No.**

Abstract...**i**
List of Abbreviations used in this Thesis.. **vii**
List of Figures.. **xiii**
List of Tables... **xxi**

Chapter 1: Introduction.. **1**

1.1 Crystal Structure.. 2
1.2 Crystal Field Effect 3
1.3 Magnetic Exchange Interaction... 6
  1.3.1 Direct Exchange Interaction 7
  1.3.2 Superexchange Interaction... 7
  1.3.3 Double Exchange Interaction.. 8
  1.3.4 Ruderman-Kittel-Kasuya-Yosida (RKKY) Interaction 10
  1.3.5 Dzyaloshinskii-Moriya Interaction 10
1.4 Magnetic Orderings... 11
  1.4.1 Diamagnetic Materials 11
  1.4.2 Paramagnetic Materials.. 12
  1.4.3 Ferromagnetic Materials 13
  1.4.4 Antiferromagnetic Materials 13
  1.4.5 Ferrimagnetic Materials 14
1.5 Magnetic Anisotropy.. 15
  1.5.1 Magnetocrystalline Anisotropy... 15
  1.5.2 Shape Anisotropy.. 16
  1.5.3 Stress Anisotropy.. 16
  1.5.4 Exchange Anisotropy... 17
1.6 Magnetization Reversal... 17
  1.6.1 Magnetization Reversal in Ferrimagnetic materials 18

1.6.2 Magnetization Reversal in Intermetallic compounds 19

1.6.3 Magnetization Reversal in Ferromagnetic and Antiferromagnetic Heterostructures 19

1.6.4 Magnetization Reversal in Canted Antiferromagnetic Materials 20

1.7 Exchange Bias 21

1.8 Dielectric Properties of Materials 24

1.8.1 Complex Electric Impedance 25

1.8.2. Complex dielectric constant 25

1.8.3. Complex AC conductivity 26

1.9 Rare Earth Orthochromites 26

1.9.1 $SmCrO_3$ 30

1.9.2 $GdCrO_3$ 31

1.10 Motivation 32

Chapter 2: Experimental Techniques **35**

2.1 Sample Preparation 35

2.1.1 Sol-gel Method 35

2.1.2 High Temperature Furnaces 36

2.2 Characterization Techniques 38

2.2.1 X-ray Diffraction 38

2.2.2 Raman Spectroscopy 40

2.2.3 Field Emission Scanning Electron Microscope 42

2.2.4 Energy Dispersive X-ray Spectroscopy 44

2.2.5 Vibrating Sample Magnetometer 45

2.2.6 Dielectric Measurement 47

Chapter 3: Magnetization Reversal and Exchange Bias in $Sm(Cr,Mn)O_3$ and $Sm(Cr,Fe)O_3$ Compounds **49**

3.1 Mn Substituted $SmCrO_3$ 49

3.1.1 Sample Preparation and Characterization 49

3.1.2 Structural Properties 50

3.1.3 Magnetic Properties 55

(i) Magnetization Reversal 59
(ii) Magnetization Switching 67
(iii) Exchange Bias 67
3.2 Fe Substituted $SmCrO_3$ 73
3.2.1 Sample Preparation and Characterization 73
3.2.2 Structural properties 73
3.2.3 Magnetic Properties 78
(i) Magnetization Reversal 80
(ii) Magnetization Switching 83
(iii) Exchange Bias 84
3.3 Conclusions 88
Chapter 4: Magnetic Properties of Mn and Fe Substituted $GdCrO_3$ 91
4.1 Mn Substituted $GdCrO_3$ 91
4.1.1 Sample Preparation and Characterization 91
4.1.2 Structural properties 92
4.1.3 Magnetic Properties 97
(i) Magnetization Reversal 99
(ii) Magnetization Switching 101
(iii) Exchange Bias 102
4.2 Fe Substituted $GdCrO_3$ 108
4.2.1 Sample Preparation and Characterization 108
4.2.2 Structural properties 108
4.2.3 Magnetic Properties 115
4.2.4 Impedance spectroscopy 120
4.3 Conclusions 127
Chapter 5: Magnetic Properties of (Gd,Y)CrO_3 Compounds 129
5.1 Yttrium (Y) Substituted $GdCrO_3$ 129
5.1.1 Sample Preparation and Characterization 129
5.1.2 Structural properties 130

5.1.3 Magnetic Properties 137
5.2 Conclusions 147

Chapter 6: Conclusions **149**

References **157**

Publications **165**

List of Figures

Chapter 1

Figure 1.1: Crystal structure of (a) Cubic perovskite, (b) orthorhombic perovskite unit cell. The green, blue and orange spheres represent the A (R^{3+}), B (Cr^{3+}), and oxygen ions, respectively [20]. 2

Figure 1.2: The electronic distribution of five d orbitals. In presence of cubic crystal field, the fivefold degeneracy of d orbital is lifted, and it splits into two e_g $(dx2-y2$ and $d3z2-r2)$ and three t_{2g} (d_{xy}, d_{yz} and d_{zx}) orbitals. Adapted from [26]. 4

Figure 1.3: The crystal field in an (a) octahedral environment and (b) tetrahedral environment of d orbital in transition elements. 5

Figure 1.4: The Jahn-Teller effect in Mn^{3+} ($3d^4$) ion that leads to splitting of both t_{2g} and e_g levels. 6

Figure 1.5: Schematic diagram showing the spin arrangements in (a) an antiferromagnetic superexchange interaction and (b) a ferromagnetic superexchange interaction. 8

Figure 1.6: (a) Schematic of double exchange mechanism involving two Mn ions and one O ion. (b) The mobility of e_g electrons improves if the localized spins are polarized and parallel to each other. 9

Figure 1.7: Different types of antiferromagnetic order in a magnetic cell. The up and down arrows represent the orientation of the spin. Adapted from [37] 14

Figure 1.8: Reversal of magnetization observed in the temperature dependent field cooled magnetization of Co_2VO_4 for H = 700 Oe. Adapted from [45]. 19

Figure 1.9: Schematic representation of spin configuration of a FM-AFM couple at different stages of a shifted hysteresis loop for a system with large AFM anisotropy [18]. 23

Figure 1.10: Magnetic spin configuration in Γ_1, Γ_2 and Γ_4 with *Pbnm* symmetry. Adapted from [10]. 27

Figure 1.11: Magnetization reversal observed during the field cooled magnetization of $TmCrO_3$ for H = 300 Oe. Adapted from [70]. 29

Chapter 2

Figure 2.1: Block diagram of furnace with maximum operating temperature of 1200 ˚C. ... 37

Figure 2.2: Ray diagram of X- ray diffractometer. ... 39

Figure 2.3: Schematic diagram of Raman spectrometer. ... 42

Figure 2.4: Schematic view of the field emission scanning electron microscope. ... 43

Figure 2.5: (a) Electrons and photons emanating from tear-shaped interaction volume during electron beam impingement on specimen surface, and (b) Energy spectrum of electrons emitted from the specimen surface. ... 44

Figure 2.6: Block diagram of a vibrating sample magnetometer. ... 46

Chapter 3

Figure 3.1: XRD patterns of $SmCr_{1-x}Mn_xO_3$ samples for $x = 0 – 0.50$. ... 51

Figure 3.2: XRD patterns along with Rietveld refined data for x = 0, 0.30 and x = 0.50 samples. The circles represent the experimental points and solid line (black) represents the refined data. The bottom line (green) shows the difference between experimental and refined data. The vertical lines (blue) are the allowed Bragg position. ... 52

Figure 3.3: FESEM micrographs of (a) x = 0, (b) x = 0.30 and (c) x = 0.50 samples along with the EDS spectrum of x = 0.30 sample (d). ... 54

Figure 3.4: Temperature variation of magnetization of $SmCr_{1-x}Mn_xO_3$ ($x = 0 – 0.50$) samples under ZFC and FC modes for H = 100 Oe. Inset shows the temperature variation of dM_{ZFC}/dT for x = 0 sample (a) and enlarged view of relevant ZFC curves. ... 57

Figure 3.5: The temperature dependence of inverse susceptibility (χ^{-1}) for the samples (a) x = 0.10, (b) x = 0.30, (c) x = 0.40 and (d) x = 0.50 along with the fitting to the Curie-Weiss (CW) law. ... 58

Figure 3.6: Temperature variation of magnetization of (a) x = 0.10 (b) x = 0.15 (c) x = 0.20 and (d) x = 0.30 samples under ZFC and FC modes for H = 100 Oe. The solid line (black) represents fit to eq. 3.1. ... 61

Figure 3.7: M_{Cr} and H_I as a function of Mn concentration (x) for H = 100 Oe in FC mode. 61

Figure 3.8: M-T curves in ZFC and FC conditions of x = 0.10 samples at (a) H = 100 Oe, (b) H = 500 Oe, (c) H = 1000 Oe and (d) H = 2000 Oe. The solid curve (black) represents the fitted data obtained using eq. 3.1. ... 63

Figure 3.9: M-T curves in ZFC and FC conditions of $x = 0.15$ sample at (a) $H = 100$ Oe, (b) $H = 500$ Oe, (c) $H = 1000$ Oe and (d) $H = 2000$ Oe. The solid curve (black) represents the fitted data obtained using eq. 3.1. 63

Figure 3.10: M-T curves in ZFC and FC conditions of $x = 0.20$ sample at (a) $H = 100$ Oe, (b) $H = 500$ Oe, (c) $H = 1000$ Oe and (d) $H = 2000$ Oe. The solid curve (black) represents the fitted data obtained using eq. 3.1. 64

Figure 3.11: M-T curves in ZFC and FC conditions of $x = 0.30$ sample at (a) $H = 100$ Oe and (b) $H = 500$ Oe. The solid curve (black) represents the fitted data obtained using eq. 3.1. ... 64

Figure 3.12: Variations of (a) M_{Cr} and (b) H_I as a function of applied field (H) for $x = 0.10$, 0.15 and $x = 0.20$ samples. 65

Figure 3.13: ${}^{\Delta M}/_{M_{ZFC}}$ versus temperature plots for $x = 0.10$ and $x = 0.20$ samples. For clarity, the data of $x = 0.10$ is multiplied by a factor of 10. 66

Figure 3.14: Bipolar switching of magnetization for (a) $x = 0.15$ and (b) $x = 0.20$ samples at $T = 90$ K and $T = 110$ K respectively. 67

Figure 3.15: M-H loops recorded at different temperatures for $x = 0.10$ sample under FC condition for an applied field of $H = 5000$ Oe. 68

Figure 3.16: M-H loops recorded at different temperatures for (a) $x = 0.20$ and (b) $x = 0.30$ samples under FC condition for an applied field of $H = 5000$ Oe. 69

Figure 3.17: Enlarged view of M-H loops in the vicinity of coercive fields under FC condition for $H = 5000$ Oe measured at different temperatures for $x = 0.10$ sample. 69

Figure 3.18: The temperature dependence of (a) exchange bias field, H_{EB} (upper panel) and (b) effective coercive field, H_c^{eff} (lower panel) for $x = 0.10$ ($SmCr_{0.90}Mn_{0.10}O_3$) sample measured under a cooling field of $H = 5000$ Oe. 70

Figure 3.19 Schematic diagram representing the arrangement of canted Cr^{3+} moment and the PM component of Sm^{3+} and Mn^{3+} moments under field cooled condition at (a) $T > T_{comp}$ and (b) $T < T_{comp}$. 72

Figure 3.20: XRD patterns of $SmCr_{1-x}Fe_xO_3$ compounds for $x = 0 – 0.50$. 74

Figure 3.21: XRD patterns along with Rietveld refinement of $SmCr_{1-x}Fe_xO_3$ for (a) $x = 0$, (b) 0.30 and (c) $x = 0.50$ samples. The circles represent the experimental points and solid line (black) represents refined data. The bottom line (green) shows the difference between experimental and refined data. The vertical lines (blue) are the allowed Bragg position. 75

Figure 3.22: FESEM micrographs of (a) $x = 0.10$ and (b) $x = 0.50$ samples along with their EDS spectrum in (c) and (d), respectively. 77

Figure 3.23: Temperature variation of magnetization in ZFC and FC conditions for $SmCr_{1-x}Fe_xCrO_3$ ($x = 0 - 0.50$) samples under an applied field of $H = 100$ Oe. Insets show the enlarged view of ZFC magnetization of $x = 0.10$ and $x = 0.15$ samples (c and d). 79

Figure 3.24: *M-T* curves of (a) $x = 0.10$ and (b) $x = 0.15$ samples measured at different magnetic fields under FC condition showing the decrease in compensation temperature (T_{comp1}). The magnetization shifts to the positive values when the field is increased to $H = 2000$ Oe. 80

Figure 3.25: *M-T* curves of $x = 0.10$ sample under FC condition for (a) $H = 100$ Oe (b) $H = 200$ Oe (c) $H = 500$ Oe and (d) $H = 1000$ Oe. 81

Figure 3. 26: *M-T* curves of $x = 0.15$ sample under FC condition for (a) $H = 100$ Oe (b) $H = 200$ Oe (c) $H = 500$ Oe and (d) $H = 1000$ Oe. 82

Figure 3.27: Variations of (a) M_{Cr} and (b) $-H_I$ as a function applied magnetic field for $x = 0.10$ and $x = 0.15$ samples. 83

Figure 3.28: Bipolar switching of magnetization for (a) $x = 0.10$ and (b) $x = 0.15$ samples at $T = 50$ K and $T = 120$ K respectively. 84

Figure 3.29: *M-H* loops of $x = 0.10$ sample recorded at different temperatures under FC condition for $H = 5000$ Oe. 85

Figure 3.30: (a) – (f) Enlarged view of *M-H* loops in the vicinity of coercive fields measured at different temperatures for $x = 0.10$ sample under field cooled conditions for $H = 5000$ Oe. 86

Figure 3.31: The temperature dependence of (a) exchange bias field, H_{EB} (upper panel) and (b) effective coercive field, H_c^{eff} (lower panel) for $x = 0.10$ ($SmCr_{0.90}Fe_{0.10}O_3$) sample measured under a cooling field of $H = 5000$ Oe. 87

Chapter 4

Figure 4.1: XRD patterns of $GdCr_{1-x}Mn_xO_3$ samples for $x = 0 – 0.50$. 93

Figure 4.2: XRD patterns along with Rietveld refinement for $x = 0$, 0.10, 0.30 and 0.50 samples. The circles represent the experimental points and solid line (black) represents

refined data. The bottom line (green) shows the difference between experimental and refined data. The vertical lines (blue) are the allowed Bragg position. 94

Figure 4.3: FESEM images recorded for (a) $x = 0$ and (b) $x = 0.50$ samples along with their EDS spectrum shown in Figs. (c) and (d) respectively. 96

Figure 4.4: Temperature variation of magnetization in ZFC and FC conditions for $GdCr_{1-x}Mn_xO_3$ ($x = 0$ to 0.50) samples. Insets (a, g and h) show the relevant ZFC magnetization in expanded scale. 98

Figure 4.5: *M-T* curves in ZFC and FC conditions for $x = 0$ sample at (a) $H = 100$ Oe, (b) $H = 200$ Oe, (c) $H = 500$ Oe and (d) $H = 1000$ Oe. The solid curve (black) represents the fitted data. 99

Figure 4.6: *M-T* curves in ZFC and FC conditions for $x = 0.05$ sample at (a) $H = 100$ Oe, (b) $H = 500$ Oe, (c) $H = 1000$ Oe and (d) $H = 2000$ Oe. The solid curve (black) represents the fitted data. 100

Figure 4.7: Variation of M_{Cr} and H_I as a function of cooling fields H for $x = 0$ and $x = 0.05$ samples. 101

Figure 4.8: Bipolar switching of magnetization at $T = 110$ K for (a) $x = 0$ and (b) $x = 0.05$ samples. 102

Figure 4.9: *M-H* loops of (a) $x = 0$ and (b) $x = 0.05$ samples under FC mode at $T = 30$ K and 200 K for $H = 3000$ Oe. 103

Figure 4.10: (a) - (f) Enlarged view of *M-H* loops in the vicinity of coercive fields under FC condition for $H = 3000$ Oe measured at different temperatures for $x = 0$ and $x = 0.05$ samples. 104

Figure 4.11: (a) - (f) Enlarged view of *M-H* loops in the vicinity of coercive fields under FC condition for $H = 3000$ Oe measured at different temperatures for $x = 0.50$ sample. 104

Figure 4.12: Temperature dependence of exchange bias field (H_{EB}) for (a) $x = 0$ (b) $x = 0.05$ and (c) $x = 0.50$ samples. 105

Figure 4.13: XRD patterns of $GdCr_{1-x}Fe_xO_3$ samples for $x = 0 – 0.50$. 109

Figure 4.14: XRD patterns of $x = 0.10$, 0.30 and 0.50 samples along with their Rietveld refined data shown as solid lines. The circles represent the experimental points and solid line (black) represents the refined data. The bottom line (green) shows the difference between experimental and refined data. The vertical lines (blue) are the allowed Bragg position. ... 110

Figure 4.15: Lattice parameters *a*, *b*, and *c* as a function of Fe concentration (x). Inset shows the variation of average Cr/Fe – O bond length with x. 111

Figure 4.16: FESEM images recorded for (a) x = 0.20 and (b) x = 0.50 samples along with their EDS spectrum shown in Figs. (c) and (d) respectively. 113

Figure 4.17: (a) Raman spectra measured at room temperature for $GdCr_{1-x} Fe_xO_3$ (x = 0 – 0.50) samples. (b) Expanded view of the Raman spectra over the wave number range of 100 – 600 cm^{-1} for x = 0 – 0.50 samples. 114

Figure 4.18: Magnetization as a function of temperature for $GdCr_{1-x}Fe_xO_3$ (x = 0 – 0.50) samples in ZFC and FC conditions for an applied field of H = 100 Oe. The inset (a) shows the ZFC magnetization of x = 0 sample in an expanded scale. 117

Figure 4.19: Inverse of susceptibility (χ^{-1}) vs. temperature for x = 0.0, 0.05, 0.10, 0.20, 0.30 and 0.40 samples along with the Curie-Weiss (CW) fit shown as solid lines in the PM region. 118

Figure 4.20: *M-H* loops of $GdCr_{1-x}Fe_xO_3$ (x = 0 – 0.50) samples recorded at T = 25 K under ZFC condition. The inset shows the variation of M_r as a function of Fe concentration (x).. 119

Figure 4.21: Frequency dependence of the real part of the impedance (Z′) for (a) x = 0.0, (b) x = 0.10, (c) x = 0.30 and (d) x = 0.50 samples in the temperature range of 323 to 423 K. . 120

Figure 4.22: Frequency dependence of the imaginary part of the impedance (-Z″) for the samples (a) x = 0.0 (b) x = 0.10 (c) x = 0.30 and (d) x = 0.50 measured at different temperatures. 121

Figure 4.23: Plots of $\ln f_{max}$ vs. 10^3/T along with fit to Arrhenius law (solid line). The vertical lines represent the error in the fitted data. 122

Figure 4.24: -Z″ vs Z′ plots for (a) x = 0, (b) x = 0.10, (c) x = 0.30 and (d) x = 0.50 samples at some selected temperatures. 123

Figure 4.25: Frequency dependence of σ' for different concentration of Fe (x = 0, 0.10, 0.20, 0.30, 0.40, and 0.50) measured at T = 393 K. 124

Figure 4.26: Frequency dependence of real part of ac conductivity (σ') for (a) x = 0, (b) x = 0.10, (c) x = 0.30 and (d) x = 0.50 samples measured at different temperatures. The solid lines represent fit to Jonscher's power law (JPL). 125

Figure 4.27: Variation of dc conductivity as a function of inverse of temperature (*1/T*) for $x = 0$, 0.10, 0.30 and $x = 0.50$ samples. Solid lines (red) represent the fitted data as per Arrhenius law for conductivity both for grains and grain boundaries contribution. 126

Chapter 5

Figure 5.1: X- ray diffraction patterns of $Gd_{1-x}Y_xCrO_3$ ($x = 0 – 1.0$) samples. The inset shows the enlarged view of (112) peak of various samples.. 131

Figure 5.2: XRD patterns of $x = 0$, 0.50 and 1.0 samples along with their Rietveld refinement. The circles represent the experimental points and solid line (black) represents refined data. The bottom line (green) shows the difference between experimental and refined data. The vertical lines (blue) are allowed Bragg position. 132

Figure 5.3: Variation of lattice parameters *a*, *b*, *c*, and unit cell volume (*Vol*) of $Gd_{1-x}Y_xCrO_3$ ($x = 0 – 1.0$) samples as a function of Y concentration (x). 133

Figure 5.4: Raman Spectra of $Gd_{1-x}Y_xCrO_3$ samples for $x = 0$ to 1.0 measured at room temperature. Arrows indicate the blue shifting and the splitting of $A_g(5)$ mode. 135

Figure 5.5: FESEM micrographs of (a) $x = 0$, (b) $x = 0.30$, (c) $x = 0.70$ and (d) $x = 1.0$ samples along with the EDS spectrum of (e) $x = 0.30$ and (f) $x = 0.70$ samples. 136

Figure 5.6: *M-T* curves of (a) $x = 0$, (b) $x = 0.10$, (c) $x = 0.30$, (d) $x = 0.50$, (e) $x = 0.70$ and (f) $x = 1.0$ samples measured in zero field cooled (ZFC) and field cooled (FC) conditions with an applied field of $H = 100$ Oe. The solid black lines represent the fitted data. Insets show the expanded view of the ZFC magnetization data measured at $H = 100$ Oe. 137

Figure 5.7: Inverse susceptibility (χ^{-1}) as a function of temperature for (a) $x = 0$, (b) $x = 0.10$, (c) $x = 0.30$, (d) $x = 0.50$, (e) $x = 0.70$ and (f) $x = 1.0$ samples. The solid line (red) represents the fitting to the Curie-Weiss law. 138

Figure 5.8: Schematic diagram showing the orientation of weak FM component of Cr^{3+} (M_{Cr}) and the net PM moment of Gd^{3+} ions (M_{Gd}) above and below the compensation temperature (T_{comp})... 140

Figure 5.9: Magnetization switching between negative and positive values under different positive magnetic fields for (a) $x = 0.10$ (b) $x = 0.30$ and (c) $x = 0.50$ samples at $T = 100$K, 80 K and $T = 60$ K respectively. 141

Figure 5.10: M-H loops recorded at T = 25 K under zero field cooled condition (ZFC) for x = 0 – 1.0 samples. 143

Figure 5.11: (a) – (f) Enlarged view of M-H loops in the vicinity of coercive fields measured under the field cooled condition for H = 3 kOe at different temperatures for x = 0 and x = 0.10 samples. 144

Figure 5.12: (a) – (f) Enlarged view of M-H loops in the vicinity of coercive fields measured under the field cooled condition for H = 3 kOe at different temperatures for x = 0.30 and x = 0.50 samples. 144

Figure 5.13: The temperature dependence of (a) exchange bias field, H_{EB} (upper panel) and (b) effective coercive field, H_c^{eff} (lower panel) for $Gd_{1-x}Y_xCrO_3$ samples with x = 0, x = 0.10, x = 0.30 and x = 0.50 samples measured under a cooling field of H = 3 kOe. 145

List of Tables

Chapter 1

Table 1.1: Atomic positions in rare earth orthochromites with *Pbnm* space group................ 3

Chapter 3

Table 3.1: Parameters obtained from the Rietveld refinement of XRD patterns of $SmCr_{1-x}Mn_xO_3$ ($x = 0$ to 0.50) samples.. 53

Table 3.2: The cationic ratio determined from EDS analysis for $x = 0 – 0.50$ samples. 55

Table 3.3: Parameters obtained from Curie-Weiss law fit, compensation temperature (T_{comp}) and Neel temperature (T_N) for $SmCr_{1-x}Mn_xO_3$ ($x = 0$ to 0.50) samples................................. 59

Table 3.4: Parameters obtained from the Rietveld refinement of XRD patterns of $SmCr_{1-x}Fe_xO_3$ ($x = 0$ to 0.50) samples. 76

Chapter 4

Table 4.1: Parameters obtained from the Rietveld analysis of the samples $GdCr_{1-x}Mn_xO_3$ ($x =$ 0 to 0.50). 95

Table 4.2: The cationic ratio determined from EDS analysis for $x = 0$, 0.20, 0.30, 0.40 and 0.50 samples.. 96

Table 4.3: Parameters obtained from the Rietveld analysis of the samples $GdCr_{1-x}Fe_xO_3$ ($x =$ 0 to 0.50). 112

Table 4.4: The cationic ratio determined from EDS analysis for $x = 0 - 0.50$ samples. 113

Chapter 5

Table 5.1: Parameters obtained from the Rietveld analysis of the samples $Gd_{1-x}Y_xCrO_3$ ($x = 0$ to 1.0). 133

Table 5.2: The AFM transition temperature (T_N), magnetic compensation temperature (T_{comp}) and parameters obtained from the fitting to FC magnetization data using eq. 5.1 at an external field of $H = 100$ Oe for $Gd_{1-x}Y_xCrO_3$ samples. 142

Chapter 1

Introduction

Magnetism has been an important topic of interest among physicists, material scientists and engineers since its discovery in loadstone by the ancient Greeks. Magnetic materials play key role in many essential areas of modern technology such as generation and distribution of electrical power, communication, information storage, industrial machines, medical equipments, *etc*. The discovery of giant magnetoresistance (GMR) in magnetic multilayer brought tremendous technological applications in the areas of magnetic field sensors and information storage [1–3]. GMR is the change in electrical resistance of a sample in response to an external magnetic field and it shows that the transport properties can be controlled by the applied magnetic field. Such materials find potential application in spintronics, where the spin properties can be exploited in addition to charge degrees of freedom while designing the electronic devices [4]. This additional degree of freedom is expected to increase efficiency, speed and miniaturization, *etc.*, of the device. Magnetic properties such as exchange bias and magnetization reversal are also known to play a key role in controlling the properties of spin valve and spintronic devices [5,6]. Therefore, exchange bias and magnetization reversal have drawn special interest in multilayer thin films as well as in bulk magnetic materials such as orthovandates, orthomanganites, orthochromites, spinels, intermetallic alloys, *etc* [7].

In the recent years among all magnetic perovskites, the Rare earth (R) orthochromites, $RCrO_3$ have drawn a significant research interests due to their rich magnetic, ferroelectric, and magneto-electric properties [8–11]. In addition to that these materials also exhibit interesting magnetization reversal and exchange bias behavior [12–16]. Recently, $RCrO_3$ compounds have emerged as a potential candidate for magnetic refrigeration in the low temperature regime [17]. Beside their multiferroic property, $RCrO_3$ compounds have also been studied for catalytic properties towards the development of solid oxide fuel cell due to their high conductivity at elevated temperature. The above properties suggest that $RCrO_3$ can be a potential candidate for technological applications in spin valves, temperature assisted magnetic random access memory, spintronics, magnetic refrigeration and thermomagnetic switches, *etc* [6,18,19].

The present thesis work is mainly dedicated to the study of magnetization reversal and exchange bias properties in orthochromites. In the following sections the structural and magnetic properties of rare earth orthochromites along with some of the basic mechanisms responsible for magnetism are briefly reviewed.

1.1 Crystal Structure

The rare earth orthochromites, $RCrO_3$ exhibit the orthorhombic distorted perovskite structure with space group *Pbnm* at room temperature [9]. The ideal perovskite is an ABO_3 type compound with simple cubic structure where the A cations occupy corners of the cube (0, 0, 0), B cation takes the body-centre position (½, ½, ½) and the O ions are at the face centered position (½, ½, 0) of the cube as shown in Fig 1.1(a). The deviation of $RCrO_3$ compounds from the ideal cubic structure to orthorhombic *Pbnm* structure is due to three structural modifications, namely (i) displacement of the cation, (ii) tilt/rotation in the CrO_6 octahedra, and (iii) CrO_6 distortion.

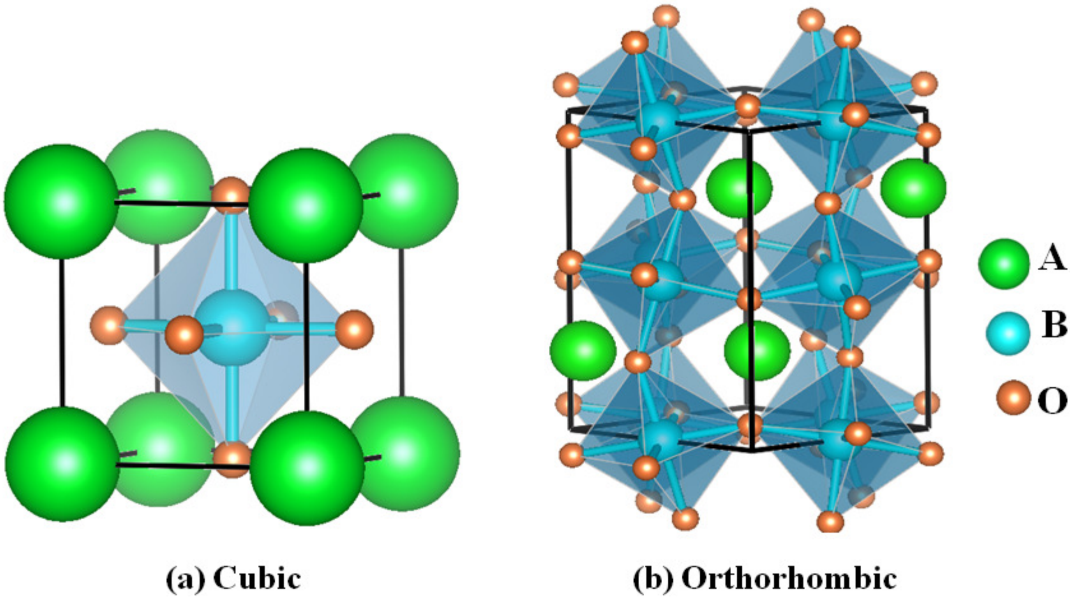

(a) Cubic (b) Orthorhombic

Figure 1.1: Crystal structure of (a) Cubic perovskite, (b) Orthorhombic perovskite unit cell. The green, blue and orange spheres represent the A (R^{3+}), B (Cr^{3+}), and oxygen ions, respectively [20].

The degree of distortion from the ideal cubic perovskite structure can be calculated using the Goldschmidt's tolerance factor [21], $t = \frac{(r_A + r_O)}{\sqrt{2}(r_B + r_O)}$, where r_A, r_B and r_O are the ionic radii of the A site and B site cations, and the oxygen ions, respectively. The value of 't' is one (t = 1) for the cubic structure while any deviation from t = 1 gives rise to the structural distortion. For a small decrease in t from its ideal value of one, the crystal structure changes from cubic to orthorhombic or rhombohedral symmetry. The perovskite structure is possible only for $0.75 \leq t \leq 1.00$ [22,23]. In $Nd_{1-x}La_xCrO_3$, the value of t increases from 0.882 (x = 0) to 0.907 (x = 1) which indicates a reduction in lattice distortion and its tendency towards the ideal cubic structure with La substitution [24]. The crystal structure of $RCrO_3$ compounds with orthorhombic symmetry is shown in Fig. 1.1(b) where a lowering in symmetry from the ideal cubic structure can be seen due to tilt in the CrO_6 octahedra. The general atomic positions in *Pbnm* settings for $RCrO_3$ are given in Table 1.1

Table 1.1: Atomic positions in rare earth orthochromites with *Pbnm* space group.

Atoms	**Location**	**Point Symmetry**	**(x, y, z)**
R	(4c)	m	(x, y, 1/4) ≅ (0.99, 0.03, 1/4)
Cr	(4b)	$\bar{1}$	(½, 0, 0) ≅ (1/2, 0, 0)
O (1)	(4c)	m	(x, y, 1/4) ≅ (0.07, 0.049, 1/4)
O (2)	(8d)	1	(x, y, z) ≅ (0.72, 0.28, 0.04)

1.2 Crystal Field Effect

The local environment within a crystal of a solid greatly influences the energy levels of an atom. The net electric field produced from the neighboring atoms in the crystal is known as the crystal field [25]. The symmetry of the local environment plays a major role in determining the nature of the crystal field effects. In ABO_3 type structure, the hybridization and electrostatic interaction of the outermost *3d* orbital of *B* cation with that of the oxygen ion gives rise to the crystal field effect. In the absence of crystal field, the *d* orbital has fivefold degenerate energy levels namely d_{xy}, d_{yz}, d_{zx}, $d_{x^2-y^2}$ and $d_{3z^2-r^2}$. The first three are known as t_{2g} orbitals whereas the last two are called e_g orbitals as shown in Fig 1.2.

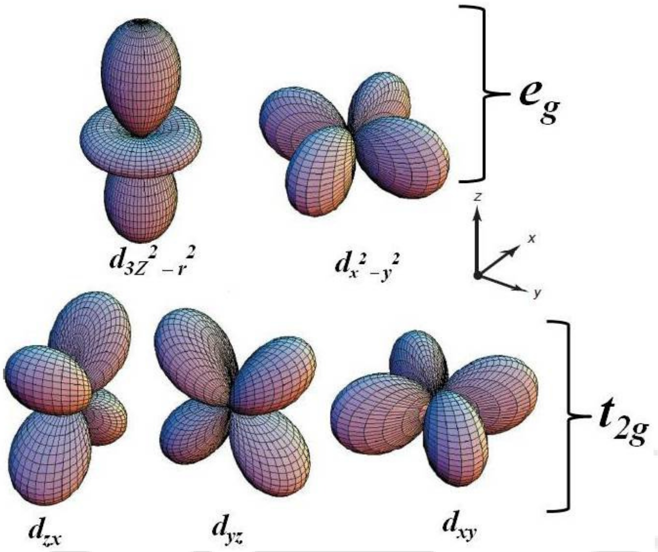

Figure 1.2: The electronic distribution of five *d* orbitals. In presence of cubic crystal field, the fivefold degeneracy of *d* orbital is lifted, and it splits into two e_g ($d_{x^2-y^2}$ and $d_{3z^2-r^2}$) and three t_{2g} (d_{xy}, d_{yz} and d_{zx}) orbitals. Adapted from [26].

The t_{2g} orbitals are oriented in between *x*, *y* and *z* axes, but the e_g orbitals point along the direction of *x, y* and *z* axes. However, in an octahedral environment, there exists a Coloumb interaction between 3*d* electrons of the transition metal ions and 2*p* electrons of O ions. Since the p_x, p_y, p_z orbitals of the oxygen point long the *x*, *y* and *z* direction respectively, there will be an overlapping with e_g orbitals of the transition metal ions. So, the energy of e_g orbitals is raised compared to the t_{2g} orbitals. On the other hand, no such overlapping occurs in case of t_{2g} orbital. In view of the above crystal field effect, the degeneracy of *d* orbitals is lifted by raising the energy of e_g orbitals with respect to the t_{2g} orbitals. The splitting in an octahedral environment is shown in Fig. 1.3. In case of tetrahedral environment, the t_{2g} orbitals are lifted up and e_g orbitals are pushed down [25]. The ground state spin configuration (high spin or low spin state) of the transition metal ions is determined from the competition between the crystal field energy and the Hund's pairing energy. A high spin state is favorable if the crystal field energy is lower than that of the pairing energy, where electrons occupy the orbitals as per Hund's rule. However, electrons will doubly occupy the lower energy orbitals before entering into the higher energy orbitals favoring a low spin state when the crystal field energy is stronger than the pairing energy.

Another important aspect of the crystal field effect is the orbital quenching, commonly observed in the 3d transition metal ions. The effective magnetic moment (μ_{eff}) of transition metal ions can be calculated from the total angular momentum (J) using the relation $\mu_{eff} = g\sqrt{J(J+1)}\,\mu_B$ but the experimental effective moment doesn't match with the above values for most of the 3d transition metal ions. This discrepancy arises due to the presence of a stronger crystal field effect compared to that of the spin orbit interaction in 3d elements which results in quenching of the orbital angular momentum *i.e.* $L = 0$. Thus, the effective magnetic moment of orbitally quenched elements is calculated considering only the spin angular momentum (S) using the relation $\mu_{eff} = g\sqrt{S(S+1)}\,\mu_B$. However, in case of rare-earth elements with 4f electrons, no crystal field effect is observed because the 4f levels are deep inside from the outermost orbital and have negligible overlapping with the electronic configuration of the neighboring ions.

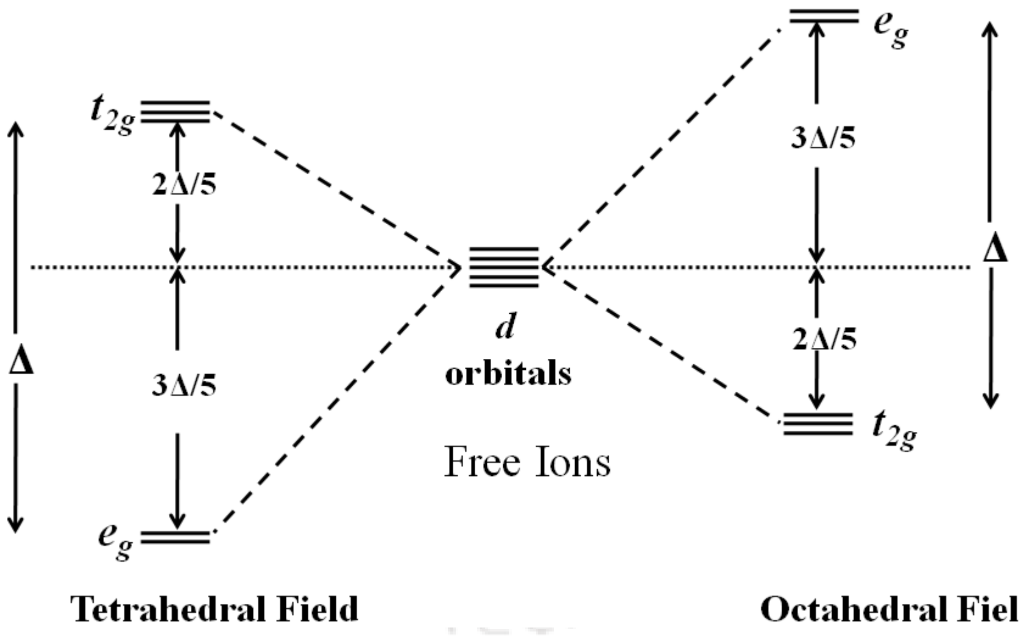

Figure 1.3: The crystal field in an (a) octahedral environment and (b) tetrahedral environment of d orbital in transition elements.

In certain electronic configurations the degeneracy associated with the e_g and t_{2g} orbitals can be further lifted by the spontaneous distortion of the lattice such that the overall energy is reduced. This effect is known as the Jahn-Teller (JT) effect [25,27]. For example, Mn^{3+} ($3d^4$) ions in an octahedral environment exhibits this kind of behavior as shown in

Fig.1.4. The spontaneous distortions can occur in two ways, one by elongation and other by compression. In case of elongation in an octahedron, the overlapping of one of the e_g orbitals, $d_{3z^2-r^2}$ with the neigbouring p orbital of oxygen is reduced, whereas for other e_g orbital, $d_{x^2-y^2}$ it is enhanced. Therefore, the $d_{x^2-y^2}$ level is lifted up compared to $d_{3z^2-r^2}$ level. Similarly, in t_{2g} orbital, d_{xy} level is lifted up compared to d_{yz} and d_{zx} levels. On the other hand, the compression in the octahedron lifts up the $d_{3z^2-r^2}$ level compared to $d_{x^2-y^2}$ level in the e_g orbital and similarly d_{yz} and d_{zx} levels are lifted up with respect to d_{xy} level in t_{2g} orbital. Cr^{3+} is Jahn-Teller inactive ion while Mn^{3+} is a Jahn-Teller active ion.

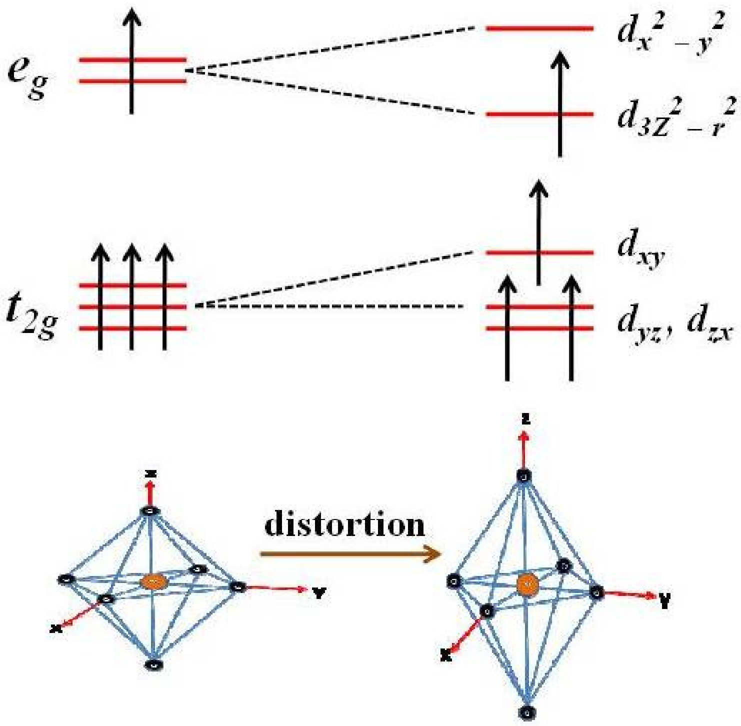

Figure 1.4: The Jahn-Teller effect in Mn^{3+} ($3d^4$) ion that leads to splitting of both t_{2g} and e_g levels.

1.3 Magnetic Exchange Interaction

It is the exchange interaction which makes the magnetic dipoles inside a material to interact with each other and tries to align themselves in particular arrangements in such a way that the total energy of the material is minimized. It is basically a quantum mechanical phenomenon which arises from the electrostatic interaction between the neighboring atoms.

The exchange interaction is the outcome of Pauli's exclusion principle. When the spins of two interacting electrons are parallel, the spatial part of the total wave function is anti-symmetric under the exchange while the wave function becomes symmetric when they are opposite. The probability distribution associated with the symmetric and anti-symmetric wave function is different as a result the electrostatic energy for the symmetric and anti-symmetric case will be different. This difference in electrostatic energy is known as exchange interaction, which depends on the orientation of the spins of electrons [28]. In microscopic scale various types of magnetic interactions are responsible for long range magnetic ordering and some of them are briefly described below.

1.3.1 Direct Exchange Interaction

When the exchange interaction between the electrons of two neighboring magnetic atoms occur without any aid of an intermediate ion, then such interaction is known as direct exchange. However, in real physical system the existence of such simple interaction is very rare because of insufficient direct overlapping between the neighboring magnetic orbitals. The direct exchange interaction is not an important interaction to justify the magnetic properties of different magnetic materials and therefore it is required to look for some kind of indirect type exchange interaction.

1.3.2 Superexchange Interaction

Superexchange interaction is an indirect exchange interaction which occurs between two non-neighboring magnetic ions through a non-magnetic ion located in between them. According to Kramer's model [29], the interaction between the cations having more than half filled *d*-shells gives rise to the antiferromagnetic interaction while such interaction among cations having less than half filled *d*-shells gives rise to ferromagnetic interaction.

The mechanism of superexchange interaction between two Mn - 3*d* orbitals leading to antiferromagnetism and ferromagnetism is depicted in Fig 1.5 (a & b). In Fig 1.5(a) the core spins of magnetic cations are aligned antiparallel to each other via an intermediate non-magnetic ion like oxygen. This situation facilitates the AFM interaction due to the strong Hund's coupling. Following the Hund's rule, the spin up electron of the oxygen ion shares some time with the cation having spin up arrangement while the spin down electron of oxygen ion shares the spin down configuration of the other cation. The above process results a ferromagnetic spin alignment in the cation-anion pair whereas the net interaction of magnetic cation-cation pair becomes antiferromagnetic. Thus, the oxygen mediated exchange interaction leads to an overall AFM alignment between the two Mn^{4+} ions. According to Goodenough [30], when the cation-anion-cation interaction is asymmetric, *i.e.* one side the bond is covalent, and the other side is ionic then the superexchange interaction gives rise to ferromagnetism. Such a situation for Mn^{3+} - O^{2-} - Mn^{4+} pair is shown in Fig. 1.5 (b). In this case, the spin up electron of the oxygen forms covalent bond with the spin up electron Mn^{3+} cation (on left), while the spin down electron of oxygen forms ionic bond with the spin up electron of Mn^{4+} cation (on right). So, the overall interaction between the Mn^{3+} and Mn^{4+} ions become ferromagnetic in nature.

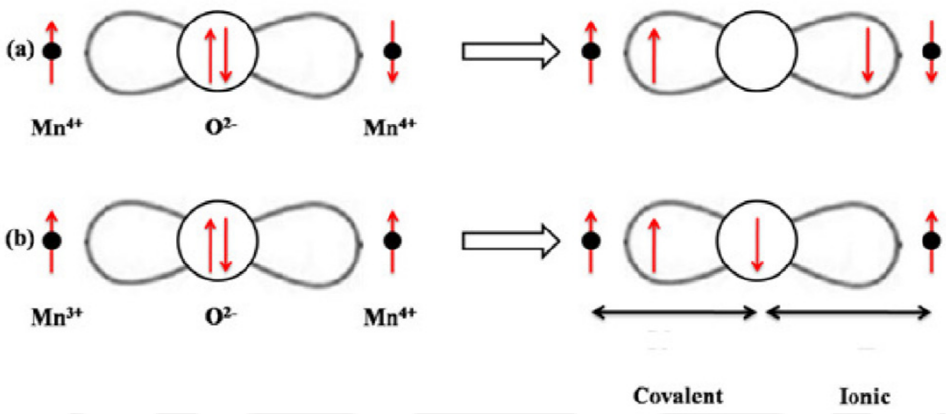

Figure 1.5: Schematic diagram showing the spin arrangements in (a) an antiferromagnetic superexchange interaction and (b) a ferromagnetic superexchange interaction.

Thus, the superexchange interaction in Mn^{3+} - O^{2-} - Mn^{3+}, Mn^{4+} - O^{2-} - Mn^{4+}, Cr^{3+} - O^{2-} - Cr^{3+} and Fe^{3+} - O^{2-} - Fe^{3+} networks are AFM in nature, while the interaction between mixed valent magnetic ions such as Mn^{3+} - O^{2-} - Mn^{4+} network promotes FM. Rare earth orthochromites exhibit AFM ordering due to the superexchange interaction in Cr^{3+} - O^{2-} - Cr^{3+} networks which is greatly affected by the ionic radius of R^{3+} ion.

1.3.3 Double Exchange Interaction

Double exchange interaction is a type of magnetic exchange interaction which occurs between magnetic ions that exist in different oxidation states. First proposed by

Zener [31], in 1951, according to which the carrier electron can hop from the lower valent magnetic cation to higher valent magnetic cation through an intermediate non-magnetic anion like oxygen. Such exchange interaction between Mn^{3+} and Mn^{4+} through an oxygen ion gives rise to double exchange ferromagnetism and is shown in Fig. 1.6(a). In the ground state, the electron spins in each of the Mn ions are parallel in accordance with the Hund's rule. Here, the e_g orbitals of the Mn^{3+} ions are directly interacting with the *2p* orbitals of the oxygen ions as a result the oxygen ion gives up its spin up electron to Mn^{4+} ion and thus an electron from Mn^{3+} ion is transferred to vacant orbital of oxygen ion. In this way the electron is involved in two simultaneous motions between the neighboring ions, retaining its spin, due to which it is known as double exchange interaction.

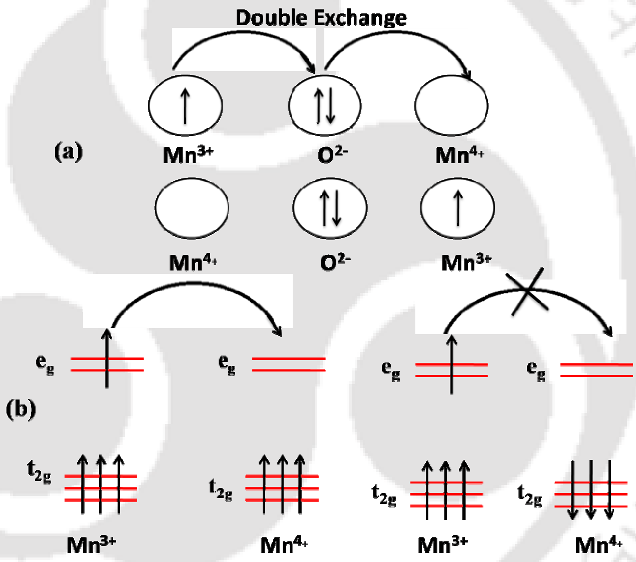

Figure 1.6: (a) Schematic of double exchange mechanism involving two Mn ions and one O ion. (b) The mobility of e_g electrons improves if the localized spins are polarized and parallel to each other.

According to Zener model, the carrier electrons can hop between two Mn ions only if their core electron spins are parallel to each other. If the Mn spins are not parallel, the electron transfer becomes difficult due to strong onsite Hund's coupling as shown in Fig. 1.6(b). The electron transfer becomes difficult when the Mn – O – Mn bond angle deviates considerably from 180° because the deviation reduces the overlap between *d*-orbital of Mn and *p* orbital of oxygen ion. Thus, double exchange interaction always gives rise to ferromagnetism. The movement of electron can be represented as, $Mn^{3+}_{1\uparrow}O_{2\uparrow,3\downarrow}Mn^{4+} \rightarrow Mn^{4+}O_{1\uparrow,3\downarrow}Mn^{3+}_{2\uparrow}$ where the electron spins are labeled as 1, 2 and 3. Anderson and Hasegawa [32] presented the double exchange mechanism in detail by visualizing a second order process in which the electron transfer takes as follows $Mn^{3+}_{1\uparrow}O_{2\uparrow,3\downarrow}Mn^{4+} \rightarrow Mn^{3+}_{1\uparrow}O_{3\downarrow}Mn^{3+}_{2\uparrow} \rightarrow Mn^{4+}O_{1\uparrow,3\downarrow}Mn^{3+}_{2\uparrow}$.

1.3.4 Ruderman-Kittel-Kasuya-Yosida (RKKY) Interaction

It is an indirect exchange interaction which is seen in metals where the exchange interaction between the magnetic ions is mediated by the conduction electrons. A localized magnetic moment spin polarizes the conduction electron which in turn gets couple with the neighboring localized magnetic moment located at a distance *r* away. As the exchange interaction between the neighboring magnetic moments doesn't involve any direct coupling, it is indirect in nature. At large distance *r*, the coupling between the magnetic moments is described by an *r*-dependent exchange interaction $J_{RKKY}(r)$ given by [25]

$$J_{RKKY}(r)\,\alpha\,\frac{\cos(2k_F r)}{r^3} \tag{1.1}$$

where, k_F is the radius of an assumed spherical Fermi surface. This interaction is oscillatory in nature and it depends on the separation between the magnetic moments. It is a long range exchange interaction. Depending upon the separation between the magnetic moments the interaction is may be either FM or AFM.

1.3.5 Dzyaloshinskii-Moriya Interaction

Dzyaloshinskii-Moriya (DM) interaction is an anisotropic exchange interaction proposed by Dzyaloshinskii and Moriya [33–35]. The presence of DM interaction leads to the tilting of the magnetic moments of antiparallel spins towards each other which gives rise to a net magnetic moment. However, such a canted spin arrangement is possible only if the magnetic crystal symmetry remains same as that of the initial antiparallel spin arrangement. The exchange energy between the magnetic moments with canted configuration can be written as,

$$H_{DM} = \vec{D}.\left(\vec{S}_1 \times \vec{S}_2\right) \tag{1.2}$$

where, $\vec{S}_1$ and $\vec{S}_2$ represent the spins of two interacting magnetic ions and $\vec{D}$ is DM vector. Vector $\vec{D}$ vanishes when the crystal field has inversion symmetry with respect to the middle point connecting the two magnetic ions. Usually $\vec{D}$ lies either parallel or perpendicular to the line connecting the two spins, depending on the symmetry. The DM interaction tries to align $\vec{S}_1$ and $\vec{S}_2$ at right angle to each other in a plane perpendicular to $\vec{D}$. Its effect is therefore very often to cant (*i.e.* slightly rotate) the spins by a small angle. It commonly occurs in antiferromagnets where the canted spins give rise to a small FM component of the moments perpendicular to the spin-axis of the antiferromagnet. Such DM interaction leads to the appearance of weak ferromagnetism or canted antiferromagnetism. Some of the AFM crystals like α-Fe_2O_3, Cr_2O_3, $MnCO_3$, $CoCO_3$, *etc.*, exhibit such weak FM behavior [28,36]. The weak FM behavior in rare earth orthochromites arises mainly due to the DM interaction and it plays an important role in explaining some of the anomalous magnetic properties observed in orthochromites.

1.4 Magnetic Orderings

Diamagnetism and paramagnetism in magnetic materials arise from isolated magnetic moments which do not have any interaction with each other. But the presence of any exchange interaction among magnetic moments gives rise to collective magnetism. Depending on the nature of interaction the magnetic material can be classified as ferromagnet, antiferromagnet and ferrimagnet. In this section the basic magnetic orderings observed in magnetic materials are discussed briefly.

1.4.1 Diamagnetic Materials

Diamagnetism in a material is defined as the tendency to oppose the external magnetic field. Typically, it is exhibited by atoms with closed or completely filled outermost electronic shells. In presence of an external magnetic field, a magnetic moment is induced in the diamagnetic material in such a way that it opposes the external magnetic field that causes it in accordance with the Lenz's law. The diamagnetism will continue as long as magnetic field is applied. Diamagnetic materials exhibit negative susceptibility which implies that the induced magnetization is opposite to applied magnetic field. Diamagnetism is an inherent property exhibited by all materials. Some of the examples of diamagnetic materials are inert gases, metals like Zn, Cu, Au, Ag *etc,* most nonmetals like Si, C, Ge and many organic compounds [36].

1.4.2 Paramagnetic Materials

In paramagnetic materials, the atoms or ions have a net magnetic moment due to the presence of unpaired electron in partially filled orbitals. However, at room temperature, in the absence of any external magnetic field, the atomic moments are randomly oriented due to the thermal agitation and it gives rise to zero magnetization. The application of an external field prompts the magnetic moments to partially align along the direction of the applied field, resulting a net positive magnetic moment and positive susceptibility. In addition, the partial alignment along the external magnetic field is reduced with the increase in temperature due to randomization of spins. This indicates that the susceptibility of a paramagnetic material shows temperature dependence. Based on the semi-classical treatment the susceptibility of a paramagnetic material is governed by Curie's law and is given as [28]

$$\chi = \frac{\mu_0 N \mu^2}{3k_B T} \tag{1.3}$$

where, N is the number of magnetic dipoles (magnetic ions) per unit volume each having a magnetic moment of μ. The above equation shows that the paramagnetic susceptibility follows an inverse relation with the temperature.

In quantum mechanical treatment, the paramagnetic susceptibility for low field can be described as,

$$\chi = \frac{N\mu_0 g^2 \mu_B^2 J(J+1)}{3k_B T} \tag{1.4}$$

where, $$g = \frac{3}{2} + \frac{S(S+1) - L(L+1)}{2J(J+1)}$$

The constant g is known as Lande's g factor and L, S and J represent orbital, spin and total angular momentum of the magnetic element respectively.

Some diatomic gases like O_2, NO; ions of transition elements, rare earth metals, salts and oxides of rare earth are some of the examples of strong paramagnetic materials [28].

1.4.3 Ferromagnetic Materials

Ferromagnetic materials consist of ordered regions known as domains where the magnetic moments are oriented in a one direction giving rise to large finite magnetization even in the absence of a magnetic field. The parallel alignment of the magnetic moments is due to the presence of a molecular field which is strong enough to magnetize the material even in the absence of an external field. The phenomenon of ferromagnetism is observed below a critical temperature known as Curie temperature (T_C) above which the ferromagnetic materials generally behave like a paramagnet, and their susceptibilities follow the Curie-Weiss law [28],

$$\chi = \frac{C}{T - \theta_C} \tag{1.5}$$

where, C and θ_C are Curie constant and Curie temperature, respectively. Here $C = \mu_o N g^2 \mu_B^2 J (J+1)/3k_B$ or $C = \mu_o N \mu^2/3k_B$. Typical θ_C values for common ferromagnetic materials like Fe, Ni and Co are 1043 K, 1394 K and 631 K, respectively [28].

1.4.4 Antiferromagnetic Materials

In antiferromagnetic materials the exchange interaction is negative as a result the molecular field is oriented in such a way that the nearest neighbour magnetic moments prefer to align antiparallel to each other giving rise to zero net magnetization. Antiferromagnetism is observed below a certain temperature known as Néel temperature (T_N), and above which the material becomes normally a paramagnet. The magnetic susceptibility in the paramagnetic state (*i.e.* for temperatures, $T > T_N$) for an antiferomagnetic material can be written as,

$$\chi = \frac{C}{T + T_N} \tag{1.6}$$

Examples of AFM materials include metallic chromium, manganese, various transition metal oxides such as MnO, FeO, Cr_2O_3, peovskites such as $BiFeO_3$, $GdCrO_3$, $SmCrO_3$ *etc.*

In antiferromagnetism, equal number of up and down spins on a lattice can be arranged in a large number of ways. Some selected arrangements of spins in perovskites are shown in Fig. 1.7. In A type AFM ordering, in each lattice plane (001) the magnetic spins are parallel to each other but they are opposite to adjacent planes leading to net AFM as shown in Fig. 1.7 (a). $LaMnO_3$ falls in this category. In C type ordering the atoms in the (110) and $(1\bar{1}0)$ planes are ferromagnetically aligned such that net coupling is AFM. G type ordering is the most common type of ordering where each atom is coupled AFM to all its nearest neighbours. It is found in $SmCrO_3$, $GdCrO_3$, $LaCrO_3$ and $LaFeO_3$, *etc* [25]. The E type ordering represents a zigzag magnetic structure which does not contain any obvious planes of ferromagnetism.

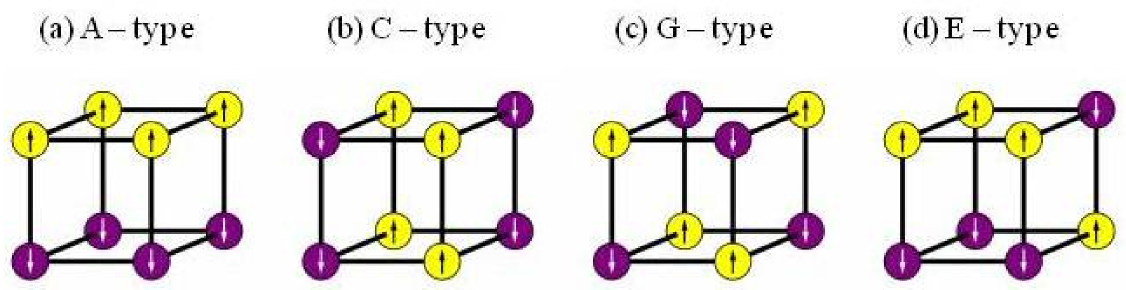

Figure 1.7: Different types of antiferromagnetic order in a magnetic cell. The up and down arrows represent the orientation of the spin. Adapted from [37].

1.4.5 Ferrimagnetic Materials

Ferrimagnetism is a special case of antiferromagnetism which arises when the magnetic moment of the two sublattices are opposite in direction but not equal in magnitude leading to the presence of a net magnetization in the material. Due to the difference in the molecular field of each sublattice, the temperature dependences of spontaneous magnetization of the sublattices differ from each other. As a result, one sublattice magnetization dominates over other in certain temperature region and vice versa in some other temperature region. Such temperature dependence and the competition between the magnetization of two sublattices give rise to state where the net magnetization reduced to zero at a certain temperature known as the compensation temperature (T_{comp}) below which the magnetization becomes negative. Examples of ferrimagnetic materials are Fe_3O_4, Fe_2O_3 $CoFe_2O_4$, $NiFe_2O_4$, $Y_3Fe_5O_{12}$, *etc* [28].

1.5 Magnetic Anisotropy

Magnetic anisotropy is defined as the dependence of magnetic properties on the direction of applied magnetic fields. Properties such as magnetization, coercivity, remnant magnetization, hysteresis curves *etc.,* of magnetic materials are greatly affected by the magnitude and type of anisotropy present in the materials. Thus, the nature of magnetic anisotropy present in a magnetic material plays an important role in determining the suitability of the material for a practical application. Some of the important types of magnetic anisotropies are discussed below:

I. Magnetocrystalline anisotropy
II. Shape anisotropy
III. Stress anisotropy
IV. Exchange anisotropy

1.5.1 Magnetocrystalline Anisotropy

It is defined as the tendency of magnetization to align itself along a preferred crystallographic direction. The magnetic saturation can be easily obtained with quite low fields along the preferred direction which is known as the "easy direction/axis" of magnetization while the direction along which it is difficult to magnetize the sample is known as "hard direction" of magnetization. In the demagnetized state, the easy direction of magnetization of a crystal is the direction of spontaneous domain magnetization. Thus, the crystal anisotropy may be considered as a force which has the tendency to hold the magnetization in certain equivalent crystallographic direction in a crystal. Therefore, it is also defined as the difference in the energy per unit volume between samples magnetized along easy and hard axis. The crystal anisotropy energy (E_a) for a cubic crystal is given as,

$$E_a = K_0 + K_1\left(\alpha_1^2\alpha_2^2 + \alpha_2^2\alpha_3^2 + \alpha_3^2\alpha_1^2\right) + K_2\left(\alpha_1^2\alpha_2^2\alpha_3^2\right) + \ldots\ldots.. \qquad (1.7)$$

where K_0, K_1 and K_2 are called anisotropy constants for a particular crystal at a particular temperature and, α_1, α_2 and α_3 are the direction cosines of the magnetization with respect to crystallographic axes *a*, *b* and *c*. The first term, K_0, is independent of angle and generally ignored. The anisotropy energy (E_a) represents that energy which is stored in the crystal when work is done against the anisotropy force to move the magnetization away from an easy direction. Crystals having lower symmetry generally possess large anisotropic energy. For example, cubic Fe has K_1 = 4.8x10^4 Jm^{-3} but for hexagonal Co, K_1 = 5x10^5 Jm^{-3} [38]. For all materials, the magnitude of crystal anisotropy decreases with increase in temperature, and close to transition temperature (T_C) it tends to zero as the paramagnetic state doesn't have any preferred orientation for magnetization. Since the anisotropy has a strong influence on the coercive field, the coercive field generally goes to zero together with the anisotropy [28,38].

The magnetocrystlline anisotropy arises mainly due to presence of spin-orbit coupling in the magnetic materials. When an external field tries to reorient the direction of spin of an electron, the orbital also gets reoriented due to the spin orbit coupling [28]. However, as the orbital is strongly coupled with the lattice, the attempt to rotate the spin axis by the external field is resisted. In most of the materials, the spin-orbit coupling is reasonably weak giving rise to weak magnetocrystalline anisotropy. However, in case of rare earth compounds the spin-orbit coupling is very strong. Therefore, the rare earth materials are generally used as permanent magnets [38].

1.5.2 Shape Anisotropy

Eventhough some of the single crystalline materials exhibit magneto-crystalline anisotropy, such anisotropy is mostly absent in polycrystalline materials due to random orientation of grains. In spherical shape polycrystalline materials, the magnetization produced by the applied field will be isotropic *i.e.* uniform in every direction. However, in non-spherical samples the magnetization will be easier along the longer axis compared to the shorter axis due to the small demagnetizing field along the longer axis. Such a dependence of anisotropy on the shape of a material is known as shape anisotropy [38].

1.5.3 Stress Anisotropy

Along with the magnetocrystalline anisotropy, another effect that is related to the spin-orbit coupling is magnetostriction which arises due to the strain dependences of the anisotropy constants. Due to magnetostriction, when a magnetic material is magnetized it may undergo a change in its dimension. The inverse effect is also possible where stress on the material can produce a change in the magnetization. The presence of uniaxial stress can produce an easy axis of magnetization when the stress is enough to overcome all other anisotropies [38]. Stress can create one or more easy axis of magnetization by changing the domain structure of a material. Therefore, the presence of any kind of stress in a magnetic material must be taken into account with other anisotropy.

1.5.4 Exchange Anisotropy

Exchange anisotropy appears when a material having a FM and AFM interface is cooled through the Néel temperature (T_N) of the antiferromagnet in the presence of a static magnetic field. The presence of exchange anisotropy is manifested by the shift in the center of hysteresis loops from the origin towards either negative or positive field axis. The above shift of hysteresis loop is known as exchange bias (EB). The presence of exchange anisotropy was first observed in Co/CoO nanoparticles by Meiklejohn and Bean in 1956 [39]. The pinning of the FM spins by the hard AFM spins at interface gives rise to unidirectional exchange anisotropy and its energy can be written as,

$$E = -K_u \cos\theta \tag{1.8}$$

where, K_u and θ represent the unidirectional anisotropy constant and angle between the magnetization and the direction of cooling field, respectively.

1.6 Magnetization Reversal

The magnetization reversal (MR) or negative magnetization (NM) is defined as the change in the magnetization from a positive value to a negative value under a fixed positive applied magnetic field, either by varying the magnitude of applied magnetic field or by varying the temperature. The temperature at which the net magnetization within the material becomes zero (M = 0) is known as compensation temperature (T_{comp}) below which the magnetization becomes negative. It was Neel who first predicted the magnetization reversal in ferrimagnetic material in 1948 and later it was experimentally observed in spinel ferrites in 1950 [40]. Beside ferrimagnetic material, magnetization reversal has also been reported in various magnetically ordered materials such as canted antiferromagnets, intermetallic alloys, ferromagnets, molecular magnets and multilayers [7,41]. The materials exhibiting magnetization reversal find potential technological application in thermomagnetic switches, magnetic memory, spin valves, thermally assisted magnetoresistive random access memory (TAMRAM) [7,19,42]

Magnetization reversal is an intrinsic phenomenon that appears in a material when two or more specifically arranged magnetic moments coupled with a magnetic anisotropy. Thus, the presence of finite magnetic anisotropy is very much essential for the occurrence of MR. In the absence of any magnetic anisotropy, a compensation behavior is observed but without any reversal of magnetization because below the compensation temperature the magnetization of the dominant component (opposite to the applied field) rotates and gets aligned in the direction of the applied magnetic field. Such a behavior is observed in some of the garnets [7,43,44]. Magnetization reversal has been reported in a variety of magnetic materials and the mechanism of its origin can be explained differently in different classes of materials which are briefly discussed below.

1.6.1 Magnetization Reversal in Ferrimagnetic materials

Magnetization reversal was first predicted by Neel in ferrimagnetic materials and its origin was explained by considering the different temperature dependence of the antiferromagnetically coupled sublattice magnetization corresponding to different crystallographic sites [40]. At $T = T_{comp}$ the magnetization of the two antiparallel sublattices becomes equal resulting zero magnetization in the sample, whereas for $T < T_{comp}$ the magnetization becomes negative.

The temperature dependence of FC magnetization of polycrystalline Co_2VO_4 manifesting magnetization reversal is shown in Fig. 1.8. Negative magnetization is observed below T_{comp} = 70 K which is explained by considering the antiparallel moments of Co^{2+} located at octahedral site and Co^{2+}/V^{4+} at tetrahedral site and their different temperature dependent behavior in accordance with the Neel's hypothesis [45]. Fe_2MoO_4 [46], $Co(Cr_{1-x}Fe_x)_2O_4$ [47], $Ni(Cr_{1-x}Fe_x)_2O_4$ [48] and $FeCr_{2-x}Al_xS_4$ [49] are few more examples of spinel compounds where the observed magnetization reversal can be explained satisfactorily by considering the above framework. Beside spinel compounds, magnetization reversal has also been observed in rare earth garnets [50] and Prussian blue analogues [51,52] where its origin can be explained with the same framework of Neel's mean field theory.

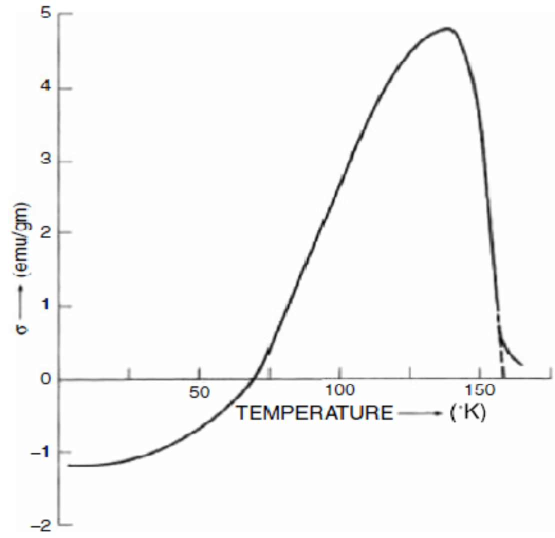

Figure 1.8: Reversal of magnetization observed in the temperature dependent field cooled magnetization of Co_2VO_4 for H = 700 Oe. Adapted from [45].

1.6.2 Magnetization Reversal in Intermetallic compounds

In these compounds, the magnetization reversal is observed due to the competition between the antiparallely arranged spin and orbital moments of an atom or ion occupying the same crystallographic site and their different temperature dependences. Ferromagnetic alloys of $(Sm_{1-x}Gd_x)Al_2$ [41,53] shows the MR behavior and its origin is explained on the basis of different temperature dependences of spin and orbital moments of Sm^{3+} and Gd^{3+} ions and the moments of polarized conduction of electrons [54]. Magnetic compensation along with the negative magnetization observed in bulk $Nd_{0.75}Ho_{0.25}Al_2$ [55], Sm_2Al and $Sm_{1.988}Gd_{0.012}Al$ [56] can be explained with similar mechanism.

1.6.3 Magnetization Reversal in Ferromagnetic and Antiferromagnetic Heterostructures

In multilayer compounds with FM and AFM interfaces, the magnetization reversal behavior is observed due to different temperature dependence of these layers. In Ni-FeF_2 multilayer system, the negative magnetization is observed as a result of the strong interfacial AFM coupling between the FM Ni layer and the AFM FeF_2 layer [57]. The negative magnetization reported in Gd-Fe, Gd-Co, and Gd-CoNi multilayers is attributed to the antiparallel alignment of the Gd moments at low temperature with respect to that of transition elements [58,59].

1.6.4 Magnetization Reversal in Canted Antiferromagnetic Materials

In some materials, the presence of spin canted AFM sublattices occupying different crystallographic sites and their interaction leads to MR. For example, rare earth orthovandates such as YVO_3 [60], $LaVO_3$ [61,62], $SmVO_3$ [63], and $NdVO_3$ [64] fall in this category of materials. In the case of $LaVO_3$, the observed magnetization reversal is explained in terms of the response of vanadium orbital moments to the first order structural transition at T_o = 138 K which can create a canted spin component opposite to the applied field below T_o [62,65]. In YVO_3 single crystals, the magnetization reversal is ascribed to the competition between the canted spin moments of V^{3+} ions produced by DM interaction and single ion magnetic anisotropy [60]. However, in $NdVO_3$ and $SmVO_3$, it is ascribed to the different quenching rates of orbital moments of V^{3+} ions [63,64].

The temperature dependence of FC magnetization of $BiFe_{0.5}Mn_{0.5}O_3$, which crystallizes in an orthorhombic structure, shows the magnetization reversal behavior with T_{comp} = 208 K. Here the origin of magnetization reversal is explained by considering the competition between the single-ion magnetocrystalline anisotropy and the antisymmetric DM interaction [66].

In some materials the presence of a paramagnetic sublattice along with the FM/canted AFM sublattice also leads to the magnetization reversal. The competition between paramagnetic moment and the FM/canted AFM sublattices residing at different crystallographic sites bring about the MR in such systems. The moments of the paramagnetic atom or ion get partially aligned opposite to the moments of the FM/canted AFM sublattices under the influence of an effective molecular field arising from the ordered FM/AFM sublattices. The net magnetization of such compounds can be expressed as [12]

$$M = M_{Cr} + \frac{C(H+H_I)}{T-\theta_C} \tag{1.9}$$

where, M_{Cr} is the weak FM moment of canted Cr^{3+} ions, and C is the Curie constant. H and H_I represent the external magnetic field and internal field respectively.

In the single crystal of $La_{1-x}Gd_xMnO_3$ [67], the Gd spins behave like a paramagnet and are partially aligned antiparallel with respect to the FM component of Mn spins. When the net Gd moment exceeds the FM component of Mn moments, reversal in the sign of magnetization or negative magnetization is observed. The above mechanism of also holds good for the observed negative magnetization in $SmMnO_3$ [68], $ErCo_{0.5}Mn_{0.5}O_3$, and $GdNi_{0.3}Mn_{0.7}O_3$ [69] compounds. The MR observed in some rare earth orthochromites $RCrO_3$ (R = Gd, Ce, Tm, Yb, Sm) [12,15,70–72] and in polycrystalline $NdCr_{1-x}M_xO_3$ (M = Fe, Mn) [73,74] can be satisfactorily explained by the above phenomenological model of competition between the paramagnetic moment of the rare earth ion and the net FM moment of canted transition metal ion.

1.7 Exchange Bias

Exchange bias (EB) in a system is defined as the anisotropic exchange interaction at the interface between a FM and an AFM phase after cooling the system in a static magnetic field through the T_N. Such an effect is manifested by the shift of isothermal magnetic hysteresis loop along the magnetic field axis. Meiklejohn and Bean first observed the EB effect in core shell structure of FM Co and AFM CoO in 1956 [39]. Since then EB has been observed in wide variety of heterostructured systems such as oxidized FM particles, bilayer and multilayer of FM/AFM, FM/FIM, FM/spin glass, core-shell structures, *etc* [18,75–77]. Bulk materials like binary alloys, intermetallic alloys and oxide materials are also known to exhibit EB [78,79]. The EB phenomenon has drawn a significant interest due to its potential application in magnetic recording media, permanent magnets, and spintronic devices [5,6,18].

The shift in the hysteresis loop can be expressed quantitatively in terms of exchange bias field (H_{EB}) using the relation [70]

$$H_{EB} = (H_+ + H_-)/2 \tag{1.10}$$

The effective coercive field, H_c^{eff} can be obtained using the relation,

$$H_c^{eff} = (H_+ - H_-)/2 \tag{1.11}$$

where, H_+ and H_- represent the field values corresponding to the loop crossing the $M = 0$ axis during the ascending and descending branches of M-H loop.

The presence of interfacial coupling due to the exchange anisotropy at the AFM-FM interface during the field cooled condition is responsible for the origin of exchange bias. In the temperature range $T_N < T < T_C$, when an external magnetic field is applied, the FM spins get aligned along the field direction, while the spins in the AFM region remain random at $T > T_N$ as shown in Fig. 1.9(a). After field cooling the system to temperature $T < T_N$, the AFM spins lying next to the FM spins at the AFM-FM interface align parallel (ferromagnetically) to the FM spins due to ferromagnetic exchange coupling at the interface (Fig. 1.9(b)). The rest of the AFM spins in the AFM layer simply follow the regular AFM ordering. When the direction of field is reversed, the FM spins start to rotate along the field direction while the AFM spins at the interface try to resist the rotation of FM spins due to large AFM anisotropy as shown in Fig. 1.9 (c). In other words, The FM spins experience a microscopic torque by the AFM spins at the interface to keep their alignment FM at the interface. As a result, the FM spins acquires unidirectional anisotropy at the interface.

Thus, larger negative field is required to reverse completely the spins of FM layer when it is in contact with an AFM layer compared to an isolated FM. This results an increase in coercive field in the negative field branch as shown in Fig. 1.9 (d). However, changing the magnetic field back to its original direction, the FM spins will rotate easily along the field direction because the AFM spins now exerts a torque in the same direction as applied field Fig. 1.9 (e). This leads to a decrease in coercive field in the positive branch of the field axis. Thus, the above process leads to shifting of the hysteresis loop along the magnetic field axis. In the above process we have considered FM coupling at the interface which results a shift in the M-H loop along the negative field axis. If the coupling at the interface is AFM, one would expect shifting of the loop along the positive field axis [18].

Recently exchange bias effect has been observed in several compounds of spinels, manganites, cobalites, orthochromites, double perovskites. For example, nanoparticles of $NiCr_2O_4$ [80] and $CoCr_2O_4$ [81], bulk samples of $Ni(Cr_{1-x}Fe_x)_2O_4$ [48,82], $Sm_{0.5}Ca_{0.5}MnO_3$ [83,84], $NdMnO_3$ [85], $Nd_{1-x}Sr_xCoO_3$ [86], $La_{0.82}Sr_{0.18}CoO_3$ [87], $SmCrO_3$ [72], $YbCrO_3$ [88], Sr_2FeCoO_6 [89] and Sr_2YbRuO_6 [90] exhibit such EB. In majority of the materials, either a positive EB field or a negative EB field is reported.

However, similar to the reversal in the sign of magnetization, sign reversal of exchange bias field is quite uncommon. In very few materials such as Co/CuMn bilayers, FeF_2/Fe bilayers and $GdCo_2$/Co multilayers [91–93] the sign reversal of EB field can be achieved by changing the external parameters like temperature and cooling field. Such a change in the sign of EB fields either by changing the magnitude of field or temperature is known as tunable exchange bias behavior.

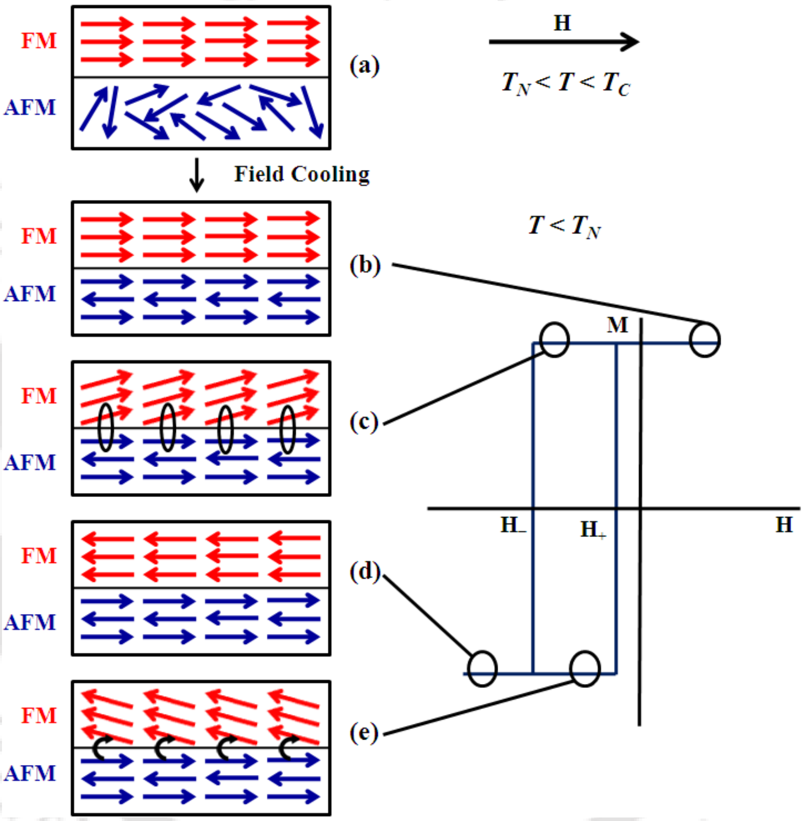

Figure 1.9: Schematic representation of spin configuration of a FM-AFM couple at different stages of a shifted hysteresis loop for a system with large AFM anisotropy [18].

The coexistence of sign reversal of both magnetization and exchange bias field in a single system finds potential application in fabricating storage devices such as TAMRAM [7,16]. The tunable exchange bias behavior is generally expected to occur in compounds which show the temperature induced magnetization reversal and the sign of H_{EB} can be related to the magnetization reversal. In the single crystal of rare earth intermetallic $Nd_{0.75}Ho_{0.25}Al_2$ compound temperature induced magnetization reversal is observed at T_{comp} = 24 K and in addition it also exhibits tunable exchange bias behavior across the $T_{comp.}$. The presence of tunable exchange bias field in $Nd_{0.75}Ho_{0.25}Al_2$ is attributed to the various exchange coupling between the moments corresponding to the conduction electron polarization and two different rare earth atoms [55]. Similarly, in Sr_2YbRuO_6 the temperature dependence of EB field shows a sign reversal from positive to negative values close to its T_{comp} (= 33 K) value [90]. Sign reversal of both exchange bias field and the magnetization has also been reported in compounds such as $LaCr_{1-x}Mn_xO_3$ (x = 0.15, 0.20) [94,95], $Ni(Cr_{1-x}Fe_x)_2O_4$ [48], $Co(Cr_{0.95}Fe_{0.05})_2O_4$ [47], and $NdMnO_3$ [85], *etc*. The polarity of the EB field (H_{EB}) can also be tuned by the external magnetic field and such tunable exchange bias behavior is reported in Ni-FeF_2 and Fe-FeF_2 bilayers system and polycrystalline compounds of $La_{1-x}Pr_xCrO_3$, Sr_2YbRuO_6, and $NdMnO_3$ [57,85,90,92,96].

1.8 Dielectric Properties of Materials

Dielectric materials are electrically insulator without any free charges, but they are polarizable under the influence of an external electric field E which gives rise to net dipole moment. The dipole moment can be measured in terms of polarization (P). For a linear isotropic and uniform dielectric, the polarization depends on the strength of the applied electric field E given by the relation,

$$P = \varepsilon_o \chi E$$

where ε_o is the permittivity of free space and χ is the dielectric susceptibility of the material. In general, there are four basic mechanisms of dielectric polarization: (1) electronic polarization, (2) ionic polarization, (3) orientational polarization, and (4) interfacial (Maxwell-Wagner) polarization. In an atom, the distortion of the electron cloud in presence of an applied field leads to electronic polarization. This polarization disappears when the external field is removed. In case of ionic crystals, the ionic polarization arises due to the change in the average position of positive and negative ions under the influence of external electric field. The orientational polarization is observed due to the orientation of permanent or induced dipoles under an applied field. Finally, the interfacial polarization occurs when the material possesses different phases or permittivity zones. It doesn't involve any dipole displacement unlike other polarization. Dielectric properties of a material depend on the polarization mechanism that can be quantified in terms of few complex parameters which are discussed below.

1.8.1 Complex Electric Impedance

Complex electric impedance is represented as Z^* and is defined as the resistance offered to the AC current in a system which can be described by the relation [97],

$$Z^*(\omega) = Z' - jZ'' = \frac{V^*(\omega)}{I^*(\omega)}$$

where Z' and Z'' represent the real and imaginary parts of the complex impedance. V^* is the voltage across the dielectric and I^* is the current through the dielectric. In case of an ideal dielectric, $Z' = 0$ as a result, the net impedance is capacitive, given by $Z^* = 1/j\omega C$, where C is the capacitance. The complex electric impedance in complex plane (Z' vs. Z'') can be visulalized by a special representation known as Nyquist plots. The parallel combination of R and C components of a sample forms a semi-circle in the Nyquist plot. A perfect semicircle, without any depression is observed only for ideal R and C elements. But in reality, the R and C are never ideal as a result a depressed semicircle with its centre below the Z' axis is formed. However, in case of polycrystalline samples the situation is different as it is composed of grains and grain boundaries. Grains are often more conductive and less capacitative compared to grain boundaries. Therefore, the Nyquist plot of polycrystalline sample consists of two distinct semicircles. The grains and grain boundaries resistance can be estimated from the diameters of the corresponding semicircles.

1.8.2. Complex dielectric constant

The complex dielectric constant (ε^*) of a dielectric material is given by [97]

$$\varepsilon^* = \varepsilon' - j\varepsilon'' = \frac{1}{j\omega C_o Z^*}$$

where ε' and ε'' are the real and imaginary parts of the complex dielectric constant which are expressed by the relation,

$$\varepsilon' = \frac{Z''}{\omega C_o(Z'^2 + Z''^2)}$$

$$\varepsilon'' = \frac{Z'}{\omega C_o(Z'^2 + Z''^2)}$$

The quantity C_o in the denominator represents the geometrical capacitance.

1.8.3. Complex AC conductivity

The complex AC conductivity (σ^*) is defined as [97]

$$\sigma^*(\omega) = \sigma' + j\sigma'' = j\omega\varepsilon_o\varepsilon^*$$

where σ' and σ'' represent the real and complex part of the conductivity and are given by

$$\sigma'(\omega) = \omega\varepsilon_o\varepsilon''$$

$$\sigma''(\omega) = \omega\varepsilon_o\varepsilon'$$

The frequency dependence of real part of AC conductivity (σ') can be analyzed based on Jonscher's power law which is expressed as [98,99]

$$\sigma'(\omega) = \sigma_{dc} + A\omega^n$$

Here, σ_{dc} is the frequency independent dc conductivity, A is the pre-exponential factor and n is the frequency exponent.

1.9 Rare Earth Orthochromites

$RCrO_3$ crystallizes in orthorhombically distorted perovskite structure (*Pbnm* space group) with four formula units per unit cell. The Cr^{3+} ions order in a G-type canted AFM structure with Neel temperature varying from 100 to 300 K [9], depending on the radius of the R^{3+} ion. The magnetic properties are governed by temperature dependent Cr^{3+}- Cr^{3+}, Cr^{3+}-R^{3+} and R^{3+}- R^{3+} exchange interactions. The $RCrO_3$ compounds are represented by three G type magnetic spin configurations namely, $\Gamma_1(A_x, G_y, C_z)$, $\Gamma_2(F_x, C_y, G_z)$, and $\Gamma_4(G_x, A_y, F_z)$ following the Bertaut's notation as shown in Fig. 1.10 [9,10,100]. The Γ_1 configuration doesn't allow weak ferromagnetism, whereas Γ_2 and Γ_4 configurations have weak FM along the *x* and *z* directions, respectively [10,30,100]. The magnetic configuration of $RCrO_3$ can be Γ_4 or Γ_2 depending upon the magnetic or non magnetic nature of the R^{3+} ion. However, in some orthochromites a low temperature spin reorientation transition is observed where the magnetic spin structure becomes *Γ*$_2$ or *Γ*$_1$ due to anisotropic magnetic interaction between the R^{3+} and canted Cr^{3+}ions [10].

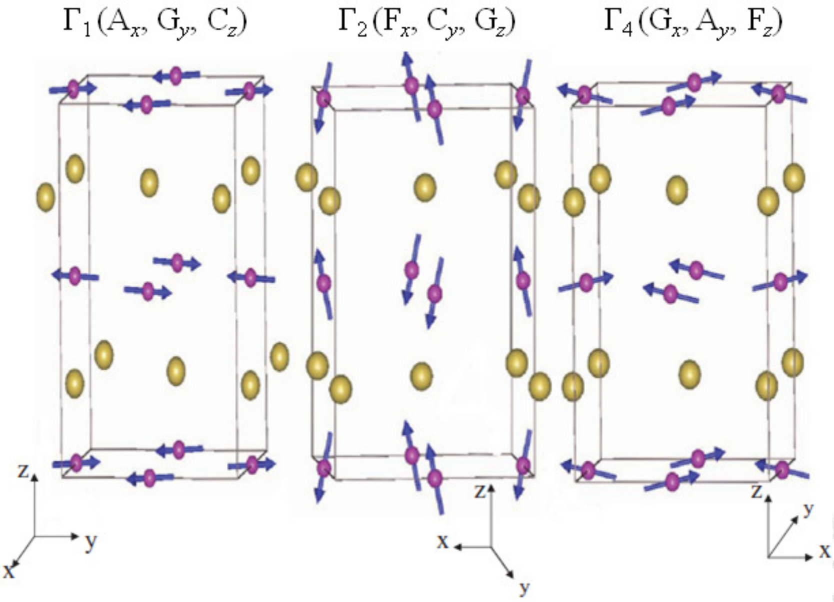

Figure 1.10: Magnetic spin configuration in *Γ*$_1$, *Γ*$_2$ and *Γ*$_4$ with *Pbnm* symmetry. Adapted from [10].

In addition, several other $RCrO_3$ (R = Dy, Ho, Tb, Lu, Y) compounds are known to exhibit magnetoelectric (ME) and multiferroic (MF) properties simultaneously due to the coexistence of both ferroelectric and magnetic ordering [10,11,101]. The magnetoelectric and multiferroic behaviors have also been observed in Mn and Fe substituted materials like $DyFe_{0.50}Cr_{0.50}O3$ [102] and $YCr_{1-x}M_xO_3$ (M = Mn or Fe) [103]. However, the origin of ferroelectricity and its relationship with the magnetic ordering in $RCrO_3$ is still not clear due to the centrosymmetric nature of orthochromites. The existence of a ferroelectric transition near the magnetic transitions suggests the type II magnetoelectric (ME) multiferroic (MF) behavior of $RCrO_3$. The semiconducting (*p* type) nature of $RCrO_3$ compounds have attracted further interest for photocatalytic activity and other solar energy harvesting applications [104–106]. Gupta *et al.* studied the ultraviolet-visible absorption spectra and photocatalytic activity of $DyCrO_3$ nanoparticles [104]. The presence of strong absorption mode in $RCrO_3$ compounds in the visible frequency range gives them an advantage compared to the conventional photocatalytic materials like TiO_2 [107]. Recently, $RCrO_3$ compounds have emerged as a potential material for low temperature magnetic refrigeration due to their giant magnetocaloric effect observed below 30 K [17,108,109]. A maximum magnetic entropy change, ΔS_M^{max} = 31.6 J kg^{-1} K^{-1} for a field change of 44 kOe at low temperature has been reported in single crystal of $GdCrO_3$ [17]. Similarly, bulk $DyCrO_3$ and $HoCrO_3$ were reported to have large magnetic entropy change of 8.4 J kg^{-1} K^{-1} and 7.2 J kg^{-1} K^{-1} respectively at $T \sim 20$ K [106,108].

Recently the $RCrO_3$ compounds have been intensely investigated for their unique properties of magnetization reversal and exchange bias. In $RCrO_3$ compounds, the origin of MR is due to the different temperature dependence of oppositely aligned R^{3+} sublattice moment with respect to the canted Cr^{3+} moments under the influence of internal field of AFM ordered Cr^{3+} sublattice [12,13]. Magnetization reversal in bulk polycrystalline samples of $TmCrO_3$ compound (Fig. 1.11) arises due to the antiparallel coupling of Tm^{3+} ion with canted component of Cr^{3+} moments [70]. However, the second compensation (~7 K) observed in $TmCrO_3$ is attributed to the rotation of Cr^{3+} and Tm^{3+} moments. A similar mechanism also holds good for explaining the magnetization reversal observed in orthochromites $GdCrO_3$, $CeCrO_3$, $YbCrO_3$ [13,15,71]. A similar explanation holds good for the magnetization reversal observed in polycrystalline samples of $La_{1-x}Pr_xCrO_3$ (x=0.70-0.85) [96] $La_{0.75}Nd_{0.25}CrO_3$ [110], and $La_{0.1}Gd_{0.9}CrO_3$ [111]. In the $La_{0.20}Ce_{0.80}CrO_3$ nanoparticles the origin of negative magnetization is attributed to the core shell type configuration [16].

The substitution of transition elements in place of Cr ions also reported to induce magnetization reversal. Azad *et al.* have studied the magnetic properties of $LaFe_{0.50}Cr_{0.50}O_3$ (T_N = 265 K) and observed temperature induced magnetization reversal for $T \leq 200$ K [112]. Bora *et al.* observed magnetization reversal in polycrystalline compounds of $NdCr_{1-x}M_xO_3$ (M = Fe/Mn) and $LaCr_{1-x}M_xO_3$ (M = Fe/Mn) [73,74,94,113] where its origin is explained by considering the temperature dependent competition between the PM moments and the canted Cr^{3+} moments. In the case of Mn and Fe substituted $LaCrO_3$ and $NdCrO_3$ compounds, maximum magnetic compensation of 169 K is observed for $NdCr_{0.85}Fe_{0.15}O_3$ compound.

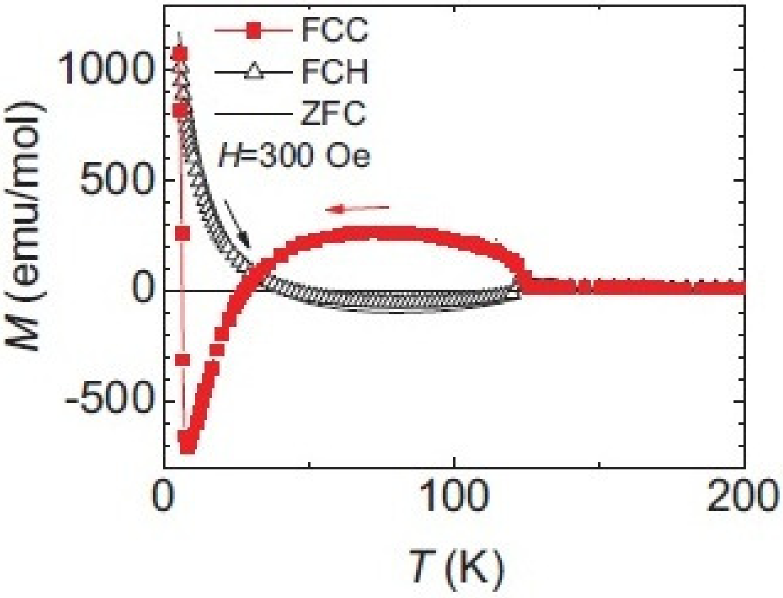

Figure 1.11: Magnetization reversal observed during the field cooled magnetization of $TmCrO_3$ for H = 300 Oe. Adapted from [70].

In addition to negative magnetization, tunable exchange bias has also been observed in $TmCrO_3$, $YbCrO_3$, $La_{1-x}Pr_xCrO_3$ (x = 0.7-0.85), $LaCr_{1-x}Mn_xO_3$ (x = 0.15 and 0.20), $NdCr_{1-x}Mn_xO_3$ (x = 0.05 to 0.20). The positive and negative EB observed in these compounds is ascribed to the anisotropic exchange interaction between the canted component of Cr^{3+} moments and the paramagnetic moments of R^{3+} ions and the substituted element under the influence of internal field. The sign reversal of both magnetization and exchange bias field in $La_{0.80}Ce_{0.20}CrO_3$ nanoparticles is due to the presence of core-shell structure with an antiferromagnetic core consisting of Cr^{3+} and Ce^{3+} spins and a disordered surface-shell with the uncompensated spins [16]. In $YFe_{0.5}Cr_{0.5}O_3$ the coexistence of sign reversal of both magnetization and exchange bias field is attributed to the competition between the single ion magnetic anisotropy and the DM interaction [114,115]. In compared to other compounds showing negative magnetization, $YFe_{0.50}Cr_{0.50}O_3$ exhibits higher T_{comp} (= 248 K) along with magnetocaloric effect and field induced bipolar switching of magnetization above 230 K.

The presence of above discussed interesting features such as magnetization reversal, exchange bias, magnetocaloric effect, *etc.,* in orthochromites encouraged us to study the magnetic properties of $SmCrO_3$ and $GdCrO_3$ based orthochromites with the expectation that magnetization reversal and EB may exist either in the parent compounds or substituted compounds. Some of the earlier works done on $SmCrO_3$ and $GdCrO_3$ based compounds are reviewed below.

1.9.1 $SmCrO_3$

$SmCrO_3$ crystallizes in an orthombically distorted perovskite structure with the G type AFM ordering below T_N = 197 K [10]. The canting of the Cr moments out of true antiferromagnetic alignment is due to the antisymmetric DM interaction. The presence of two magnetic elements and the temperature dependent isotropic, antisymmetric, and anisotropic exchange interaction among the Cr^{3+} - Cr^{3+}, Cr^{3+} - Sm^{3+} and Sm^{3+} - Sm^{3+} pairs give rise to a complex magnetic phase diagram that comprises of multiple phase transitions [116]. In the specific heat measurement of $SmCrO_3$ compound a λ - shaped peak around the T_N was observed indicating the conventional second order AFM to PM phase transitions [117]. Temperature dependent magnetization curve (M-T) of $SmCrO_3$ exhibits an abrupt fall in the magnetization below 33 K which is ascribed to the temperature driven spin reorientation (SR) transition where the spin configuration Cr^{3+} changes from a high temperature $\Gamma_4(G_x, A_y, F_z)$ to low temperature $\Gamma_2(F_x, C_y, G_z)$ spin structure [116]. The abrupt SR in $SmCrO_3$ observed in a narrow temperature range finds potential application in ultrafast spin switching and magnetic refrigeration [118].

The interesting negative magnetization and exchange bias behavior have been recently reported in both nanocrystalline and bulk $SmCrO_3$ compound. The negative magnetization is observed in the ZFC mode and is attributed to the antiparallel alignment of the PM Sm^{3+} moments with respect to the FM component of canted Cr^{3+} moments. The polycrystalline $SmCrO_3$ compound exhibits both inverse and normal magnetocaloric effect (MCE) with a typical maximum magnetic entropy change (ΔS_M) of -24 x 10^{-2} and -11 x 10^{-2} J kg^{-1} K^{-1} at the spin reorientation temperature (T_{SR}) and T_N, respectively for a field change of 5T [117].

Though lots of reports are available on the magnetic and electrical properties of $SmCrO_3$ but study on the effect of substitution at the Sm or the Cr site is still lacking. Qian *et al.* studied the magnetic glassy behaviors in polycrystalline $Sm_{1-x}Ba_xCrO_3$ ($x = 0$ and 0.1) compounds, which arise from the kinetic arrest of FM-AFM phase transition due to frozen fractions of AFM state [119]. The substitution of Bi in the Sm site induces ZFC negative magnetization whereas the glassy behavior disappears in $Sm_{0.9}Bi_{0.1}CrO_3$ [120]. The AFM transition temperature and spin reorientation transition temperature decreased significantly after Bi substitution. Magnetization reversal and exchange bias have been observed in $SmCr_{0.90}Fe_{0.10}O_3$ sample with T_{comp} = 93 K [121]. A decrease in the exchange bias field was observed upon substitution of non magnetic La^{3+} in place of Sm^{3+} due to the weakening of the coupling between Sm^{3+} and Cr^{3+} ions [122].

1.9.2 $GdCrO_3$

$GdCrO_3$ compound exhibits an orthorhombic structure at room temperature (*Pbnm* space group) with typical lattice parameters of a = 5.312 Å, b = 5.514 Å, and c = 7.611 Å [13]. The bulk polycrystalline sample of $GdCrO_3$ shows a canted antiferromagnetic ordering due to localized Cr^{3+} moments at T_N = 170 K [12]. Below T_N the Gd^{3+} moments behave like a paramagnetic entity which tends to align opposite to the direction of the FM component of canted Cr^{3+} moments under the influence of an internal field due to the AFM ordered Cr^{3+} ions. Around T = 7 K the Cr^{3+} spins undergo spontaneous spin reorientation from high temperature G_xF_z to low temperature G_zF_x configuration as a result of an antisymmetric exchange interaction or a pseudo-dipolar interaction between Gd^{3+} and Cr^{3+} ions. At sufficiently low temperatures the magnetic interaction between the Gd^{3+} moments become significant which leads to the ordering of the Gd^{3+} moments at T_N^{Gd} = 2.3 K [12,13].

In nanocrystalline and bulk polycrystalline samples of $GdCrO_3$, the FC magnetization measured as a function of temperature shows the interesting negative magnetization behavior below the compensation temperature of T_{comp} = 130 K [13,105]. Such a behavior originates from the antiparallel alignment of the paramagnetic moments of Gd^{3+} with respect to FM component of the canted Cr moments (M_{Cr}). However, a second compensation at T = 17 K was also observed due to the low temperature spin reorientation phenomenon. The net magnetization of $GdCrO_3$ can be approximated as $M = M_{Cr} + C_{Gd} (H_I + H_a) / (T + \theta)$, where M_{Cr} is the canted Cr moments, θ is the Weiss constant and C_{Gd} is the Curie constant of Gd moments [12]. Typical reported values of M_{Cr}, H_I and θ are 100 emu/mol, -1900 Oe, -13 K, respectively [13]. Sharma *et al.* observed the negative magnetization in $La_{0.50}Gd_{0.50}CrO_3$ with T_{comp} = 75 K due to the antiparallel coupling between Gd^{3+} moments and the canted Cr^{3+}

moments. The M_{Cr}, H_I and θ values obtained were 42 emu/mol, -511 Oe and -0.6 K respectively for H = 100 Oe [123].

In addition to negative magnetization, multiferroicity has also been reported in $GdCrO_3$ compound. Cheng *et al.* observed both ferroelctricity and weak ferromagnetism in polycrystalline bulk compounds and thin films of $GdCrO_3$ [101]. Rajeswaran *et al.* observed magnetic field induced electric polarization in both $GdCrO_3$ and $SmCrO_3$ in the vicinity of Neel temperature (T_N) [10]. The electric polarization of $GdCrO_3$ can be tuned by the applied magnetic field which indicates strong coupling between magnetization and electric polarization. Bulk $GdCrO_3$ is also a promising material for low temperature magnetic refrigeration due to its large magnetic entropy change (31.6 $Jkg^{-1}K^{-1}$) which is higher compared to that of bulk polycrystalline samples of $RMnO_3$ and $RFeO_3$ family [109].

Although $GdCrO_3$ exhibits a variety of properties but the study of pure compound as well the effect of substitution at the Gd or Cr site is quite limited. Biswas *et al.* have studied the effect of Ca substitution in place of Gd on the magnetic and transport properties [124]. The substitution of Ca leads to a fall in AFM transition temperature. However, the substitution of 50 at% of La at Gd site increases the T_N to 225 K [123]. A giant MCE was reported for $GdCr_{0.50}Fe_{0.50}O_3$ with a maximum value of $-\Delta S_M$ = 29 $Jkg^{-1}K^{-1}$ at T = 3 K for ΔH = 4.5 T [125].

1.10 Motivation

Based on the literature review it was found that rare earth orthochromites are an important class of single phase multifunctional materials. The presence of interesting negative magnetization and exchange bias makes them technologically important in application perspectives. If both magnetization reversal and exchange bias could be observed in single phase compound of multiferroic $RCrO_3$, it would enhance the potential of their technological applications. As reviewed in previous sections, most of the magnetic properties observed in rare earth orthochromites can be explained by considering the temperature dependent competition between the R^{3+} moments and Cr^{3+} moments. Thus, substitution either at the rare earth site or Cr site may give rise to interesting magnetic properties like magnetization reversal. The main motive of the present work is to explore the negative magnetization and exchange bias behavior in orthochromites.

For $SmCrO_3$ and $GdCrO_3$ compounds, many reports on their structural and magnetic properties are available but a systematic study about the effect of substitution at the rare earth site or Cr site is still limited. In similar orthohochromites such as $LaCrO_3$ and $YCrO_3$, *etc.,* the substitution at the rare earth site or Cr site by another rare earth or transition elements, respectively are known to induce magnetization reversal. Therefore, in search of possible magnetization reversal, we have taken up the study of structural and magnetic properties of transition elements (Fe and Mn) substituted $SmCrO_3$ and $GdCrO_3$ along with Y doped $GdCrO_3$ compounds for the present thesis work.

For the present thesis work five series of samples were prepared

1. $SmCr_{1-x}Mn_xO_3$ ($x = 0 – 0.50$)
2. $SmCr_{1-x}Fe_xO_3$ ($x = 0 – 0.50$)
3. $GdCr_{1-x}Mn_xO_3$ ($x = 0 – 0.50$)
4. $GdCr_{1-x}Fe_xO_3$ ($x = 0 – 0.50$)
5. $Gd_{1-x}Y_xCrO_3$ ($x = 0 – 0.50$)

The structural and microstructural properties of the above samples were characterized by X-ray diffraction (XRD), Raman spectroscopy, field emission scanning electron microscope (FESEM) and Energy dispersive X-ray analysis. The XRD patterns recorded at room temperature using the Rigaku make TTRAX III diffractometer were used to confirm the phase formation and analyze the crystal structure. The magnetic properties of the prepared samples were analyzed from the dc magnetization measured as a function of temperature and field using Lakeshore make vibrating sample magnetometer of model no. 7410. The techniques used for synthesis and characterization of above samples along with the working principle of instruments are presented in chapter 2.

Chapter 2

Experimental Techniques

In the present thesis work various experimental techniques were used for the collection and analysis of the data. Thus, it is essential to understand the operational details of the instruments along with their working principle in order to extract worthy information from the experimental data. The samples used in the current investigations were prepared using sol-gel routes. The heat treatment of the samples at various stages of sample preparation was carried out by using both commercial and homemade furnaces. The design and fabrication details of the homemade furnace are presented in this chapter. Different experimental tools were used to study the characteristic properties of different samples. Crystal structure and phase purity of the samples were confirmed using X-ray diffraction (XRD) technique and the data were further analyzed by Rietveld refinement technique. Morphological and compositional characterizations of the samples were performed by Field emission scanning electron microscope (FESEM) and energy dispersive spectroscopy respectively (EDS). Raman spectroscopy was further used to confirm any structural disorder in the samples. Temperature and field dependent magnetic properties of the samples were measured using a vibrating sample magnetometer (VSM). However, for a selected few samples *M-H* loops were recorded using Quantum Design make PPMS-VSM. The dielectric properties of a few samples were studied in terms of impedance spectroscopy using an LCR meter. In this chapter, above mentioned techniques used for preparation and characterization of the samples are discussed.

2.1 Sample Preparation

2.1.1 Sol-gel Method

Sol-gel method is one of the most well-established methods to prepare samples with good chemical homogeneity because it involves molecular scale mixing of reactants at comparatively low temperatures. This method provides a good control over the reactions involved during the synthesis of the materials. The *sol* is formed from the stable suspension of colloidal particles in a solvent and a *gel* is a porous three dimensionally interconnected solid network that expands in a stable fashion throughout the solvent. The starting compounds usually oxides, nitrates, carbonates or hydroxides are weighed as per the stoichiometric ratio and then they are dissolved in either distilled water or nitric acid to form a mixture with the help of a magnetic stirrer. The resultant mixture is then kept at temperature of around 70 °C under continuous stirring by placing it on a hot plate. Citric acid is added to the solution in the molar ratio of 2:1 with respect to the metal cation in order to convert the nitrates to citrates. Since citric acid is a chelating agent, it binds up only the metal ions and removes the non-metallic ions. Ethylene glycol is then added to the citrate solution after 1hr and the solution is stirred for another 3-4 hours. The mixture is then kept at 100 °C for 10-12 hours and finally a homogeneous gel is formed. Further heating of the gel at 200 °C yields voluminous fine precursor. The precursor is grounded to obtain fine powder which is then heated at different temperature to obtain the final product.

All the samples for the present thesis work were prepared by sol-gel technique. The starting compounds used for the preparation of the samples are Samarium Oxide (Sm_2O_3, 99.9%), Gadolinium Oxide (Gd_2O_3, 99.9%), Yttrium Oxide (Y_2O_3, 99.9%), Chromium Nitrate ($Cr(NO_3)_3.9H_2O$, 98%), Manganese Acetate ($C_4H_6MnO_4.4H_2O$, 98.5%), Ferric Nitrate ($Fe(NO_3)_3.9H_2O$, 98%). The starting compounds as per stoichiometric ratio were weighed using an electronic balance supplied by Mettler Toledo of model no. AG135 with an accuracy of ± 0.01 mg. The voluminous precursor obtained after the sol-gel method was grinded and then presintered at 600 °C for 12 h followed by grinding. These powders were then pressed into pellets with the help of a 13 mm cylindrical die and a hydraulic press supplied by Techno Search instruments, Thane, India with a maximum load of 6 Ton/cm^2. The pressed pellets were then sintered at 900 °C and 1000 °C for 12 h with intermediate grinding and the final sintering in pellet form was carried out at 1100 °C for 24 h followed by furnace cooling.

2.1.2 High Temperature Furnaces

For heat treatment of the samples, high temperature homemade muffle furnaces were used with a maximum operating temperature of 1200 °C and commercial high temperature furnaces with the maximum operating temperature of 1400 °C. The commercial furnaces were supplied by N. R. Enterprises and Bysakh & Company, Kolkata, India. The furnace supplied by N. R. Enterprises was powered by a thyristor unit of 30 A rating. The temperature was controlled using Honeywell make PID programmable temperature controller model no. DC 1040 with 16 segment programming features. The platinum versus platinum-rhodium (Platinum + 10 % Rh) thermocouple was used for sensing the temperature. The heating elements were based on Si-carbide (SiC) rods.

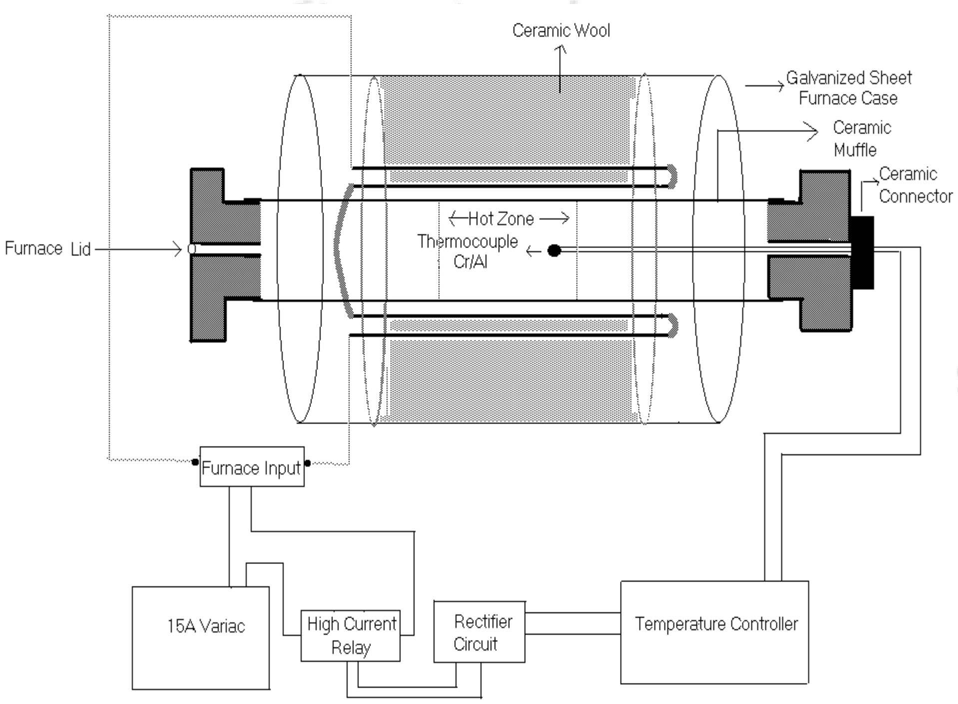

Figure 2.1: Block diagram of furnace with maximum operating temperature of 1200 ˚C.

The temperature was controlled to an accuracy of ± 1 ºC. The furnace could be operated up to a maximum temperature of 1400 ºC. The other furnace supplied by Bysakh & Co. contains (1) a thyristor unit with a rating of 35 A, (2) a PID programmable temperature controller (model no. PRC-300) with 16 segment programming features, (3) a platinum versus platinum-rhodium (Platinum + 13 % Rh) thermocouple wire and (4) Si-carbide rods based heating elements. The maximum operating temperature is 1450 ºC.

The homemade furnace (upto 1200 ^{o}C) was fabricated using a cylindrical alumina muffle with an inner diameter of 5.8 cm and 50 cm length. Six Si-carbide rods of 45 cm length each were used as heating element. The muffle loaded with heating elements is housed in a cylindrical container of 50 cm diameter and 50 cm length and it is made up of galvanized aluminum sheet. High temperature ceramic bricks and ceramic wools are used as thermal insulation. Chromel-Alumel (Cr-Al) thermocouple and a commercial on/off type temperature controller are being used for temperature measurement and controlling. The input power to the furnace is regulated using a variac (dimmerstat) of 15 A capacity. An external on/off relay (15 A capacity) controls the power supply to the heater wire. The relay is triggered using the temperature controller. The block diagram of the furnace is shown in Fig. 2.1. The furnace could be operated up to a maximum temperature of 1200 ºC. The temperature could be controlled with an accuracy of ± 5 ºC.

2.2 Characterization Techniques

2.2.1 X-ray Diffraction

To confirm the phase purity and crystal structure of the annealed samples, powder XRD patterns were recorded at room temperature using Rigaku make TTRAX III (*Theta – Theta Rotating anode X- Ray*) diffractometer by employing Cu-Kα radiation ($\lambda = 1.54056$ Å). During the measurement, the voltage and current of the X-ray generator were kept at 50 kV and 180 mA respectively. The instrument is based on the principle of Bragg-Brentano geometry which is shown in Fig. 2.2. In this geometry, both X-ray generator and detector are placed at equidistance from the sample holder. The data were collected in a usual $\theta - \theta$ mode with an angular scanning speed of 3º/min and a step size of 0.03º.

The structural investigation of the prepared samples was accomplished by analyzing the XRD patterns by Rietveld refinement technique using the Fullprof software [126]. The experimentally observed XRD pattern was simulated using the phases obtained from the crystallographic database in which user selected parameters were refined to minimize the difference between the experimentally observed pattern and the calculated pattern by non-linear least square method. The background was refined using a polynomial function. Pseudo-Voigt function was chosen for peak shape refinement. The global parameters, such as coefficients of background polynomial, scaling factor, half width parameters (u, v, w) and lattice parameters (a, b, c) were mainly varied during the refinement.

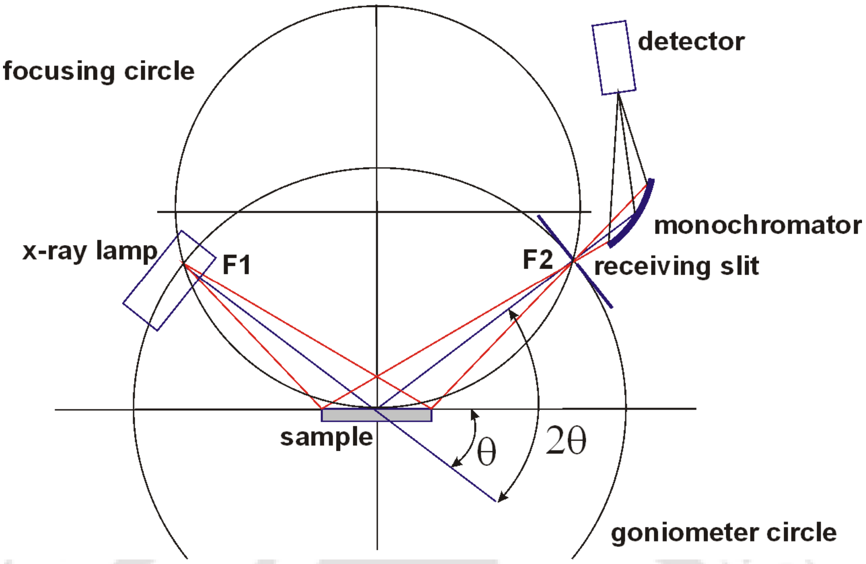

Figure 2.2: Ray diagram of X- ray diffractometer.

In addition, fractional atomic co-ordinates (*x*, *y*, *z*), isotropic displacement (temperature) parameters and occupancy values were also varied. Here, occupancy is the chemical occupancy normalized to the multiplicity of the general position of the group. The quality of the refinement was monitored using the values of reliability factors such as, R_p, R_{wp}, R_{exp}, R_{Bragg}, R_F and χ^2 and they are defined as [127],

Profile factor,
$$R_p = 100\frac{\sum_{i=1,n}\left|y_i - y_{c,i}\right|}{\sum_{i=1,n} y_i} \tag{2.2}$$

Here, y_i is the observed point (experimental) and $y_{c,i}$ is the calculated point and n represents the number of data points.

Weighted profile factor,
$$R_{wp} = 100\left[\frac{\sum_{i=1,n}\omega_i\left|y_i - y_{c,i}\right|^2}{\sum_{i=1,n}\omega_i y_i^2}\right]^{1/2} \tag{2.3}$$

Here $\omega_i = \frac{1}{\sigma_i^2}$, σ_i^2 is the variance of observation y_i.

Expected weight factor, $$R_{\exp} = 100\left[\frac{n-p}{\sum_{i=1,n}\omega_i y_i^2}\right]^{1/2} \qquad (2.4)$$

Here (n – p) is the number of degrees of freedom. n is the total number of experimental points and p is the number of refined parameters.

Reduced chi-square, $$\chi^2 = \left[\frac{R_{wp}}{R_{\exp}}\right]^2 \qquad (2.5)$$

Bragg factor, $$R_B = 100\frac{\sum_h \left|I_{obs,h} - I_{calc,h}\right|}{\sum_h I_{obs,h}} \qquad (2.6)$$

Here h represents the particular hkl Bragg peak. The $I_{obs,h}$ is the observed integrated intensities and $I_{calc,h}$ is the calculated intensities.

Crystallographic R_F factor, $$R_F = 100\frac{\sum_h \left|F_{obs,h} - F_{calc,h}\right|}{\sum_h F_{obs,h}} \qquad (2.7)$$

Here $F_{obs,h}$ and $F_{calc,h}$ are the observed and calculated structural factors respectively.

Bond lengths and bond angles were calculated using the refined fractional coordinates and lattice parameters using Fullprof software.

2.2.2 Raman Spectroscopy

Raman spectroscopy is a light scattering technique, and it is used to study properties such as crystalline phases, characterization of molecular structures, effects of bonding, strain, *etc.*, in a system. In simplest form it can be thought of as a process where a photon interacts with a sample to produce scattered radiation of different wavelength. Raman scattering is an inelastic event which probes the molecular vibrations. In Raman spectroscopy, the sample is illuminated with a mononchromatic laser beam which interacts with the vibrating molecules of the samples and most of the lights gets scattered elastically (Rayleigh scattering). A small fraction of the scattered radiation having a frequency different from that of the incident radiation constitutes the main features of Raman spectrum. If the frequency of incident radiation is higher than the frequency of scattered radiation, the scattered lines are known as stokes line, whereas if the frequency of incident radiation is lower than scattered radiation, then antistokes lines appear in the Raman spectrum. The Raman spectra studied in the present thesis work were recorded at room temperature by using micro-Raman spectrometer (LabRam HR800, Horiba Jobin Yvon) in the wave number range of 100 – 1000 cm^{-1} with an excitation wavelength of 514 nm. The frequency shift or the Raman shift is a measure of the energy of the molecular vibrational modes. Hence, the Raman spectra provide valuable structural information about crystalline phases, strain, defect, distortion, *etc*., present in a material.

Raman spectrometer can be dispersive and non-dispersive. Dispersive spectrometer uses a diffraction grating to disperse the light scattered from a sample while non-dispersive spectrometer uses an interferometer such as Michelson interferometer. Fig. 2.3 shows the basic building block of a dispersive micro-Raman spectrometer which we have used for sample characterization. Here the intense laser beam is incident on a sample through a microscope with spot size of a few microns. The microscope is coupled confocally to a spectrometer of 800 mm focal length with two switchable gratings. The excitation photon generally can be supplied by using two sources namely He-Ne laser (λ = 632.8 nm) and Argon laser (λ = 488 nm and 514 nm). The laser beam from the source is totally reflected by the beam splitter, which splits the beam into two parts having equal wavelengths. The beam was allowed to fall on the sample where both Rayleigh and Raman scattering occur. The notch filter blocks the Rayleigh scattered wavelength whereas it allows the Raman scattered wavelength. The inelastically scattered light was allowed to pass through the grating and etalon which in turn resolve the weak inelastic scattered wavelength coming from the sample more efficiently. Further the beam was allowed to enter into a charge couple device where it detects the change in polarizability of the sample from the change in wave length and converts into the intensity. The variation of intensity as a function of the wave number is displayed on the computer screen for the user.

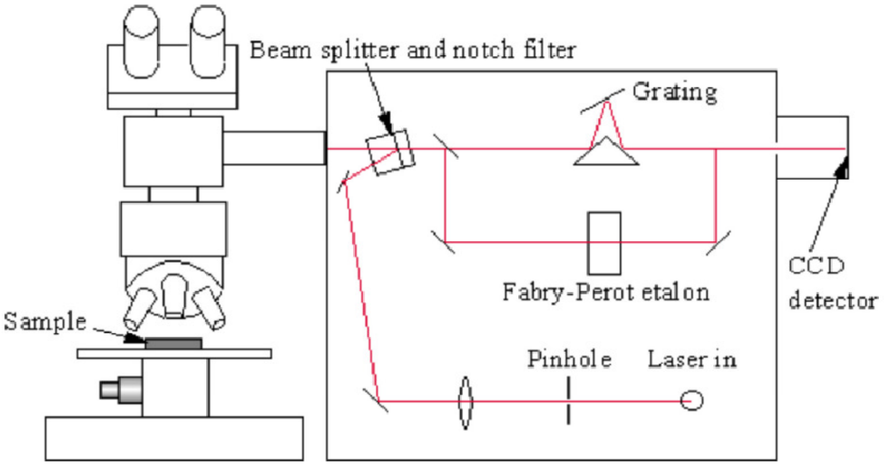

Figure 2.3: Schematic diagram of Raman spectrometer.

2.2.3 Field Emission Scanning Electron Microscope

Field emission scanning electron microscopy (FESEM) provides topographical details of the surface and elemental information of a wide variety of samples at different magnifications ranging from 10X to 300,000X. The FESEM produces clearer, electrostatically less distorted images with high spatial resolution down to 1 nm compared to that of the conventional scanning electron microscope (SEM). The in-lens FESEM can be used for ultra-high magnification imaging. In the present work the surface morphology of the samples was studied using ZEISS make FESEM (∑IGMA).

An FESEM works with highly energetic beam of electrons which are liberated from a field emission (FE) source known as “cold emission” source when it is placed under a huge electrical potential gradient. The FE source is basically a zirconium oxide coated tungsten (ZrO_2/W) emitter, which operates in a thermally assisted Schottky emission mode. This type of gun provides narrower probing beams as well as high electron energy, resulting in both improved spatial resolution and minimized sample charging and damage. The electrons liberated from the FE source are accelerated in a high electrical field gradient under extreme vacuum. The accelerating voltage between cathode (electron gun) and anode is commonly in the order of magnitude of 0.5 to 30 kV. The electron beam produced by the FE source is about 1000 times smaller compared to that of a standard scanning electron microscope; as a result, the quality of image is significantly better. The high vacuum allows the electrons to move along a column without scattering which helps to prevent discharges inside the instrument. Within the high vacuum column, these so-called primary electrons are focused and deflected by the electromagnetic lenses (Fig. 2.4) to produce a narrow scan beam that bombards the specimen. As a result of this bombardment different types of electrons are emitted from each spot of the specimen as shown in Fig. 2.5. Upon electron impingement on the surface, the interaction volume assumes a tear shape. These dislodged electrons are known as secondary electrons and the angle and velocity of these secondary electrons relates to the surface structure of the object. A highly efficient annular in-lens ac-detector catches the secondary electrons and produces an electronic signal. This signal is then amplified and transformed into a digital image of the sample.

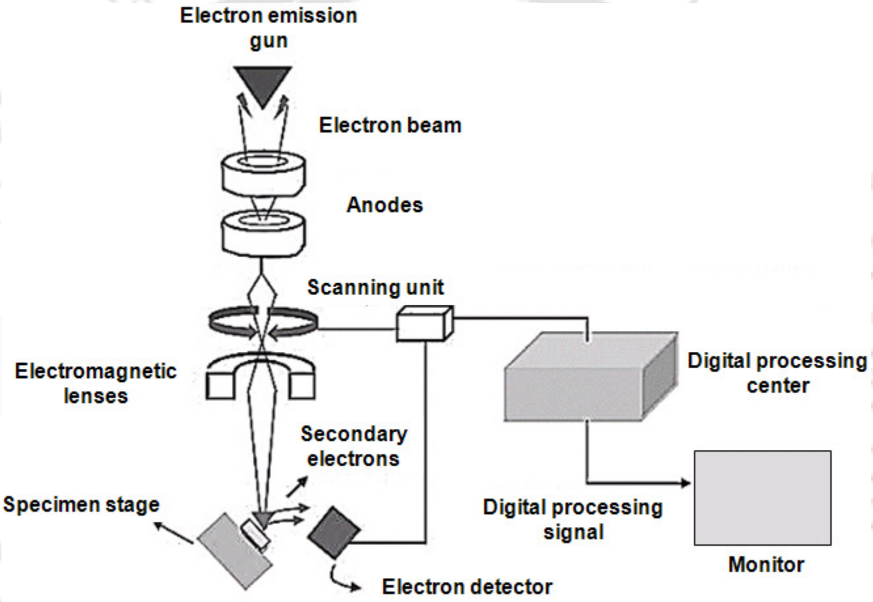

Figure 2.4: Schematic view of the field emission scanning electron microscope.

Apart from secondary electrons, the back scattered electrons (BSE), characteristic X-rays, light (cathode-luminescence), specimen current and transmitted electrons are also emitted from the specimen surface. These types of signal require specialized detectors and all such detectors are not present in a single machine. The primary electron beam results in the emission of BSE from the specimen. BSE possess more energy than secondary electrons and have a definite direction. As such, they cannot be collected by a secondary electron detector, unless the detector is directly in their path of travel. All emissions above 50 eV are considered to be BSE. BSE imaging is useful in distinguishing one material from another, since the yield of the collected BSE increases monotonically with the specimen's atomic number Z (~ 0.05 $Z^{1/2}$). Backscattered imaging can distinguish elements with atomic number difference of at least 3. In FESEM, one more detector, i.e., solid state back scattered detector is used to detect the BSE.

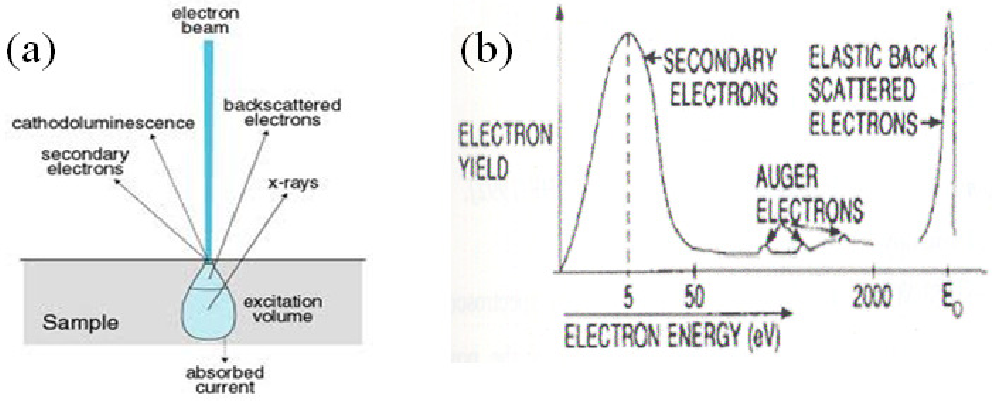

Figure 2.5: (a) Electrons and photons emanating from tear-shaped interaction volume during electron beam impingement on specimen surface, and (b) Energy spectrum of electrons emitted from the specimen surface.

The advantages of FESEM over SEM are as follows, (1) FESEM produces clearer, less electrostatically distorted images with spatial resolution down to 1 nm. That is 3 to 6 times better than conventional SEM; (2) smaller-area contamination spots can be examined at electron accelerating voltages compatible with Energy Dispersive X-ray Spectroscopy; (3) closer to the immediate material surface can be probed due to the reduced penetration of low kinetic energy electrons; (4) high quality, low voltage (0.5 to 30 kV) images are obtained with negligible electrical charging of samples.

Samples in the present thesis work are semiconducting in nature, thus before recording the FESEM images a small piece of the sample was placed on the FESEM sample holder using carbon tape and then coated with a extremely thin layer of gold (1.5 - 3.0 nm) to make them electrically conducting during the measurement.

2.2.4 Energy Dispersive X-ray Spectroscopy

Energy dispersive X-ray spectroscopy (EDS, EDX) is an analytical technique that uses the X-ray spectrum emitted by a solid sample when bombarded with a focused beam of electrons to obtain a localized elemental analysis or chemical characterization of the sample. The equipment is attached to the FESEM to allow for elemental information to be gathered about the specimen under investigation. Its characterization capabilities originate from the fact that each element has a unique atomic structure, which emits its unique characteristic X-ray. To stimulate the emission of characteristic X-rays from a specimen, a high energy beam of charged particles such as electrons or protons, or a beam of X-rays, is focused into the sample being studied. At rest, an atom within the sample contains ground state (or unexcited) electrons in discrete energy levels or electron shells bound to the nucleus. The incident beam may excite and eject an electron from an inner shell and it results in a hole or electron vacancy in the shell. An electron from an outer higher-energy shell then fills the hole, and the difference in energy between the higher-energy shell and the lower energy shell is released in the form of an X-ray. The atoms of every element releases X-rays with unique amounts of energy during the above process. Thus, by measuring the value of energy of X-rays being released by a specimen during electron beam bombardment, the identity of the atoms present in the specimen can be established. Thus, we get the EDS spectrum as an output and it is just a plot of how frequently an X-ray is received for each energy level. An EDS spectrum normally displays peaks corresponding to the energy levels for which the X-rays had been received. Each of these peaks is unique to an atom, and therefore corresponds to a single element. The intensity of the peaks depends on the concentration of the elements present.

The EDS spectra of the samples in the present thesis work were recorded using ZEISS make FESEM (ΣIGMA) equipped with EDS facility.

2.2.5 Vibrating Sample Magnetometer

Vibrating Sample Magnetometry (VSM) is a simple and effective measurement technique used for measuring the properties of various magnetic materials. It was invented by Simon Foner at MIT and has been the most successful instrument for low temperature and high magnetic field studies of most of the magnetic materials [128]. It has a flexible design and combines high sensitivity with ease of sample mounting and exchange. Using a VSM, the dc magnetic moment can be measured as a function of temperature, magnetic field and time. So, it allows performing susceptibility and magnetization study. Magnetic moments as small as 5×10^{-5} emu can be measured with a VSM [128].

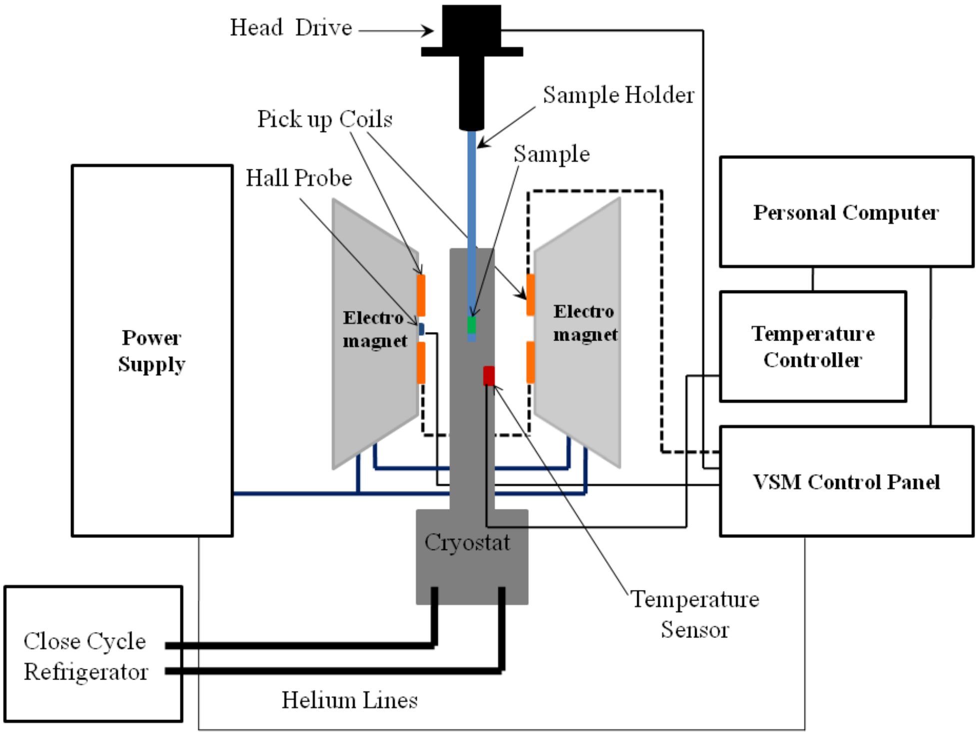

Figure 2.6: Block diagram of a vibrating sample magnetometer.

The temperature variations of zero field cooled (ZFC) and field cooled (FC) magnetization (*M*) were measured by the Lakeshore make, model no. 7410 VSM. Basic block diagram of a VSM equipped with the low temperature measurement attachment is shown in Fig. 2.6. The temperature variation down to 25 K was achieved using an OXFORD make close cycle refrigerator (CCR) cryostat (model N125) along with the temperature controller. The magnetic field was produced by using a 10-inch electromagnet. The magnetization loop (*M*–*H*) was measured by varying field upto 1.2 T. Calibration of the vibrating sample magnetometer was done by measuring the magnetic moment of a standard pure Ni sample.

The VSM is based on the principle of Faraday's law of induction which states that an emf is induced in a coil when there is a change in magnetic flux occurs through the coil. If a magnetic sample is placed between the pole pieces of the electromagnet and then driven by a mechanical vibrator, the oscillatory motion of the magnetized sample will induce a voltage in the pick-up coils. This induced voltage is proportional to the magnetic moment of the sample which can be varied by changing the dc magnetic field produced by the electromagnet.

Voltage, *V*(t) can be detected to a high resolution and accuracy by means of suitable VSM signal detector like the lock in amplifier.

2.2.6 Dielectric Measurement

Impedance data were measured by Wayne Kerr make LCR meter (Model 1J4300R/43100R) in the frequency range of 10^2 – 10^6 Hz with an AC voltage of 1.0 V_{rms}. The data were collected by LCR METER software provided by WayneKerr which connects the LCR meter to personal computer through RS232 interface. The temperature variation is carried out using a high temperature oven. The Chromal-Alumel (Cr-Al) thermocouple and a Eurotherm make temperature controller (Model no. 3216) are used for temperature measurements and controlling.

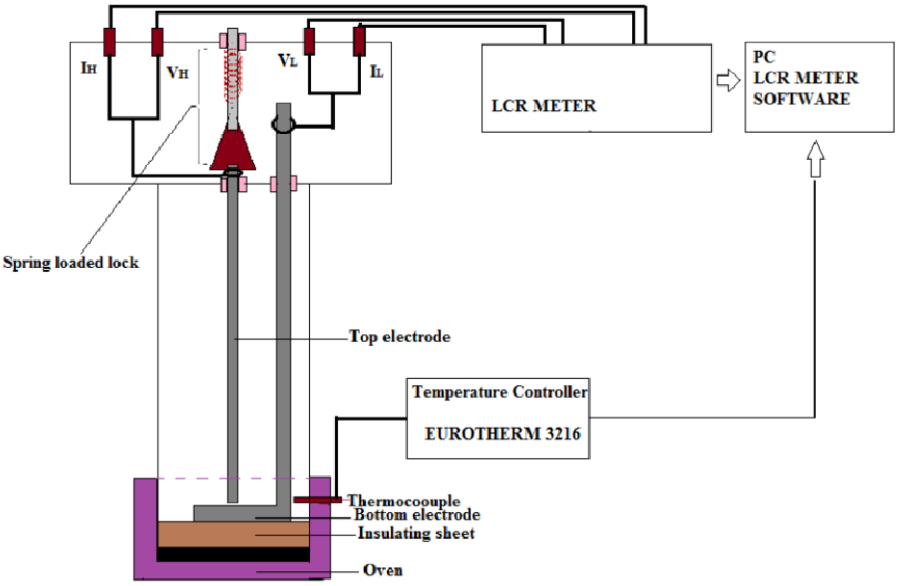

Figure 2.7: Block diagram for dielectric measurements.

For electrical measurements, samples were taken in pellet form with typical thickness of 1 – 1.5 mm and radius 9 – 10 mm. The thickness and radius are calculated using a digital vernier calliper. Electrodes are fabricated by painting silver paste on both sides of the pellets. The samples were fired at 150 °C in air for 2 h and furnace cooled to room temperature before carrying out the electrical measurement. The basic block diagram for impedance measurement set up is shown in Fig. 2.7. The set up consist of a sample holder which is connected to an LCR meter through four BNC connectors. The sample holder is made up of stainless steel. The measurements are carried out in a parallel plate capacitor arrangement by employing the four terminals method. The top electrode is supported by a spring which makes it possible to adjust according to the dimension of sample.

The top electrode is connected to the terminals VH and IH, while the bottom electrode is connected to VL and IL terminals. The IH/IL pair is connected to signal generator to pass the current through the sample, while VH/VL pair is used for voltage measurement. The LCR meter measures the voltage across the device under test (DUT) by sending current of certain frequency (ω) and calculates the impedance of DUT using the relation:

$$Z^*(\omega) = V^*(\omega)/I^*(\omega)$$

here, Z^*, V^*, I^* are complex quantities. The LCR meter used in the present work internally calculates and displays the capacitance and real (Z') and imaginary (Z'') parts of impedance Z^*. In the present study, we measure the Z' and Z'' in the frequency range of 10^2 - 10^6 Hz and calculated the related parameters such as real and imaginary part of the dielectric constant, conductivity, etc. The geometrical capacitance of the DUT with thickness *t* and area *A* can be calculated using the relation, $C_o = \frac{A\varepsilon_o}{t}$.

Chapter 3

Magnetization Reversal and Exchange Bias in Sm(Cr,Mn)O_3 and Sm(Cr,Fe)O_3 Compounds

$SmCrO_3$ is one of the interesting orthochromites with novel magnetic and dielectric properties [116,119,129,130]. Here Cr^{3+} ions undergo magnetic ordering such that they exhibit spin canted G-type AFM structure for $T < T_N$ (197 K). However, Sm^{3+} ions exhibit magnetic ordering only for $T < 10$ K [10,116]. $SmCrO_3$ also undergoes SR transition around $T_{SR} = 33$ K, which arises due to the onset of coupling between the spins of Sm^{3+} and Cr^{3+} ions [116]. Gupta *et al.* have reported MR and EB in $SmCrO_3$ which are attributed to the antiparallel coupling between the Sm^{3+} and Cr^{3+} magnetic sublattices [72]. Magnetic field induced electric polarization in the vicinity of T_N has also been observed in $SmCrO_3$ [10]. When Sm is partially replaced by La in $SmCrO_3$, zero field cooled EB is observed while, Bi substitution leads to both MR and EB behavior [120,122]. The substitution of Mn^{3+} or Fe^{3+} ions at Cr^{3+} site of $RCrO_3$ is reported to induce MR, EB, multiferroicity and giant magnetocaloric effect [73,95,102]. In $LaCr_{1-x}M_xO_3$ (M = Mn or Fe) both MR and EB behaviors are observed which are absent in $LaCrO_3$ [95,131]. Similary, the substitution of Fe in $DyCrO_3$ gives rise to multiferroicity and giant magnetocaloric effect [102]. In view of possible MR and EB behavior, we have taken up Mn and Fe substitution at Cr site of $SmCrO_3$ and studied their temperature and field dependant magnetic properties.

3.1 Mn Substituted $SmCrO_3$

This section deals with the preparation of Mn substituted $SmCrO_3$ samples, *i.e.* $SmCr_{1-x}Mn_xO_3$ ($x = 0 - 0.50$) and its effect on the structural and magnetic properties of $SmCrO_3$.

3.1.1 Sample Preparation and Characterization

Polycrystalline samples of $SmCr_{1-x}Mn_xO_3$ (x = 0, 0.05, 0.10, 0.15, 0.20, 0.30, 0.40 and 0.50) were prepared from stoichiometric ratio of Sm_2O_3, $Cr(NO_3)_3.9H_2O$ and manganese acetate all with high purity(> 98 %), using the standard sol-gel method. The above starting compounds were dissolved in either nitric acid (for oxides) or distilled water (for nitrates and acetates) to get a uniform solution of the mixture. Citric acid in 2:1 molar ratio with respect to the metallic cation was added to the solution to convert the nitrate/acetates into citrates. The solution was then converted to gel by the addition of ethylene glycol and the obtained uniform gel was heated at 70°C to get voluminous precursor. The voluminous precursor was then grinded and presintered at 600°C for 12 hrs followed by pelletisation and final sintering at 1100°C for 24 hrs. XRD patterns of the prepared samples were recorded at room temperature using Rigaku make TTRAX III X-ray diffractometer with CuK$_\alpha$ (λ = 1.54056 Å) radiation. Microstructure and compositional analysis were carried out by ZEISS make FESEM equipped with EDAX facility. Temperature and field dependent magnetic properties were studied using Lakeshore make VSM, model no. 7410 and Quantum Design make 9 Tesla physical properties measurement system (PPMS) VSM.

3.1.2 Structural Properties

The XRD patterns recorded at room temperature for $x = 0 – 0.50$ samples are shown in Fig. 3.1. The parent compound $SmCrO_3$ ($x = 0$) along with Mn substituted samples are found to be in single phase form as per the XRD patterns. XRD patterns of all samples were analyzed using the Rietveld refinement technique with the help of FULLPROF program. The best refinement was achieved by choosing *Pbnm* space group i.e. with orthorhombic structure. Typical XRD patterns of $x = 0$, $x = 0.30$ and $x = 0.50$ samples along with Rietveld refined data are shown in Fig. 3.2. The lattice parameters, volume of the unit cell and various reliability factors such as χ^2, R_P and R_{Bragg} obtained from the refinement are given in Table 3.1. It can be seen that the lattice parameters a and b are found to increase while c is found to decrease with increase in Mn concentration. This can be understood in terms of co-ordinated stretching along ab plane and compression along c direction. However, the unit cell volume is found to increase with Mn concentration having some anomaly around $x = 0.20$. This is consistent with larger Mn^{3+} (0.645 Å) ions replacing smaller Cr^{3+} (0.615 Å) ions.

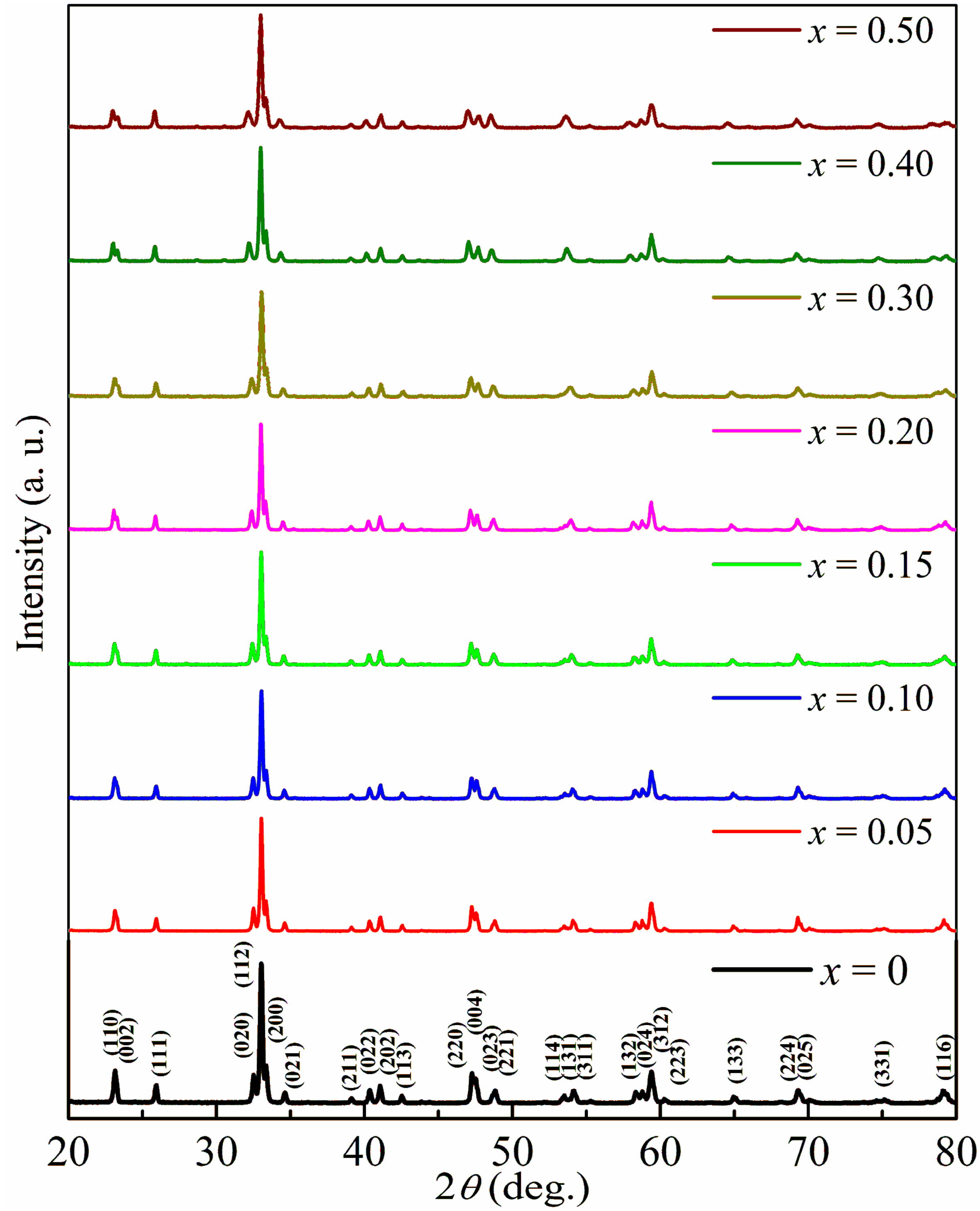

Figure 3.1: XRD patterns of $SmCr_{1-x}Mn_xO_3$ samples for $x = 0 - 0.50$.

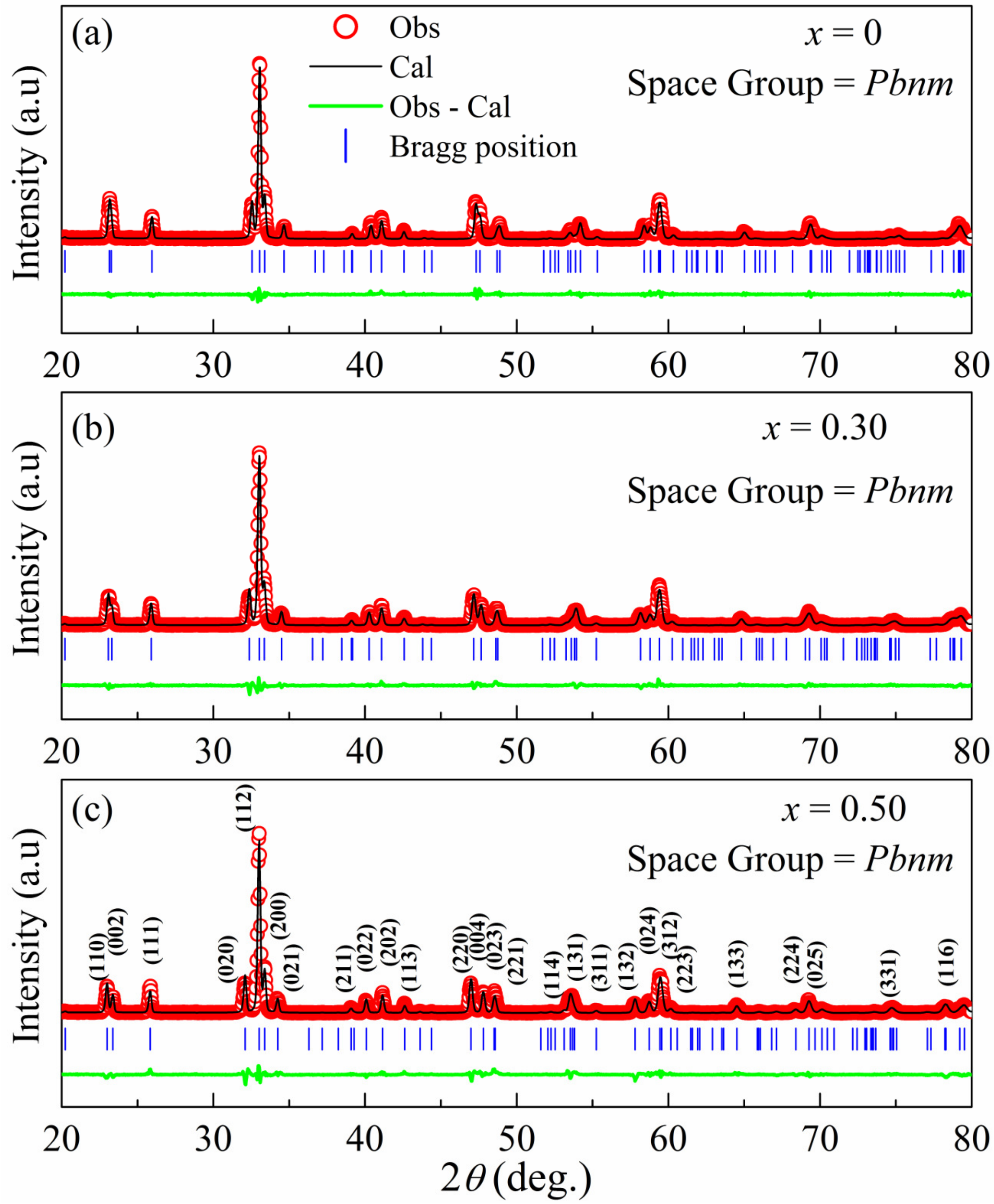

Figure 3.2: XRD patterns along with Rietveld refined data for x = 0, 0.30 and 0.50 samples. The circles represent the experimental points and solid line (black) represents the refined data. The bottom line (green) shows the difference between experimental and refined data. The vertical lines (blue) are the allowed Bragg position.

Table 3.1: Parameters obtained from the Rietveld refinement of XRD patterns of $SmCr_{1-x}Mn_xO_3$ (x = 0 to 0.50) samples.

Sample/ Parameters	**x = 0**	**x = 0.05**	**x = 0.10**	**x = 0.15**	**x = 0.20**	**x = 0.30**	**x = 0.40**	**x = 0.50**
Space group	*Pbnm*	*Pbnm*	*Pbnm*	*Pbnm*	*Pbnm*	*Pbnm*	*Pbnm*	*Pbnm*
a **(Å)**	5.3664(2)	5.36731(1)	5.3689(3)	5.3693(3)	5.3683(3)	5.3707(2)	5.3677(3)	5.3664(4)
b **(Å)**	5.5006(2)	5.50461(1)	5.5096(3)	5.5156(3)	5.5215(3)	5.5298(4)	5.5487(3)	5.5761(4)
c **(Å)**	7.6436(3)	7.6395(2)	7.6363(4)	7.6341(4)	7.6300(4)	7.6313(5)	7.6229(5)	7.6105(5)
Volume (Å^3)	225.63(1)	225.71(2)	225.88(2)	226.08(2)	226.16(2)	226.64(2)	227.03(2)	227.74(3)
R_F (%)	1.9	2.7	2.6	2.3	2.2	2.1	2.3	2.5
R_{Bragg} (%)	2.4	3.3	3.5	2.6	2.8	2.6	3.2	3.2
R_P (%)	7.2	7.9	7.9	7.3	9.5	8.5	9.3	9.9
R_{exp} (%)	6.8	7.1	6.9	6.7	8.0	7.0	7.4	7.1
χ^2	2.6	2.8	3.0	2.7	2.8	3.0	3.1	3.8
Sm/Cr/Fe Occupancy	0.987 /0.999 /0.000	1.001 /0.980 /0.050	0.996 /0.917 /0.099	0.990 /0.863 /0.144	0.984 /0.799 /0.200	0.990 /0.700 /0.299	0.996 /0.619 /0.399	0.962 /0.500 /0.490

The surface morphology of the all the samples were studied from the microstructural images recorded using FESEM. Typical FESEM images of $SmCr_{1-x}Mn_xO_3$ (x = 0, 0.30 and 0.50) samples along with the EDS spectrum of x = 0.30 sample are shown in Fig. 3.3. The surface morphology is found to be quite uniform for all the samples and the average grain size was estimated using the ImageJ software. The grain sizes are distributed over a wide range and the estimated average grain sizes of the samples are found to be 485 nm, 624 nm and 380 nm for x = 0, 0.30 and 0.50 samples respectively. The elemental analysis of the prepared samples has been carried out by recording the EDS spectra. The typical cationic ratio estimated from the analysis of EDS spectra of x = 0 – 0.50 samples are given in Table 3.2 and they are found to be comparable to their nominal starting compositions.

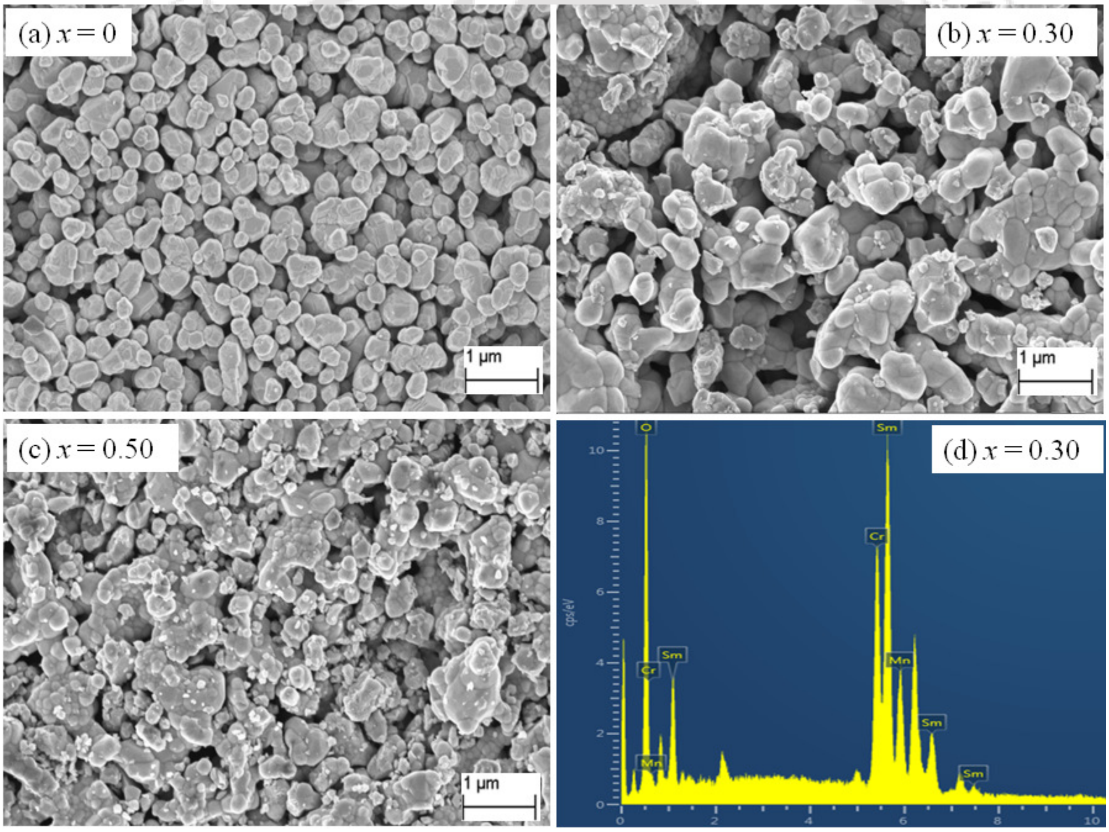

Figure 3.3: FESEM micrographs of (a) x = 0, (b) x = 0.30 and (c) x = 0.50 samples along with the EDS spectrum of x = 0.30 sample (d).

Table 3.2: The cationic ratio determined from EDS analysis for $x = 0 – 0.50$ samples.

Samples	Calculated Cationic Ratio from EDS analysis		
	Sm	**Cr**	**Mn**
$x = 0$	0.96	1.0	--
$x = 0.10$	0.96	0.92	0.08
$x = 0.20$	0.94	0.81	0.19
$x = 0.30$	0.96	0.71	0.29
$x = 0.50$	0.96	0.52	0.48

3.1.3 Magnetic Properties

Typical plots of temperature (T) variation of magnetization (M) in zero field cooled (ZFC) and field cooled (FC) conditions for an applied field of $H = 100$ Oe are shown in Fig. 3.4 for SmCr$_{1-x}$Mn$_x$O$_3$ ($x = 0 – 0.50$) samples. The ZFC M-T plot of $x = 0$ shows the antiferromagnetic (AFM) transition at $T_N = 196$ K. For $T < T_N$, it exhibits a plateau like behavior with maximum magnetization, $M \approx 7$ emu/mol and it can be attributed to the presence of weak ferromagnetic component arising from canting of Cr^{3+} ions. A sharp fall in magnetization is observed around $T_{SR} = 35$ K and it is basically due to the spin reorientation (SR) transition. Such spin reorientation transition is reported in SmCrO$_3$, where the alignment of antiferromagnetic axis rotates from a-axis for $T > T_{SR}$ to c-axis for $T < T_{SR}$ and their corresponding magnetic structure changes from Γ_4 (G_x, A_y, F_z) to Γ_2 (F_x, C_y, G_z) configuration [10,116]. The observed M-T plot of $x = 0$ sample is comparable to that reported in literature for SmCrO$_3$ [10]. The inset of Fig. 3.4(a) shows the temperature variation of derivative of magnetization under ZFC condition, where the clear negative and positive peaks at 196 K and 35 K are observed due to AFM and SR transitions respectively. The FC M-T plot of $x = 0$ sample exhibits a large irreversibility for $T < T_N$ with increase in magnetization upon cooling and reaches a maximum magnetization value of 67 emu/mol around 80 K. The plateau of maximum magnetization is maintained down to T_{SR} and for $T < T_{SR}$, a sharp fall in magnetization is seen. The large irreversibility in magnetization signifies the presence of competing AFM and canted FM components for $T < T_N$. The M-T plot of $x = 0.05$ sample follows the trend of $x = 0$ sample but with a smaller T_N value of 190 K.

However, unlike x = 0 sample, rather than a sharp fall in magnetization at T_{SR} = 35 K, a signature of rise in magnetization was observed.

The ZFC *M-T* plot of x = 0.10 sample shows the AFM transition at T_N = 179 K followed by a broad plateau like behavior as observed in x = 0 sample. However, unlike x = 0 sample, here a sharp rise in magnetization is observed as T approaches to T_{SR} as shown in the inset of Fig. 3.4(c) for clarity and it is similar to the case of x = 0.05 sample. The secondary rise in magnetization at $T < T_{SR}$ can be attributed to Zeeman energy induced spin flipping as reported in ref. [15]. The FC magnetization of x = 0.10 sample exhibits large irreversibility and its magnetization value is found to increase with decrease in temperature and attains a maximum value of 43 emu/mol at T_P =133 K. For $T < T_P$, magnetization falls continuously towards negative value by intersecting the temperature axis (M = 0) at the compensation temperature, T_{comp} = 51 K and approaches a minimum (maximum negative) magnetization value of M_{min} = -22 emu/mol. The observed increase in magnetization down to T_P as the temperature is lowered from T_N is due to the weak FM component of Cr^{3+} ions. The maximum magnetization (M_{max}) at T_P for x = 0.10 sample is found to be smaller (43 emu/mol) than that of x = 0 sample (67 emu/mol). The decrease in M_{max} with increase in Mn concentrations can be understood in terms of reduction in canted FM component of Cr^{3+} ions as a result of Mn^{3+} ions replacing some of Cr^{3+} ions. Thus, the sample x = 0.10 exhibits MR at T = 51 K. A clear signature of spin reorientation in both ZFC and FC magnetization curves can be seen at T_{SR} = 38 K for x = 0.10 sample as shown in Fig. 3.4(c). For further increase in Mn concentration up to x = 0.30, the FC curve follows the similar trend as that of the x = 0.10 sample as shown in Fig. 3.4(d - f). M_{max} value is found to decrease from 67 emu/mol for x = 0 to 1.2 emu/mol for x = 0.30 sample. The M_{min} is found to vary from -22 to -218 emu/mol for x = 0.10 to x = 0.20. However, the magnitude of negative magnetization for x = 0.30 (M_{min}= -28 emu/mol) sample is found to be smaller than that of x = 0.20 sample and this can be attributed to the presence of considerable Mn^{3+}- O^{2-}- Mn^{3+} networks and their antiferromagnetic interaction.

The *M-T* plot of x = 0.50 sample shown in Fig. 3(h) exhibits the typical FM behavior with T_C around 70 K with relatively large magnetization at $T < T_C$. The FC magnetization plot shows a further increase in magnetization by an order of magnitude. Similar behavior was observed for x = 0.40 sample. So, for $x \geq 0.40$ considerable FM behaviour is observed due to possible double exchange interaction in Mn^{3+}- O^{2-}- Cr^{3+} and Mn^{3+} - O^{2-} - Mn^{4+} networks. The large magnetic irreversibility observed in these samples suggests the existence of competing AFM interaction.

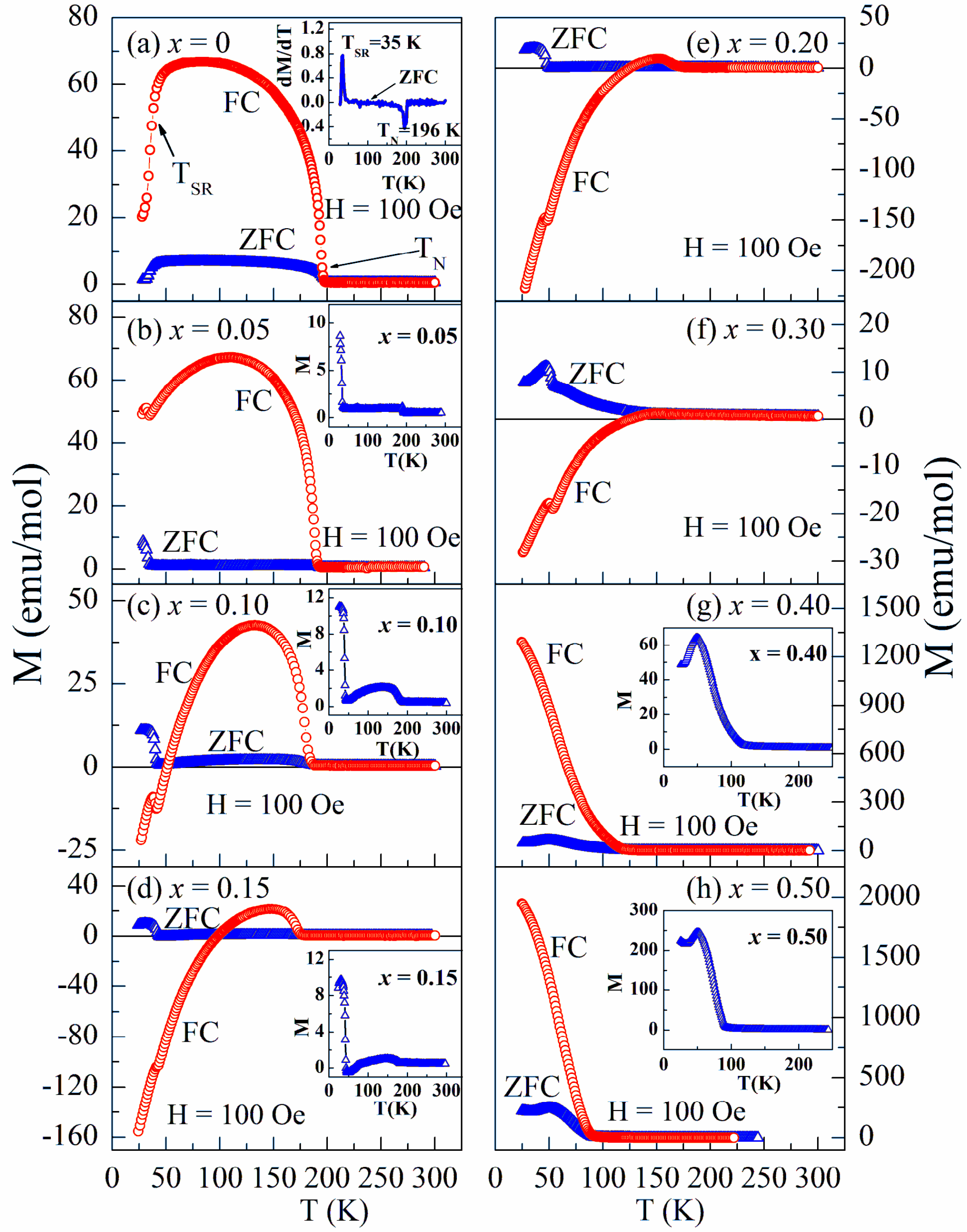

Figure 3.4: Temperature variation of magnetization of SmCr$_{1-x}$Mn$_x$O$_3$ (x = 0 – 0.50) samples under ZFC and FC modes for H = 100 Oe. Inset shows the temperature variation of dM_{ZFC}/dT for x = 0 sample (a) and enlarged view of relevant ZFC curves.

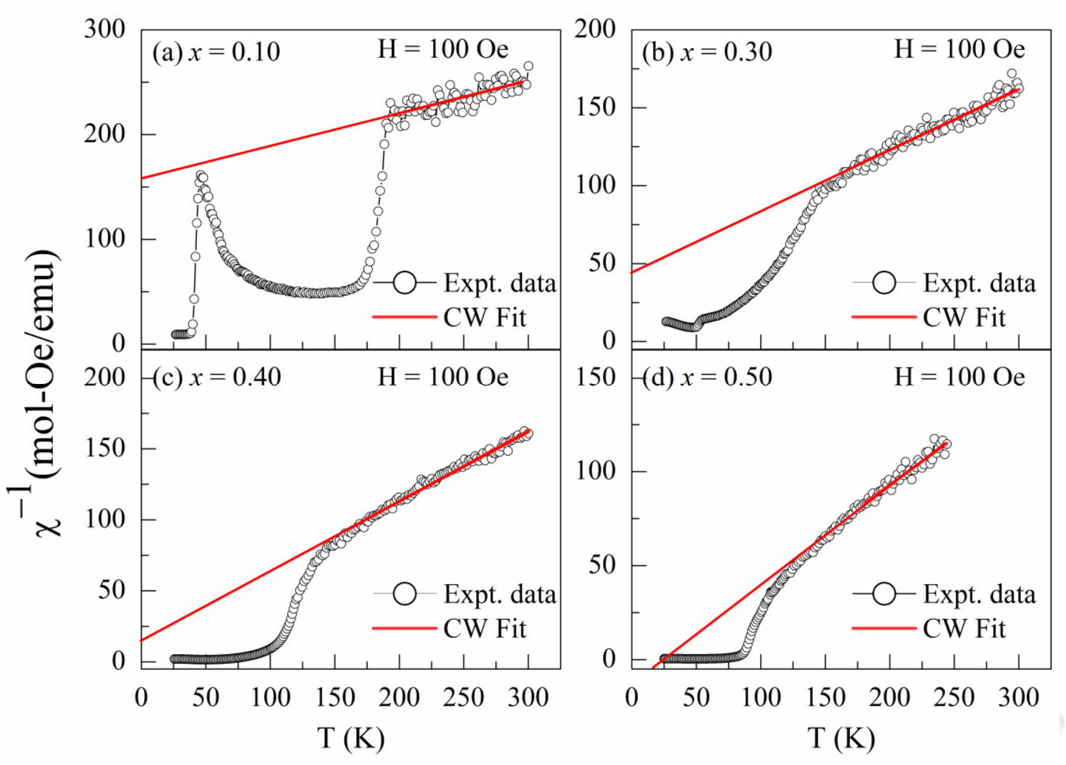

Figure 3.5: The temperature dependence of inverse susceptibility (χ^{-1}) for the samples (a) x = 0.10, (b) x = 0.30, (c) x = 0.40 and (d) x = 0.50 along with the fitting to the Curie-Weiss (CW) law.

The temperature dependence of magnetic susceptibility (χ) data in the paramagnetic region were analyzed using the Curie-Weiss (CW) law, $\chi = \frac{C}{T-\theta}$ for all samples except for x = 0 and 0.05 samples due to considerable scattering of susceptibility data in the PM region. The fitted data of the samples x = 0.10, 0.30, 0.40 and x = 0.50 are shown in Fig. 3.5. The values of Curie temperatures (θ) obtained from the fit are given in Table 3.3, and they reflect the AFM transitions. The magnitude of Curie temperature is found to decrease with increase in Mn concentration. For x = 0.50 sample, positive θ (= 4 K) is seen and it supports the observed FM like behavior with T_C = 70 K in the M-T plot. However, there is a large difference between θ and T_C which is due to the possible FM interaction in the short range scale or due to the presence of competing AFM. The experimental effective magnetic moment (${\mu_{eff}}^{exp}$) values estimated from Curie-Weiss law fit are shown in Table 3.3 along with their expected theoretical (${\mu_{eff}}^{th}$) values. The discrepancy between ${\mu_{eff}}^{th}$ and ${\mu_{eff}}^{exp}$ values, especially for the lower compositions ($x \leq 0.20$) may be ascribed to possible presence of weak FM clusters of Cr^{3+}- O^{2-}- Cr^{3+} networks in the PM region due their comparatively higher T_N values.

Table 3.3: Parameters obtained from Curie-Weiss law fit, compensation temperature (T_{comp}) and Neel temperature (T_N) for $SmCr_{1-x}Mn_xO_3$ (x = 0 to 0.50) samples.

x	μ_{eff}^{exp}	μ_{eff}^{th}	θ (K)	T_{comp} (K)	T_N (K)
0.00	--	--	--	--	196
0.05	--	--	--	--	187
0.10	5.1	4.07	-506	51	179
0.15	4.6	4.12	-320	98	170
0.20	4.7	4.18	-380	125	163
0.30	4.5	4.29	-117	126	143
0.40	4.2	4.39	-56	--	75
0.50	4.1	4.50	4	--	--

(i) Magnetization Reversal

In the present $SmCr_{1-x}Mn_xO_3$ (x = 0 – 0.50) series, we have observed the interesting temperature induced MR behavior in the composition range of x = 0.10 - 0.30. In general, the magnetization reversal can occur due to various reasons such as (a) core shell structure, (b) structural transition, (c) ferrimagnetic ordering between two sublattices magnetization having different temperature dependences, (d) competition between single ion anisotropy and DM interaction, and (e) polarization of paramagnetic moments under the influence of negative internal field [7,13,45,54,66]. The particle sizes of present set of samples are not in the nanometric range, so the core shell structure is unlikely to play any role. No structural transition is reported to appear in $SmCrO_3$ particularly in the vicinity of T_{comp} ; so the option (b) can be ruled out. For $T_{comp} \leq T \leq T_N$ we have not observed any ferro/ferri-magnetic ordering, thus the option (c) is not likely to play any role. Unlike, the magnetization behavior of $LaCr_{0.5}Fe_{0.5}O_3$ [113], here the magnetization data do not follow the expression based on single ion magnetic anisotropy - DM interaction model [60]. Thus, in present case the MR observed in x = 0.10 to 0.30 samples is studied by considering both substituted Mn^{3+} and host Sm^{3+} ions as paramagnetic entities under the influence of negative internal field (H_I) due to the AFM ordered Cr^{3+} ions. Thus, the temperature dependent competition between weak FM component of canted Cr^{3+} ions and the paramagnetic moments of Sm^{3+} and Mn^{3+} ions, under the negative internal field and the dominance of one component over the other at different temperature is expected to cause the MR.

So, the field cooled M-T data of $x = 0.10$ to $x = 0.30$ samples were fitted to the following equation [12]

$$M = M_{Cr} + \frac{C(H_I + H)}{T - \theta_C} \tag{3.1}$$

where, M is the net magnetization at a temperature T, M_{Cr} is weak FM component of canted Cr^{3+} ions, H is the applied magnetic field, H_I is the internal field, θ_C is the Curie temperature and C refers to the Curie-Weiss constant due to paramagnetic Mn^{3+} and Sm^{3+} ions. The fitted data using eq. 3.1 for $x = 0.10$, $x = 0.15$, $x = 0.20$ and $x = 0.30$ samples are shown as solid lines along with the experimental data (symbols) in Fig. 3.6 for $H = 100$ Oe. The fitted data are found to closely follow the experimental FC magnetization data. The estimated values of θ_C for different Mn concentration are found to vary from -5 K to 21 K. The estimated values of M_{Cr} and $-H_I$ as a function of doping concentration for 100 Oe field are shown in Fig. 3.7. They are found to decrease linearly with increase in Mn concentration upto $x = 0.20$ and they fall sharply with further increase in x values. The decrease of M_{Cr} and $|H_I|$ values with increase in Mn concentration can be explained in terms of weakening of the AFM interaction and the associated canted FM due to Mn^{3+} ions replacing Cr^{3+} ions. The rather sharp decrease in $|H_I|$ value for $x = 0.30$ sample can be understood in terms additional magnetic interactions in Mn^{3+}- O^{2-} - Mn^{3+} and Mn^{3+}- O^{2-}- Cr^{3+} networks by drastically weakening the AFM interaction through Cr^{3+}- O^{2-} - Cr^{3+} networks. Moreover, the T_{comp} value is found to increase from 51 K for $x = 0.10$ sample to 126 K for $x = 0.30$ sample. It is due to increase in the PM moment with increase in Mn concentration as a result it cancels the oppositely aligned weak FM component of canted Cr^{3+} ions at a higher compensation temperature.

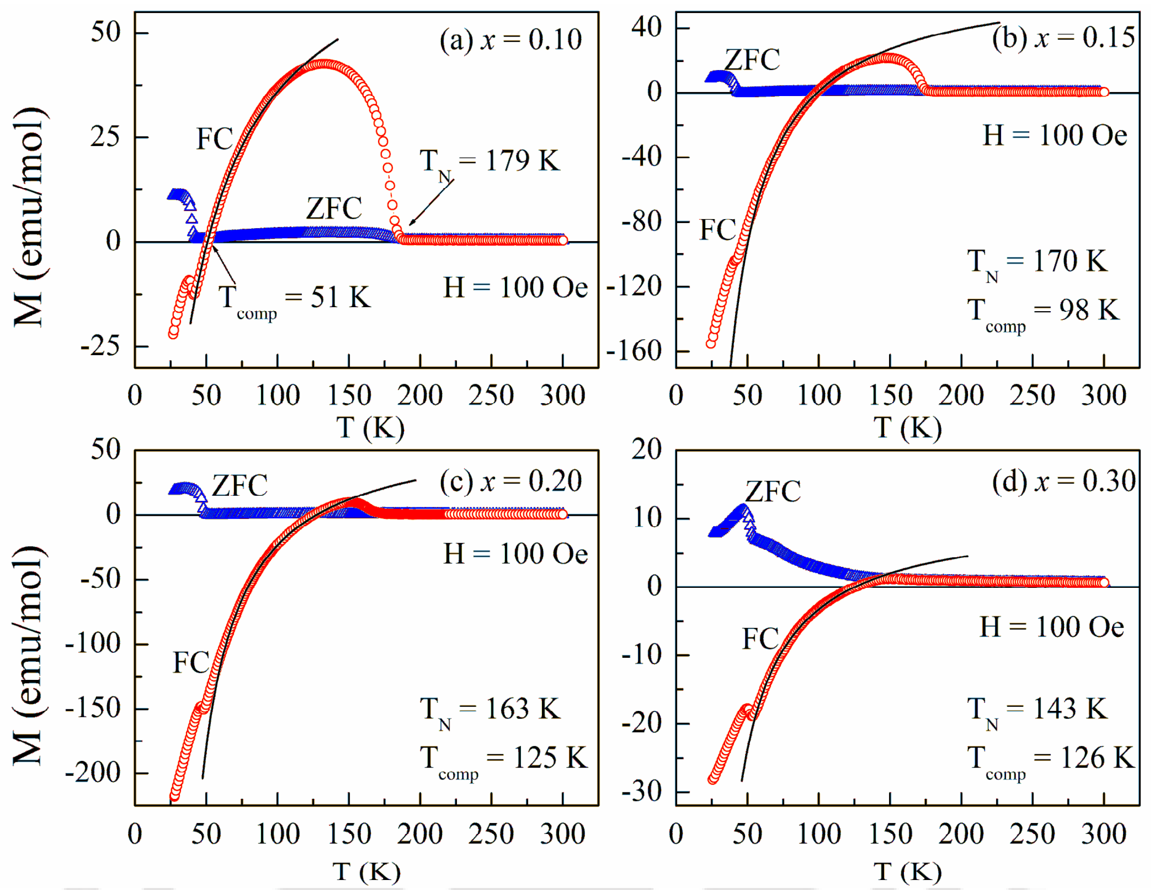

Figure 3.6: Temperature variation of magnetization of (a) $x = 0.10$ (b) $x = 0.15$ (c) $x = 0.20$ and (d) $x = 0.30$ samples under ZFC and FC modes for $H = 100$ Oe. The solid line (black) represents fit to eq. 3.1.

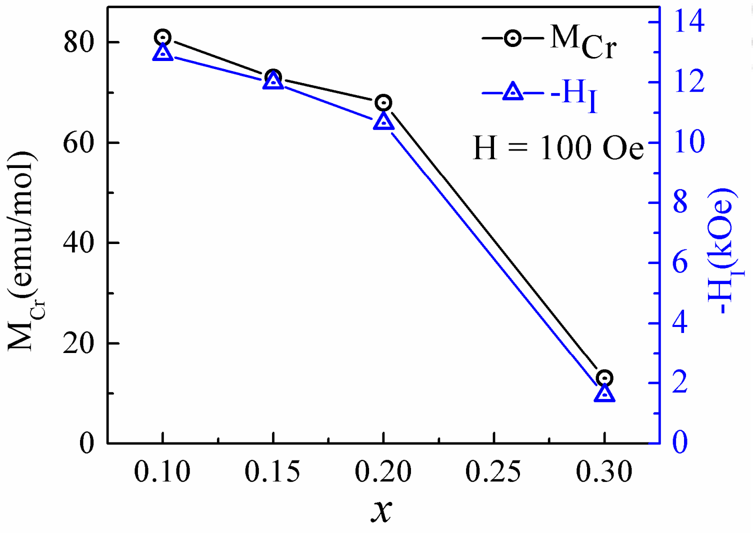

Figure 3.7: M_{Cr} and H_I as a function of Mn concentration (x) for $H = 100$ Oe in FC mode.

In order to understand the effect of the cooling field on magnetization reversal, we have measured the *M-T* data of $x = 0.10$, 0.15 and 0.20 samples by choosing different cooling fields in the range of $H = 100$ Oe to 2000 Oe and these *M-T* plots are shown in Figs. 3.8, 3.9 and 3.10 respectively. It can be seen that the trend of *M-T* curves of $x = 0.10$, 0.15 and $x = 0.20$ samples remain the same for all cooling fields. This suggests that there is no significant change in the mechanism of magnetic interaction except a shift in the entire *M-T* curves towards the positive value of magnetization. The shift is due to the enhancement in the weak canted FM component of Cr^{3+} ions with the increase in magnitude of applied field. The magnetization reversal behavior vanishes at $H = 2000$ Oe for $x = 0.10$ sample whereas it persists for $x = 0.15$ and $x = 0.20$ samples for the measured maximum H value of 2000 Oe due to the presence of a strong negative magnetization of these samples.

In case of $x = 0.30$ sample the negative magnetization disappears for a cooling field of $H = 500$ Oe as shown in Fig. 3.11. This is because of the involvement of some of the Mn^{3+} ions in the formation of M^{3+} - O^{2-} - Mn^{3+} networks. The measured FC magnetization curves of $x = 0.10$ sample was fitted to equation (3.1) for $H \leq 2000$ Oe and the fitted data (solid line) along with the experimental FC data are shown in Fig. 3.8. Similar fitting was also carried out for other samples ($x = 0.15$ and 0.20) in the field range of $H = 100$ to 2000 Oe as shown in Figs. 3.9 and 3.10 respectively. The fitted data nicely follow the experimentally measured FC magnetization data. The estimated values of θ_C are found to be in the range of -5 to -16 K for $x = 0.10$, -3 K to 12 K for $x = 0.15$ and -2 K to 20 K for $x = 0.20$ samples for a field variation of $H = 100$ Oe to 2000 Oe. It suggests the paramagnetic behavior of the Sm^{3+} ions and substituted Mn^{3+} ions. The variation of estimated M_{Cr} and H_I, as a function of H is shown in Fig. 3.12. Both the magnitude of M_{Cr} and H_I values are found to increase with the increase in H. Thus, the increase in the magnitude of applied field during the cooling results in increase in the size of the AFM domains which in turn increases the M_{Cr} and H_I values. The T_{comp} value decreases from 98 K to 89 K for $x = 0.15$ and 125 K to 112 K for $x = 0.20$ for the increase in H value from 100 Oe to 2000 Oe. With increase in H values, the FM component of Cr^{3+} ions get enhanced as a result more negative magnetization is needed to offset the increased positive magnetization (M_{Cr}). This gives rise to the shift in T_{comp} to lower temperature.

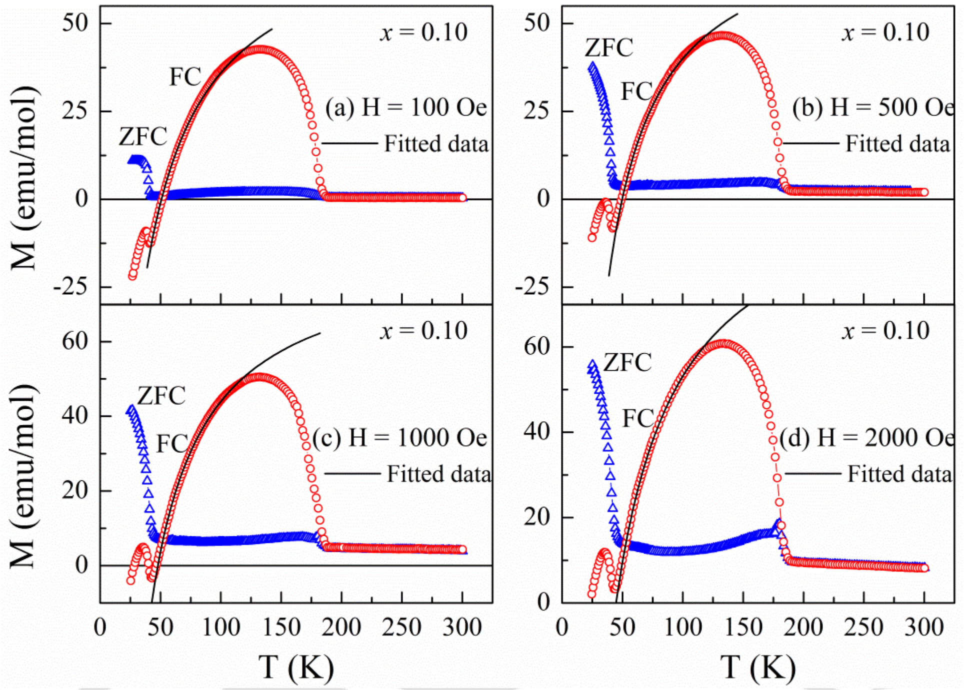

Figure 3.8: *M-T* curves in ZFC and FC conditions of $x = 0.10$ samples at (a) $H = 100$ Oe, (b) $H = 500$ Oe, (c) $H = 1000$ Oe and (d) $H = 2000$ Oe. The solid curve (black) represents the fitted data obtained using eq. 3.1.

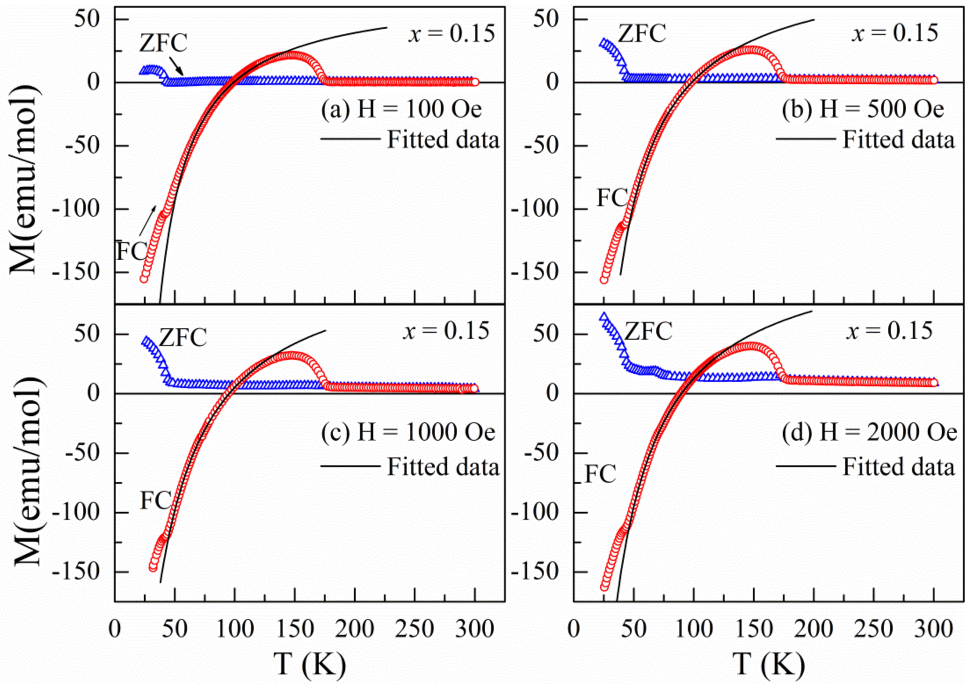

Figure 3.9: *M-T* curves in ZFC and FC conditions of $x = 0.15$ sample at (a) $H = 100$ Oe, (b) $H = 500$ Oe, (c) $H = 1000$ Oe and (d) $H = 2000$ Oe. The solid curve (black) represents the fitted data obtained using eq. 3.1.

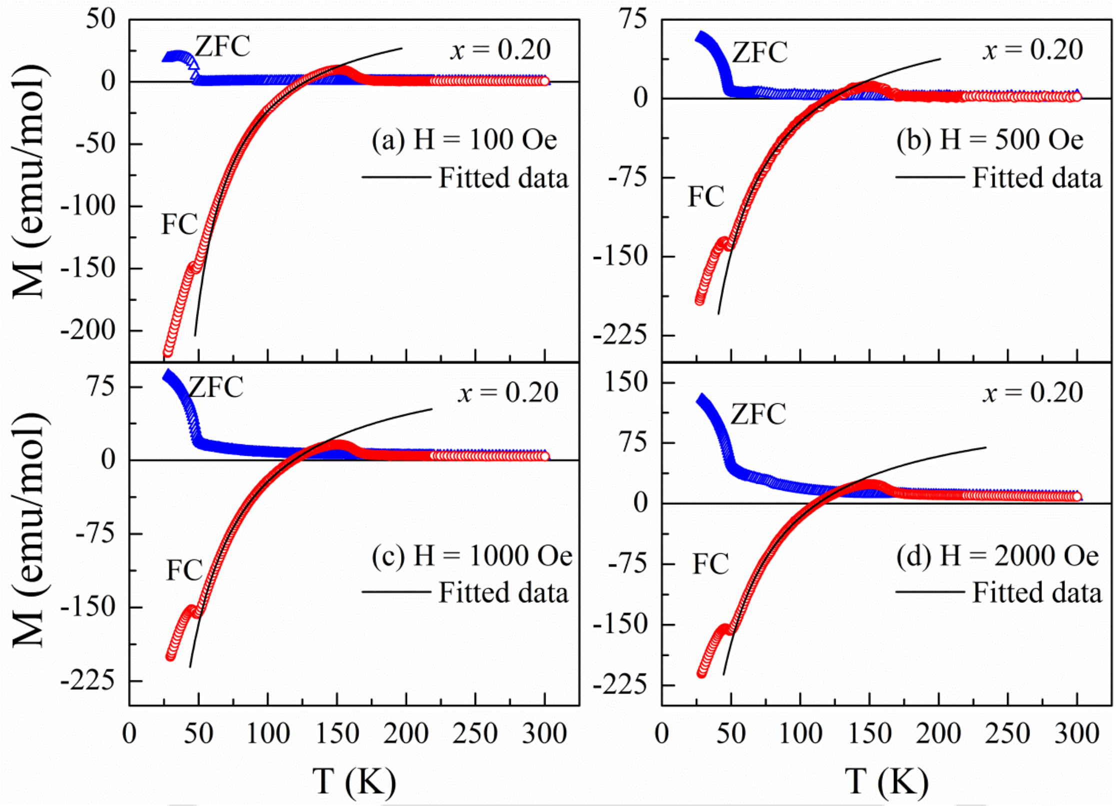

Figure 3.10: *M-T* curves in ZFC and FC conditions of $x = 0.20$ sample at (a) $H = 100$ Oe, (b) $H = 500$ Oe, (c) $H = 1000$ Oe and (d) $H = 2000$ Oe. The solid curve (black) represents the fitted data obtained using eq. 3.1.

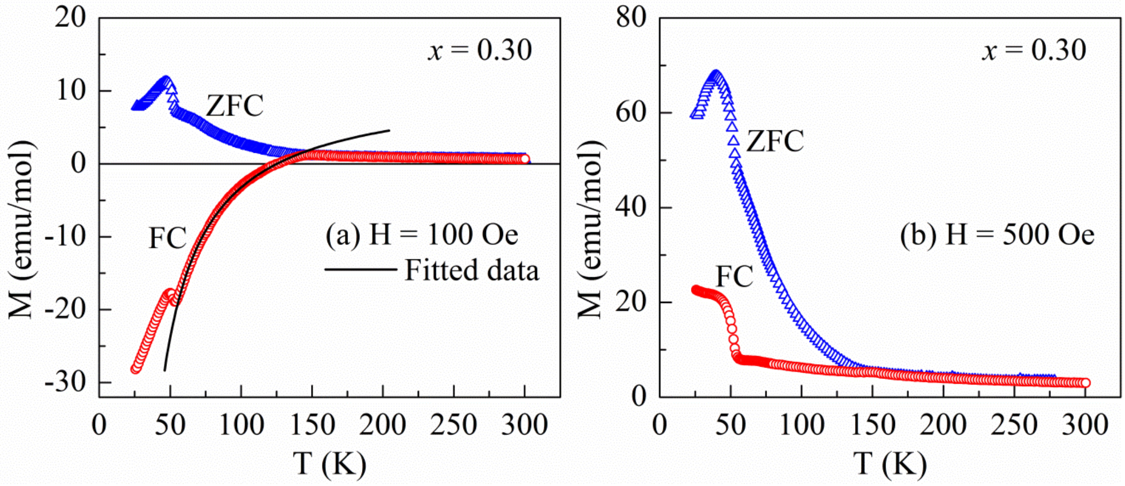

Figure 3.11: *M-T* curves in ZFC and FC conditions of $x = 0.30$ sample at (a) $H = 100$ Oe and (b) $H = 500$ Oe. The solid curve (black) represents the fitted data obtained using eq. 3.1.

In rare erath orthochromites, the magnetization reversal is achieved either by substitution of another magnetic rare earth ion at the rare earth site or by the substitution of transition metal ions at the Cr site. For example, $NdCr_{1-x}Fe_xO_3$ [73], $LaCr_{0.8}Mn_{0.2}O_3$ [95], $La_{1-x}Pr_xCrO_3$ [96], and $La_{0.75}Nd_{0.25}CrO_3$ [110] compounds exhibit the temperature induced magnetization reversal behavior. The origin of MR behavior observed in most of the rare earth orthochromites is mainly attributed to the competition between the paramagnetic moment of the magnetic rare earth ion (R^{3+}) and the canted FM component of canted Cr^{3+} ions and the dominance of one moment over the other in different region of temperature. The reported values of T_{comp} in some of the rare earth orthochromites system showing magnetization reversal like $La_{0.50}Pr_{0.50}CrO_3$ [132], $LaCr_{0.85}Mn_{0.15}O_3$ [94], $NdCr_{0.85}Mn_{0.15}O_3$ [74] are 163 K, 100 K and 147 K respectively. In the present set of samples, T_{comp} values are found to be in the range of 51 K ($x = 0.10$) to 126 K ($x = 0.30$) and are comparable to the reported values in literature on othochromites.

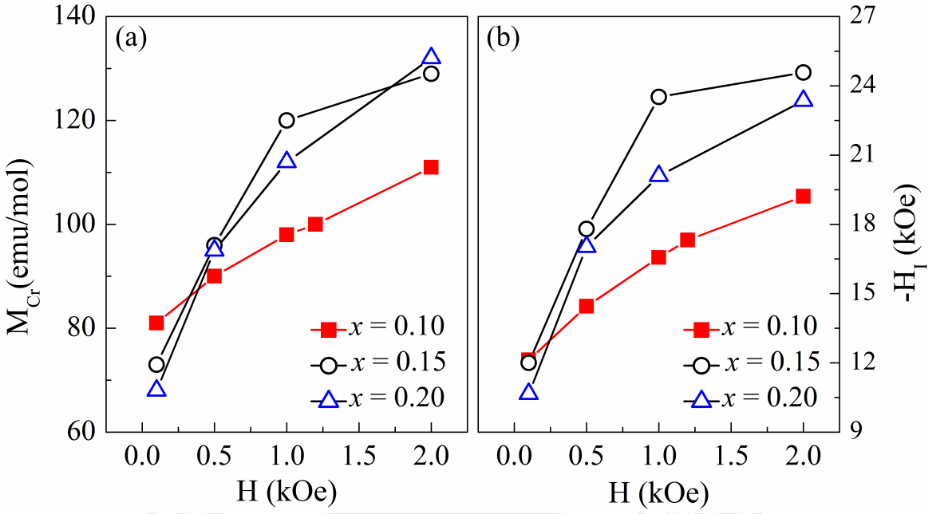

Figure 3.12: Variations of (a) M_{Cr} and (b) H_I as a function of applied field (H) for $x = 0.10$, 0.15 and $x = 0.20$ samples.

The value of internal field (H_I) in case of $La_{0.50}Pr_{0.50}CrO_3$ [14] was reported to be -8.5 kOe for $H = 100$ Oe and it varies between -4 kOe and -13 kOe for field variation of 20 Oe to 1 kOe. In $La_{0.15}Pr_{0.85}CrO_3$, it was between -2.8 and -3 kOe for a field variation of $H = 20$ Oe to 2 kOe [96]. Bora *et al* have reported the value of $H_I \approx 10 - 30$ kOe in $NdCr_{1-x}Fe_xO_3$ ($x =$ 0.10, 0.15) [73] compounds for H between 200 Oe and 2 kOe while the values reported by

Yoshii in La$_{0.25}$Pr$_{0.75}$CrO$_3$ compound [96] lie between 15 – 16 kOe which are comparable to magnitude of internal field obtained for the present set of samples.

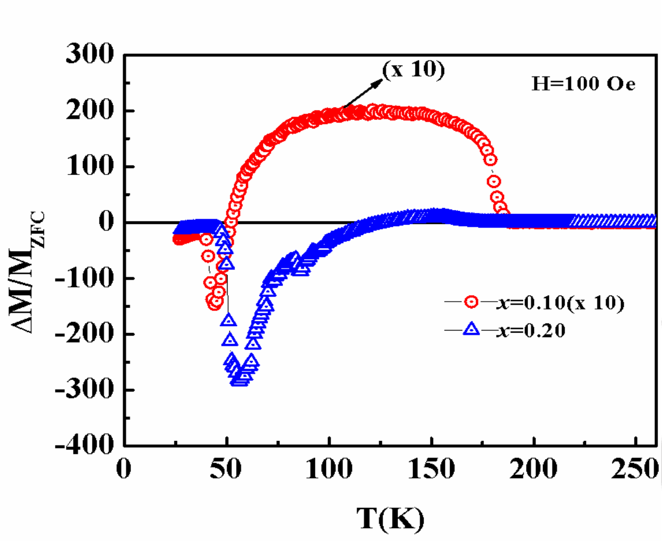

Figure 3.13: $\Delta M/M_{ZFC}$ versus temperature plots for x = 0.10 and x = 0.20 samples. For clarity, the data of x = 0.10 is multiplied by a factor of 10.

The degree of magnetization reversal is generally measured from the ratio of minimum (negative) and maximum (positive) magnetization *i.e.* M_{min}/M_{max}. In the present set of samples, the maximum absolute value of M_{min}/M_{max} is found to be 23 for x = 0.20 sample at an applied field of H = 100 Oe and it is in the same order of magnitude as reported for GdCrO$_3$, La$_{0.5}$Pr$_{0.5}$CrO$_3$ and NdCr$_{0.8}$Mn$_{0.2}$O$_3$ [13,14,74]. The fractional magnetization irreversibility at a particular temperature can be determined from the relation $\frac{\Delta M}{M_{ZFC}} = \frac{M_{FC}-M_{ZFC}}{M_{ZFC}}$. The temperature variation of $\frac{\Delta M}{M_{ZFC}}$ for x = 0.10 and 0.20 samples at H =100 Oe are shown in Fig. 3.13. A large negative peak is observed around 50 K along with the appearance of a broad positive peak above 100 K. For clarity, the data of x = 0.10 sample are multiplied by a factor of 10. The maximum negative value of $\frac{\Delta M}{M_{ZFC}}$ for x = 0.20 sample is -285. The values of such parameter reported in LaCr$_{1-x}$Mn$_x$O$_3$ and NdCr$_{1-x}$Mn$_x$O$_3$ system are -5 and -9 respectively [13,74]. Thus, the observed large negative value of $\frac{\Delta M}{M_{ZFC}}$ in the present set of sample highlights the presence of a strong magnetization reversal.

(ii) Magnetization Switching

Figure 3.14 shows the bipolar switching of magnetization *i.e.* switching of magnetization between positive and negative values at T = 90 K for x = 0.15 and T = 110 K for x = 0.20 samples just by varying the magnitude of the external magnetic field in the same direction. In order to achieve the switching behavior, the samples were first cooled down to the required temperature (below T_{comp}) under an applied field of H = 100 Oe and then at the same temperature the external field was increased to higher positive field to get an equivalent and positive value of magnetization. The switching of magnetization between positive and negative values was repeated several times and the result indicates reproducible field induced bipolar switching of the magnetization. For both the samples the switching of magnetization was performed between 100 Oe and 3500 Oe.

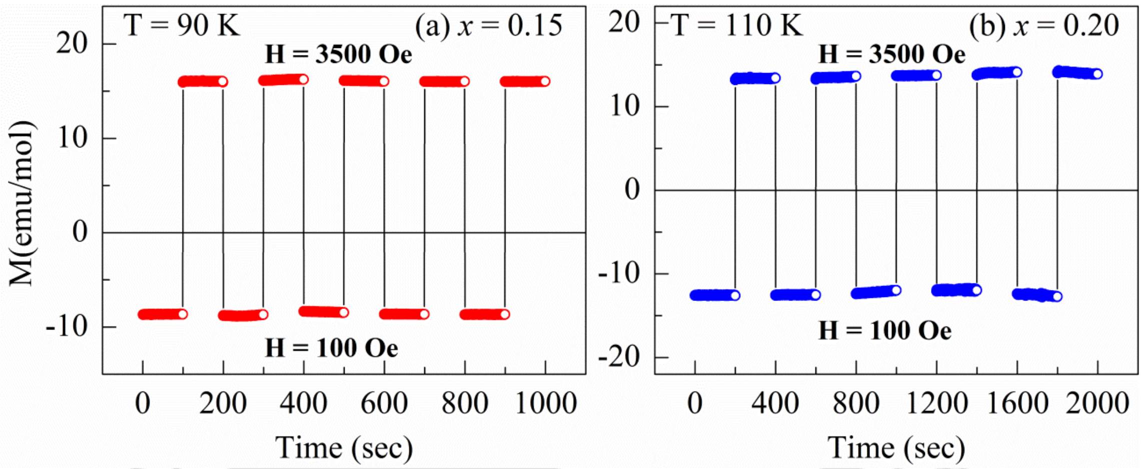

Figure 3.14: Bipolar switching of magnetization for (a) x = 0.15 and (b) x = 0.20 samples at T = 90 K and T = 110 K respectively.

(iii) Exchange Bias

In many systems, the temperature induced MR coexist with sign reversal in the exchange bias field across the T_{comp}. Therefore, it generates the interest to look for any possibility of exchange bias in the present systems. In order to explore the exchange bias behavior, *M-H* loops of x = 0.10, 0.20 and 0.30 samples were recorded under the FC condition through their respective T_N with an applied field of H = 5000 Oe in the temperature range of 5 K to 250 K. Typical *M-H* loops recorded at various temperature are shown in Fig.

3.15 for x = 0.10 while for x = 0.20 and 0.30 samples these are shown in Fig. 3.16. The isothermal *M-H* loops at T = 5 K for x = 0.10 - 0.30 samples exhibit an obvious hysteresis loop in the low field region (±0.5 T) while a linear increase in magnetization, without any saturation is observed. Such a behavior of the magnetization loop is due to weak ferromagnetism that comes from the canting of Cr^{3+} moments.

The *M-H* loops of x = 0.10 sample exhibit a shift towards negative field axis when measured in the region of $T_{comp} < T < T_N$ whereas for $T < T_{comp}$ they shift towards the positive field axis as shown in Fig. 3.17 in the expanded scale. Thus, the sample x = 0.10 exhibits both positive and negative exchange bias field whose polarity can be tuned by varying the temperature. However, the isothermal *M-H* loops, recorded under FC condition, of x = 0.20 and x = 0.30 samples do not exhibit any shift along the field axis *i.e.* absence of exchange bias behavior in the entire temperature range.

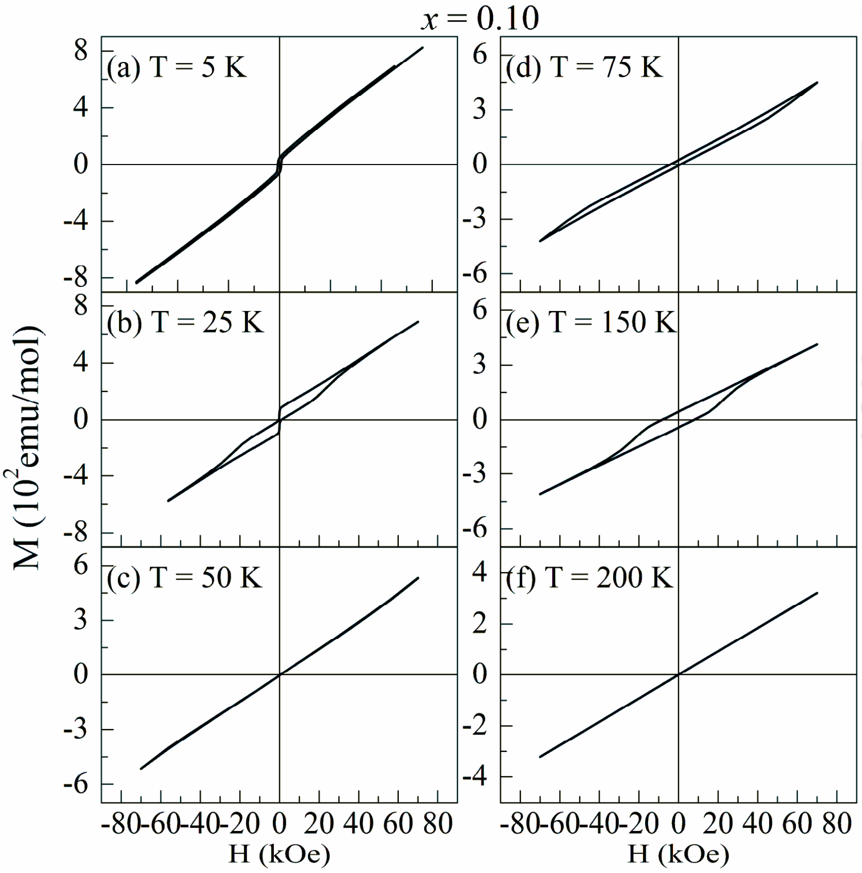

Figure 3.15: *M-H* loops recorded at different temperatures for x = 0.10 sample under FC condition for an applied field of H = 5000 Oe.

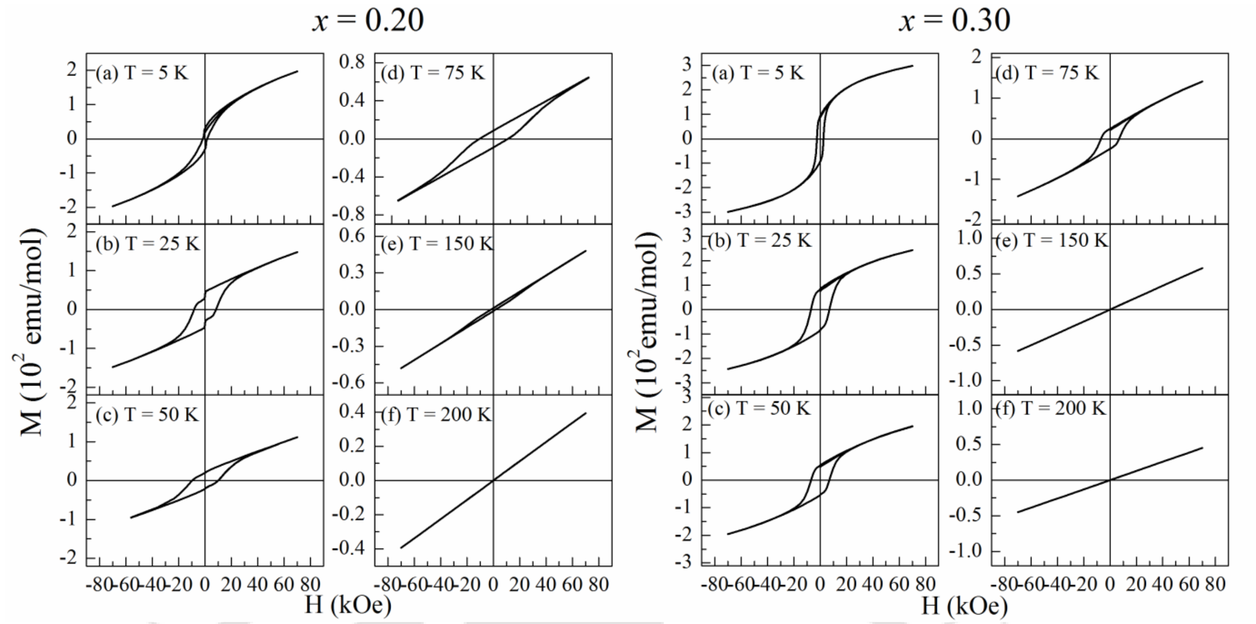

Figure 3.16: *M*-*H* loops recorded at different temperatures for (a) $x = 0.20$ and (b) $x = 0.30$ samples under FC condition for an applied field of $H = 5000$ Oe.

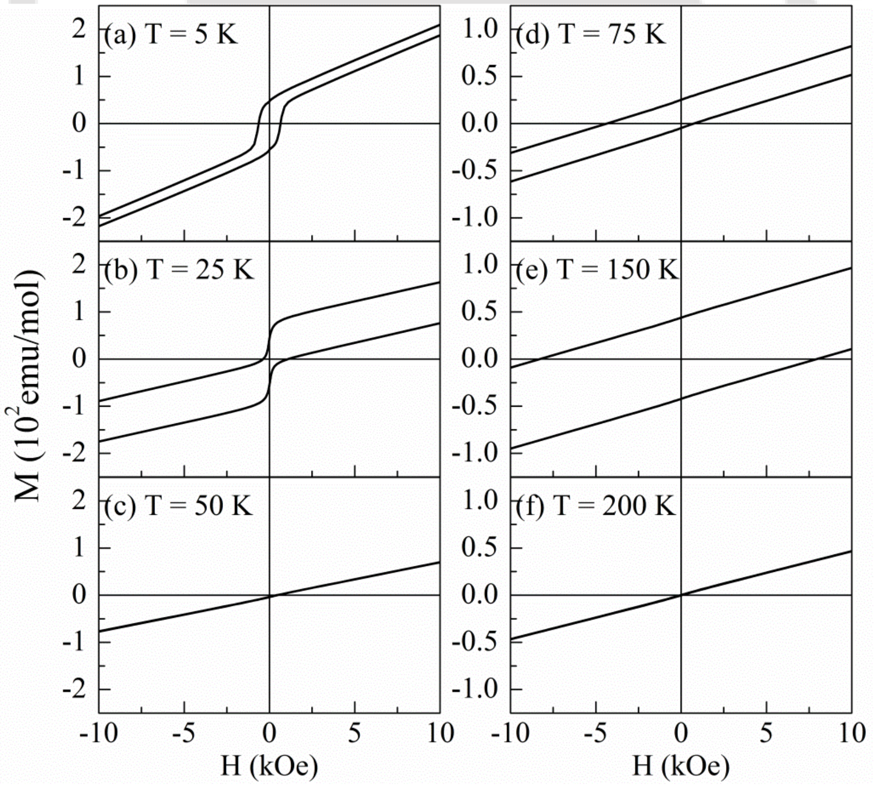

Figure 3.17: Enlarged view of *M*-*H* loops in the vicinity of coercive fields under FC condition for $H = 5000$ Oe measured at different temperatures for $x = 0.10$ sample.

The exchange bias field (H_{EB}) and effective coercive field (H_C^{eff}) were determined from the relations, $H_{EB} = (H_+ + H_-)/2$ and $H_C^{eff} = (H_+ - H_-)/2$ where H_+ and H_- represent the right and left coercive field, respectively. The temperature variations of H_{EB} and H_C^{eff} for x = 0.10 sample are shown in Fig. 3.18 (a & b). The temperature dependence of H_{EB} shows a sign reversal across the T_{comp}. As the temperature is decreased from T_N, H_{EB} decreases towards negative value and approaches a maximum negative value of -1.85 kOe at T = 75 K. For further decrease in temperature, the magnitude of H_{EB} starts to increase and it intersect the temperature axis (H_{EB} = 0) at $T \approx T_{comp}$. Below T_{comp}, the H_{EB} acquires positive values which increases to a maximum H_{EB} = 0.45 kOe at T_P = 50 K and thereafter it starts to decrease and finally approaches to zero. The temperature dependence of H_C^{eff} shows that its value drops to zero in the vicinity of T_{comp} which is due to the compensated moments across T_{comp}. The observed H_{EB} values are comparable to those reported for $NdMnO_3$ [85], $NdCr_{1-x}Mn_xO_3$ (x = 0.05, 0.15) [74].

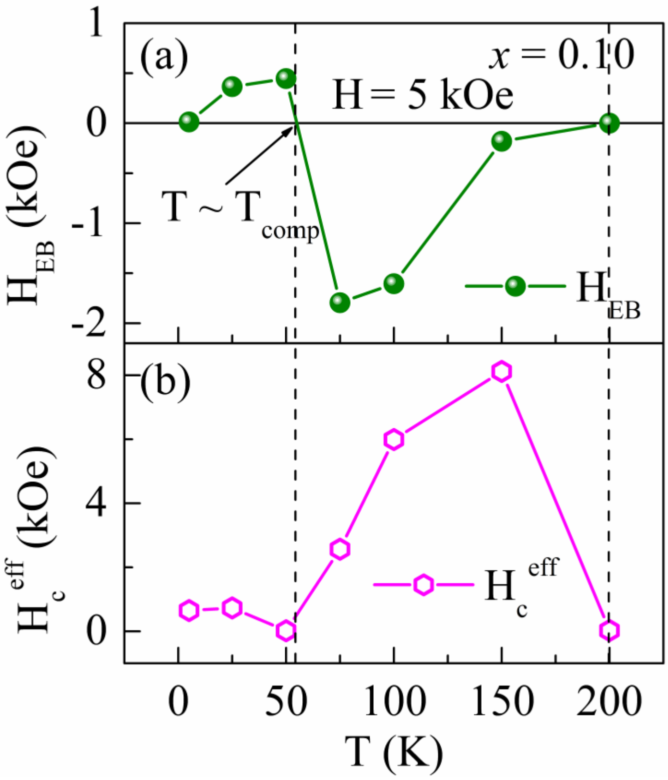

Figure 3.18: The temperature dependence of (a) exchange bias field, H_{EB} (upper panel) and (b) effective coercive field, H_c^{eff}(lower panel) for x = 0.10 ($SmCr_{0.90}Mn_{0.10}O_3$) sample measured under a cooling field of H = 5000 Oe.

Such a sign reversal of both magnetization and exchange bias has been recently observed in several compounds and the mechanism of their origin depends on the nature of material. In intermetallic compounds like $Nd_{0.75}Ho_{0.25}Al_2$ [55] the sign reversal of magnetization and EB arises from different types of exchange coupling between the moments of conduction electron polarization and the magnetic moments of dissimilar rare earth ions. In "AFM" $La_{0.20}Ce_{0.80}CrO_3$ nanoparticles [16], the sign reversal of both magnetization and EB is explained on the basis of core-shell geometry. The competition between the weak FM moment of canted Cr^{3+} ions and the PM moment of rare earth ion is responsible for the sign reversal of EB and magnetization in some orthochromites like $La_{1-x}Pr_xCrO_3$ [96], $NdCr_{1-x}Mn_xO_3$ [74] whereas in $YFe_{0.50}Cr_{0.50}O_3$ [114,115] the sign reversal is attributed to the competition between the single ion anisotropy and DM interaction. The exchange bias reversal has also been reported in many other materials like double perovskite [90], bilayers [91,92], spinel chromites [48,133,134], and solid solutions [135] and the cause of its origin is different for different kind of materials.

In the present case since we are dealing with bulk materials, the mechanism of core-shell structure which plays an important role in case of nanoparticles, is unlikely to play a role. The present data could not be fitted to the model based on the competition between single ion anisotropy and DM interaction. In the present samples, the possibility of conduction electron polarization is also not expected for $T < T_C$. Since, the present samples are not layered system, the role of FM/AFM interface is also ruled out. As mentioned above, the competition between the weak FM component of canted Cr^{3+} ions and paramagnetic moments of Sm^{3+} and Mn^{3+} ions, each having different temperature dependences, plays the major role in determining the net magnetization in the present samples. Thus, the sign reversal of exchange bias in present case is attributed to the competition between canted Cr^{3+} moments (M_{Cr}) and paramagnetic moments ($M_{PM} = M_{Sm} + M_{Mn}$) and the dominance of one component of moment over the other as the temperature is varied. In $T_{comp} < T < T_N$ region, M_{Cr} lies along the direction of applied field H, while M_{PM} tends to align along the direction of H_I which is antiparallel to H as portrayed in Fig. 3.19(a). In this temperature, M_{Cr} dominates over the M_{PM} which leads to a net positive magnetization in the system as a result larger negative field is required to reverse the direction of magnetization, so effectively the M-H loops shift towards negative field axis giving rise to negative exchange bias field. While for T

< T_{comp} region, the net PM moment (M_{PM}) under the influence of negative internal field gets enhanced and it dominates over the M_{Cr} resulting a net negative magnetization (Fig. 3.19(b)) which shifts the loop towards the positive side of the field axis during the *M-H* loop measurements and it gives rise to positive exchange bias field. At $T \approx T_{comp}$, both M_{Cr} and M_{PM} become equal in magnitude and but opposite in direction which gives rise to a linear *M-H* loop without any shift ($H_{EB} = 0$). As a result, the H_C^{eff} also reduce to zero close to the T_{comp}.

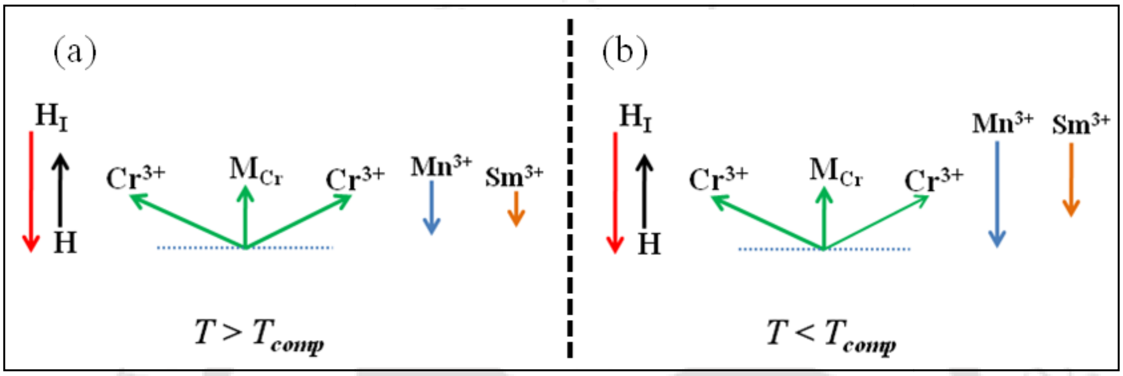

Figure 3.19 Schematic diagram representing the arrangement of canted Cr^{3+} moment and the PM component of Sm^{3+} and Mn^{3+} moments under field cooled condition at (a) $T > T_{comp}$ and (b) $T < T_{comp}$.

The observed sign reversal of exchange bias field as a function of temperature in the present sample can be compared with that of $NdMnO_3$ by Hong *et al* [85]. They observed the reversal in the sign of H_{EB} as a function of cooling field measured at $T = 30$ K and 8 K. For low applied field (say $H = 5000$ Oe), they got negative H_{EB} at $T = 30$ K which switches to a positive value as the temperature is lowered to 8 K. The origin of EB is due to the AFM coupling between the canted FM component of the Mn^{3+} sublattice and the FM ordering of Nd^{3+} sublattice while its sign reversal depends on the coupling intensity between the Nd^{3+} ordering and Mn^{3+} FM component. Yoshii has reported positive EB below T_{comp} due to magnetization reversal in $La_{0.15}Pr_{0.85}CrO_3$ [96] for low cooling field which is consistent with the present result. The origin of EB is explained on the basis of antiparallel coupling between the paramagnetic behavior of the Pr^{3+} moment and FM component of canted Cr^{3+} ions.

3.2 Fe Substituted $SmCrO_3$

This section deals with the preparation of Fe substituted $SmCrO_3$ samples, *i.e.* $SmCr_{1-x}Fe_xO_3$ ($x = 0 – 0.50$) and study of the effect of Fe substitution on the structural and magnetic properties of $SmCrO_3$.

3.2.1 Sample Preparation and Characterization

Polycrystalline samples of $SmCr_{1-x}Fe_xO_3$ (x = 0, 0.05, 0.10, 0.15, 0.20, 0.30, 0.40 and 0.50) were prepared from stoichiometric ratio of Sm_2O_3, $Cr(NO_3)_3.9H_2O$ and $Fe(NO_3)_3.9H_2O$ using the standard sol-gel method. Uniform solution of the mixture of the above starting compounds was obtained by dissolving them either in either nitric acid (for oxides) or distilled water (for nitrates). Citric acid in the molar ratio of 2:1 with respect to the metallic cation was added to the solution to convert it into citrates. Ethylene glycol was added to the uniform solution to convert it into gel and then it was heated at 70°C to get voluminous precursor. The voluminous precursor was grinded and presintered at 600°C for 12 hrs followed by pelletisation and final sintering at 1100°C for 24 hrs. XRD patterns of the prepared samples were recorded at room temperature using Rigaku make TTRAX III X-ray diffractometer with CuK_α (λ = 1.54056 Å) radiation. Microstructure and compositional analysis were carried out by ZEISS make FESEM equipped with EDS facility. Temperature and field dependent magnetic properties were recorded using Lakeshore make VSM, model no. 7410 and Quantum Design make 9 Tesla physical properties measurement system (PPMS) VSM.

3.2.2 Structural properties

The parent compound $SmCrO_3$ ($x = 0$) along with Fe substituted samples are found to be in single phase form as per the XRD patterns recorded at room temperature. The XRD patterns for $x = 0 – 0.50$ samples are shown in Fig. 3.20. XRD patterns of all samples were analyzed using the Rietveld refinement technique with the help of FULLPROF program. The best refinement was achieved by choosing *Pbnm* space group *i.e.* with orthorhombic structure. Typical XRD patterns for $x = 0$, $x = 0.30$ and $x = 0.50$ samples along with Rietveld refined data are shown in Fig. 3.21. The refined lattice parameters, unit cell volume and various reliability factors obtained from the refinement are given in Table 3.4. It is found that

that the lattice parameters of the substituted samples increase with the increase in Fe concentration. This is consistent with larger Fe^{3+} (0.645 Å) ions replacing smaller Cr^{3+} (0.615 Å) ions.

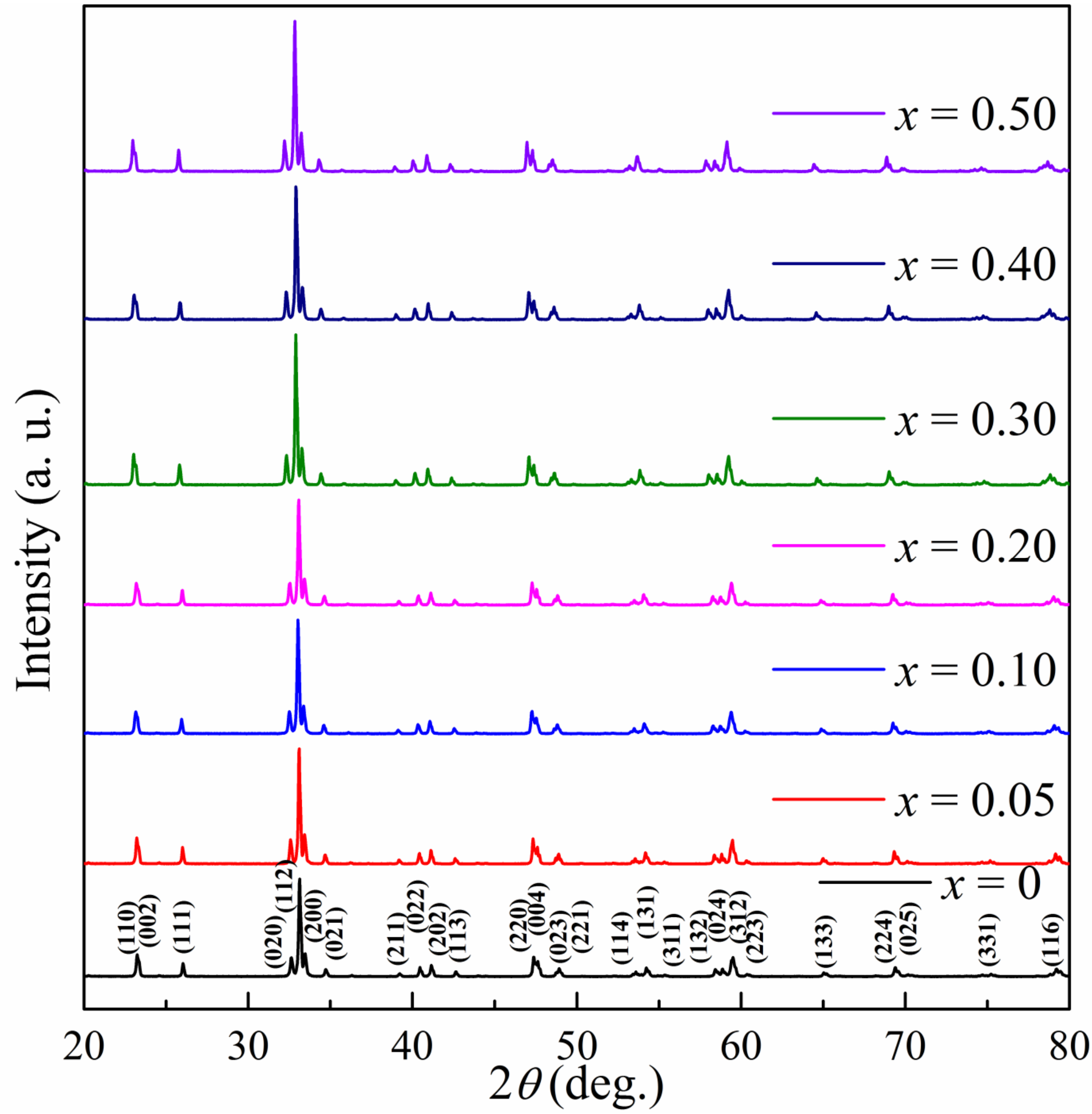

Figure 3.20: XRD patterns of $SmCr_{1-x}Fe_xO_3$ compounds for $x = 0 – 0.50$.

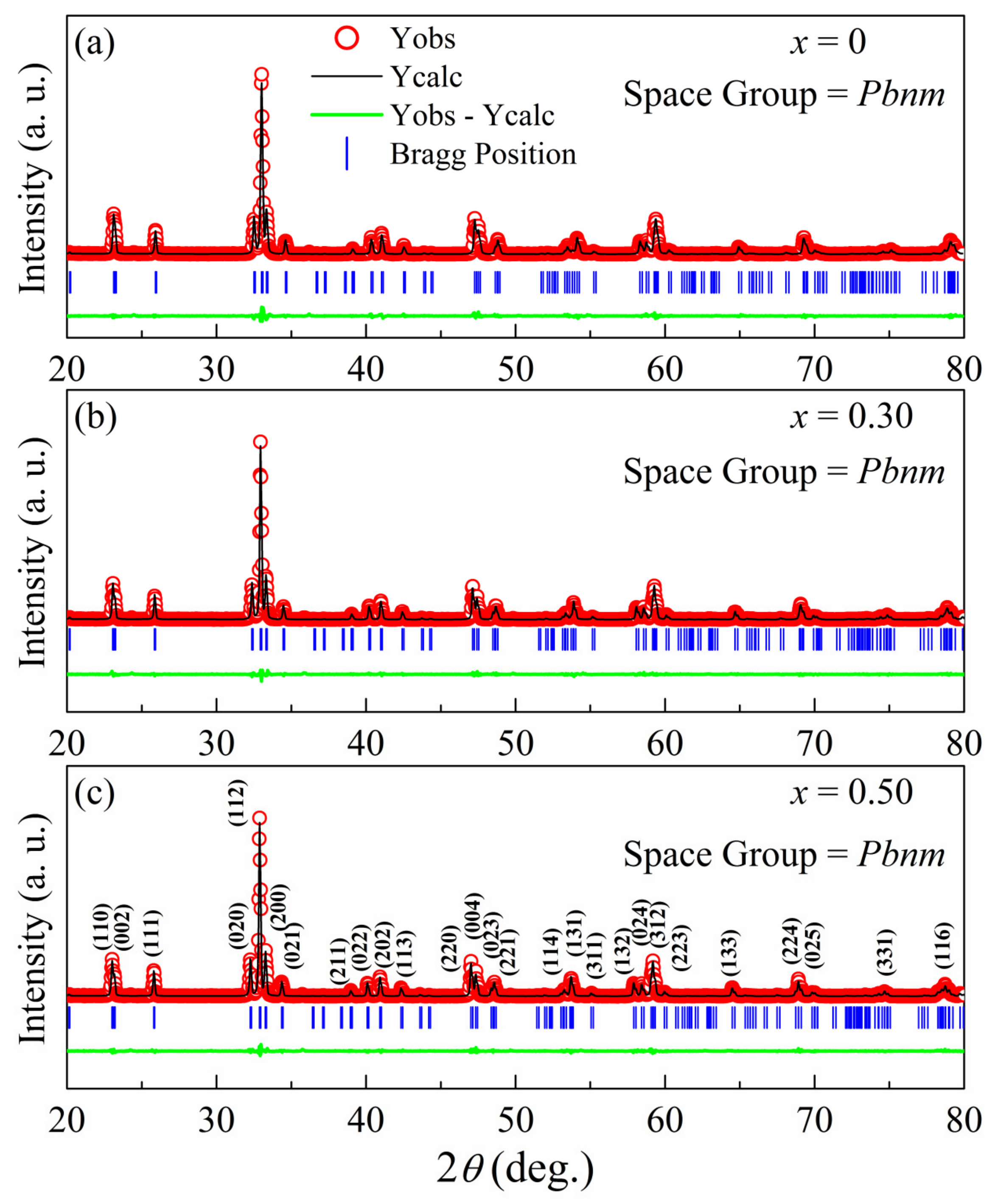

Figure 3.21: XRD patterns along with Rietveld refinement of $SmCr_{1-x}Fe_xO_3$ for (a) $x = 0$, (b) $x = 0.30$ and (c) $x = 0.50$ samples. The circles represent the experimental points and solid line (black) represents refined data. The bottom line (green) shows the difference between experimental and refined data. The vertical lines (blue) are the allowed Bragg position.

Table 3.4: Parameters obtained from the Rietveld refinement of XRD patterns of $SmCr_{1-x}Fe_xO_3$ (x = 0 to 0.50) samples.

Sample/ Parameters	***x* = 0**	***x* = 0.05**	***x* = 0.10**	***x* = 0.15**	***x* = 0.20**	***x* = 0.30**	***x* = 0.40**	***x* = 0.50**
Space group	*Pbnm*	*Pbnm*	*Pbnm*	*Pbnm*	*Pbnm*	*Pbnm*	*Pbnm*	*Pbnm*
a **(Å)**	5.3685(1)	5.3696(1)	5.3696(2)	5.3718(2)	5.3746(1)	5.3768(1)	5.3809(2)	5.3831(1)
b **(Å)**	5.5042(1)	5.5071(1)	5.5095(1)	5.5146(1)	5.5201(1)	5.5289(2)	5.5390(2)	5.5468(2)
c **(Å)**	7.6474(1)	7.6492(1)	7.6507(2)	7.6539(1)	7.6587(1)	7.6641(1)	7.6713(2)	7.6761(2)
Volume ($Å^3$)	225.98(1)	226.19(1)	226.34(1)	226.73(1)	227.22(1)	227.84(1)	228.65(1)	229.20(1)
R_F **(%)**	3.0	3.1	3.1	3.2	3.7	2.9	3.0	3.1
R_{Bragg} **(%)**	2.6	2.6	2.9	3.0	3.3	2.5	3.1	2.7
R_P **(%)**	8.1	8.3	9.0	9.1	9.7	8.3	9.1	9.1
R_{exp} **(%)**	8.1	9.2	9.2	9.2	9.3	8.0	8.2	8.3
χ^2	2.8	2.1	2.5	2.6	2.9	3.0	3.0	3.1
Sm/Cr/Fe Occupancy	0.999 /1.000 /0.000	0.991 /0.951 /0.050	0.999 /0.900 /0.099	1.000 /0.855 /0.149	1.000 /0.796 /0.199	1.000 /0.697 /0.300	0.999 /0.610 /0.400	1.000 /0.490 /0.497

The surface morphology of all the samples has been studied by recording the microstructural images using field emission scanning electron microscope. The typical FESEM micrographs recorded for $x = 0.10$ and $x = 0.50$ samples are shown in Figs. 3.22(a & b). The surface morphology is found be quite uniform for all the samples. The estimated average grain sizes of $x = 0$, 0.10, 0.30 and 0.50 samples are 485 nm, 509 nm, 561 nm and 718 nm respectively. The chemical compositions were obtained from EDS analysis and are found to be comparable to the respective nominal starting composition. Typical EDS spectra of $x = 0.10$ and 0.50 samples are shown in Figs. 3.22(c & d) and the cationic ratios estimated for $x = 0$, 0.10, 0.40 and $x = 0.50$ samples are found to be 0.96:1.0:0.0, 0:92:0.89:0.11, 0.92:0.62:0.38 and 0.94:0.52:0.48 respectively.

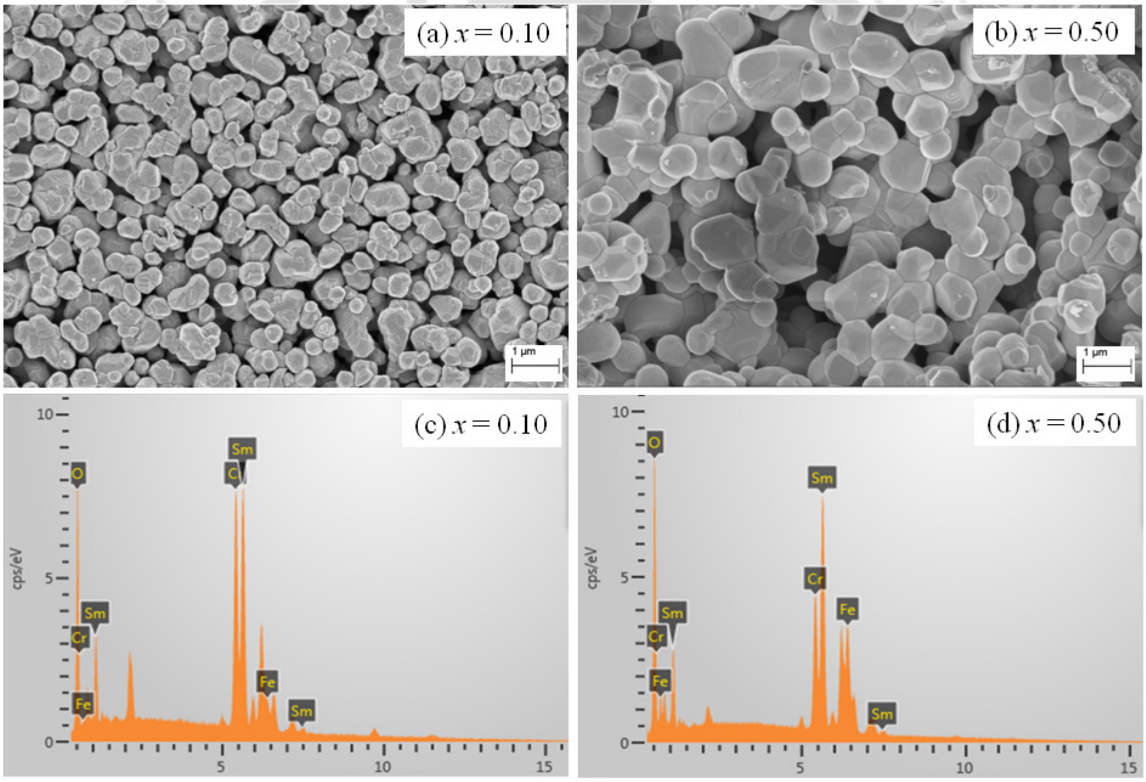

Figure 3.22: FESEM micrographs of (a) $x = 0.10$ and (b) $x = 0.50$ samples along with their EDS spectrum in (c) and (d), respectively.

3.2.3 Magnetic Properties

Temperature dependence of magnetization measured in the ZFC and FC conditions at an applied magnetic field of H = 100 Oe for $SmCr_{1-x}Fe_xO_3$ (x = 0 - 0.50) samples are shown in Fig. 3.23. The parent compound (x = 0) shows AFM transition at T_N = 196 K below which a weak FM behavior is observed due to spin canting of Cr^{3+} ions. The sharp fall in the magnetization of x = 0 sample around T = 40 K, suggests the spin reorientation behavior (Γ_4 to Γ_1) similar to the previous reports. The M-T plot of x = 0.05 sample follows a similar trend as that of the parent compound (x = 0) but with a reduced T_N of 192 K. However, the ZFC M-T curve of x = 0.10 doesn't exhibit the plateau like behavior as seen in x = 0 sample and the magnetization decreases below T_N (= 185 K) and then increases for T < 100 K and again fall around T_{SR} = 36 K as shown in inset of Fig. 3.23(c). However, the FC magnetization of the x = 0.10 sample shows magnetic irreversibility for $T < T_N$ in the form of broad peak with a maximum magnetization, M_{max} ~ 11 emu/mol at T = 156 K. For further decrease in temperature (T < 156 K) it starts to fall and then intersect the temperature axis at a compensation temperature (M = 0), T_{comp1} = 75 K, below which the magnetization acquires negative values. Such a behavior is known as magnetization reversal or negative magnetization. A minimum magnetization (maximum negative value) of M_{min} = -7 emu/mol is observed at T_{min} = 46 K. Below T_{min}, an upturn in the FC magnetization towards positive magnetization is observed due to the SR transition. M-T plot of the x = 0.15 sample also exhibits the similar behavior as that of the x = 0.10 sample but with a T_{comp1} of 148 K which is nearly twice that of x = 0.10 sample. Moreover, the broad peak observed in FC magnetization below T_N is found to be suppressed compared to x = 0.10 sample. The M_{min} value for x = 0.15 sample is found to be -12 emu/mol which is almost double to that of the x = 0.10 sample.

The M-T curve of $x \geq 0.20$ samples exhibit a quite different behavior compared to previous samples. They exhibit positive irreversible magnetization *i.e.* $M_{FC} > M_{ZFC}$ without any signature of magnetization reversal. The AFM transition temperature is found to shift towards higher temperature with increase in Fe concentration and it varies from T_N = 174 K (x = 0.20) to 244 K (x = 0.50) sample due to increase in the Fe^{3+} - O^{2-} - Fe^{3+} networks. The increase in T_N value suggest that the substituted Fe ions are involved in the long range AFM interaction via Fe^{3+} - O^{2-} - Fe^{3+} networks which increases with increase in Fe concentration.

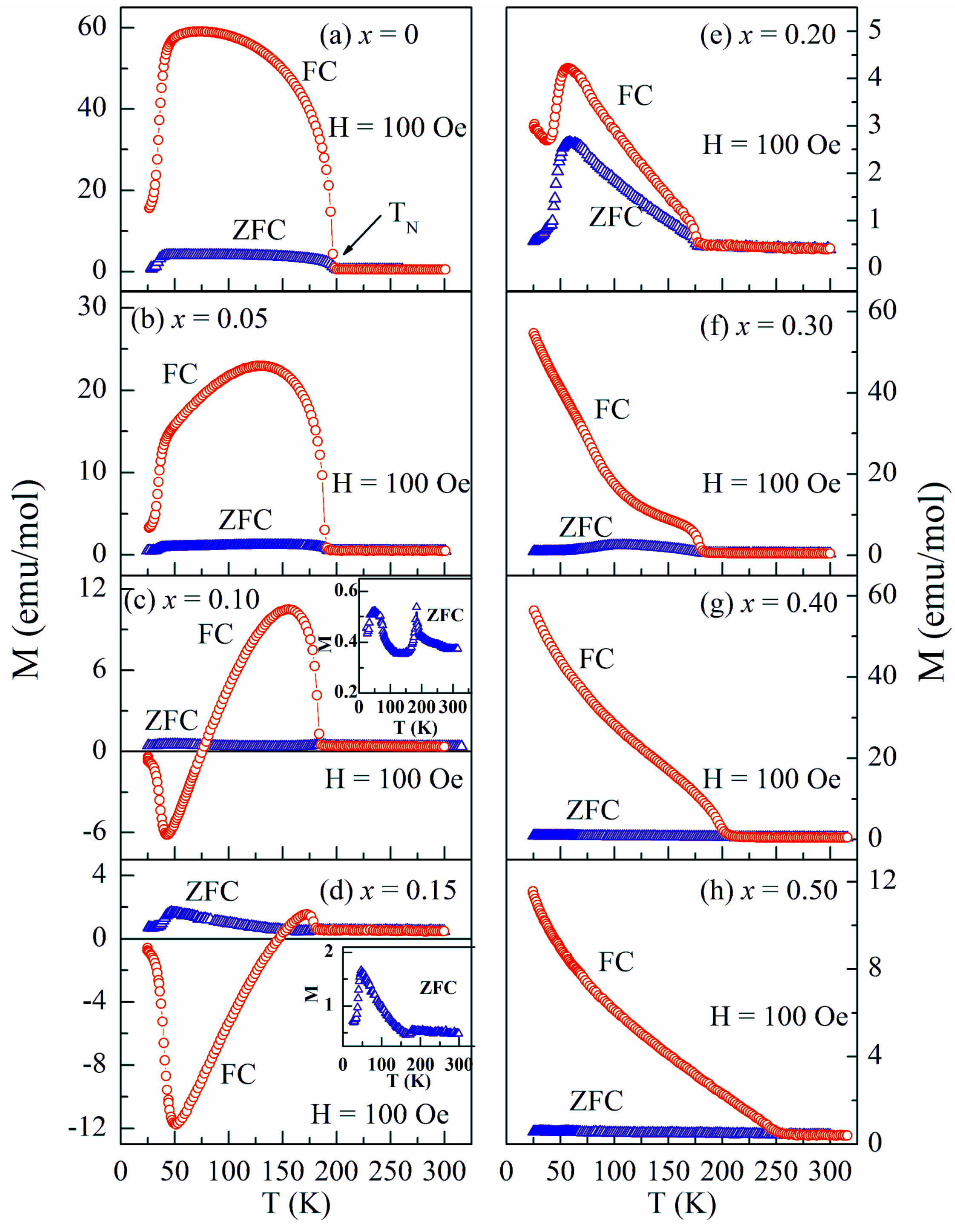

Figure 3.23: Temperature variation of magnetization in ZFC and FC conditions for $SmCr_{1-x}Fe_xCrO_3$ (x = 0 – 0.50) samples under an applied field of H = 100 Oe. Insets show the enlarged view of ZFC magnetization of x = 0.10 and x = 0.15 samples (c and d).

(i) Magnetization Reversal

Interesting temperature induced magnetization reversal is observed in case of $x = 0.10$ and 0.15 samples. In order to understand the MR further, the *M-T* curves of $x = 0.10$ and $x = 0.15$ samples were recorded under different cooling field ranging from $H = 100$ Oe to 2000 Oe. The variation of FC magnetization measured at different cooling field is shown in Fig. 3.24.

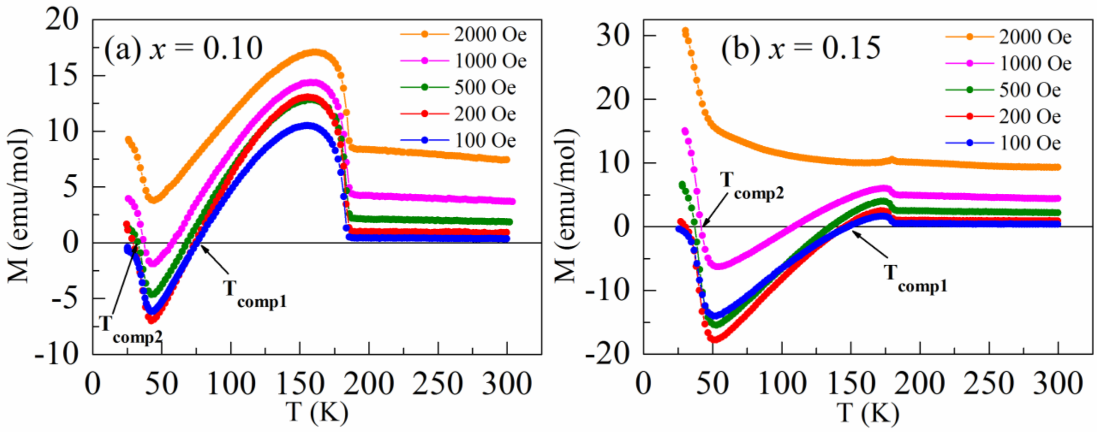

Figure 3.24: *M-T* curves of (a) $x = 0.10$ and (b) $x = 0.15$ samples measured at different magnetic fields under FC condition showing the decrease in compensation temperature (T_{comp1}). The magnetization shifts to the positive values when the field is increased to $H = 2000$ Oe.

At low field prominent negative magnetization below the compensation temperature is observed but as the magnitude of applied field is increased, the negative magnetization is found to decrease. The *M-T* plot of $x = 0.10$ and $x = 0.15$ samples show the single compensation behavior at $T_{comp1} = 75$ K and 148 K respectively for $H = 100$ Oe, with minimum magnetization (M_{min}) at $T_{min}= 43$ K and 51 K respectively. For $T < T_{min}$, a sharp rise in the magnetization towards positive magnetization is observed in both the samples due to the low temperature spin reorientation transition. However, as the external magnetic field is increased to 200 Oe, the magnitude of FC magnetization for $T < T_{min}$ acquires positive values by intersecting the temperature axis ($M = 0$) at second compensation temperature, $T_{comp2} = 30$ K. Thus, the samples exhibit multiple temperature induced magnetization reversal with two magnetic compensation temperatures, T_{comp1} and T_{comp2}. The value of T_{comp1} is found to decrease with the increase in the magnitude of external magnetic field and its value is found to be in the range of 75 K (H = 100 Oe) to 57 K (H = 1000 Oe) for x = 0.10 sample whereas for x = 0.15 sample, it varies from 148 K (H = 100 Oe) to 108 K (H = 1000 Oe). Meanwhile, the T_{comp2} increases from 30 K (H = 200 Oe) to 37 K (H = 1000 Oe) for x = 0.10 sample and for x = 0.15 sample it increases from 30 K to 42 K. When the external field is increased to 2000 Oe, no magnetization reversal is observed in both the samples and the magnetization switches to positive value. It is clear from the Fig. 3.24 (a) and Fig. 3.24(b) that with increase in the magnitude of H, no appreciable change in the trend of M-T behavior of x = 0.10 and x = 0.15 samples is observed except a shift in the entire M-T curves towards the higher positive magnetization value. This is due to the field induced enhancement in the weak ferromagnetic component of canted Cr^{3+} ions that leads to a reduction in the T_{comp1} value.

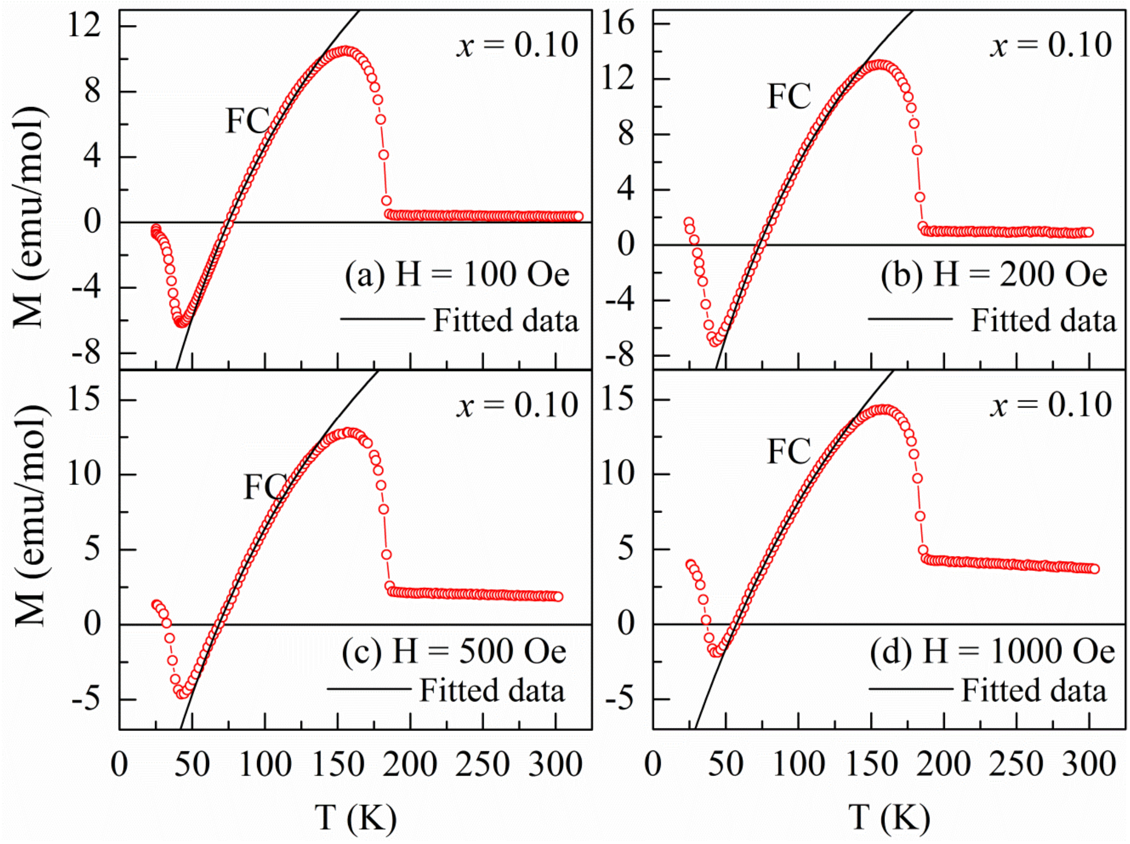

Figure 3.25: M-T curves of x = 0.10 sample under FC condition for (a) H = 100 Oe (b) H = 200 Oe (c) H = 500 Oe and (d) H = 1000 Oe.

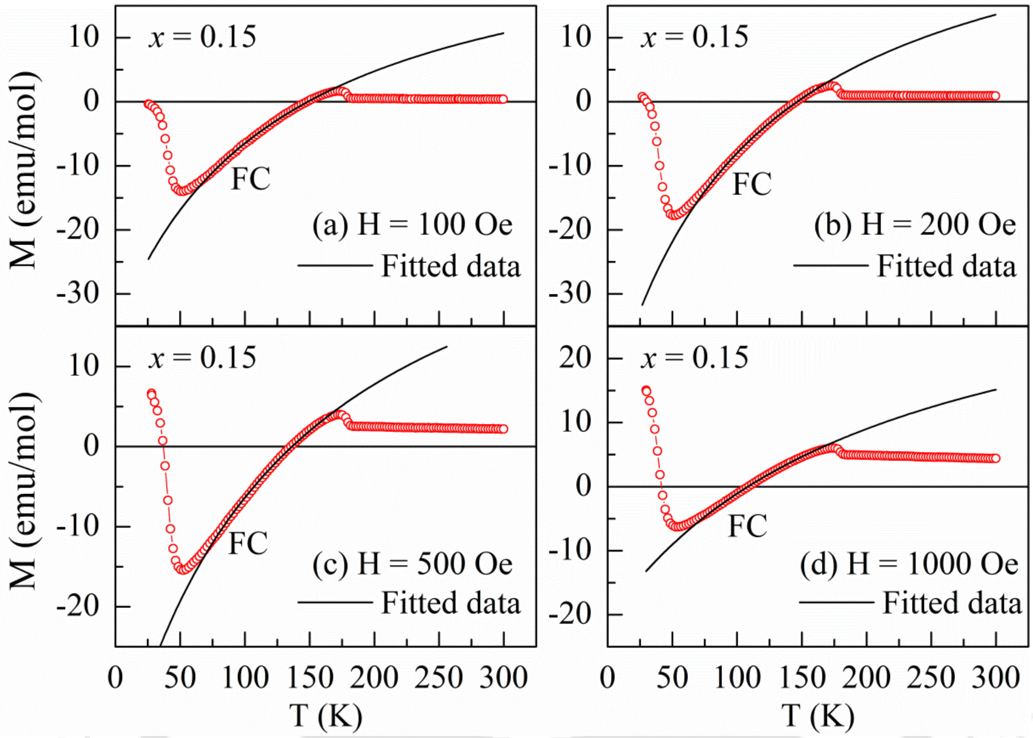

Figure 3.26: *M*-*T* curves of x = 0.15 sample under FC condition for (a) H = 100 Oe (b) H = 200 Oe (c) H = 500 Oe and (d) H = 1000 Oe.

The observed temperature induced MR can be explained by considering the temperature dependant competition between the weak ferromagnetic component of canted Cr^{3+} ions (M_{Cr}) and the paramagnetic moment of Sm^{3+} ions and the substituted Fe^{3+} ions, under the influence of the negative internal field (H_I) due to the AFM ordered Cr^{3+} ions. Based on this model the FC magnetization data (for $T > T_{min}$) of x = 0.10 and x = 0.15 samples measured at different cooling fields ($H \leq$ 1000 Oe) can be fitted to the equation (3.1). The fitted data (solid line) are shown in Figs. 3.25 and 3.26 for x = 0.10 and x = 0.15 samples respectively. The estimated values of θ_c are found to be in the range of -125 K to -190 K depending on the magnitude of applied magnetic field. The variations of estimated values of M_{Cr} and - H_I as a function of the applied field (H) are shown in Fig. 3.27. Both the M_{Cr} and -H_I values are found to increase with increase in the magnitude of field which can be ascribed to the increase in size of the AFM domains with increase in strength of the magnetic field. The disappearance of MR for higher composition of Fe ($x \geq$ 0.20) is due to the involvement of Fe in the formation of Fe^{3+} - O^{2-} - Fe^{3+} networks (confirmed from *M*-*T* plots) rather than behaving like a PM entity.

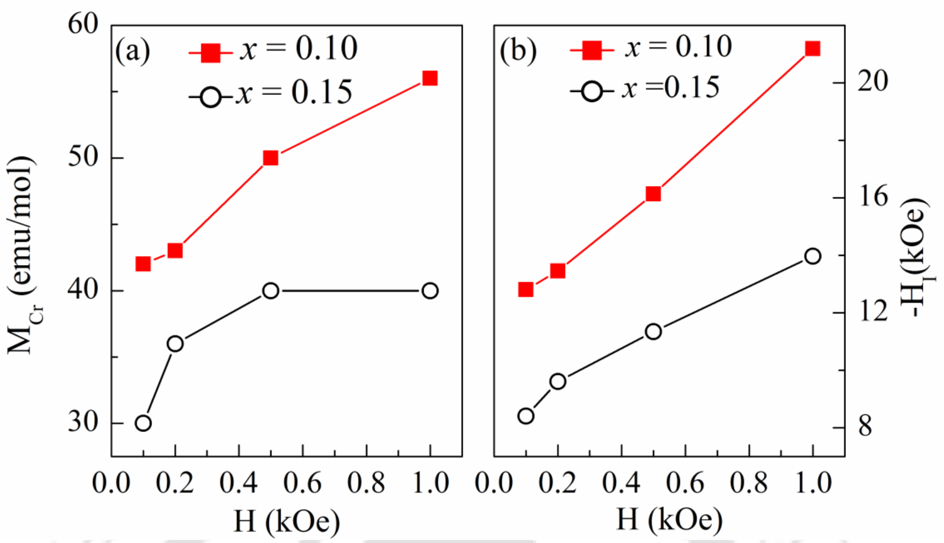

Figure 3.27: Variations of (a) M_{Cr} and (b) -H_I as a function applied magnetic field for x = 0.10 and x = 0.15 samples.

The ratio of minimum (negative) magnetization (M_{min}) to the maximum (positive) magnetization (M_{max}) value, M_{min}/M_{max} is estimated to be 7.8 for x = 0.15 sample at H = 100 Oe. This value reported to be 2 for LaCr$_{0.85}$Mn$_{0.15}$O$_3$ [94], 6 for La$_{0.5}$Gd$_{0.5}$CrO$_3$ [123] and 30 for GdCrO$_3$ [13]. The value of relative irreversible magnetization was determined from the relation, $\frac{\Delta M}{M_{ZFC}} = \frac{M_{FC} - M_{ZFC}}{M_{ZFC}}$ and its maximum negative value is found to be -8.2 for a field of H = 100 Oe. The values of irreversible magnetization lie in the range of -2 to -9 in case of magnetic rare earth orthochromites [13,123].

(ii) Magnetization Switching

The samples, x = 0.10 and x = 0.15, showing temperature induced magnetization reversal are also studied for magnetization switching behavior. In order to demonstrate the bipolar switching, both the samples were cooled down through their T_N to a temperature of T = 50 K for x = 0.10 sample and T = 120 K for x = 0.15 sample under 100 Oe field and then the magnetization was recorded as a function of time and it is found to be negative. By keeping the temperature fixed, the magnitude of H was then increased to 2500 Oe to switch the magnetization to a positive value. The same procedure was cycled several times between H = 100 Oe and H = 2500 Oe to check the reproducibility of the switching behavior. The results of the magnetization switching performed at T = 50 K (x = 0.10) and T = 120 K (x =

0.15) are shown in Fig. 3.28. It clearly indicates that change in the polarity of magnetization can be achieved by just changing the magnitude of applied field in the same direction.

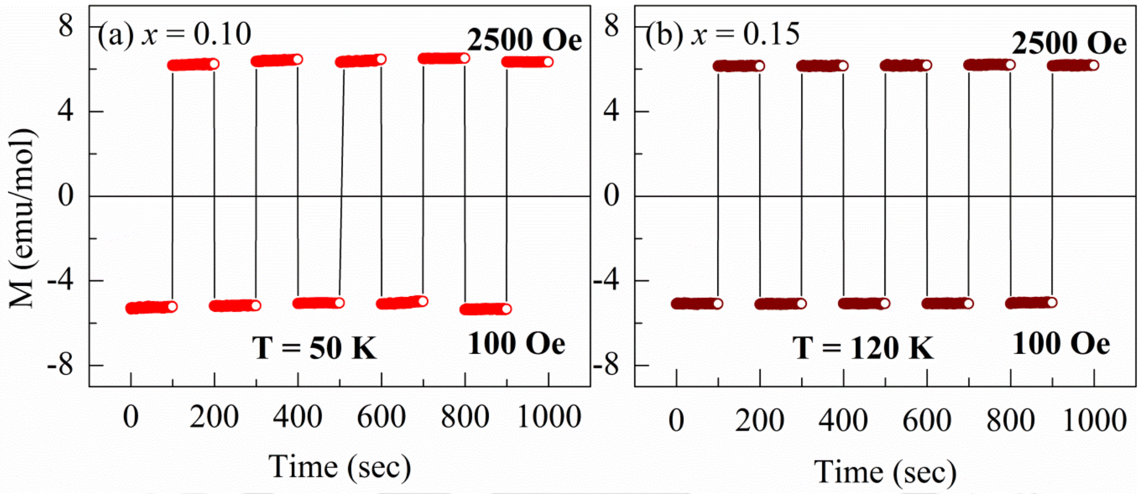

Figure 3.28: Bipolar switching of magnetization for (a) x = 0.10 and (b) x = 0.15 samples at T = 50 K and T = 120 K respectively.

(iii) Exchange Bias

The presence of interesting temperature induced magnetization reversal encouraged us to look for possible existence of exchange bias behavior. Thus, the *M-H* loops of the x = 0.10 sample were recorded at different temperatures (in the range of T = 5 K to 200 K) after cooling the sample through its T_N in presence of an external field of H = 5000 Oe to a desired measuring temperature. The isothermal *M-H* loops of x = 0.10 sample recorded at few selected temperatures are shown in Fig. 3.29 and for clarity the loops in an expanded scale are shown in Fig. 3.30.

The *M-H* loops measured in the entire temperature range are found to be linear in shape which indicates the dominant AFM nature of the sample. The *M-H* loops measured at T = 5K and T = 25 K, shown in Fig 3.30(a & b), exhibit a shift towards the negative side of the field axis which gives rise to negative exchange bias. When the temperature is increased to 50 K, the measured *M-H* loop (Fig. 3.30(c)) is found to shift completely in the opposite direction, *i.e.* along the positive side of the field axis resulting positive exchange bias. Thus, the sample exhibits exchange bias whose sign can be tuned (positive or negative value) by controlling the measuring temperature. The *M-H* loop measured at $T = T_{comp1}$ (= 75 K), shows no shift along the field axis as shown the Fig. 3.30(d). However, as the temperature is raised to T = 100 K, the loop (Fig. 3.30(e)) completely shifts to the negative field axis and the exchange bias becomes negative again. Finally, the shift in the *M-H* loop disappears when the measuring temperature, $T \geq T_N$ as shown in Fig. 3.30(f) for T = 200 K.

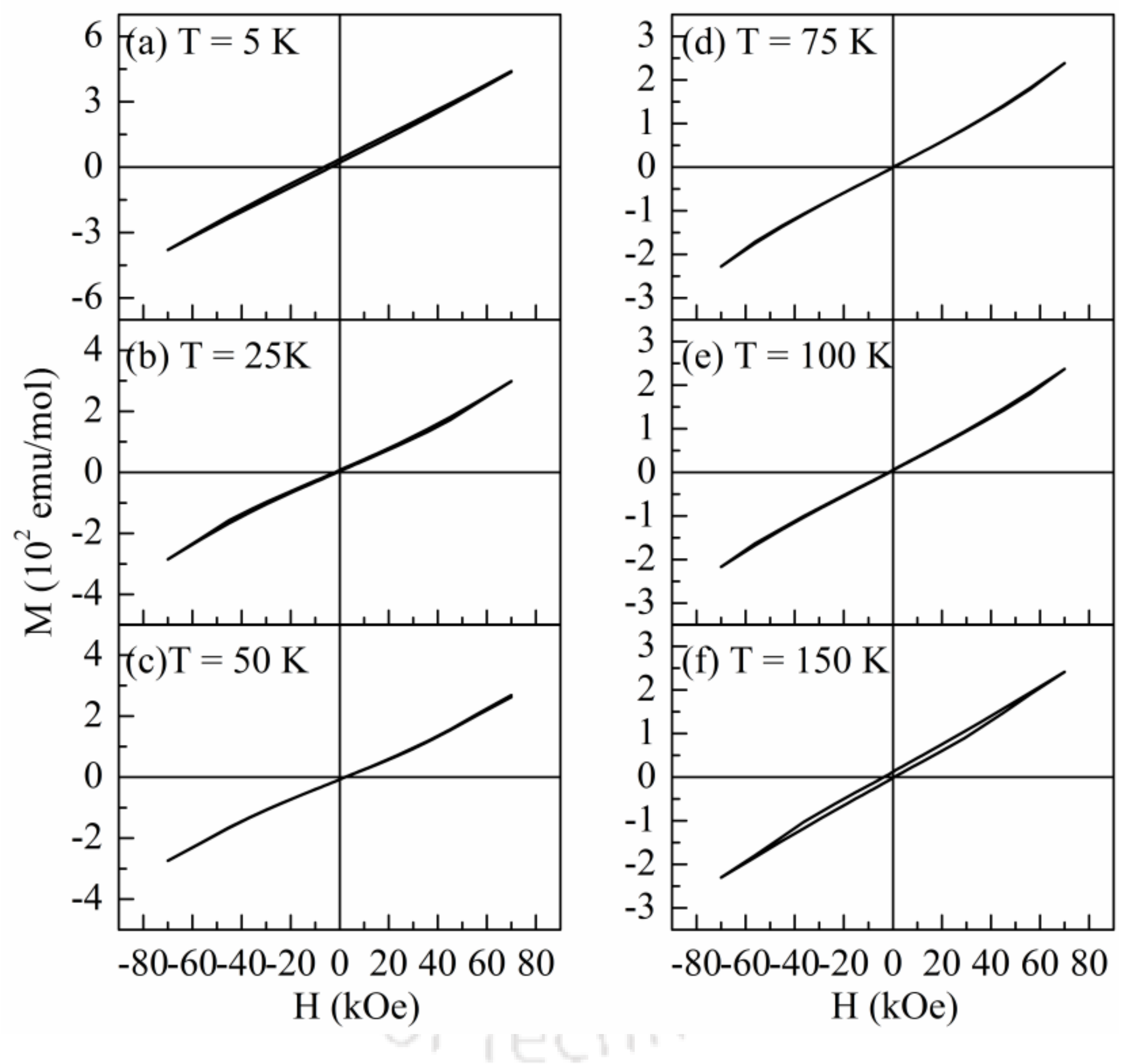

Figure 3.29: *M-H* loops of x = 0.10 sample recorded at different temperatures under FC condition for H = 5000 Oe.

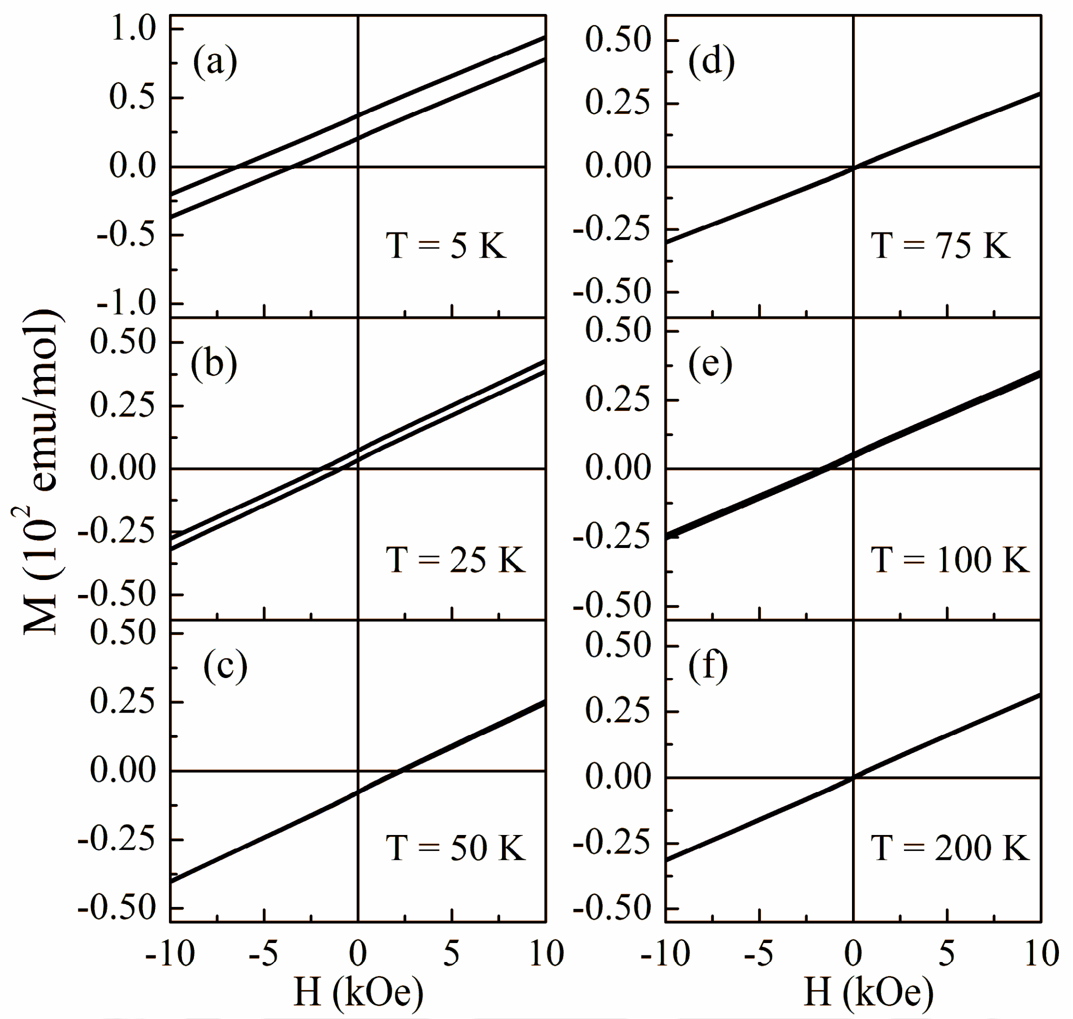

Figure 3.30: (a) – (f) Enlarged view of *M-H* loops in the vicinity of coercive fields measured at different temperatures for $x = 0.10$ sample under field cooled conditions for $H = 5000$ Oe.

The EB field (H_{EB}) and the effective coercive field (H_c^{eff}) were determined using the relations $H_{EB} = (H_+ + H_-)/2$ and $H_c^{eff} = (H_+ - H_-)/2$. The variation of H_{EB} and H_c^{eff} as a function of temperature measured for $x = 0.10$ sample under FC condition ($H = 5000$ Oe) is shown in Fig. 3.31(a & b). For $T_{comp1} < T < T_N$, the H_{EB} first fall towards negative values and attains a maximum negative value of –1.58 kOe at $T = 150$ K. For further decrease in temperature, the H_{EB} value starts to increase towards the positive value by intersecting the temperature axis ($H_{EB} = 0$) at $T = T_{comp1}$. In the $T < T_{comp1}$ region, the H_{EB} becomes positive with a maximum peak value of $H_{EB} = 2.25$ kOe at $T_P = 50$ K. interestingly, the T_P is found to be close to the temperature at which maximum negative magnetization was observed in the *M-T* plot (Fig. 3.23(c)). When the temperature is decreased further i.e. for $T < T_P$, H_{EB} begins to fall towards the negative values by crossing the temperature axis ($H_{EB} = 0$) for second time at $T \approx T_{comp2}$ (= 30 K). Thus, the H_{EB} exhibits multiple sign reversal across the compensation temperatures. The temperature dependence of H_c^{eff} exhibit a minimum value at both the compensation temperature (T_{comp1} and T_{comp2}) which is due to the compensated moment at T_{comp}. The maximum H_{EB} value observed in the present case are comparable to that reported in $NdCr_{1-x}Fe_xO_3$ [73], $La_{0.8}Ce_{0.2}CrO_3$ [16] and $NdMnO_3$ [85] compounds.

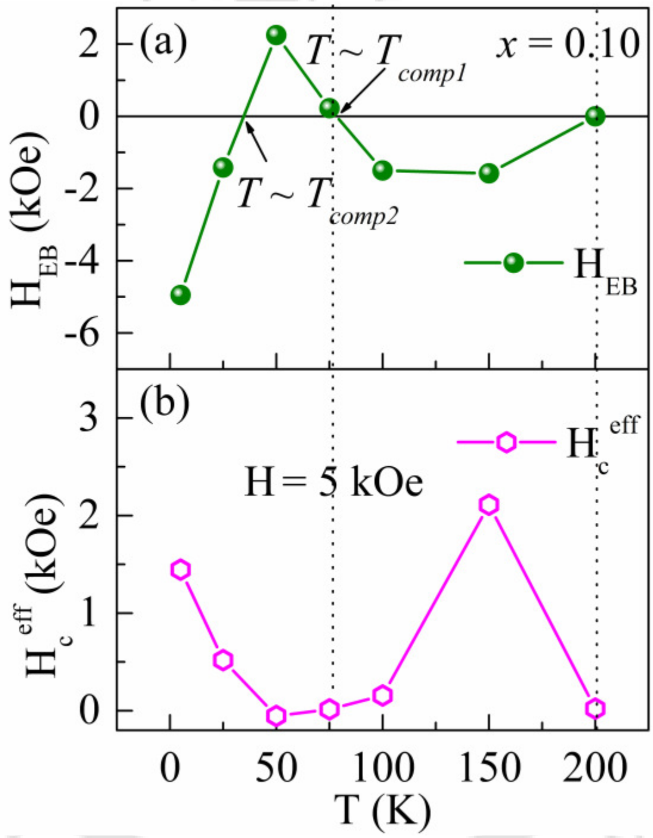

Figure 3.31: The temperature dependence of (a) exchange bias field, H_{EB} (upper panel) and (b) effective coercive field, H_c^{eff} (lower panel) for x = 0.10 ($SmCr_{0.90}Fe_{0.10}O_3$) sample measured under a cooling field of H = 5000 Oe.

The observed sign reversal of exchange bias across the compensation temperatures in x = 0.10 sample can be explained considering the AFM coupling between the ferromagnetic component of canted Cr^{3+} ions (M_{Cr}) and the net paramagnetic moments coming from the Sm^{3+} and Fe^{3+} ions ($M_{Sm} + M_{Fe}$) under the influence of negative internal field (H_I). In the temperature range, $T_{comp1} < T < T_N$, the canted Cr^{3+} moments M_{Cr} are aligned along the direction of the applied field (*H*) while the net PM moments ($M_{Sm} + M_{Fe}$) are aligned parallel to H_I but antiparallel to *H*. In this temperature range M_{Cr} dominates over the $M_{Sm} + M_{Fe}$ and their antiparallel alignment yields a net positive magnetization and hence a negative exchange bias similar to that of FM/AFM interfaces. For $T < T_{comp1}$, the paramagnetic moments of $M_{Sm} + M_{Fe}$ and the M_{Cr} are still antiparallely aligned but with a difference that $M_{Sm} + M_{Fe}$ dominates over M_{Cr} due to the enhancement in the PM moment at low temperature. This results a net negative magnetization and positive exchange bias. The PM component of $M_{Sm} + M_{Fe}$ can be visualized as FM domains which are aligned in a direction opposite to the applied field and such an arrangement requires a large positive field to bring the magnetization towards positive or zero value. This leads to a shift in the whole *M-H* loop towards the positive field axis and hence positive exchange bias is observed. At $T = T_{comp}$, since both the moments are equal and opposite to each other, the H_{EB} tends to zero giving rise to a linear hysteresis loop at T_{comp}. As a result the H_c^{eff} also vanishes around the compensation temperatures as shown in Fig. 3.31(b). The fall in the H_{EB} values for $T < T_P$ can be ascribed to the low temperature spin reorientation transition observed in the *M-T* plots which leads to further dominance of the M_{Cr} component over paramagnetic moments along the applied field direction.

3.3 Conclusions

Single phase polycrystalline samples of $SmCr_{1-x}Mn_xO_3$ ($x = 0 - 0.50$) were successfully prepared by employing the standard citrate based solgel method. The Rietveld refinement of the XRD patterns recorded at room temperature reveals that the prepared samples crystallize in orthorhombic structure with *Pbnm* space group. A systematic increase in the lattice parameter and volume of the unit cell is observed with increase in Mn concentration. Temperature dependant magnetization measurements suggest the AFM nature of the samples with T_N varying in the range of 196 K to 75 K for $x = 0$ to $x = 0.40$, while ferromagnetism is observed for $x = 0.50$ due to possible Cr^{3+} - O^{2-} - Mn^{3+} and Mn^{3+} - O^{2-} - Mn^{4+} networks. The substitution of Mn leads to interesting temperature induced magnetization reversal behavior in the FC mode for the composition range of $x = 0.10$ to $x = 0.30$ with a highest T_{comp} of 126 K for $x = 0.30$ sample. The magnetization reversal is quantitatively explained on the basis of competition between the paramagnetic behavior of

Sm^{3+} and Mn^{3+} ions under the influence of negative internal field (H_I) and the canted FM component of Cr^{3+} ions. The maximum internal field is estimated for $x = 0.15$ sample and it is found to be –24 kOe. Switching of the polarity of magnetization is demonstrated by just changing the magnitude of magnetic field in the same direction. Tunable exchange bias behavior as a function of temperature has been observed for $x = 0.10$ sample which arises from the competition between the above two moments. The sign reversal of exchange bias is due to the dominance of one of the moments over the other as the temperature is varied. The maximum exchange bias in $x = 0.10$ sample is found to be –1.85 kOe.

Polycrystalline samples of $SmCr_{1-x}Fe_xO_3$ ($x = 0$ - 0.50) have also been prepared by the sol gel route. The prepared samples are found to crystallize in orthorhombic structure with *Pbnm* space group. Temperature dependant of magnetization reveals the AFM nature of the samples for all compositions. Interesting magnetization reversal with two compensation temperatures, in the FC mode, is observed for $x = 0.10$ and $x = 0.15$ samples with a maximum compensation temperature of 148 K for $x = 0.15$ sample. The magnetization data measured under FC condition for samples showing magnetization reversal have been analyzed on the basis of the competition between the canted FM component of Cr^{3+} ions and the net paramagnetic moments of Sm^{3+} and Fe^{3+} ions under the negative internal field from AFM ordered Cr^{3+} ions. The maximum internal field is found to be –21 kOe for $x = 0.10$ sample. Bipolar switching of magnetization has been demonstrated for $x = 0.10$ and $x = 0.15$ samples by varying the magnitude of magnetic field along a fixed direction. The *M-H* loops measured under the FC condition for $x = 0.10$ sample show the presence of exchange bias behavior. Its origin is explained considering the antiparallel orientation of the FM component of canted Cr^{3+} ions and the paramagnet moments of Sm^{3+} and Fe^{3+} ions under the influence of negative internal field. Reversal in the sign of H_{EB} is observed across the two compensation temperature which arises due to the different temperature dependences of the above competing moments. The maximum H_{EB} value is found to be –4.9 kOe at a cooling field of $H = 5000$ Oe.

When the Cr^{3+} ion is replaced by Fe^{3+}/Mn^{3+} in $SmCrO_3$, magnetization reversal was observed for both the substitution over different composition range. On comparison, it is found that the Fe substituted samples (showing MR) exhibit higher compensation temperature than that of Mn substituted samples. This is due to the larger T_N values of Fe substituted samples compared to those of Mn. The large T_N values open the competition between weak FM component and paramagnetic moment where the latter is expected to be weak at higher temperature. Higher concentration of Mn substitution ($x > 0.40$) is found to promote ferromagnetism while AFM persist for all compositions of Fe substitution upto $x = 0.50$. The FC magnetization of 10 and 15 at. % of Fe substituted samples are found to exhibit multiple compensation temperature due to low temperature spin reorientation while such behavior is absent in Mn substituted samples. Substitution of both Fe and Mn for $x = 0.10$ composition exhibit tunable exchange bias behavior as a function temperature. However, multiple reversals in the sign of H_{EB} are observed for Fe substitution due to the presence of a second compensation temperature (T_{comp2}) at low temperature.

Chapter 4

Magnetic Properties of Mn and Fe Substituted $GdCrO_3$

$GdCrO_3$ is a well-known perovskite compound having G-type antiferomagnetic structure with a weak ferromagnetism below its Neel temperature (T_N) of 170 K [13]. Cooke reported that below T_N the net canted moment of Cr^{3+} ions lies along the direction of crystallographic *c* axis (along F_z) whereas the Gd^{3+} moments lie opposite to that of the canted Cr^{3+} moments under the influence of an effective internal field. At T ~ 7 K, the magnetic configuration of Cr^{3+} ion changes from G_xF_z to G_zF_x due to the SR transition which changes the orientation of the net canted Cr^{3+} moment from crystallographic *c* to *a* axis. The antiparalell alignment between the moments of Gd^{3+} and Cr^{3+} sublattices and their different temperature dependences [12,13] leads to the temperature driven MR behavior in its bulk compound. Thus, it would be interesting to dilute the canted Cr^{3+} moments by substituting other transition elements like Fe or Mn and study their effect on the magnetic properties of $GdCrO_3$. Furthermore, as per our knowledge the work on Fe or Mn substitution at Cr site of $GdCrO_3$ is limited. Therefore, we have taken up Mn and Fe substituted $GdCrO_3$ compounds and studied their effect on the crystal structure and magnetic properties of $GdCrO_3$. This chapter deals with the preparation of $GdCr_{1-x}Mn_xO_3$ and $GdCr_{1-x}Fe_xO_3$ samples with $x = 0 – 0.50$ and study of their structural, temperature and field dependent magnetic properties.

4.1 Mn Substituted $GdCrO_3$

This section deals with the effect of Mn substitution at the Cr site of $GdCrO_3$. The preparation of the samples along with the results obtained from the dc magnetization measurements and their interpretation are presented.

4.1.1 Sample Preparation and Characterization

Polycrystalline samples of $GdCr_{1-x}Mn_xO_3$ (x = 0 - 0.50) were prepared from stoichiometric ratio of Gd_2O_3, $Cr(NO_3)_3.9H_2O$ and manganese acetate all with high purity

(>98%), using the standard sol-gel method. The starting oxide compound Gd_2O_3 was dissolved in nitric acid where as the nitrates/acetates were dissolved in distilled water to get a uniform solution of the mixture. Citric acid in 2:1 molar ratio with respect to the metallic cation was added to the solution to convert the nitrates/acetates into citrates and then the uniform solution was heated at 70°C to get voluminous precursor. The precursor was grinded and presintered at 600°C for 12 hrs followed by pelletisation and final sintering at 1100°C for 24 hrs. Phase purity of the samples was checked by recording X-ray diffraction (XRD) patterns using Rigaku make TTRAX III X-ray diffractometer with Cu-Kα radiation. The surface morphology and composition analyses were carried out using ZEISS make FESEM equipped with energy dispersive X-ray spectroscopy (EDS) facility. Magnetization as a function of temperature, time and field in zero field cooled (ZFC) and field cooled (FC) conditions were measured with the help of Lakeshore make vibrating sample magnetometer (VSM) of model no. 7410.

4.1.2 Structural properties

The XRD patterns of $GdCr_{1-x}Mn_xO_3$ (x = 0 – 0.50) samples recorded at room temperature are shown in Fig. 4.1. These patterns were refined using the Rietveld refinement [126] technique by choosing *Pbnm* space group (SG) in orthorhombic structure. As per the XRD analysis all prepared samples are found to be in single phase form. Typical XRD patterns along with their Rietveld refined data for x = 0, 0.10, 0.30 and 0.50 samples are shown in Fig. 4.2. The lattice parameters of the parent compound (x = 0) are found to be a = 5.3127(2) Å, b = 5.5227(2) Å, c = 7.6045(3) Å and they are comparable to those of literature [13]. The lattice parameters, reliability factors and unit cell volume obtained from the refinement of all the samples are given in Table 4.1. The cell parameters a and b are found to increase with increase in Mn concentration whereas the lattice constant c shows a decreasing trend. The increase in a and b parameters is due the replacement of smaller Cr^{3+} (0.615 Å) ions by larger Mn^{3+} (0.645 Å) ions whereas the decrease in the c value is due to the cooperative stretching of ab plane of Cr/MnO$_6$ octahedra. The unit cell volume is also found to increase with Mn concentration. However, as the doping concentration is increased to x = 0.50, considerable decrease in lattice constant 'a' is observed and this could be attributed to the presence of considerable concentration of Mn^{4+} (0.530 Å) ions due to some oxygen off stoichiometry.

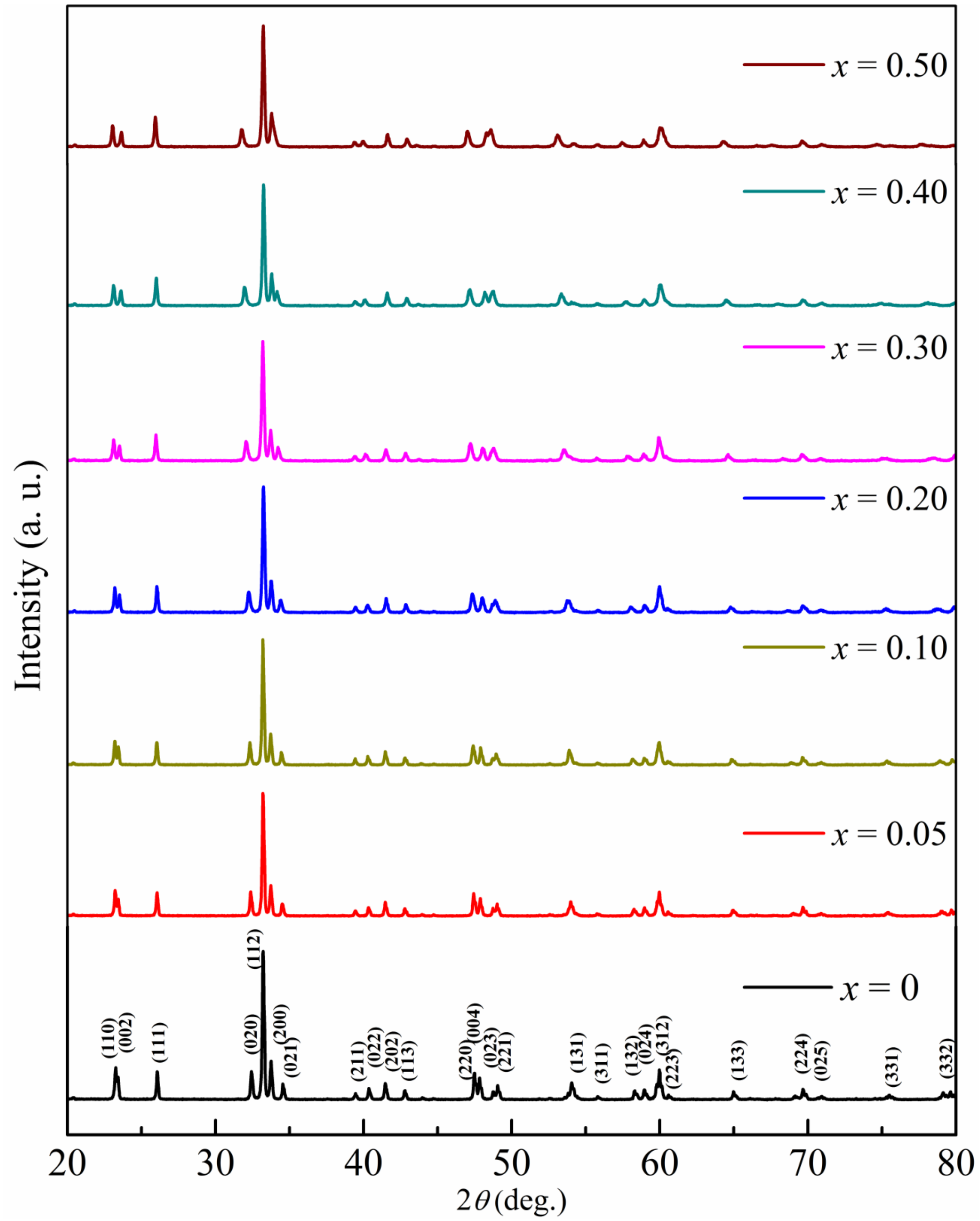

Figure 4.1: XRD patterns of GdCr$_{1-x}$Mn$_x$O$_3$ samples for $x = 0 - 0.50$.

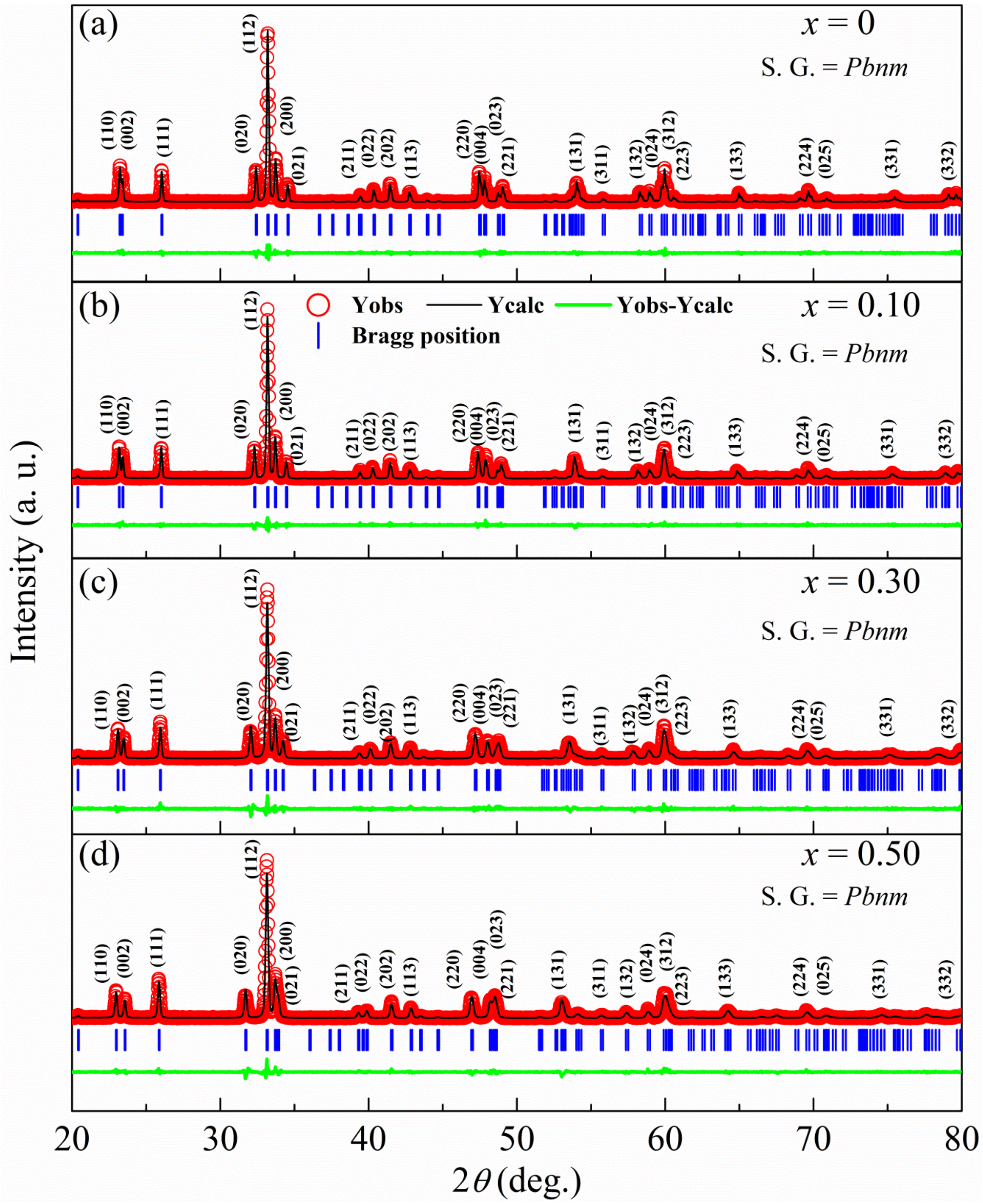

Figure 4.2: XRD patterns along with Rietveld refinement for $x = 0$, 0.10, 0.30 and $x = 0.50$ samples. The circles represent the experimental points and solid line (black) represents refined data. The bottom line (green) shows the difference between experimental and refined data. The vertical lines (blue) are the allowed Bragg position.

Table 4.1: Parameters obtained from the Rietveld analysis of GdCr$_{1-x}$Mn$_x$O$_3$ (x = 0 to 0.50).

Sample/ Parameters	**x = 0**	**x = 0.05**	**x = 0.10**	**x = 0.15**	**x = 0.20**	**x = 0.30**	**x = 0.40**	**x = 0.50**
Space Group	*Pbnm*	*Pbnm*	*Pbnm*	*Pbnm*	*Pbnm*	*Pbnm*	*Pbnm*	*Pbnm*
***a* (Å)**	5.3127 (0.0002)	5.3144 (0.0001)	5.3159 (0.0002)	5.3162 (0.0003)	5.3175 (0.0003)	5.3178 (0.0004)	5.3186 (0.0003)	5.3161 (0.0002)
***b* (Å)**	5.5227 (0.0002)	5.5307 (0.0002)	5.5409 (0.0002)	5.5490 (0.0003)	5.5608 (0.0003)	5.5837 (0.0004)	5.6133 (0.0002)	5.6427 (0.0002)
***c* (Å)**	7.6045 (0.0003)	7.5986 (0.0002)	7.5937 (0.0002)	7.5885 (0.0004)	7.5856 (0.0005)	7.5764 (0.0006)	7.5659 (0.0002)	7.5486 (0.0003)
Volume (Å^3)	223.12 (0.01)	223.34 (0.01)	223.67 (0.01)	223.86 (0.02)	224.30 (0.03)	224.97 (0.03)	225.68 (0.03)	226.49 (0.02)
R_F (%)	3.7	3.1	3.0	3.1	3.5	3.3	2.7	2.3
R_{Bragg} (%)	3.1	3.0	3.1	2.8	4.0	4.0	3.7	3.3
R_P (%)	9.1	9.5	9.5	9.6	10.7	11.1	9.8	9.7
R_{exp} (%)	7.8	8.0	8.0	8.1	8.3	8.3	8.4	8.3
χ^2	2.9	3.1	3.1	3.2	3.4	3.4	2.6	2.7
Gd/Cr/Mn Occupancy	1.002 /0.993 /0.000	1.001 /0.945 /0.049	1.001 /0.889 /0.099	1.006 /0.846 0.149	1.014 /0.798 /0.199	1.006 /0.691 /0.299	1.006 /0.601 /0.400	1.012 /0.498 /0.499

The surface morphology of all the samples was characterized by recording the FESEM micrographs. Typical microstructural images of x = 0.0 and 0.50 samples are shown in Fig. 4.3(a and b) along with their EDS spectrum in Fig 4.3(c and d). The grain sizes were estimated using ImageJ software and the grain sizes are found to be distributed over a wide range. The average grain sizes of the samples are found to be 482 nm, 598 nm and 611 nm for x = 0, 0.30 and 0.50 samples respectively. The typical cationic ratio of the samples was estimated from the recorded EDS spectra and it is found to be comparable to the nominal starting composition. The cationic ratios obtained for x = 0.0 to 0.50 samples are given in Table 4.2.

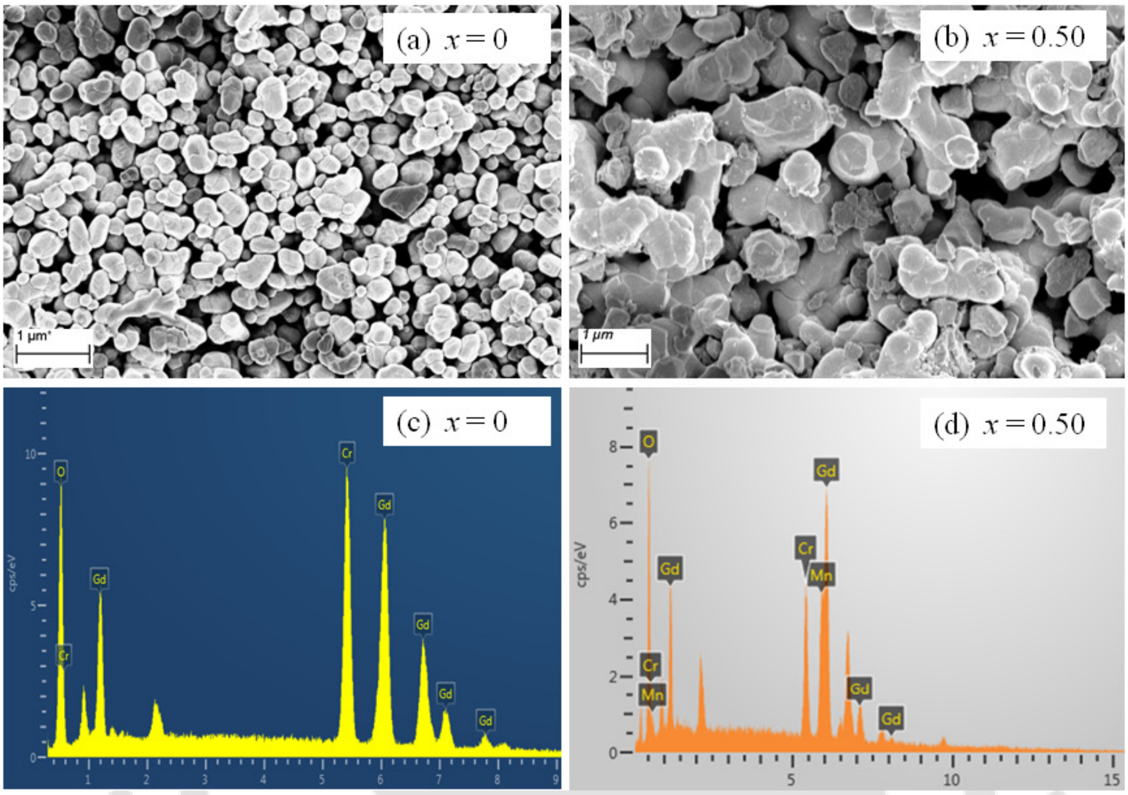

Figure 4.3: FESEM images recorded for (a) x = 0 and (b) x = 0.50 samples along with their EDS spectrum shown in Figs. (c) and (d) respectively.

Table 4.2: The cationic ratio determined from EDS analysis for x = 0, 0.20, 0.30, 0.40 and 0.50 samples.

Samples	**Calculated Cationic Ratio from EDS analysis**		
	Gd	**Cr**	**Mn**
$x = 0$	0.96	1.0	--
$x = 0.20$	0.96	0.78	0.22
$x = 0.30$	0.96	0.70	0.30
$x = 0.40$	0.98	0.61	0.39
$x = 0.50$	0.94	0.51	0.49

4.1.3 Magnetic Properties

Temperature (T) dependence of magnetization (M) under zero field cooled (ZFC) and field cooled (FC) conditions for $x = 0$, 0.05, 0.10, 0.15, 0.20, 0.30, 0.40 and 0.50 samples at an applied field of $H = 100$ Oe are shown in Fig. 4.4. For the parent compound ($x = 0$), the AFM transition is observed at $T_N \sim 174$ K. The magnetization value measured in the ZFC mode is found to gradually increase with decrease in temperature for $T < T_N$ as shown in the inset of Fig. 4.4(a). Under FC condition, initially the magnetization increases for $T < T_N$ reaching a maximum value of ~ 7 emu/mol at $T_{max} = 163$ K and for further decrease in temperature it falls towards the negative value by crossing the temperature axis ($M = 0$) at the compensation point, $T_{comp} = 136$ K and, approaches to the minimum magnetization value of $M_{min} = -280$ emu/mol at $T_{min} = 25$ K. This behavior of change in the sign of magnetization with the change in temperature is known as magnetization reversal. The M-T plot of $x = 0.05$ sample shows the similar trend as that of the parent compound ($x = 0$) but with a smaller T_N value of 165 K. Under FC condition this sample also exhibits magnetization reversal but at slightly higher T_{comp} of 139 K. In this case, the maximum magnetization (M_{max}) and the minimum magnetization (M_{min}) values are found to be 5 emu/mol and -190 emu/mol respectively. The decrease in M_{max} value with increase in Mn concentration is ascribed to the lack of contribution of FM moment as a result of doping of Mn^{3+} ions. Due to the suppression of the canted FM component, the T_{comp} value also increases from 136 K for $x = 0$ sample to 139 K for $x = 0.05$ sample.

For intermediate compositions of $x = 0.10$ to 0.30 no signature of MR was observed. The M-T plots of $x = 0.20$ and 0.30 samples show gradual increase in magnetization with decrease in temperature and however a peak like behavior is observed especially under FC condition at $T_p = 35$ K and 46 K respectively. M-T plots of $x = 0.40$ and $x = 0.50$ samples exhibit similar peak like behavior in both ZFC (insets of Fig. 4.4g & h) and FC conditions but with a rather sharp fall in the FC magnetization for $T < T_p$ and it approaches negative magnetization with $T_{comp} = 26$ K and 29 K respectively. This can be attributed to spin reorientation transition from Γ_4 to Γ_1 magnetic structure, similar to that reported in $YFe_{1-x}Mn_xO_3$ [136] and $ErCrO_3$ [137] compounds.

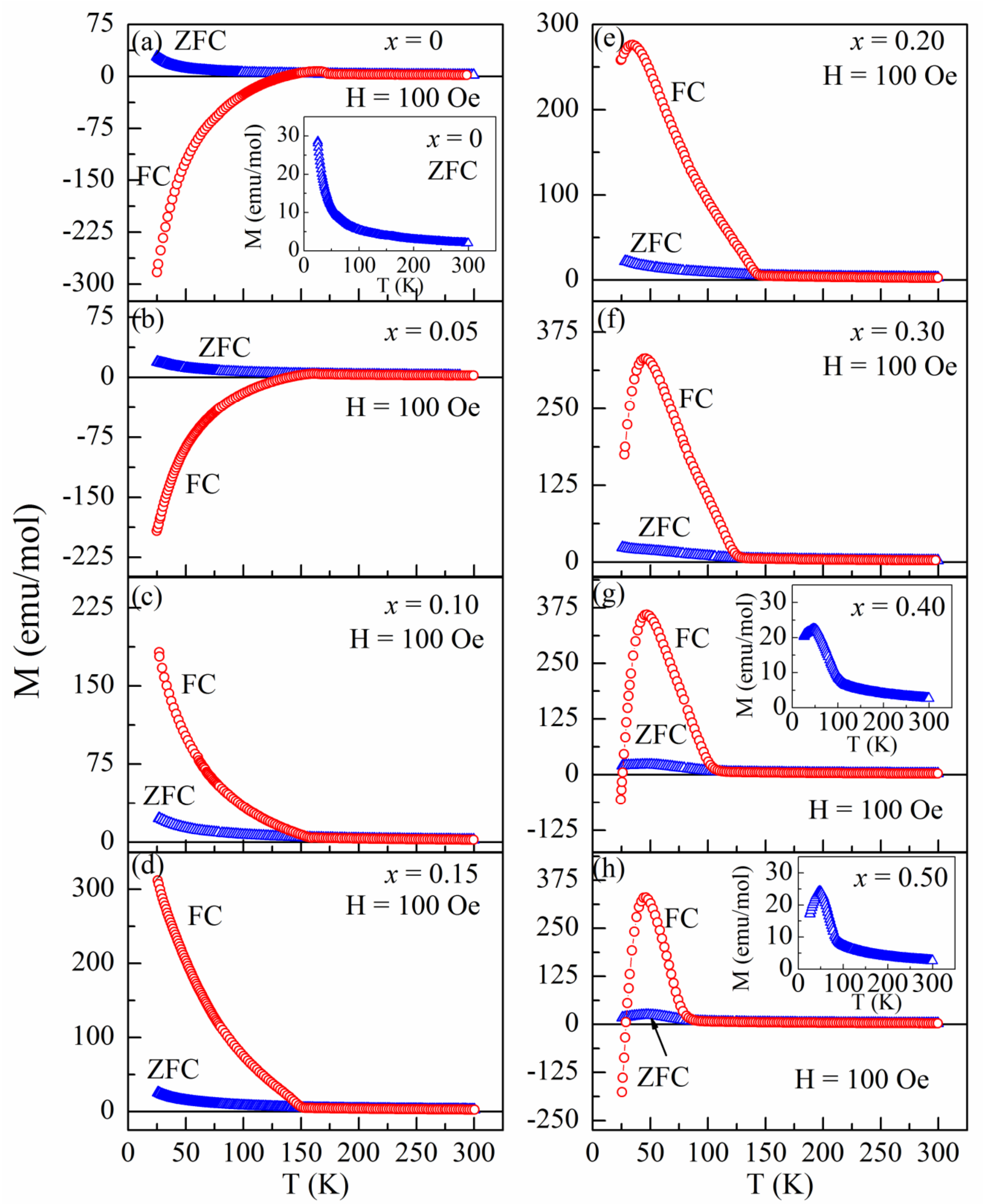

Figure 4.4: Temperature variation of magnetization in ZFC and FC conditions for GdCr$_{1-x}$Mn$_x$O$_3$ (x = 0 to 0.50) samples. Insets (a, g and h) show the relevant ZFC magnetization in expanded scale.

(i) Magnetization Reversal

For further understanding of temperature induced magnetization reversal behavior in FC mode, the *M-T* curves of the $x = 0$ and $x = 0.05$ samples were recorded at different cooling fields varying from 100 Oe to 2000 Oe. Typical *M-T* plots of $x = 0$ sample for $H =$ 100 Oe to 1000 Oe are shown in Fig 4.5 while plots of $x = 0.05$ sample for $H = 100$ to 2000 Oe are shown in Fig 4.6. The observed negative magnetization is prominent for low applied field and its magnitude is found to decrease with the increase in the strength of cooling field. The T_{comp} value also follows the decreasing trend with increase in field. The T_{comp} value is found to decrease from 136 K ($H = 100$ Oe) to 69 K ($H = 700$ Oe) for $x = 0$ sample whereas it varies from 139 K ($H = 100$ Oe) to 60 K ($H = 1500$ Oe) for $x = 0.05$. For $x = 0$ sample, no MR was observed for $H = 1000$ Oe while for $x = 0.05$ sample the MR disappears at $H > 2000$ Oe.

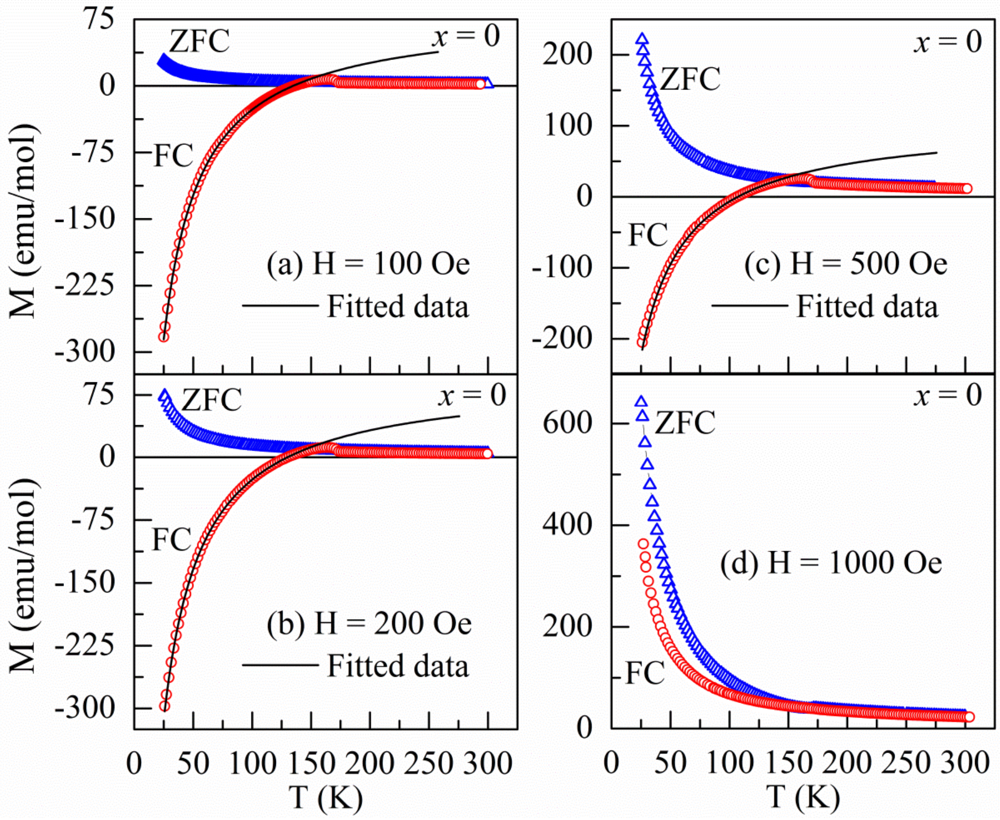

Figure 4.5: *M-T* curves in ZFC and FC conditions for $x = 0$ sample at (a) $H = 100$ Oe, (b) $H = 200$ Oe, (c) $H = 500$ Oe and (d) $H = 1000$ Oe. The solid curve (black) represents the fitted data.

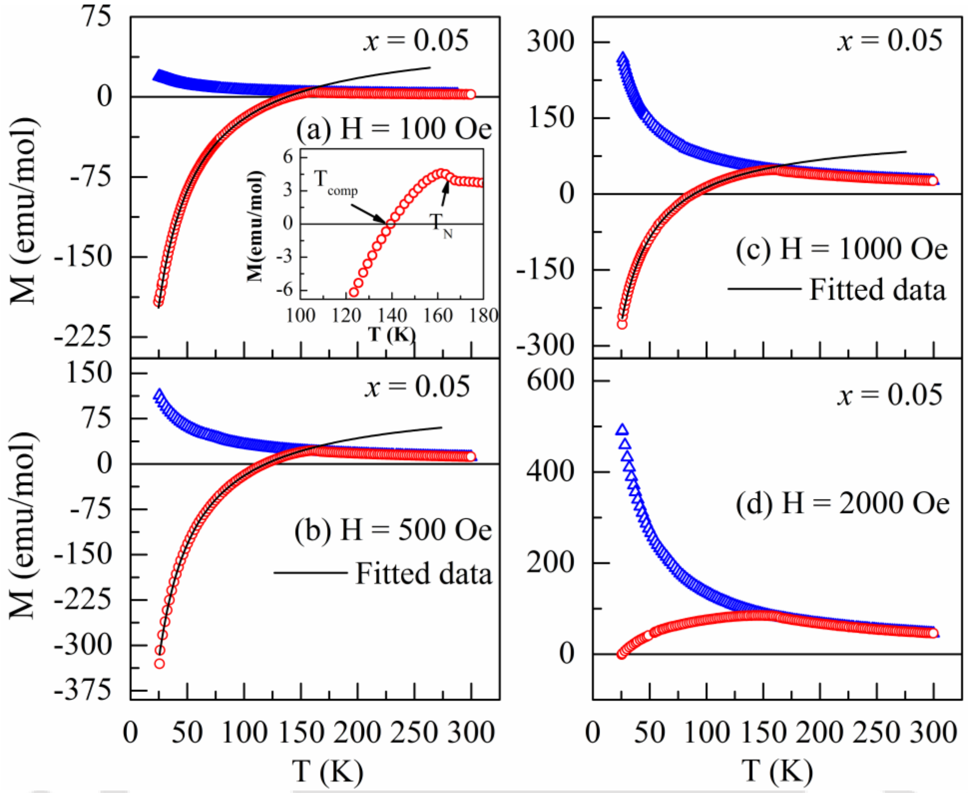

Figure 4.6: *M-T* curves in ZFC and FC conditions for $x = 0.05$ sample at (a) $H = 100$ Oe, (b) $H = 500$ Oe, (c) $H = 1000$ Oe and (d) $H = 2000$ Oe. The solid curve (black) represents the fitted data.

The origin of MR for $x = 0$ and 0.05 samples can be explained by considering Gd^{3+} and Mn^{3+} ions as paramagnetic (PM) entities under the influence of negative internal field arising from AFM ordered Cr^{3+} ions. So, the temperature dependence of magnetization (M) for an applied field of H in the FC mode were fitted to the following equation [12]

$$M = M_{Cr} + \frac{C(H_I + H)}{T - \theta_C} \tag{4.1}$$

Here, M_{Cr}, H_I, and θ_C represent weak canted FM component of Cr^{3+} ions, internal field and Curie temperature respectively. The constant C refers to Curie-Weiss constant due to paramagnetic Gd^{3+} and Mn^{3+} ions. The fitted *M-T* data using eq. 4.1 for $x = 0$ and $x = 0.05$ samples for an applied field of $H = 100$ Oe are shown as solid lines in Figs. 4.5(a) and 4.6(a) respectively. The obtained values of M_{Cr} and H_I for $x = 0$ sample are 80 emu/mol and -1600 Oe respectively whereas θ_C is found to be -7 K. These values are comparable to those reported in literature for GdCrO$_3$ [12,13]. The obtained values of M_{Cr}, H_I, and θ_C for $x = 0.05$

are 60 emu/mol, -1200 Oe and -9 K, respectively. The decrease in M_{Cr} and $|H_I|$ values upon Mn doping can be attributed to the weakening of the superexchange interaction in Cr^{3+} - O^{2-} - Cr^{3+} networks due to the Mn^{3+} doping and the associated reduction in canted FM moment. The FC M-T measurements carried out for x = 0.0 and x = 0.05 samples at different cooling fields were also analyzed using eq. 4.1 and the fitted data are shown as solid line in Figs 4.5 and 4.6 respectively. The estimated values of M_{Cr} and $-H_I$ as a function of cooling field are shown in Fig. 4.7. As H increases both M_{Cr} and $-H_I$ values are found to increase and the increase in M_{Cr} and $-H_I$ values with increase in applied field H is due to the possible increase in the size of AFM domains and such behavior is reported in other orthochromites [94].

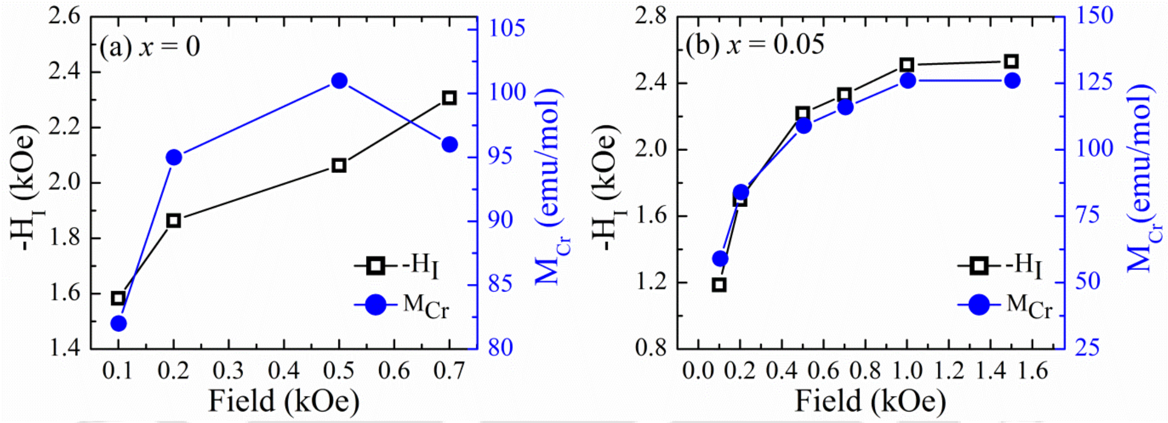

Figure 4.7: Variation of M_{Cr} and H_I as a function of cooling fields (H) for x = 0 and x = 0.05 samples.

(ii) Magnetization Switching

The bipolar switching of magnetization at T = 110 K for x = 0 and x = 0.05 samples by just varying the magnitude of magnetic field is shown in Fig. 4.8. In order to demonstrate the switching, the samples were FC down to 110 K with an applied field of 100 Oe and then at the same temperature the external field was increased to a higher value in order to get an equivalent and positive value of magnetization. The switching of M between positive and negative values was repeated several times and the result indicates reproducible bipolar switching of magnetization. For x = 0 sample the switching was performed between 100 and 550 Oe whereas for x = 0.05 it was between 100 and 500 Oe.

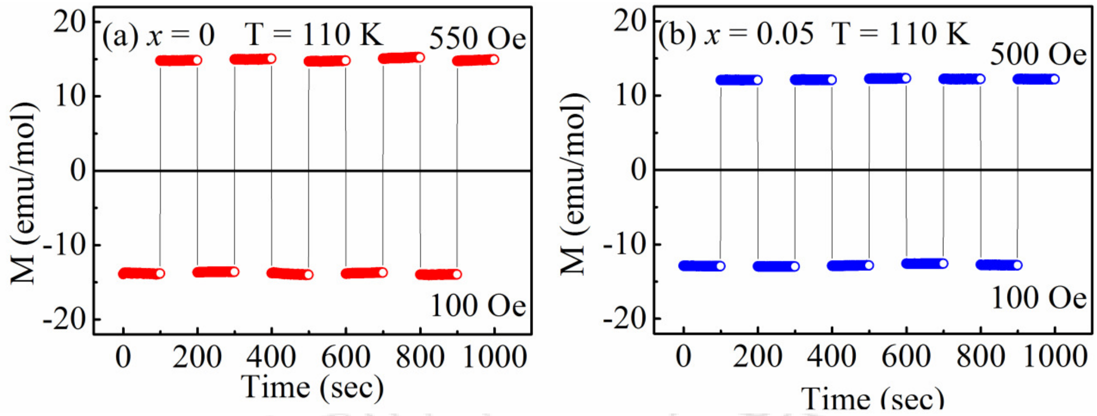

Figure 4.8: Bipolar switching of magnetization at T = 110 K for (a) x = 0 and (b) x = 0.05 samples.

(iii) Exchange Bias

The system showing MR behavior, in some cases, is reported to coexist with sign reversal of EB field which increases the technological importance of the material in application perspective. Therefore, it generates interest to look for possible EB in the samples showing the MR behavior. In order to explore the EB effect, we have recorded the *M-H* loops of x = 0, 0.05 and 0.50 samples under FC condition, in a wide range of temperature for a cooling field of H = 3000 Oe. Before recording the *M-H* loop at each of the subsequent desired temperature, the sample was warmed up above T_N followed by further cooling through T_N for H = 3000 Oe to the desired temperature. The *M-H* loops recorded under FC condition (with H = 3000 Oe) for x = 0 and 0.05 samples at T = 30 K and 200 K are shown in Fig. 4.9. For x = 0 sample the *M-H* loop at 30 K indicates the presence of a weak FM behavior at lower field along with a linear behavior at higher field indicating the presence of competing AFM. The *M-H* curve at 200 K shows the typical paramagnetic behavior. Typical *M-H* loops (expanded scale) under FC condition for x = 0 and 0.05 samples recorded at selected temperatures are shown in Fig. 4.10. The loops are found to be unsymmetrical indicating the presence of exchange anisotropy in the system. Similar behavior is also observed for x = 0.50 sample but for T < 50 K as shown in Fig. 4.11. In case of x = 0 sample, the loops were found to move towards the positive side of the field axis upto T ~ 120 K and then for further increase in temperature *i.e.* T > 120 K the loops start shifting towards the negative field axis. Similarly, in case of x = 0.05 sample the loops are found to be shifted towards the positive field axis upto 130 K and beyond that they move towards negative field axis. Such a behavior of *M-H* loop, measured in different temperature region, suggests that the EB field can also be tuned between positive and negative values by varying the temperature similar to that of the temperature driven sign reversal of magnetization.

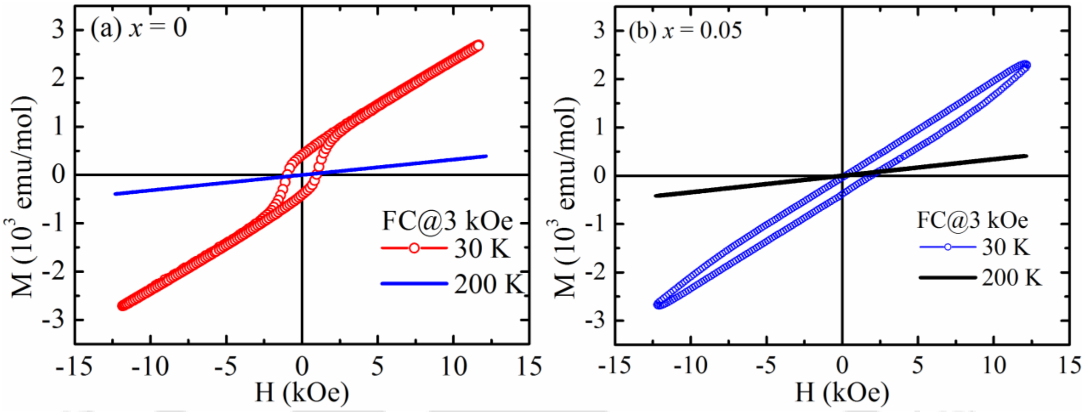

Figure 4.9: *M-H* loops of (a) $x = 0$ and (b) $x = 0.05$ samples under FC mode at $T = 30$ K and 200 K for $H = 3000$ Oe.

Usually exchange bias is quantitatively defined as $H_{EB} = (H_+ + H_-)/2$, where H_+, H_- represent the right and left coercive fields, respectively. Figs. 4.12 (a) and (b) show the temperature dependence of estimated values of H_{EB} for $x = 0$ and $x = 0.05$ samples respectively. For $T < T_N$, the H_{EB} is found to be negative and its magnitude increases with decrease in temperature with a maximum negative value (valley point) of $H_{EB} = -0.1$ kOe at $T_V = 155$ K for $x = 0$ sample. For further decrease in temperature the magnitude of H_{EB} starts to decrease and as T approaches T_{comp}, H_{EB} is found to be close to zero. Further decrease in temperature *i.e.* for $T < T_{comp}$, H_{EB} acquires positive values which increases with decrease in T, reaching a maximum H_{EB} of 0.35 kOe at $T_P = 115$ K and 1.6 kOe at $T_P = 50$ K for $x = 0$ and $x = 0.05$ respectively. Thereafter, H_{EB} starts decreasing and falls towards zero. The observed values of H_{EB} in the present set of samples are almost comparable to those reported for $NdCr_{1-x}Mn_xO_3$ and $NdMnO_3$ [74,85]. The temperature dependence of EB field for $x = 0.50$ sample also exhibits a similar sign reversal behavior across the T_{comp} and the maximum negative H_{EB} is found to be 1.1 kOe as shown in Fig. 4.12(c).

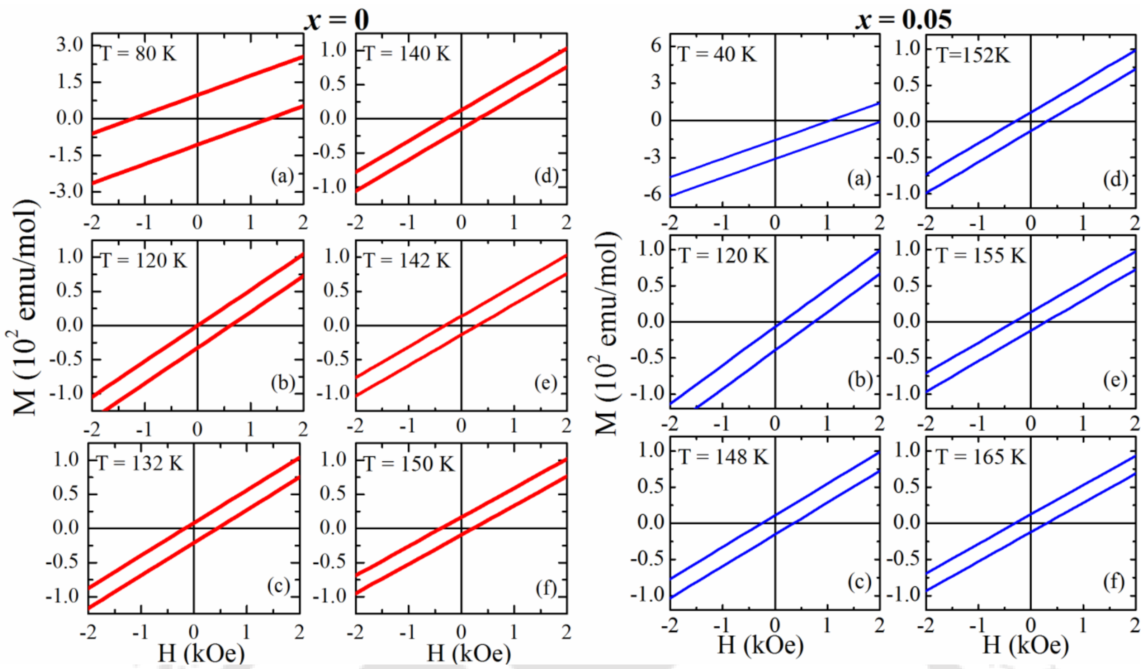

Figure 4.10: (a) - (f) Enlarged view of *M-H* loops in the vicinity of coercive fields under FC condition for H = 3000 Oe measured at different temperatures for x = 0 and x = 0.05 samples.

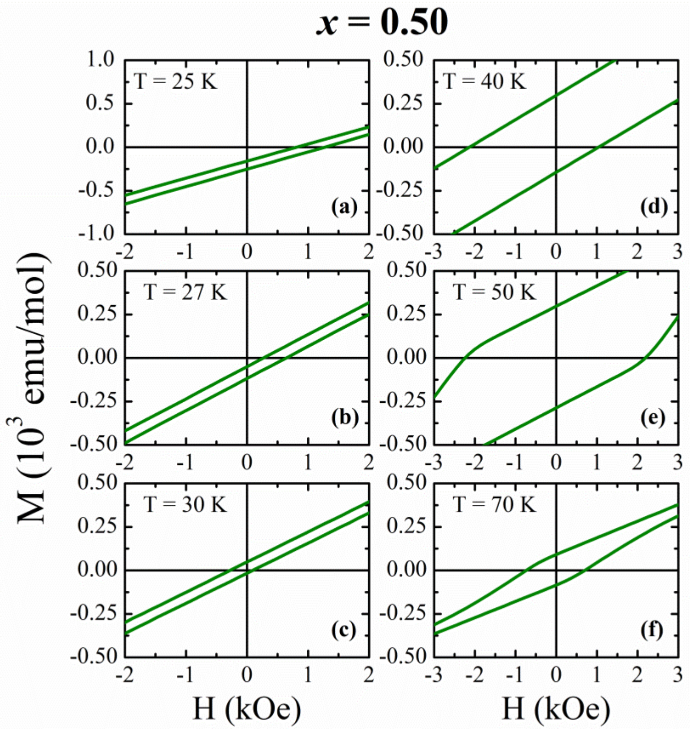

Figure 4.11: (a) - (f) Enlarged view of *M-H* loops in the vicinity of coercive fields under FC condition for H = 3000 Oe measured at different temperatures for x = 0.50 sample.

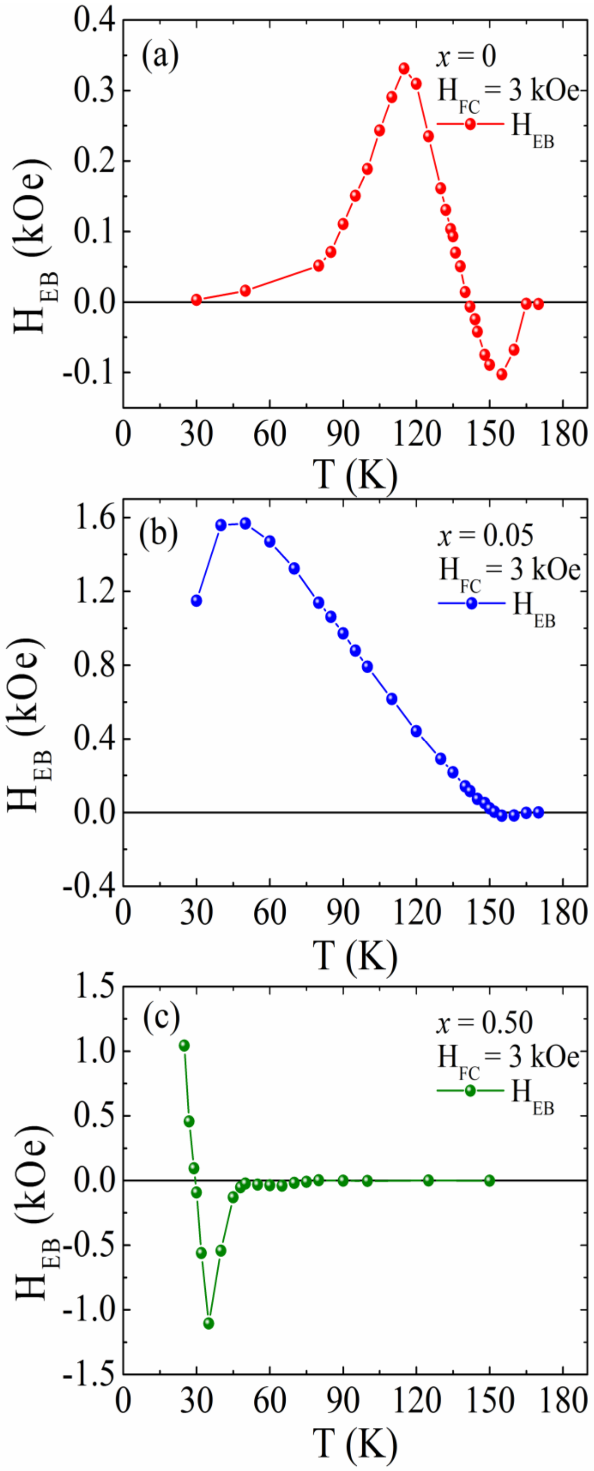

Figure 4.12: Temperature dependence of exchange bias field (H_{EB}) for (a) $x = 0$ (b) $x = 0.05$ and (c) $x = 0.50$ samples.

The sign reversal of H_{EB} with temperature in samples $x = 0$ and 0.05 can be explained by considering the competition between FM component from Cr^{3+} ions (M_{Cr}) and PM component ($M_{PM} = M_{Gd}+M_{Mn}$) due to Gd^{3+} ions and substituted Mn^{3+} ions under the influence of negative internal field (H_I). In the temperature range of $T_{comp} < T < T_N$ canted Cr^{3+} moments (M_{Cr}) *i.e.* the weak ferromagnetic component lies along the direction of applied field H, while M_{PM} tends to align along H_I which is opposite to H. In this temperature region, the dominance of M_{Cr} over M_{PM} leads to net positive magnetization as a result larger negative field is required to reverse the direction of magnetization. This causes a shift in the M-H loops towards negative field axis and it gives rise to negative EB field. The negative peak of H_{EB} observed in the range of $T_{comp} < T < T_N$ for $x = 0.05$ sample is found to be suppressed as compared to $x = 0$ sample, which is due to the decrease in the strength of the ferromagnetic components of Cr^{3+} ions (M_{Cr}) upon Mn doping. While for $T < T_{comp}$, the net PM moments (M_{PM}) under negative internal field is enhanced and it dominates over the M_{Cr}, causing the loops to shift towards the positive field axis, thereby giving rise to positive EB field. At $T \approx T_{comp}$, no EB is observed as both M_{Cr} and M_{PM} are equal in magnitude but opposite in direction. The H_{EB} values approaching zero for $T < T_P$ can be explained in terms of dominant paramagnetic component of Gd^{3+} and Mn^{3+} ions and thereby quenching of exchange bias. Similar behavior of EB field is reported in other orthochromites [95,138]. The sign reversal of the EB field in the present samples can be understood from the schematic diagram shown in Fig. 3.19 (Chapter 3). The presence of temperature induced magnetization reversal in $x = 0.40$ and 0.50 samples and EB in $x = 0.50$ sample can be explained by considering the competing canted AFM interaction in $Cr^{3+} – O^{2-} – Cr^{3+}$ networks and collinear AFM interaction in $Mn^{3+} – O^{2-} – Mn^{3+}$ networks in the presence of paramagnetic entities such as Gd^{3+} and some of Mn^{3+} ions.

The observed sign reversal of magnetization and exchange bias behavior especially in $x = 0$ and $x = 0.05$ samples resembles with that of the behavior reported in some of the intermetallic compounds, nanoparticles and other orthochromites; but the mechanism of their origin is different for different kind of materials. In intermetallic compound like $Nd_{0.75}Ho_{0.25}AlO_3$ [55,139] the origin of sign reversal of EB is attributed to the sign reversal of different sub components of magnetic moment of rare earth ions and conduction electron polarization while for nanoparticles sample like $La_{0.20}Ce_{0.80}CrO_3$ [16] it is attributed to the core shell structure. In some orthochromites like LaFe$_{0.50}$Cr$_{0.50}$O$_3$ [113]and YFe$_{0.50}$Cr$_{0.50}$O$_3$ [114] the competition between the DM interaction and single ion anisotropy leads to the sign reversal of EB. As the samples under consideration are bulk in nature the mechanism of core-shell structure is ruled out. The possibility of conduction electron polarization is also not expected in present case. The measured FC M-T data could not be fitted to the model based on competition between single ion anisotropy and DM interaction. Since these samples are in single phase form and do not exhibit any layered structures, the mechanism of EB involved in FM/AFM bilayers [18,92] is also not valid. However, in present samples the competition between the M_{Cr} and M_{PM}, each having different temperature dependences, plays a major role in determining the net magnetization (either positive or negative) at a particular temperature T. Therefore, in present system the EB is attributed to the competition between the above two moments and the dominance of one moment over the other with change in temperature leads to the sign reversal of H_{EB}.

4.2 Fe Substituted $GdCrO_3$

This section deals with the effect of Fe substitution at the Cr site of $GdCrO_3$ *i.e.* $GdCr_{1-x}Fe_xO_3$ ($x = 0 - 0.50$). The preparation and characterization of the samples along with the analysis of the results obtained from the dc magnetization measurements are presented. Here the electrical properties of the prepared samples are also discussed.

4.2.1 Sample Preparation and Characterization

Polycrystalline samples of $GdCr_{1-x}Fe_xO_3$ for $x = 0$, 0.05, 0.10, 0.15, 0.20, 0.30, 0.40 and 0.50 were prepared from the stoichiometric ratio of Gd_2O_3, $Cr(NO_3)_3.9H_2O$ and $Fe(NO_3)_3.9H_2O$, all with purity better than 98%, using the standard sol-gel method as discussed in section 4.1.1. XRD patterns were recorded using Rigaku make TTRAX III diffractometer. Raman spectra at room temperature were recorded using a Horiba Jobin Vyon, Model LabRam HR Raman spectrometer with the help of Ar-ion laser source of wavelength 514 nm. Magnetic measurements were done with the help of Lakeshore make VSM of model no. 7410. The impedance and dielectric measurements were carried out using Wayne Kerr LCR meter with model number 4300. Here the electrodes were connected by painting silver paste on both sides of the sample.

4.2.2 Structural properties

XRD patterns recorded at room temperature for $GdCr_{1-x}Fe_xO_3$ ($x = 0 - 0.50$) samples are shown in Fig. 4.13. These patterns were analyzed based on *Pbnm* space group as per the Rietveld refinement technique [126]. Typical XRD patterns along with the Rietveld refined data (solid lines) are shown in Fig. 4.14 for $x = 0.10$, 0.30 and 0.50 samples. All the observed peaks coincide with Rietveld refined data and it highlights the single phase nature of the samples. The refined lattice parameters and unit cell volume are given in Table 4.3. The lattice parameters obtained from the refinement are found to increase with increase in Fe concentration as shown in Fig. 4.15. The increase in lattice constant values can be understood in terms of larger Fe^{3+} (0.645 Å) ions substituting the Cr^{3+} (0.615 Å) ions. The average Cr/Fe– O bond length determined from the Rietveld refinement is found to increase with Fe concentration as shown in the inset of Fig. 4.15.

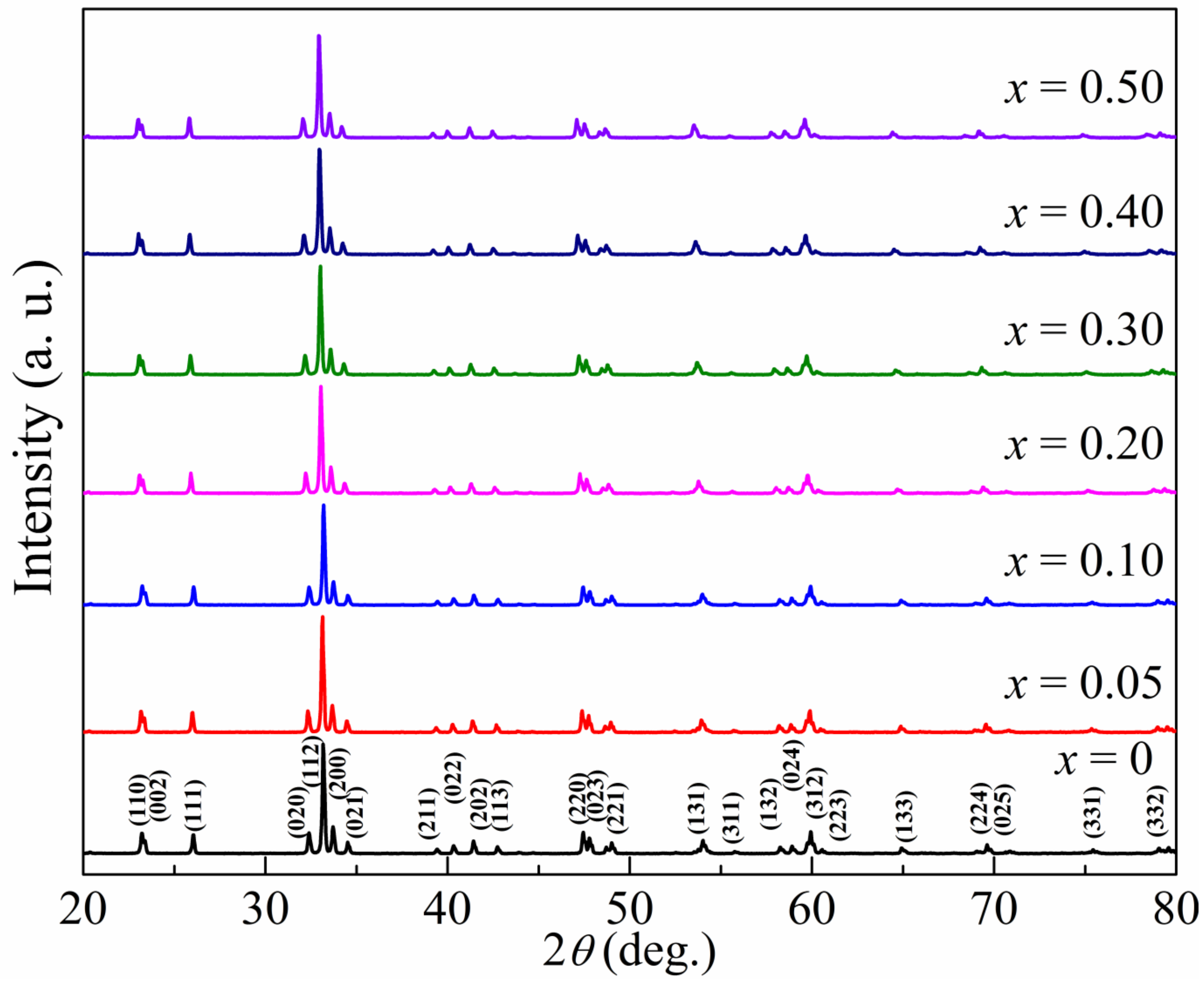

Figure 4.13: XRD patterns of GdCr$_{1-x}$Fe$_x$O$_3$ samples for $x = 0 - 0.50$.

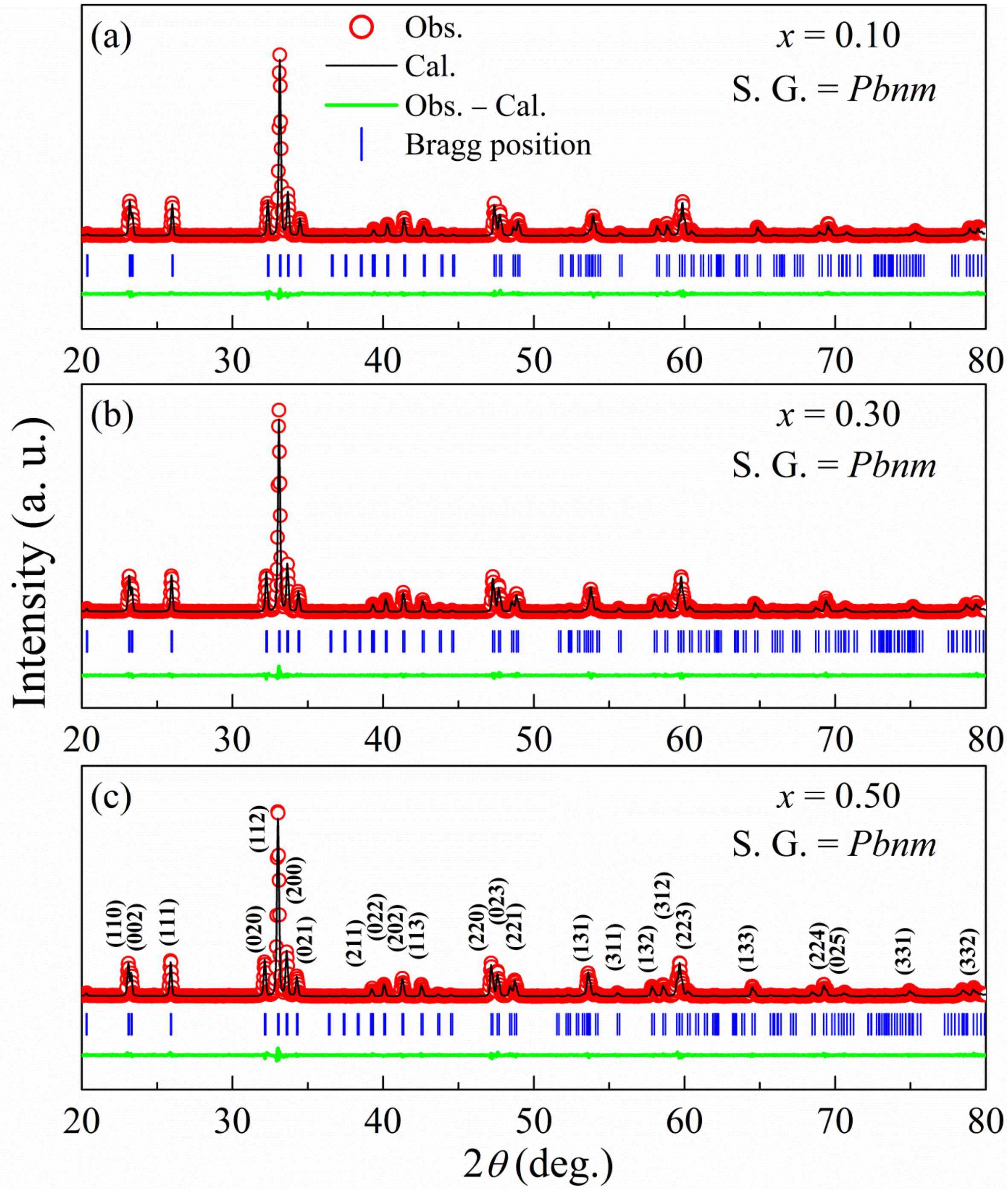

Figure 4.14: XRD patterns of x = 0.10, 0.30 and 0.50 samples along with their Rietveld refined data shown as solid lines. The circles represent the experimental points and solid line (black) represents the refined data. The bottom line (green) shows the difference between experimental and refined data. The vertical lines (blue) are the allowed Bragg position.

The structural distortion due to Fe substitution can be studied by estimating the Goldschmidt's tolerance factor (t) [21], given by the relation $t = \frac{r_A + r_O}{\sqrt{2}\,(r_B + r_O)}$. Here r_A, r_B, and r_O correspond to average ionic radii of A and B site cations and the oxygen ion respectively. The calculated value of t using the above relation is found to decrease from 0.865 (x = 0) to 0.858 (x = 0.50) and it highlights the increase in lattice distortion. As the origin of ferroelectricity in $RCrO_3$ is associated with the structural distortion [11,140] it can be expected that Fe^{3+} substitution would be helpful in tuning the magnetic and electrical properties of $GdCrO_3$.

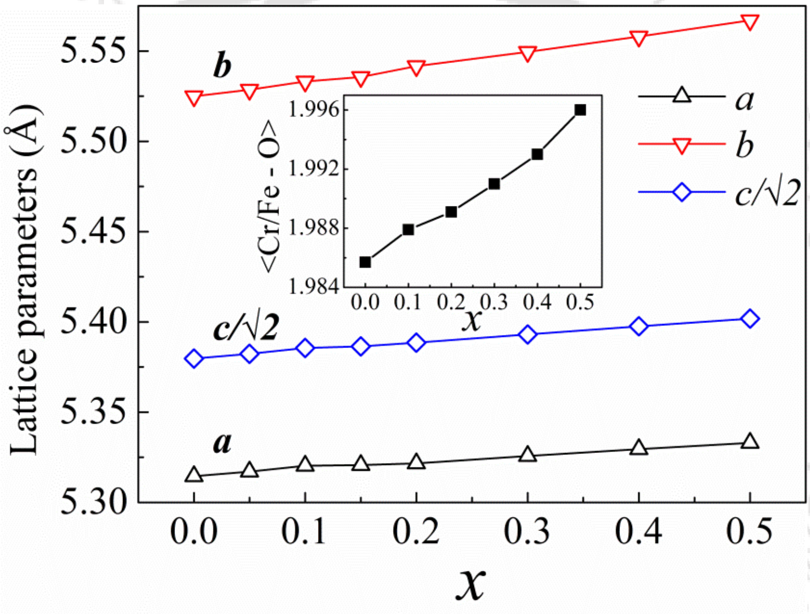

Figure 4.15: Lattice parameters *a*, *b*, and *c* as a function of Fe concentration (*x*). Inset shows the variation of average Cr/Fe – O bond length with *x*.

The microstructural images of all the samples were recorded using FESEM. Fig. 4.16 shows the FESEM images of x = 0.20 and 0.50 samples along with their EDS spectrum. The surface morphology of all the samples is found to be quite uniform. The average grain size of the particles was determined using ImageJ software and the estimated values of average grain size of x = 0, 0.10, 0.20 and 0.50 samples are found to be 482 nm, 512 nm, 535 nm and 499 nm respectively. The values of cationic ratio obtained from the analysis of EDS spectra for x = 0, 0.10, 0.20, 0.40 and 0.50 samples are given in Table 4.4 and they are found to be comparable to the nominal starting composition of the samples.

Table 4. 3: Parameters obtained from the Rietveld analysis of the samples GdCr$_{1-x}$Fe$_x$O$_3$ (x = 0 to 0.50).

Sample/ Parameters	**x = 0**	**x = 0.05**	**x = 0.10**	**x = 0.15**	**x = 0.20**	**x = 0.30**	**x = 0.40**	**x = 0.50**
Space group	*Pbnm*	*Pbnm*	*Pbnm*	*Pbnm*	*Pbnm*	*Pbnm*	*Pbnm*	*Pbnm*
***a* (Å)**	5.3145(2)	5.3171(2)	5.3203(2)	5.3207(2)	5.3216(2)	5.3257(2)	5.3295(2)	5.3330(2)
***b* (Å)**	5.5249(2)	5.5286(2)	5.5331(2)	5.5356(2)	5.5416(2)	5.5495(3)	5.5580(2)	5.5670(2)
***c* (Å)**	7.6068(2)	7.6106(3)	7.6151(2)	7.6164(4)	7.6193(2)	7.6257(3)	7.6322(2)	7.6382(2)
Volume (Å^3)	223.35(1)	223.63(2)	224.17(1)	224.33(3)	224.69(1)	225.38(2)	226.08(1)	226.77(1)
R_F (%)	3.27	3.59	3.25	2.26	2.42	2.21	2.19	2.47
R_{Bragg} (%)	3.72	3.85	3.55	2.37	2.71	2.34	2.14	2.52
R_P (%)	8.21	8.43	8.11	9.6	7.7	7.25	7.21	7.56
R_{exp} (%)	7.23	7.10	7.46	7.00	7.10	7.16	7.04	7.23
χ^2	2.55	3.02	2.44	2.30	2.23	2.13	2.17	2.12
Gd/Cr/Fe Occupancy	0.987 /0.997 /0.000	0.998 /0.962 /0.050	0.999 /0.899 /0.099	1.000 /0.848 /0.149	0.998 /0.816 /0.199	0.999 /0.705 /0.299	1.000 /0.599 /0.398	1.000 /0.499 /0.499

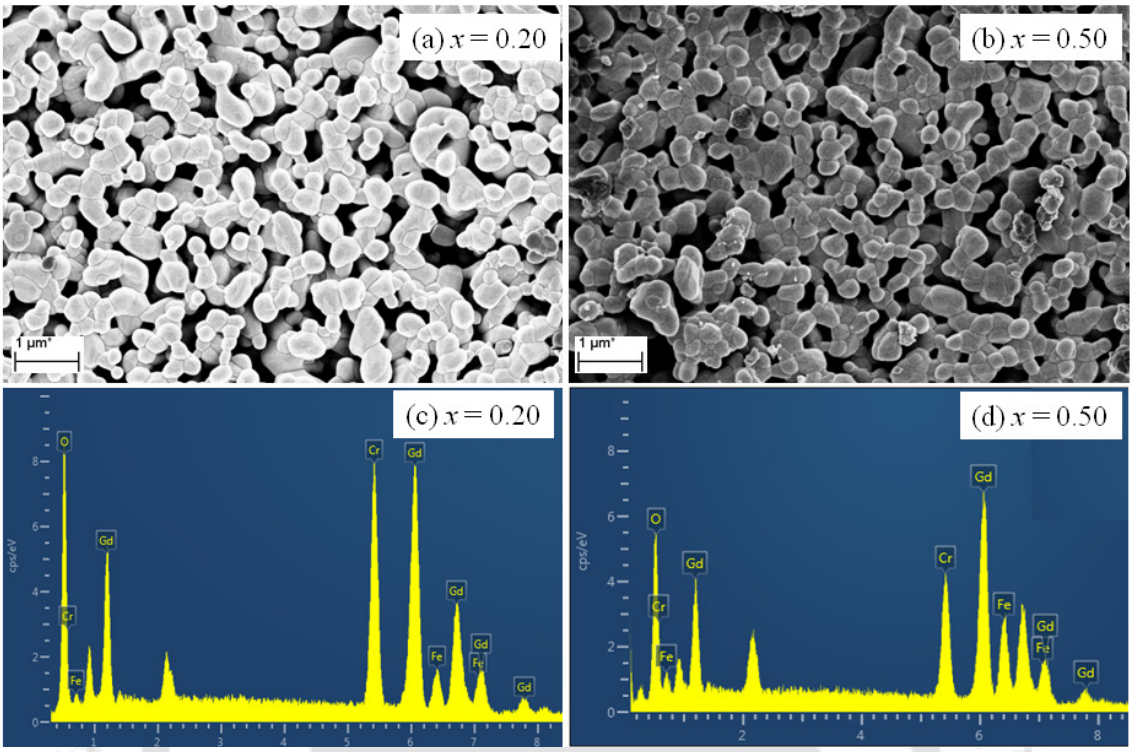

Figure 4.16: FESEM images recorded for (a) x = 0.20 and (b) x = 0.50 samples along with their EDS spectrum shown in Figs. (c) and (d) respectively.

Table 4.4: The cationic ratio determined from EDS analysis for x = 0 - 0.50 samples.

Samples	**Calculated Cationic Ratio from EDS analysis**		
	Gd	**Cr**	**Fe**
$x = 0$	1.00	0.96	--
$x = 0.10$	0.98	0.89	0.11
$x = 0.20$	0.98	0.80	0.20
$x = 0.40$	0.96	0.59	0.41
$x = 0.50$	1.00	0.50	0.50

In order to further study the effect of Fe substitution on the crystal structure of $GdCrO_3$ Raman spectra were recorded in $GdCr_{1-x}Fe_xO_3$ ($0 \leq x \leq 0.50$) samples at room temperature in the wave number range of 100 – 800 cm^{-1} and they are shown in Fig 4.17(a). Rare earth orthochromites crystallize in orthorhombically distorted perovskite structure with *Pbnm* space group and based on group theory calculation, the *Pbnm* space group is known to exhibit 24 Raman active modes namely [141]: $7A_g + 5B_{1g} + 7\ B_{2g} + 5B_{3g}$. The parent compound $GdCrO_3$ ($x = 0$) exhibits eight prominent Raman modes at ~141, 159, 225, 284, 325, 390, 477 and 568 cm^{-1} and the present spectrum is consistent with previous report [142]. The two Raman modes observed below 200 cm^{-1} are mainly associated with the vibrations of the rare earth ions while the Raman modes observed in the mid spectral region (B_{1g}, A_g, B_{2g} and A_g) are sensitive to the change in the orthorhombic distortion of the lattice. The phonon modes observed in the higher wave number region are mainly associated with the vibrations of the CrO_6 octahedra.

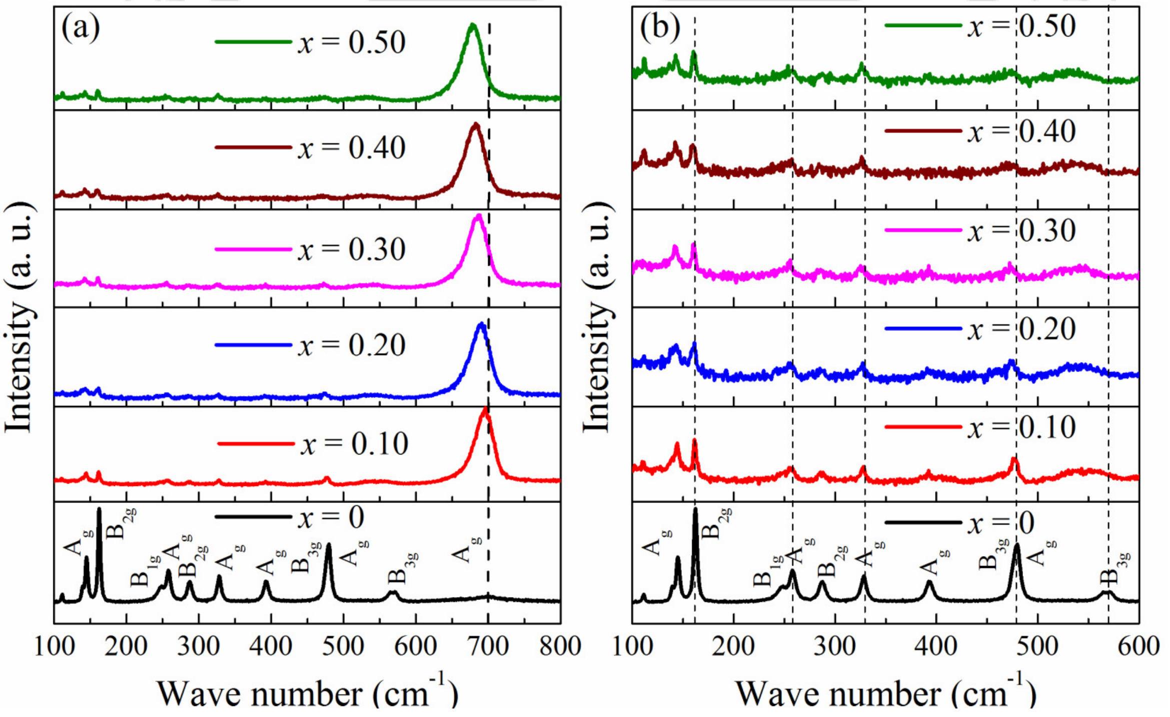

Figure 4.17: (a) Raman spectra measured at room temperature for $GdCr_{1-x}\ Fe_xO_3$ ($x = 0$ – 0.50) samples. (b) Expanded view of the Raman spectra over the wave number range of 100 – 600 cm^{-1} for $x = 0 – 0.50$ samples.

To clearly see the effect of Fe substitution at Cr site, expanded view of Raman spectra of x = 0 to 0.50 samples over the wave number range of 100 – 600 cm^{-1} are shown in Fig. 4.17(b) where one can see the decrease in the intensity of Raman modes along with considerable broadening with increase in Fe concentration. The above reduction in the intensity can be attributed to the substitution of Fe ions at random Cr site affecting the cooperative motion of the CrO_6 octahedra as these modes depend on the tilting of CrO_6 octahedra and, bending and stretching of Cr – O bonds [143]. In addition to the reduction in the intensity, the above Raman modes are found to marginally shift towards lower wave number with increase in Fe concentration and it can be attributed to the increase in Cr/Fe – O bond length as observed from XRD analysis and such trend is already reported [144,145]. In addition to the above Raman modes, an additional intense mode is observed around 700 cm^{-1}, especially for Fe substituted samples. The mode at 700 cm^{-1} is observed only when B site contains both Fe and Cr ions while it is absent in the parent compound (x = 0). Such an interesting behavior is reported in similar perovskites such as $LaCr_{1-x}Fe_xO_3$ [146] and $HoCr_{1-x}Fe_xO_3$ [147] and it is attributed to the activation of local in-phase oxygen breathing mode, due to the transfer of electron between Fe^{3+} and Cr^{3+} ions [146]. During this process, the *d* orbitals of B site (Fe and Cr) ions couple with the *p* orbitals of all six surrounding oxygen ions leading to a self trapping motion of the oxygen octahedral [146]. In this way, the charge transfer leads to an orbital mediated activation of local oxygen breathing mode of A_g like symmetry around 700 cm^{-1} in Fe substituted samples. The absence of such charge transfer mechanism is the reason for the absence of A_g mode around 700 cm^{-1} in the parent compound (x = 0). The observed shift of the A_g mode towards lower wave number can be ascribed to the increase in lattice distortion due to Fe substitution [147].

4.2.3 Magnetic Properties

Figure 4.18 shows the magnetization (M) as a function of temperature (T) for x = 0 - 0.50 samples under the zero field cooled (ZFC) and field cooled (FC) conditions for an applied field of H = 100 Oe. The parent compound (x = 0) and the Fe substituted samples show antiferromagnetic (AFM) transition and the Neel temperature (T_N) initially decreases from T_N = 172 K (x = 0) to T_N = 161 K (x = 0.20). However, with further increase in Fe concentration the T_N value is found to increase. These values are found to be 178 K, 204 K and 260 K for $x = 0.30$, $x = 0.40$ and $x = 0.50$ samples respectively. The decrease in T_N upto $x = 0.20$ can be attributed to the dilution of $Cr^{3+} – O – Cr^{3+}$ networks by Fe^{3+} substitution at random Cr^{3+} site. However, the rise in T_N value for $x > 0.20$ can be attributed to the establishment of $Fe^{3+} – O^{2-} – Fe^{3+}$ networks.

The ZFC magnetization of $x = 0$ sample is found to increase gradually down to $T = 50$ K and below that it exhibits a sharp increase in magnetization due to the strong paramagnetic response of Gd^{3+} ions at low temperature as shown in inset of Fig. 4.18(a). Similar trend of ZFC magnetization is observed for all the Fe substituted samples. The magnetization in the FC mode of $x = 0$ sample exhibits an interesting behavior of temperature induced magnetization reversal with a T_{comp} of 136 K. The MR arises due to the competition between the weak FM component of the canted Cr^{3+} ions (M_{Cr}) and the paramagnetic (PM) moment of Gd^{3+} ions, each of them have different temperature dependences, under the influence of negative internal field from the AFM ordered Cr^{3+} ions [12]. For $T < T_{comp}$, the paramagnetic moment of Gd^{3+} ions dominate over the M_{Cr} giving rise to negative magnetization; while for $T_{comp} < T < T_N$, the FM component of canted Cr^{3+} ions dominate over the PM moment resulting in a net positive magnetization in the system. However, the MR is not observed when Fe is substituted in place of Cr ions. The disappearance of MR even at a very low concentration of 5 at% Fe suggests that the substitution of Fe ions leads to a considerable enhancement in the canting of Cr^{3+} moments and hence the corresponding increase in weak FM moment. Thus, the weak FM moment dominates over the PM moment in the entire temperature range of $T < T_N$. So, the PM moment can't overtake the FM component of canted Cr^{3+} moment and hence no MR is observed.

With further increase in Fe concentration, the FC magnetization is found to decrease and is mainly due to reduction in Cr^{3+} content at the B site which reduces the net FM component of canted Cr^{3+} ions. Beyond $x = 0.20$, the considerable concentration of $Fe^{3+} – O^{2-} – Fe^{3+}$ networks promote the collinear AFM and hence it results in reduction in net magnetization. This can be seen from the *M-T* plots of $x = 0.30$ to $x = 0.50$ samples where the magnitude of magnetization decreases drastically compared to those of lower concentration samples. This leads to the appearance of a magnetic compensation like behavior ($M = 0$), without any magnetization reversal in $x = 0.40$ sample around $T = 125$ K as shown in Fig 4.18(g). For $x = 0.50$ sample the ZFC magnetization is found to be further reduced due to collinear AFM in Fe^{3+} - O^{2-} – Fe^{3+} networks and the FC magnetization is found to increase sharply at $T < 50$ K due to dominant PM contribution of Gd^{3+} ions.

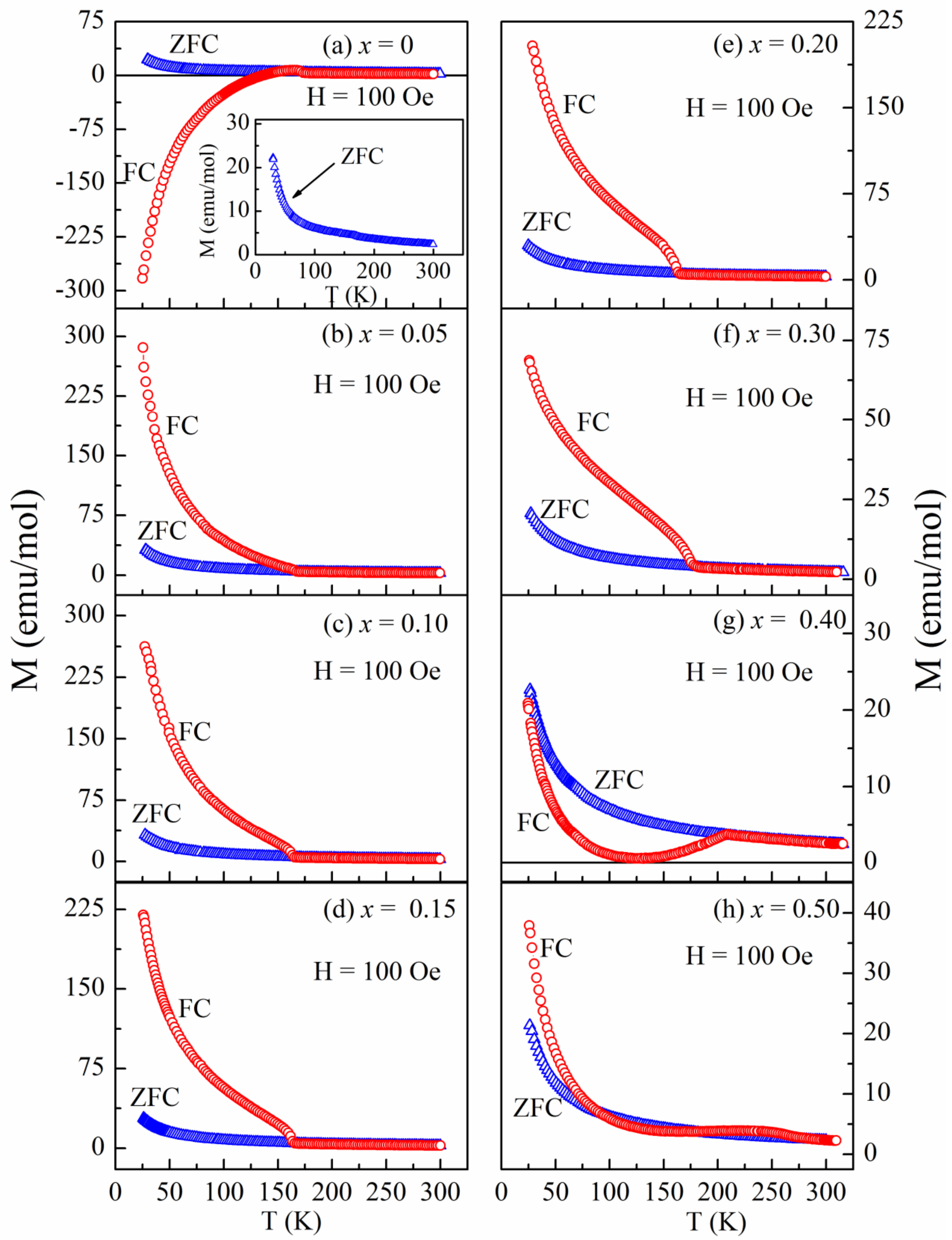

Figure 4.18: Magnetization as a function of temperature for GdCr$_{1-x}$Fe$_x$O$_3$ (x = 0 – 0.50) samples in ZFC and FC conditions for an applied field of H = 100 Oe. The inset (a) shows the ZFC magnetization of x = 0 sample in an expanded scale.

The inverse susceptibility as a function of temperature in the paramagnetic region was analyzed in terms of Curie Weiss law (CW), $\chi = C/(T - \theta)$ where C and θ are the Curie constant and Curie temperature respectively [28]. Experimental effective magnetic moments (μ_{eff}^{exp}) of the samples were calculated from the C values obtained from the CW fit to the experimental data as shown in Fig. 4.19 using the relation $C = \frac{N\mu_{eff}^2}{3k_B}$, where N is the Avogadro's number and k_B is the Boltzmann's constant. The corresponding theoretical moment was calculated using the relation, $\mu_{eff}^{Th} = [\mu_{Gd}^2 + (1-x)\mu_{Cr}^2 + (x)\mu_{Fe}^2]^{1/2}$ where μ_{Gd}, μ_{Cr} and μ_{Fe} represent the magnetic moments of Gd^{3+}, Cr^{3+} and Fe^{3+} ions respectively.

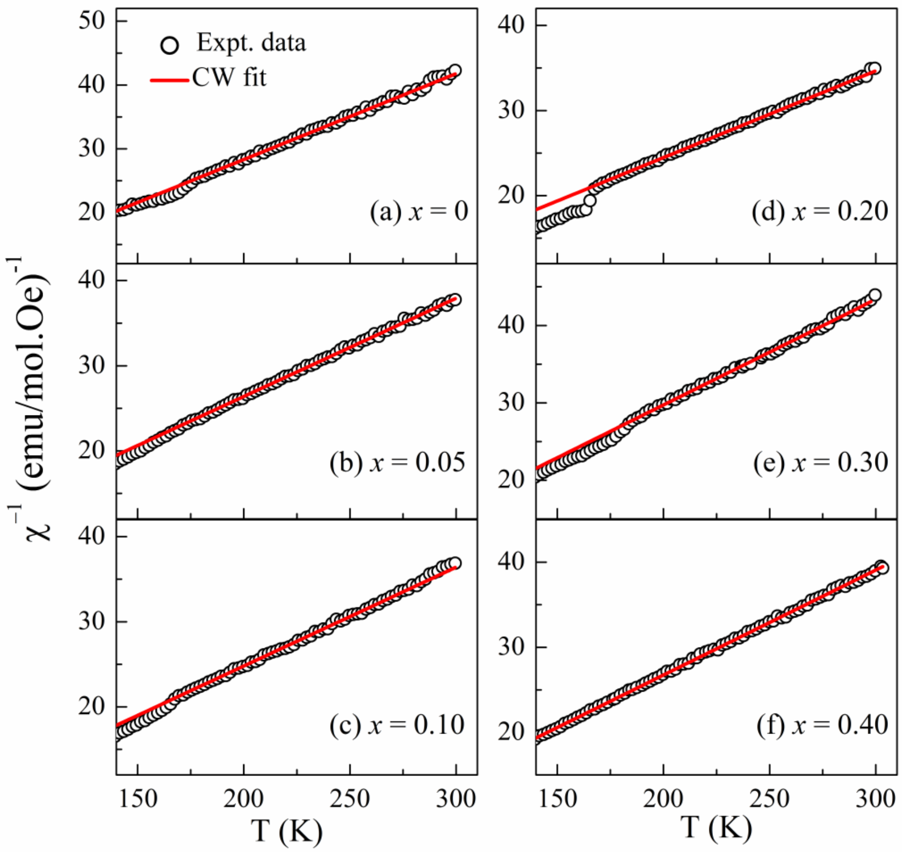

Figure 4.19: Inverse of susceptibility (χ^{-1}) vs. temperature for x = 0.0, 0.05, 0.10, 0.20, 0.30 and 0.40 samples along with the Curie-Weiss (CW) fit shown as solid lines in the PM region.

The effective magnetic moments obtained from the CW fit are found to be 7.88, 8.20, 8.34, 8.89, 7.87 8.20 μ_B for x = 0, 0.05, 0.10, 0.20, 0.30, 0.40 respectively. The effective magnetic moment for x = 0.50 sample couldn't be obtained as the T_N value is close to the room temperature limiting the PM region. Their corresponding theoretical magnetic moments are found to be 8.83, 8.88, 8.95, 9.06, 9.17, 9.28 μ_B respectively. The μ_{eff}^{exp} values are found to increase with increase in Fe concentration and are consistent with the μ_{eff}^{Th} values. However, for $x \geq 0.30$, μ_{eff}^{exp} values are found to be considerably small compared to those of theoretical values and this can be attributed to the presence of antiferromagnetic Cr^{3+} - O^{2-} - Cr^{3+} and Fe^{3+} - O^{2-} - Fe^{3+} networks/clusters of short range type in the paramagnetic region of these samples due to larger T_N values. The Curie temperature (θ) lies in the range of -15 K to - 40 K signifying the AFM nature of the samples.

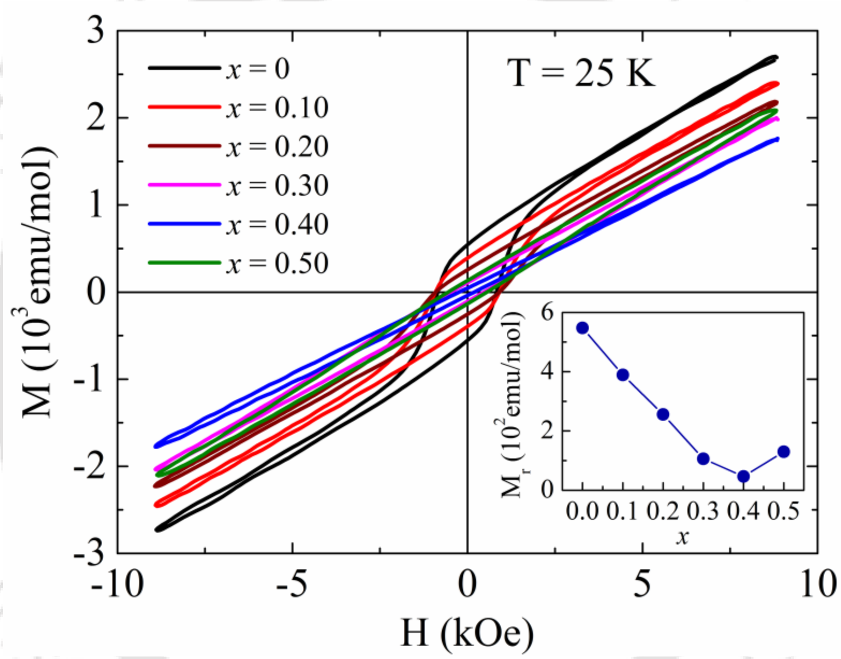

Figure 4.20: *M*-*H* loops of $GdCr_{1-x}Fe_xO_3$ ($x = 0 – 0.50$) samples recorded at $T = 25$ K under ZFC condition. The inset shows the variation of M_r as a function of Fe concentration (x).

Figure 4.20 shows isothermal *M* - *H* loops of all the samples measured at $T = 25$ K under the ZFC condition. A clear hysteresis loop is observed in the low field region for $x = 0$ to $x = 0.20$ samples which arises due to the weak FM behavior of the samples. For higher Fe concentration ($x > 0.20$) samples, the loops are almost linear in nature indicating decrease in the weak ferromagnetism with Fe doping. The remnant magnetization (M_r) value is found to decrease from 2.2 emu/g ($x = 0$) to 0.18 emu/g ($x = 0.40$) as shown in inset of Fig. 4.20. The decrease in M_r value is attributed to decrease in the weak FM component of canted Cr^{3+} ions.

The linear increase in magnetization with magnetic field in the high field region is due to the PM moments of the rare earth sublattice and dominant AFM contribution from Cr^{3+} sublattice.

4.2.4 Impedance spectroscopy

Complex impedance spectroscopy (CIS) analysis is a very well-known tool to describe the electrical properties of polycrystalline dielectric samples. The contribution of grains, grain boundaries and the electrode-interface to the electrical properties can be obtained by analyzing the data.

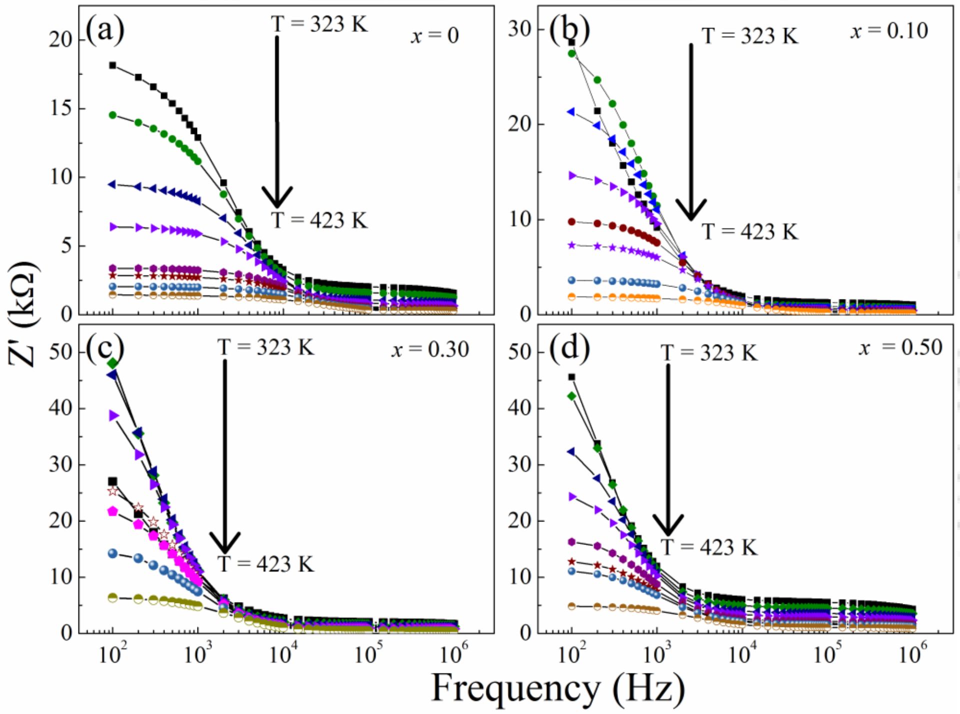

Figure 4.21: Frequency dependence of the real part of the impedance (Z′) for (a) $x = 0.0$, (b) $x = 0.10$, (c) $x = 0.30$ and (d) $x = 0.50$ samples in the temperature range of 323 to 423 K.

The real part of the impedance (Z′) measured as a function of frequency at different temperatures for $GdCr_{1-x}Fe_xO_3$ ($x = 0 - 0.50$) samples are shown in Fig. 4.21. The magnitude of Z′, measured at given temperature, decreases with increase in frequency which suggests the presence of a relaxation process. It is also observed that in the low frequency regime, the magnitude of Z′ decreases with increase in temperature due to thermal activation of charge carriers across grains and grain boundaries. The Z′ values of the Fe substituted samples are found to be larger than that of the parent compound ($x = 0$). The frequency dependence of the imaginary part of the impedance (Z″) for *x* = 0, 0.10, 0.30 and 0.50 samples measured at different temperatures is shown in Fig. 4.22. The observed impedance spectrum measured at each temperature demonstrates a clear peak at a particular frequency (f_{max}) indicating the presence of a relaxation behavior [99].

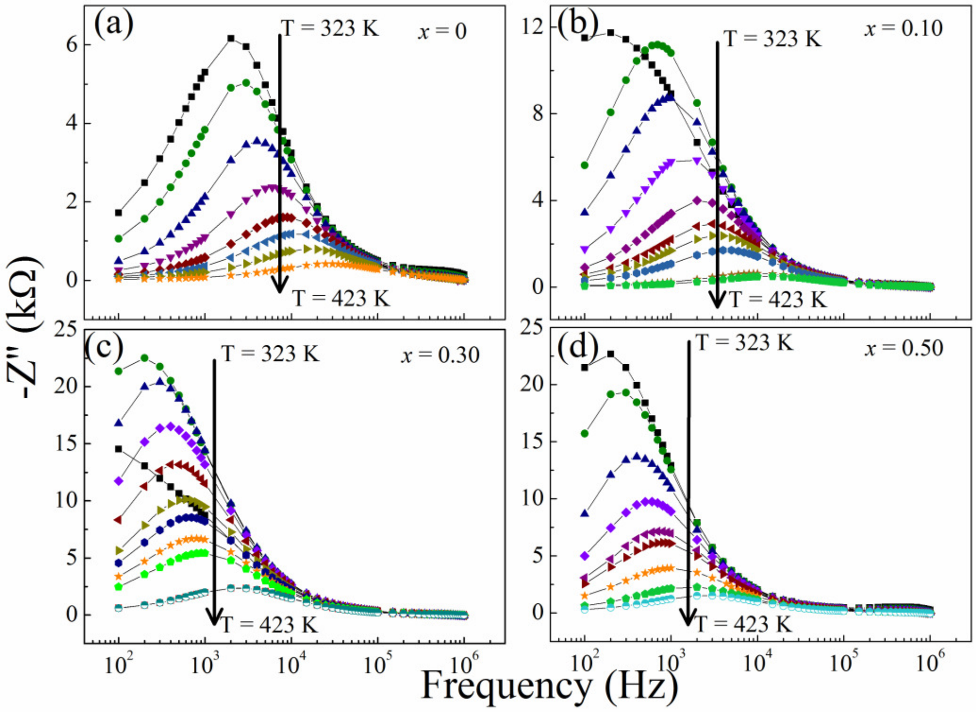

Figure 4.22: Frequency dependence of the imaginary part of the impedance (-Z″) for the samples (a) x = 0.0 (b) x = 0.10 (c) x = 0.30 and (d) x = 0.50 measured at different temperatures.

The magnitude of relaxation peak is found to be suppressed and the f_{max} is found to be shifted towards higher frequency as the temperature is increased. This highlights the presence of thermally activated relaxation process and this can be analyzed based on the Arrhenius law, $f_{max} = f_0\ exp(-E_a/k_BT)$, where E_a is the relaxation activation energy, k_B is the Boltzmann constant and f_0 is the pre factor [148]. The relaxation activation energy, E_a can be determined from a linear fit to the relaxation frequency (ln f_{max}) vs. 10^3/T plot as shown in Fig 4.23. The estimated values of E_a are 0.33(1) eV, 0.34(1) eV, 0.30(1) eV, 0.29(2) eV, 0.24(1) eV, and 0.28(2) eV for *x* = 0, 0.10, 0.20, 0.30, 0.40, and 0.50 samples respectively.

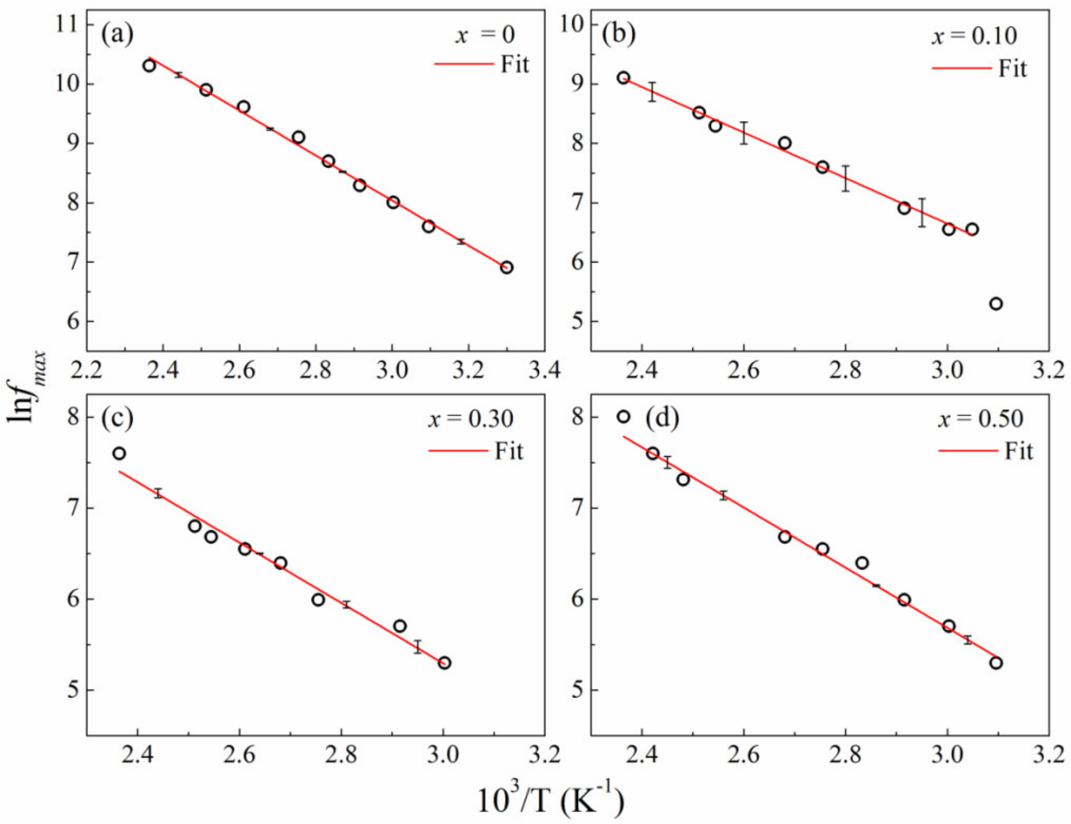

Figure 4.23: Plots of $\ln f_{max}$ vs. 10^3/T along with fit to Arrhenius law (solid line). The vertical lines represent the error in the fitted data.

Figure 4.24 shows the Nyquist plots (Z″ vs. Z′) of x = 0, 0.10, 0.30 and 0.50 samples measured at some selected temperatures. The Nyquist plots of all the samples show depressed semicircles with their centre located below the Z′ axis revealing the deviation from ideal Debye type relaxation. It is observed that at each temperature the Nyquist plot shows two semicircular arcs which indicate the contribution of two electroactive regions towards the relaxation dynamics. The bigger semicircular arc appearing in the lower frequency (higher Z′) region is associated with the grain boundaries contribution whereas the smaller semicircular arc at higher frequency (smaller Z′) corresponds to contribution of grains. The radius of the semicircle is found to decrease with increase in temperature and it indicates the decrease in resistance with increase in temperature.

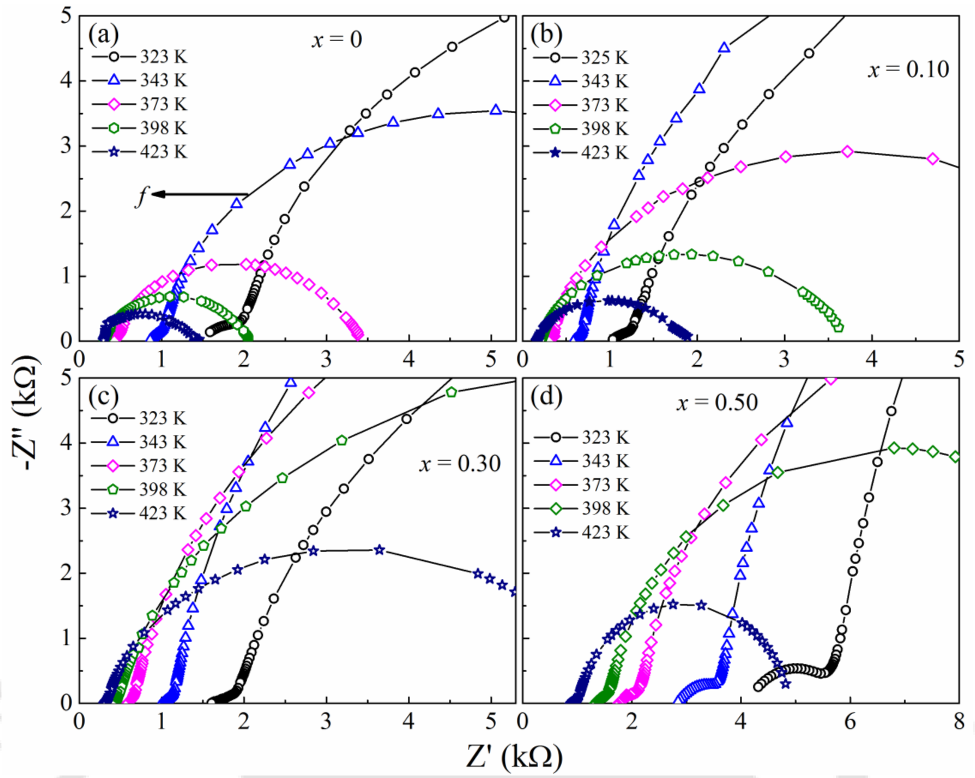

Figure 4.24: -Z″ vs Z′ plots for (a) x = 0, (b) x = 0.10, (c) x = 0.30 and (d) x = 0.50 samples at some selected temperatures.

The real part (σ') of ac conductivity (σ_{ac}) for the GdCr$_{1-x}$Fe$_x$O$_3$ samples were determined using the relation, $\sigma' = \omega\varepsilon_0\varepsilon''$ as per the ref [148,149]. Here ω is the angular frequency, ε_0 is the permittivity of free space and ε'' is the imaginary part of the dielectric constant, determined from the measured Z′ and Z″ values using the relation $\varepsilon'' = \frac{Z'}{\omega C_0\,(Z'^2 + Z''^2)}$. Fig. 4.25 shows the frequency dependence of σ' for x = 0 to 0.50 samples measured at a temperature, T = 393 K and it is observed that conductivity of the Fe substituted samples are lower than that of the parent compound GdCrO$_3$. This can be attributed to the increase in the average bond length of Cr/Fe – O bond which results in a weaker overlap between the p orbitals of oxygen and d orbitals of Cr^{3+} cation leading to a fall in the conductivity of the samples. However, the conductivity of x = 0.40 and 0.50 samples is more than that of the x = 0.30 sample due to the possible hopping of charge carriers across Fe^{3+} - Fe^{2+} ions due to the increased concentration of Fe^{3+}- O^{2-} - Fe^{3+} networks.

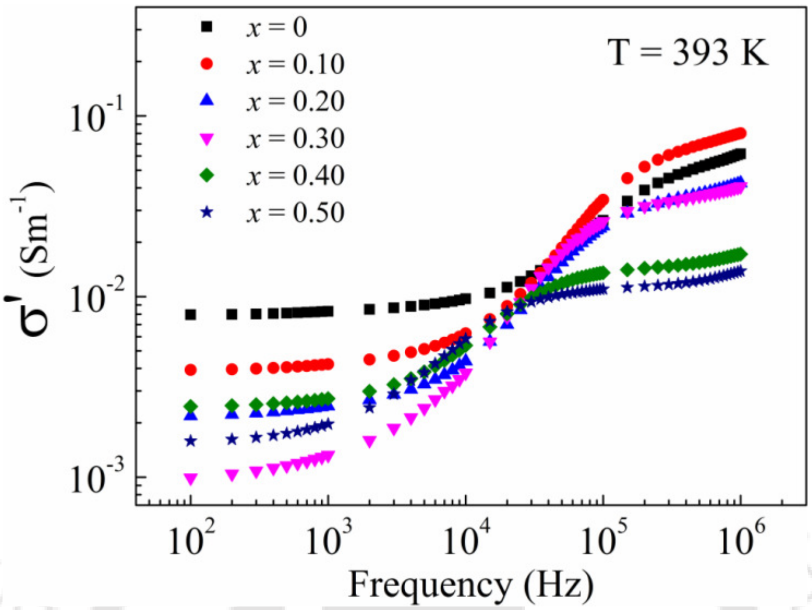

Figure 4.25: Frequency dependence of σ' for different concentration of Fe (x = 0, 0.10, 0.20, 0.30, 0.40, and 0.50) measured at T = 393 K.

The frequency dependence plots of σ' for x = 0, 0.10, 0.30 and x = 0.50 samples in the temperature range of T = 323 K to 423 K are shown in Fig. 4.26. It can be seen that the low frequency region displays a plateau like (frequency independent) behavior due to long range translational motion of charge carriers which contributes to the dc conductivity (σ_{dc}). The conductivity exhibits frequency dispersion behavior in the mid frequency region (10^3 - 10^4 kHz) which is due to increase in successful hopping of the charge carriers. In the high frequency region (> 10^4 kHz) of higher Fe concentration ($x \geq 0.30$) samples the conductivity again starts to follow frequency dispersion behavior and it represents the contribution from grains to the total conductivity. Thus, the entire conductivity spectra were analyzed by separating them into low and high frequency regions. The real part (σ') of the conductivity data measured at a given temperature were analyzed using the Jonscher's power law [99], $\sigma'(\omega) = \sigma_{dc} + A\omega^n$, where σ_{dc} represents the frequency independent dc conductivity and $A\omega^n$ represents the frequency dependant term. A is the pre-exponential factor and n is the power law exponent which generally lies between 0 and 1. The temperature dependence of n suggests the underlying conduction mechanism involved in the samples. It is observed that for all samples, n first increases upto a certain temperature and then it decreases with further increase in the temperature. Such a variation of n with temperature suggests that short range translational hopping assisted by both small and large polaron [150] is likely the conduction mechanism in these samples. The value of n lies in the range of $0.82 < n < 1.33$ for all samples.

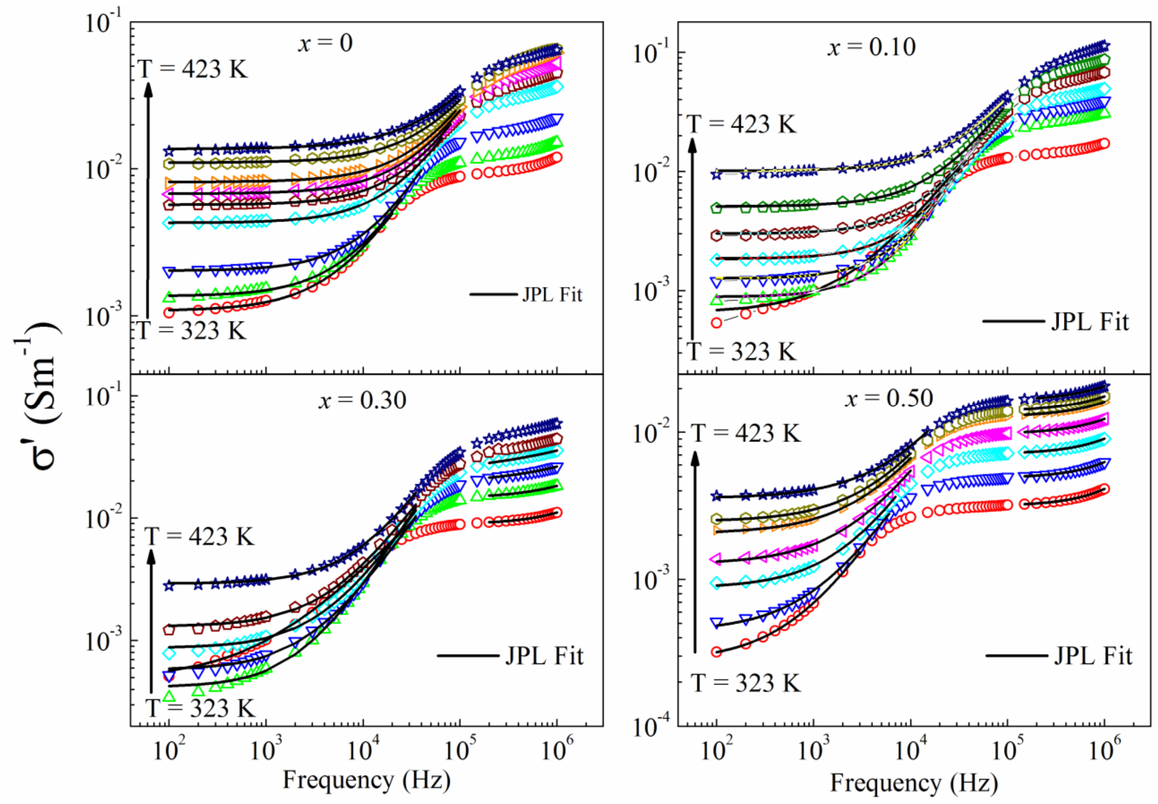

Figure 4.26: Frequency dependence of real part of ac conductivity (σ') for (a) $x = 0$, (b) $x = 0.10$, (c) $x = 0.30$ and (d) $x = 0.50$ samples measured at different temperatures. The solid lines represent fit to Jonscher's power law (JPL).

The dc conductivity is found to increase with increase in temperature which indicates the thermal activation of charge carriers. The $\ln\sigma_{dc}$ vs. 10^3/T plots (shown in Fig. 4.27) were fitted to Arrhenius law of conductivity, $\sigma_{dc} = \sigma_0\, exp(-E_C\,/k_B T)$ for both grains and grain boundaries contributions. The estimated values of activation energy, E_C corresponding to grain boundaries (GB) are found to be 0.31(1), 0.32(1), 0.30(1), 0.29(3), 0.26(1) and 0.28(1) eV for x = 0, 0.10, 0.20, 0.30, 0.40 and x = 0.50 samples respectively. The value corresponding to grains (G) contribution lies in the range of 0.22 eV to 0.19 eV. The estimated value of E_C for x = 0 is in well agreement with previous report [151]. The activation energy values estimated from conductivity analysis are comparable to those obtained from Z″ data and it indicates that same kinds of charge carriers are responsible for both the relaxation process.

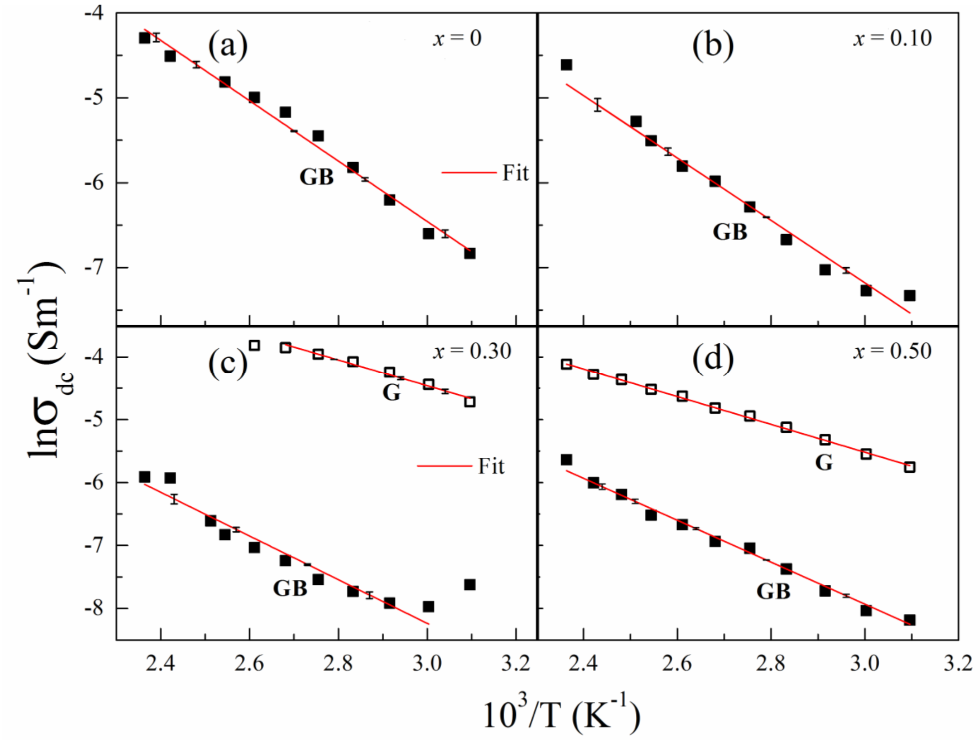

Figure 4.27: Variation of dc conductivity as a function of inverse of temperature (*1/T*) for $x = 0$, 0.10, 0.30 and $x = 0.50$ samples. Solid lines (red) represent the fitted data as per Arrhenius law for conductivity both for grains and grain boundaries contribution.

The activation energy values estimated for the conduction process (E_c) across the grain boundaries are comparable to that of singly ionized oxygen vacancies that lie in the range of 0.3 – 0.4 eV. Thus, the conduction process in the present samples is ascribed to the motion of singly ionized oxygen vacancies [152,153]. A marginal decrease in activation energy is observed both from the analysis of temperature dependence of relaxation frequency and dc conductivity in terms of Arrhenius law. This can be attributed to generation of considerable concentration of Fe^{2+} ions due to oxygen vacancies for higher Fe concentration and the hopping of charge carriers between Fe^{3+} and Fe^{2+} ions.

4.3 Conclusions

To conclude, Mn and Fe have been substituted at the Cr site of $GdCrO_3$ and the effect of substitution on the structural and magnetic properties of $GdCrO_3$ along with the electrical properties of Fe substituted samples are studied in this chapter.

Polycrystalline samples of $GdCr_{1-x}Mn_xO_3$ ($x = 0.0 – 0.50$) have been prepared using the citrate route based sol-gel method and the samples are found to crystallize in an orthorhombic structure (S.G - *Pbnm*). The AFM transition temperature was found to decrease upon Mn substitution *i.e.* 174 K for $x = 0$ to 91 K for $x = 0.50$. Samples for $x = 0$, 0.05, 0.40 and $x = 0.50$ samples exhibit interesting temperature induced magnetization reversal under field cooled condition. The magnetic compensation temperature is found to be 136 K for $x = 0$ sample which increases to 139 K for $x = 0.05$ sample whereas a low T_{comp} values of 27 K and 29 K were observed in case of $x = 0.40$ and 0.50 samples respectively. Bipolar switching of magnetization was demonstrated at 110 K for $x = 0$ and 0.05 samples just by varying the magnitude of the positive field. The origin of magnetization reversal for $x = 0.0$ and 0.05 samples is explained in terms of the competition between net PM moments from Gd^{3+} ions and substituted Mn^{3+} ions in the negative internal field (H_I) arising from AFM ordered Cr^{3+} ions and the canted FM component of Cr^{3+} ions. The value of internal field obtained for $x = 0$ and 0.05 samples lie in the range of 1.5 kOe to 2.5 kOe. Magnetization reversal in $x = 0.40$ and 0.50 samples is explained in terms of competing canted and collinear antiferromagnetism and the paramagnetic moment of host Gd^{3+} ions and some of the substituted Mn^{3+} ions. Tunable positive and negative exchange bias fields have been observed for $x = 0$, 0.05 and 0.50 samples by varying the temperature which arises due to the dominance of one moment (M_{Cr} or paramagnetic moments) over the other as the temperature is varied.

Single phase polycrystalline samples of $GdCr_{1-x}Fe_xO_3$ ($x = 0 - 0.50$) have been prepared using sol-gel method. Raman spectra reveals the presence of an oxygen breathing mode (A_g) in samples containing both Fe and Cr ions due to the possible charge transfer between Fe^{3+} and Cr^{3+} ions. All samples exhibit antiferromagnetic transition with a considerable weak ferromagnetic component due to spin canting. The Neel temperature is found to decrease marginally upto $x = 0.20$ and beyond that it increases due to considerable concentration of Fe^{3+} - O^{2-} - Fe^{3+} networks. The observed magnetization reversal in $x = 0$ sample is completely suppressed even for 5 at% of the Fe doping due to corresponding increase in spin canted weak ferromagnetism. However, magnetic compensation behavior is observed for $x = 0.40$ sample due to the predominant collinear antiferromagnetism in Fe^{3+} - O^{2-} - Fe^{3+} networks that suppress the weak ferromagnetic component. Complex impedance spectroscopy reveals the presence of non-Debye type thermally activated dielectric relaxation process. Complex impedance plane plots show the contribution of both grains and grain boundaries to the conduction process. The ac conductivity data were analyzed based on Johnscher's power law. The relaxation time of charge carriers and dc conductivity follow the Arrhenius law with comparable activation energy values.

Temperature driven magnetization reversal is observed in Mn substituted GdCrO$_3$ samples for $x = 0.05$, 0.40 and 0.50 whereas such a behavior was absent in the Fe substituted samples. This is mainly due to the enhancement in the spin canted weak ferromagnetic component of Cr^{3+} ions upon Fe substitution as a result the paramagnetic component couldn't offset the net canted Cr^{3+} moments in the temperature range $T < T_N$. Spin reorientation induced magnetization reversal is observed in case of Mn substitution for $x = 0.40$ and $x = 0.50$ samples while only magnetic compensation like behavior without any sign reversal is observed in Fe substituted, $x = 0.40$ sample due to considerable concentration of Fe^{3+} - O^{2-} - Fe^{3+} networks which promotes collinear antiferromagnetism.

Chapter **5**

Magnetic Properties of (Gd,Y)CrO_3 Compounds

5.1 Yttrium (Y) Substituted $GdCrO_3$

$RCrO_3$ compounds are known to exhibit many fascinating magnetic properties such as temperature induced MR, exchange bias, magnetic field induced switchable electric polarization, spin reorientation transition, magnetocaloric effect *etc.* The temperature induced magnetization reversal observed in $GdCrO_3$, $TmCrO_3$, $YbCrO_3$, and $CeCrO_3$ is known to arise from the competition between the canted Cr^{3+} moments and the R^{3+} moments where each sublattice moment has different temperature dependence. Similarly, the observed EB effect in orthochromites, which frequently coexists with the MR is mostly associated with the opposite alignment of the R^{3+} moments with respect to the weak FM component of canted Cr^{3+} ions. However, the origin of MR and EB in orthochromites is also attributed to other mechanism like competition between single ion anisotropy and DM interaction in case of $LaFe_{0.5}Cr_{0.5}O_3$ and $YFe_{0.5}Cr_{0.5}O_3$ [113,114] Therefore, the coupling between R^{3+} and Cr^{3+} ions plays a crucial role in determining the magnetic properties in $RCrO_3$.

As discussed in previous chapter (chapter 4), $GdCrO_3$ exhibits temperature induced MR and tunable EB behavior which can be explained considering the different temperature dependences of antiparallel alignment of canted Cr^{3+} moments and Gd^{3+} moments. Therefore, in the present work magnetic Gd^{3+} ion is substituted by non magnetic Y^{3+} ion to dilute the magnetic moment of R^{3+} (Gd^{3+}) site and study its effect on MR and EB behavior. The effect of Y substitution on the structural and magnetic properties of $GdCrO_3$ is discussed in this chapter.

5.1.1 Sample Preparation and Characterization

Polycrystalline samples of $Gd_{1-x}Y_xCrO_3$ (x = 0.0, 0.10, 0.30, 0.50, 0.70 and 1.0) were prepared using citrate based sol-gel combustion method following the same protocol as discussed in chapter 4. Highly pure Gd_2O_3 (99.9 %), Y_2O_3 (99.9%) and $Cr(NO_3)_3.9H_2O$ (99 %) were used as the starting compounds to prepare the samples. The obtained voluminous precursor was grinded and presintered at 600 °C for 12 hrs and the final sintering in pellet form was performed at 1100°C for 24 hrs. XRD patterns at room temperature, morphology and composition analysis, Raman spectra along with the temperature, time and field dependant magnetization data were recorded in accordance with the procedure discussed in chapter 4.

5.1.2 Structural properties

The XRD patterns of $Gd_{1-x}Y_xCrO_3$ (x = 0, 0.10, 0.30, 0.50, 0.70 and 1.0) samples recorded at room temperature are shown in Fig. 5.1. It is observed that due to the substitution of Y^{3+} ions, the diffraction peaks shift systematically towards the higher 2θ value. The shifting of (112) peak towards higher 2θ value with increase in Y concentration is shown in the inset of Fig. 5.1. The above shift indicates the reduction in lattice constant values as the Y – concentration is increased. All the XRD patterns were analyzed by the Rietveld refinement method using the FULLPROF software by choosing *Pbnm* space group *i.e.* with orthorhombic structure. Typical XRD patterns of x = 0, 0.50, and x = 1.0 samples (symbols) along with the Reitveld refined data (solid lines) are shown in Fig. 5.2. Here all the observed peaks are refined suggesting the single phase nature of the samples. Similar refinements were carried for other samples also. The estimated values of lattice parameters of $GdCrO_3$ (x = 0) sample are found to be a = 5.3129(2) Å, b = 5.5211(2) Å, and c = 7.6039(2) Å which are comparable to the previously reported values [13]. The reliability factors, lattice parameters and volume of the unit cell obtained from the refinement of all samples are given in Table 5.1. The lattice parameters a, c and the volume of the unit cell are found to decrease with increase in Y concentration as shown in Fig. 5.3. However, no significant variation of b with x is seen. The systematic decrease in lattice parameters can be attributed to the substitution of smaller Y^{3+} (1.019 Å, coordination number (CN) = 8) ions at the Gd^{3+} (1.053 Å, CN=8) site. Substitution of smaller ions introduce a distortion in the lattice which can be analysed by calculating the Goldschmidt tolerance factor (t) using the relation, $t = \frac{r_A + r_O}{\sqrt{2}\,(r_B + r_O)}$, where r_A, r_B and r_O are the average ionic radii of A site ion, B site ion and oxygen ion respectively [21]. It is found that the tolerance factor (t) decreases from 0.859 (x = 0) to 0.848 (x = 1.0) with increase in x value and it indicates the decrease in stability of the lattice and its deviation from the ideal cubic perovskite structure.

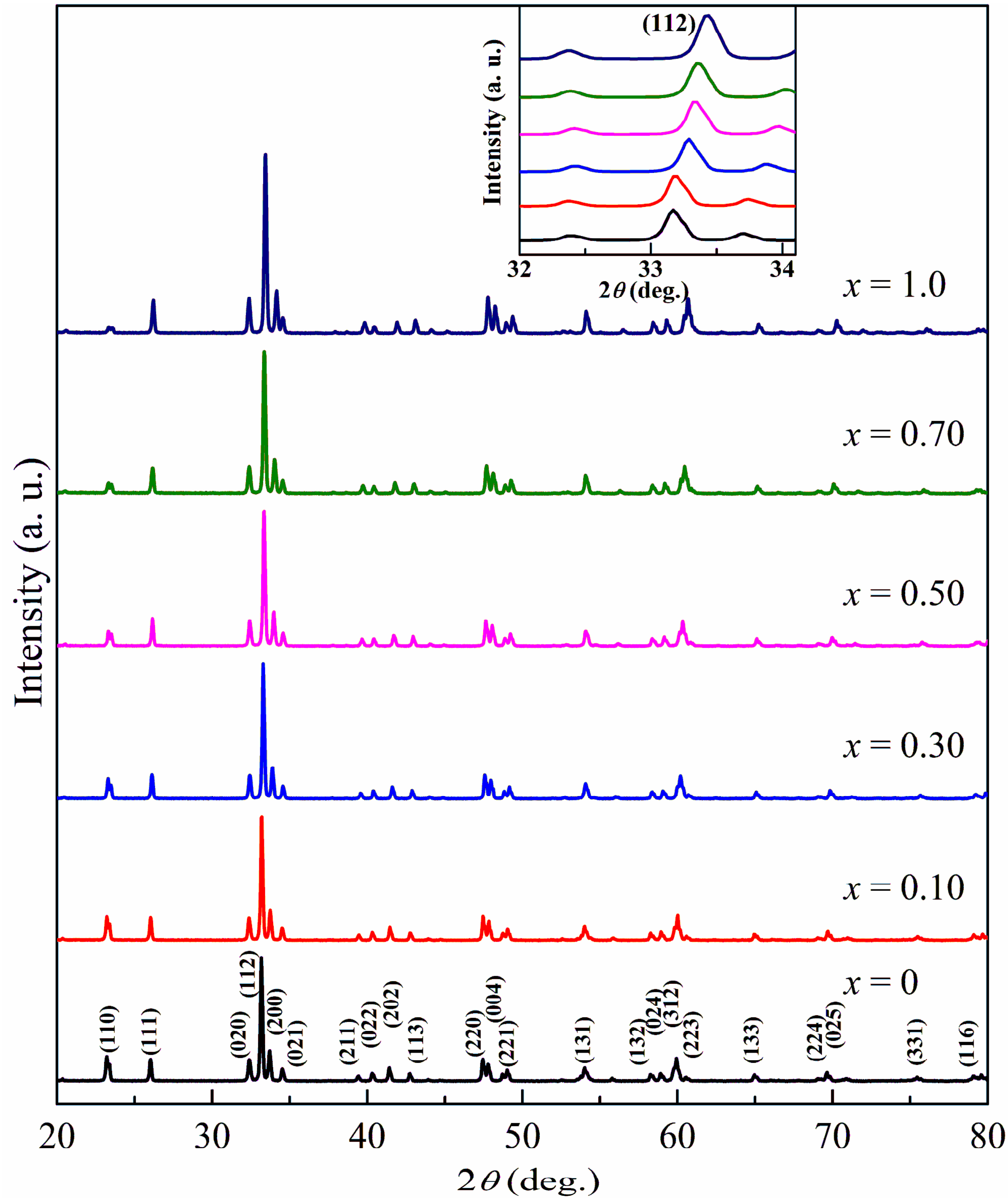

Figure 5.1: X- ray diffraction patterns of $Gd_{1-x}Y_xCrO_3$ ($x = 0 – 1.0$) samples. The inset shows the enlarged view of (112) peak of various samples.

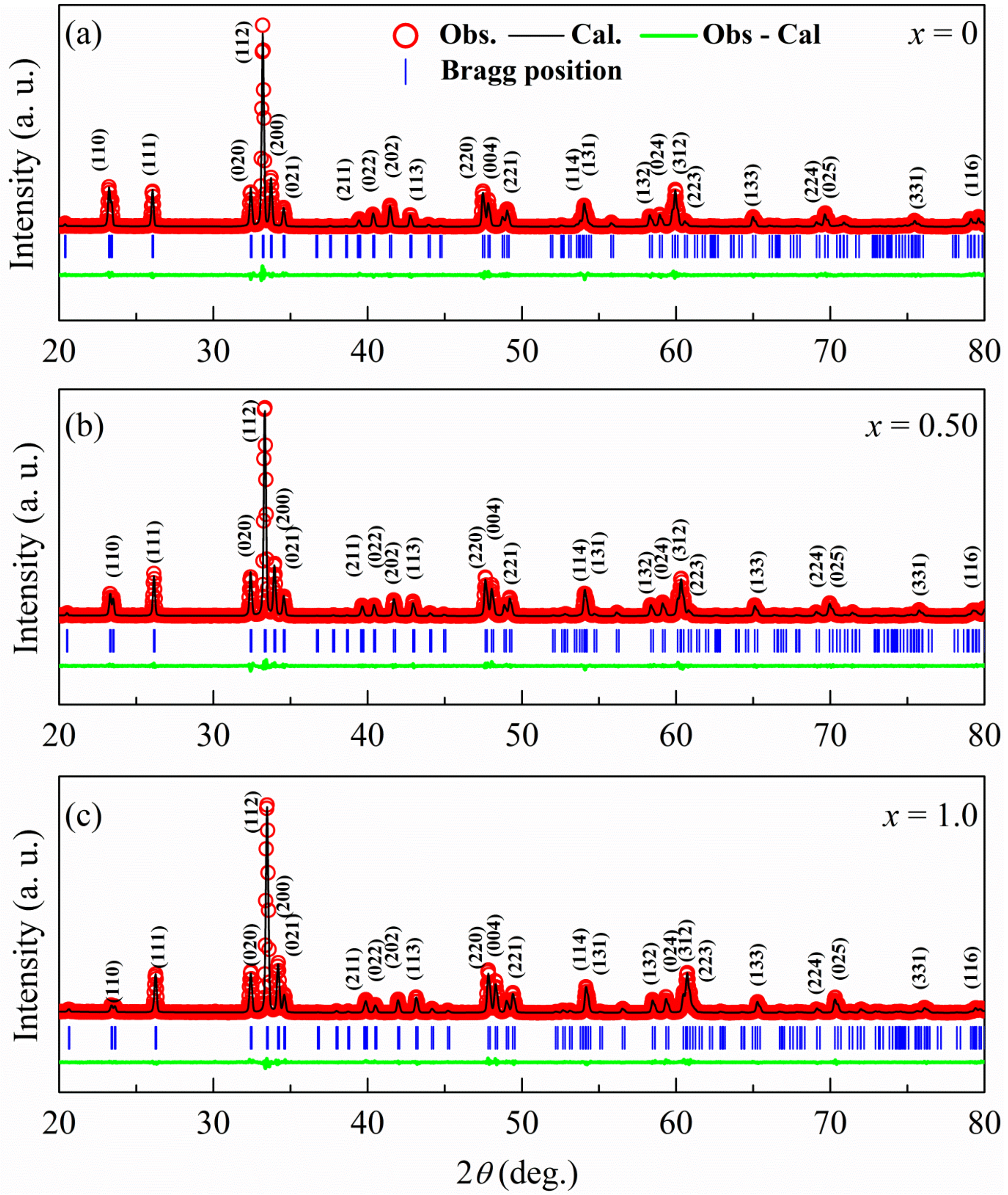

Figure 5.2: XRD patterns of x = 0, 0.50 and 1.0 samples along with their Rietveld refinement. The circles represent the experimental points and solid line (black) represents refined data. The bottom line (green) shows the difference between experimental and refined data. The vertical lines (blue) are allowed Bragg position.

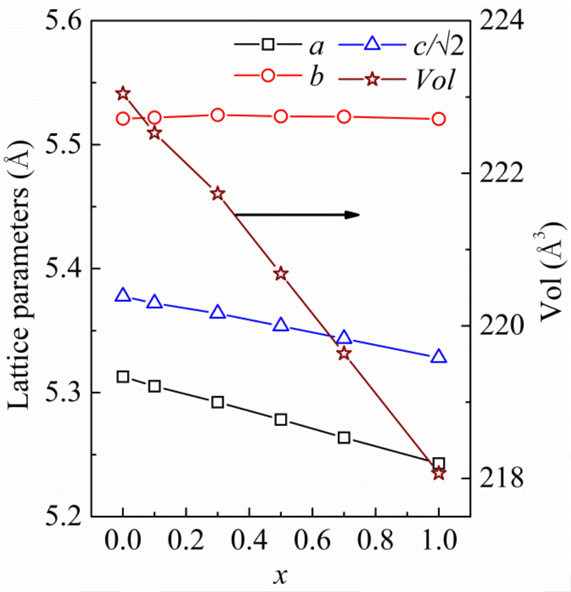

Figure 5.3: Variation of lattice parameters *a*, *b*, *c*, and unit cell volume (*Vol*) of $Gd_{1-x}Y_xCrO_3$ ($x = 0 – 1.0$) samples as a function of Y concentration (x).

Table 5.1: Parameters obtained from the Rietveld analysis of the samples $Gd_{1-x}Y_xCrO_3$ ($x = 0$ to 1.0).

Sample/ Parameters	$x = 0$	$x = 0.10$	$x = 0.30$	$x = 0.50$	$x = 0.70$	$x = 1.0$
Space group	*Pbnm*	*Pbnm*	*Pbnm*	*Pbnm*	*Pbnm*	*Pbnm*
***a* (Å)**	5.3129(2)	5.3052(2)	5.2924(1)	5.2783(2)	5.2637(2)	5.2428(2)
***b* (Å)**	5.5211(2)	5.5219(2)	5.5239(2)	5.5229(3)	5.5226(2)	5.5208(2)
***c* (Å)**	7.6039(2)	7.5960(2)	7.5864(2)	7.5702(2)	7.5557(2)	7.5339(3)
Volume(Å^3)	223.04(1)	222.53(1)	221.73(1)	220.68(2)	219.63(1)	218.06(1)
R_F (%)	2.2	2.8	2.2	2.1	1.9	2.1
R_{Bragg} (%)	2.2	3.0	2.3	2.2	1.9	2.6
R_P (%)	9.5	10.2	7.2	6.9	6.5	7.6
R_{exp} (%)	8.4	8.3	8.1	7.9	6.4	6.0
χ^2	2.2	2.3	2.4	2.2	2.1	2.4
Gd/Y/Cr Occupancy	1.005/0.000 /0.996	0.865/0.155 /1.003	0.702/0.329 /0.996	0.500/0.499 /1.000	0.297/0.699 /1.000	0.0/1.006 /1.000

Raman spectroscopy is an important tool to study the evolution of the crystal structure and the structural distortions. Raman spectra of parent compound along with Y substituted samples were recorded at room temperature and they are shown in Fig. 5.4. According to group theoretical calculation, RCrO$_3$ compounds having the orthorhombic crystal structure with *Pbnm* space group exhibit 24 Raman active modes, $\Gamma_{\text{Raman}} = 7A_g + 5B_{1g} + 7B_{2g} + 5B_{3g}$ [141]. In the present case, parent compound GdCrO$_3$ (x = 0) exhibits eight prominent Raman modes at ~ 141, 159, 255, 284, 325, 390, 477 and 568 cm^{-1} and they are consistent with the previous report [142]. The two sharp and intense Raman modes observed below 200 cm^{-1} are assigned to $A_g(2)$ and $B_{2g}(1)$ modes and are associated with the atomic vibration of the A - site cation. In between 200 to 380 cm^{-1} four phonon modes namely $B_{1g}(1)$, $A_g(3)$, $B_{2g}(2)$ and $A_g(4)$ with almost similar intensities are observed. The doublets $B_{1g}(1)$ and $A_g(3)$ at 245.2 cm^{-1} and 254.8 cm^{-1} respectively are mainly affected by the change in the mass of the A site cation whereas the well separated $B_{2g}(2)$ and $A_g(4)$ phonon modes are sensitive to change in the ionic radius of the A - site ion. In the spectral range of 350 cm^{-1} to 500 cm^{-1} two modes corresponding to $A_g(5)$ and $A_g(6)$ are observed and they give information about the structural distortion associated with CrO$_6$ octahedra. Around the wave number of 560 cm^{-1}, a broad hump consisting of two closely separated modes, $A_g(7)$ and $B_{3g}(3)$ are observed and these modes are mainly associated with the stretching vibrations of the CrO$_6$ octahedra.

From the Raman spectra of the substituted samples (Fig. 5.4) it can be seen that substitution of Y ions brings a significant change in the position of the phonon modes. The first two phonon modes A_g and B_{2g} below 200 cm^{-1} start shifting towards higher wave number with increase in Y concentration and this is due to the substitution of lighter Y atom in place of heavier Gd atom [142]. The four phonon modes, $B_{1g}(1)$, $A_g(3)$, $B_{2g}(2)$ and $A_g(4)$ also shift towards the higher wave number due to the decrease in the average ionic radii of A site cation. The single A_g (5) mode of x = 0 sample at 380 cm^{-1} starts splitting into two well separated peaks with Y substitution and the newly observed mode is assigned to B_{1g} (2) symmetry. The splitting of A_g (5) mode is also reported by Weber *et al.* [142] in RCrO$_3$ perovskites and it is ascribed to the rare earth (R^{3+}) ions having different ionic radii. From Fig. 5.4, we can see a significant shift in the position of A_g (5) mode towards higher wave number upon Y^{3+} substitution and it can be attributed to the distortion in the CrO$_6$ octahedra.

No appreciable change in the position of A$_g$(7) and B$_{3g}$(3) modes is observed with increase in x. The presence of a systematic variation in the XRD patterns and Raman spectra indicates a successful substitution of Gd by Y ions without any noticeable extra phase.

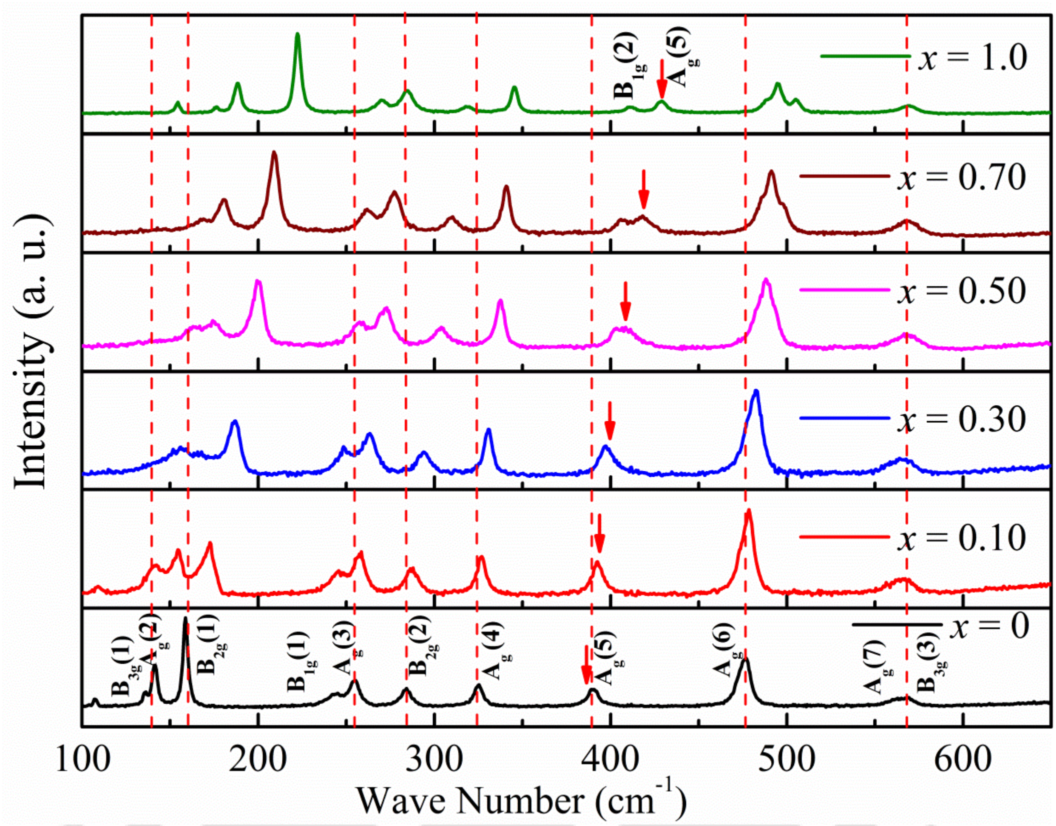

Figure 5.4: Raman Spectra of Gd$_{1-x}$Y$_x$CrO$_3$ samples for x = 0 to 1.0 measured at room temperature. Arrows indicate the blue shifting and the splitting of A$_g$(5) mode.

Figure 5.5 shows the FESEM images of x = 0, 0.30, 0.70, and 1.0 samples along with the EDS spectrum of x = 0.30 and 0.70 samples. The images show that the particles are uniformly distributed with a considerable porosity. The average grain size was determined using the ImageJ software. There is no appreciable change in the size of grain due to Y substitution and the average grain size for x = 0, 0.30, 0.70 and 1.0 samples are found to be 482 nm, 466 nm, 509 nm and 468 nm respectively**.** The values of cationic ratio Gd: Y: Cr obtained from the EDS spectra for x = 0, 0.30, 0.70, and 1.0 samples are found to be 0.98:0.0:1.00, 0.70:0.28:1.00, 0.31:0.65:1.00 and 0.0:0.91:1.00 respectively and they are in agreement with the respective nominal starting compositions.

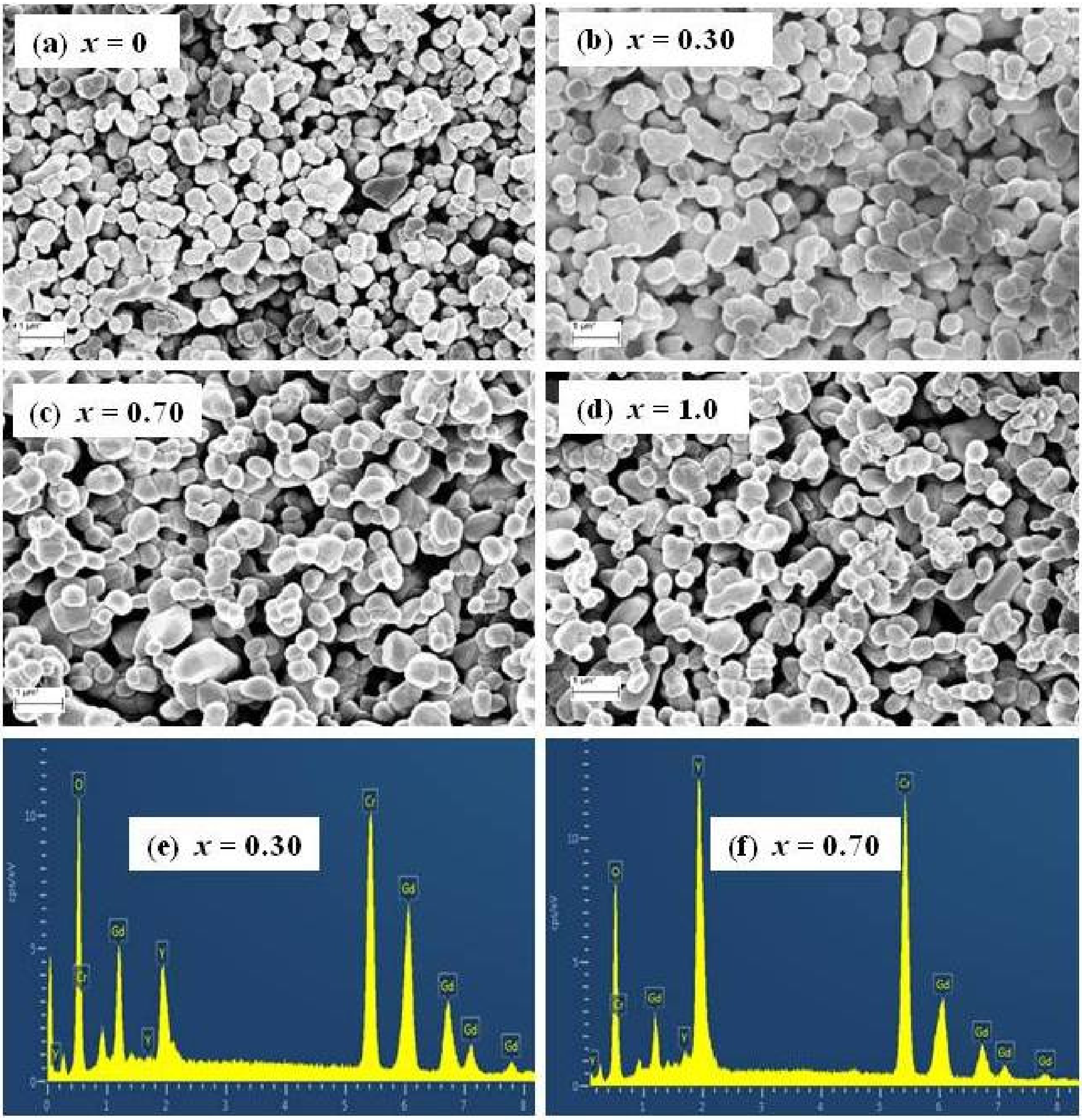

Figure 5.5: FESEM micrographs of (a) x = 0, (b) x = 0.30, (c) x = 0.70 and (d) x = 1.0 samples along with the EDS spectrum of (e) x = 0.30 and (f) x = 0.70 samples.

5.1.3 Magnetic Properties

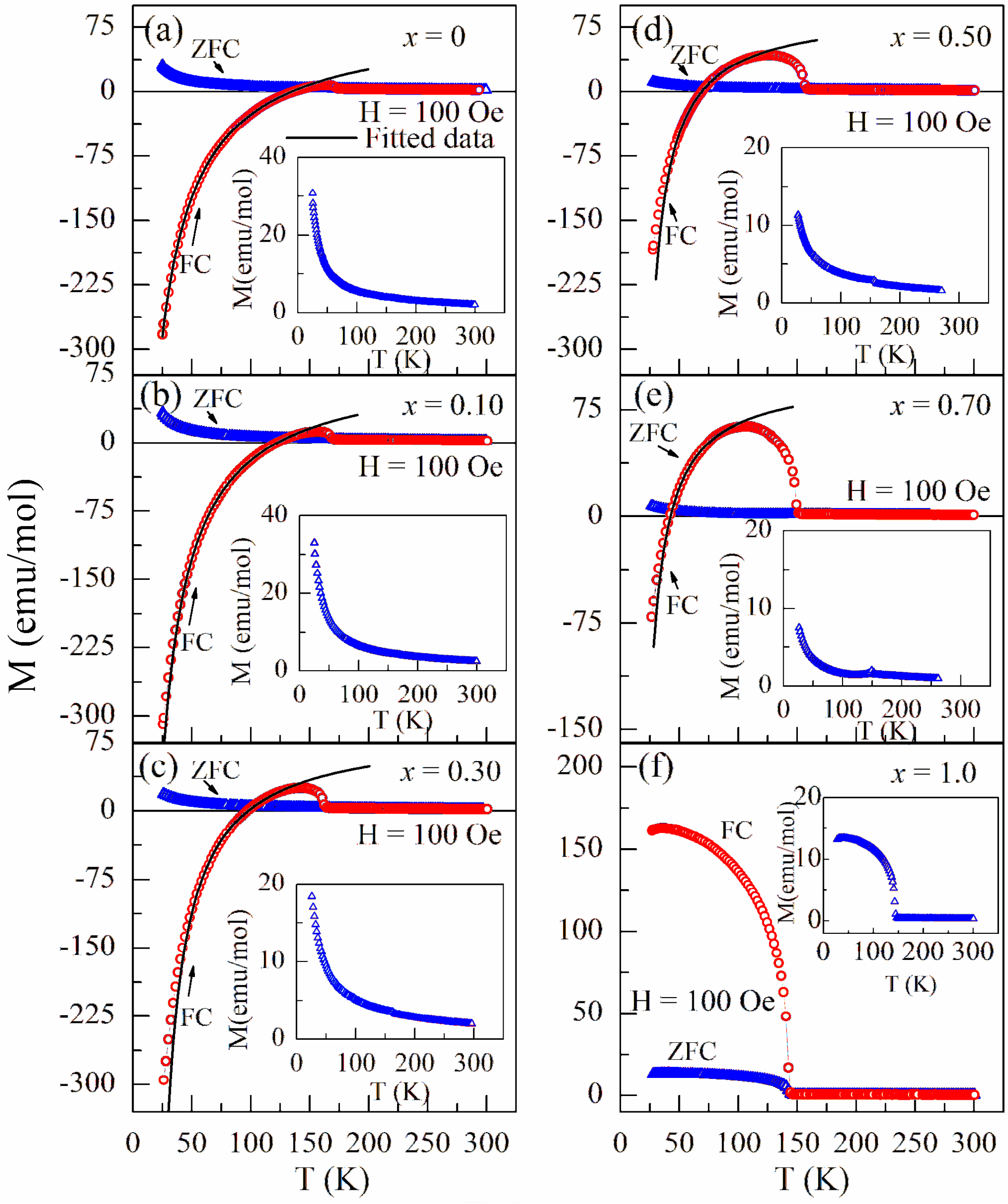

Figure 5.6: *M*-*T* curves of (a) $x = 0$, (b) $x = 0.10$, (c) $x = 0.30$, (d) $x = 0.50$, (e) $x = 0.70$ and (f) $x = 1.0$ samples measured in zero field cooled (ZFC) and field cooled (FC) conditions with an applied field of $H = 100$ Oe. The solid black lines represent the fitted data. Insets show the expanded view of the ZFC magnetization data measured at $H = 100$ Oe.

Figure 5.6 shows the temperature (*T*) variations of magnetization (*M*) measured in the ZFC and FC conditions for $x = 0$ - 1.0 samples for an applied field of $H = 100$ Oe. The parent compound, $x = 0$ shows paramagnetic to antiferromagnetic transition at $T_N = 174$ K (taken as the point of separation between the ZFC and FC curves). The T_N values of substituted samples are given in Table 5.2 and it is found to decrease with increase in Y- concentration such that for $x = 1.0$ it is reduced to 142 K. The decrease in T_N value is attributed to the weakening of superexchange interaction in Cr^{3+} - O^{2-} - Cr^{3+} networks due to lattice distortion induced by Y substitution.

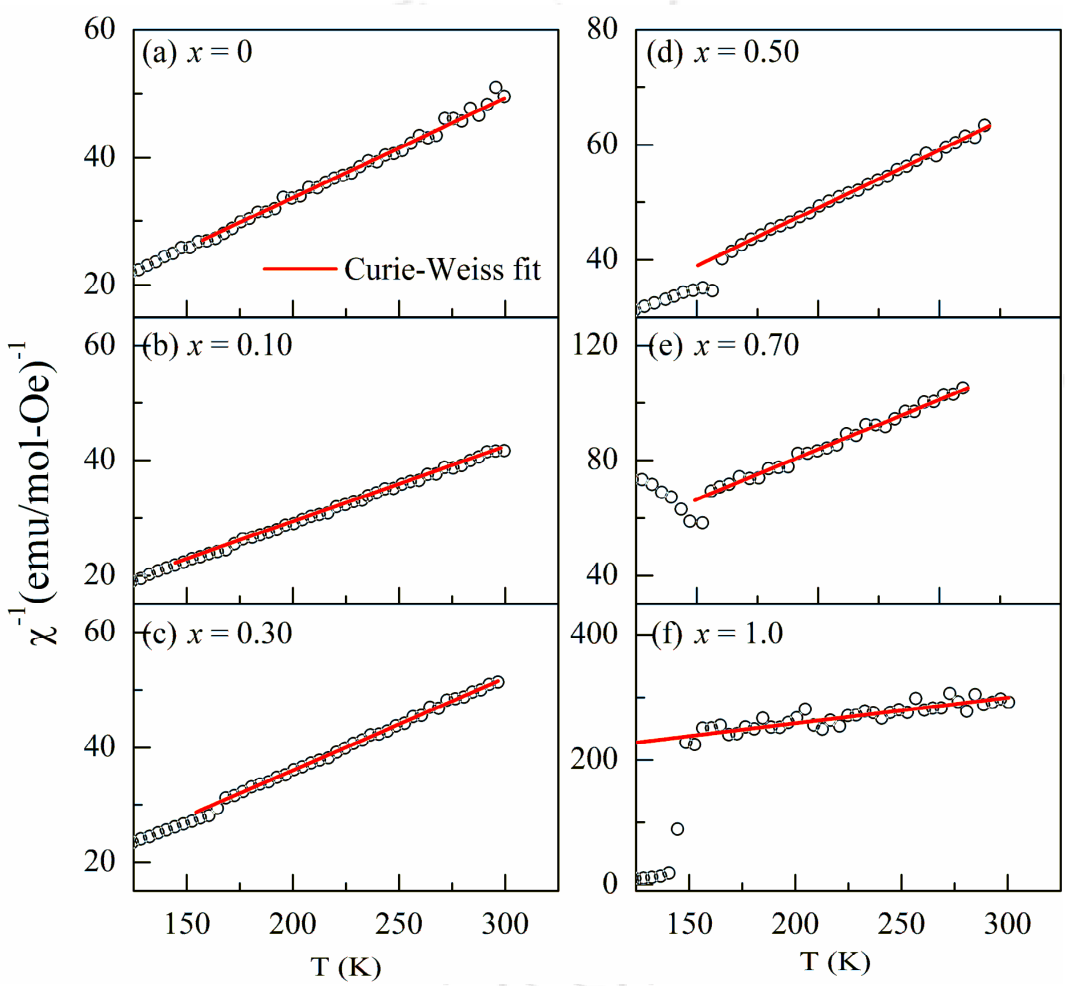

Figure 5.7: Inverse susceptibility (χ^{-1}) as a function of temperature for (a) $x = 0$, (b) $x = 0.10$, (c) $x = 0.30$, (d) $x = 0.50$, (e) $x = 0.70$ and (f) $x = 1.0$ samples. The solid line (red) represents the fitting to the Curie-Weiss (CW) law.

The inverse susceptibility ($1/\chi$) as a function of temperature in the PM region ($T > T_N$), was analyzed in terms of Curie-Weiss law, $\chi = C/(T - \theta)$ by taking C and θ as free parameters of the fit. The plots of χ^{-1} vs. T along with the CW fit are shown in Fig. 5.7. The experimental values of effective magnetic moment (μ_{eff}^{exp}) were estimated from the fitted Curie constant (*C*) values by using the relation $C = \frac{N\mu_{eff}^2}{3k_B}$, where *N* stands for Avogadro's number and k_B is the Boltzmann constant. The theoretical effective magnetic moment values for various samples were estimated using the relation, $\mu_{eff}^{Th} = [(1-x)\mu_{Gd}^2 + \mu_{Cr}^2]^{1/2}$ where μ_{Gd}, and μ_{Cr} correspond to spin only magnetic moments of Gd^{3+} and Cr^{3+} ions respectively. The values of experimental effective moments obtained from the Curie Weiss fit for x = 0, 0.10, 0.30, 0.50 0.70 and 1.0 samples are 7.37 μ$_B$, 7.99 μ$_B$, 7.17 μ$_B$, 6.46 μ$_B$, 4.94 μ$_B$ and 4.60 μ$_B$ respectively. Their corresponding theoretical values are calculated to be 8.83 μ$_B$, 8.46 μ$_B$, 7.69 μ$_B$, 6.82 μ$_B$, 5.87 μ$_B$ and 3.87 μ$_B$ respectively. In both cases, they are found to decrease with increase in Y concentration and they are mostly comparable to each other. The experimental μ_{eff}^{exp} values of x = 0 and x = 0.10 samples are found to be relatively smaller than those of the theoretical values and it can be attributed to their relatively larger T_N values. So, there is a possibility that some of the Cr^{3+} ions are engaged in the AFM interaction in the temperature range where the Curie-Weiss law fit was carried out. The Curie temperature (θ) obtained from the fitting for x = 0 to x = 0.70 samples lie in the range of -33 K to -55 K. However, for x = 1.0 it is found to be -465 K. This can be understood in terms of dominant paramagnetic moment of Gd^{3+} ions except for x = 1.0 sample.

From Fig. 5.6(a), it can be seen that the magnetization (*M*) of x = 0 sample measured in the ZFC mode is found to increase as the temperature is lowered below its T_N like a typical paramagnet due to the presence of magnetic Gd^{3+} ions. Similar behavior is observed in Y-substituted samples as shown in the inset of Fig. 5.6(b - e). However, the magnitude of ZFC magnetization at a given temperature is found to decrease with increase in Y – concentration due to the substitution of non magnetic Y^{3+} ions at Gd^{3+} site. In the case of x = 1.0 sample, the magnetization in the ZFC mode (Fig. 5.6(f)) tends to saturate for $T < T_N$ indicating the presence of weak ferromagnetic component. The FC magnetization of x = 0 sample shows a considerable irreversibility with a plateau like behavior below T_N due to the presence of weak FM moment from the canted Cr^{3+} ions. A maximum magnetization (M_{max}) of 7 emu/mol is observed at T_{max} = 163 K. For $T < T_{max}$, the FC magnetization decreases towards the negative value by crossing the temperature axis (M = 0) at a compensation temperature (T_{comp}) of 136 K. Such a behavior of change in polarity of *M* with the change in temperature is known as negative magnetization or temperature induced magnetization reversal. The FC magnetization curves of Y substituted samples with x = 0.10, 0.30, 0.50 and x = 0.70 measured at H = 100 Oe are shown in Fig 5.6(b - e). All these samples exhibit the magnetization reversal similar to that of the parent compound (x = 0) but with lower T_{comp} values which are given in Table 5.2. The compensation temperature falls from 136 K (x = 0) to 42 K (x = 0.70). Moreover, M_{max} value in the vicinity of T_N is found to increase with increase in Y concentration. A decrease in the maximum negative magnetization value from -280 emu/mol for x = 0 to -75 emu /mol for x = 0.70 is observed which indicates the role of magnetic Gd^{3+} ions for the negative magnetization. No magnetization reversal is observed for x = 1.0 sample during the FC mode.

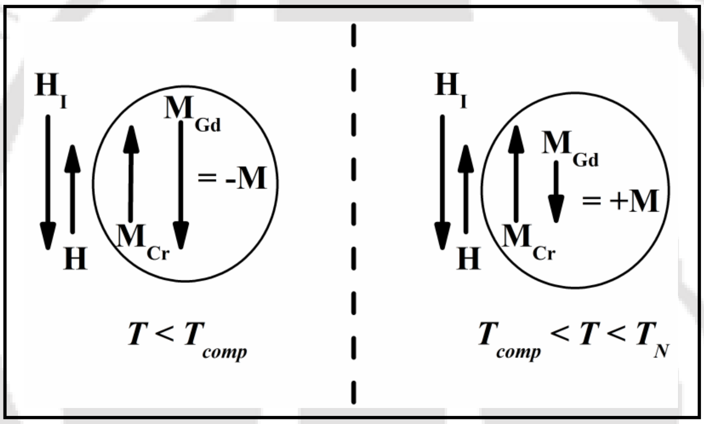

Figure 5.8: Schematic diagram showing the orientation of weak FM component of Cr^{3+} (M_{Cr}) and the net PM moment of Gd^{3+} ions (M_{Gd}) above and below the compensation temperature (T_{comp}).

The origin of negative magnetization in the present Gd$_{1-x}$Y$_x$CrO$_3$ (x = 0 – 0.70) samples can be explained by considering the competition between the weak ferromagnetic component of the canted Cr^{3+} ions (M_{Cr}) and the paramagnetic moment of Gd^{3+} ions (M_{Gd}) and their different temperature dependences under the influence of negative internal field (H_I) from AFM ordered Cr^{3+} ions. Similar MR behavior is recently reported in rare earth manganite such as (Nd$_{0.50}$Gd$_{0.50}$)$_{0.55}$Sr$_{0.45}$MnO$_3$ and GdNi$_{0.30}$Mn$_{0.70}$O$_3$ where the origin of MR is explained by considering that Gd^{3+} ions act as paramagnetic spins reacting to the internal field [154,155]. However, the ferromagnetic ordering of R^{3+} ions at low temperature (< 20 K) and its antiferromagnetic coupling with the weak FM component of transition metal ions is also reported to give rise to MR especially at low temperature [85,156]. Based on the above discussion a schematic diagram of competing weak FM and PM moments under negative internal field for $T < T_{comp}$ and $T > T_{comp}$ are shown in Fig. 5.8. Considering this fact, the temperature dependent FC magnetization (M) data obtained at an applied field of H were fitted to the following equation [12]

$$M = M_{Cr} + \frac{C(H_I + H)}{T - \theta_C} \tag{5.1}$$

where, C and θ_C represent the Curie-Weiss constant of paramagnetic Gd^{3+} ion and Curie temperature respectively. The fitted data are shown as solid line in Fig. 5.6 for $T < T_{max}$ and they clearly follow the experimental data. The values of θ_C, M_{Cr} and H_I were estimated by fitting the FC magnetization data of $x = 0 - 0.70$ samples to eq. 5.1 and are given in Table 5.2. The Curie temperature (θ_C) values obtained from the fitting lie in the range of -7 K to +1.3 K. The magnitude of negative internal field $|H_I|$ is found to decrease from 1.6 kOe to 1.3 kOe with the increase in Y– concentration, whereas the M_{Cr} value increases from 82 emu/mol ($x = 0$) to 99 emu/mol ($x = 0.70$). The increase in Y concentration having smaller ionic size is expected to introduce distortion in the lattice and such distortion in CrO$_6$ octahedra would give rise to enhanced spin canting of Cr^{3+} ions. So, the spin canted weak FM component M_{Cr} increases with increase in Y concentration. As a result, the T_{comp} value is further reduced. The above fact is clearly reflected in the FC magnetization of $x = 1.0$ sample (Fig. 5.6(f)), where no magnetization reversal is observed. The decrease in the magnitude of internal field with increase in Y – concentration is ascribed to the weakening of superexchange in Cr^{3+} – O^{2-} – Cr^{3+} networks as a result of lattice distortion introduced by the substitution of Y^{3+} ions.

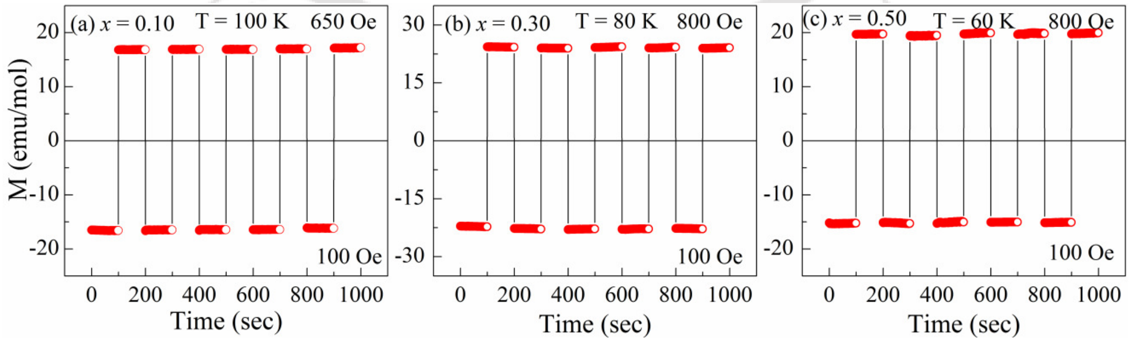

Figure 5.9: Magnetization switching between negative and positive values under different positive magnetic fields for (a) $x = 0.10$ (b) $x = 0.30$ and (c) $x = 0.50$ samples at $T = 100$ K, 80 K and $T = 60$ K respectively.

For a clear demonstration of magnetization reversal, the bipolar switching of magnetization by the application of external magnetic field has been performed below the T_{comp}. The samples were first cooled through their T_N in the FC mode for an applied field of H = 100 Oe to a desired temperature, T (< T_{comp}). Then at the fixed positive field of 100 Oe, magnetization was measured as a function of time and it is found to be negative as shown in Fig. 5.9 for x = 0.10, 0.30 and 0.50 samples. Then the field was increased to higher positive field to flip the moment from negative to an equivalent and a positive value. Now keeping the temperature fixed, this procedure was repeated for several cycles in order to see the reproducibility of field induced magnetization reversal. The result shows that the polarity of M can be switched between positive and negative values just by changing the magnitude of the external field while keeping its direction fixed.

Table 5.2: The AFM transition temperature (T_N), magnetic compensation temperature (T_{comp}) and parameters obtained from the fitting to FC magnetization data using eq. 5.1 at an external field of H = 100 Oe for $Gd_{1-x}Y_xCrO_3$ samples.

Samples/ Parameters	$x = 0$	$x = 0.10$	$x = 0.30$	$x = 0.50$	$x = 0.70$	$x = 1.0$
T_N **(K)**	174±1	168±1	162±2	158±1	152±1	142±1
T_{comp} **(K)**	136±1	122±1	97±1	69±1	42±1	--
θ_C **(K)**	-6.6±0.2	-2.5±0.5	0.8±0.2	1.2±0.4	1.3±0.4	--
M_{Cr} **(emu/mol)**	82±1	84±1	89±2	94±1	99±1	--
H_I **(kOe)**	-1.6±0.1	-1.5±0.2	-1.5±0.1	-1.4±0.1	-1.3±0.1	--

In order to further understand the magnetic behavior of the $Gd_{1-x}Y_xCrO_3$ samples, isothermal M-H loops were recorded at selected temperature for all samples under ZFC condition. Representative M-H loops of all samples measured at T = 25 K in ZFC mode are shown in Fig. 5.10. The linear part is thought to consist of the moments of paramagnetic rare earth sublattice and the pure AFM contribution from the Cr^{3+} sublattice. The weak ferromagnetic contribution comes from the canting of Cr^{3+} moments. However, the M varies almost linearly with H for $x = 0.70$ sample at $T = 25$ K implying the dominant AFM nature of the sample whereas the M-H loop of $x = 1.0$ is found to be highly elliptical in nature due to the limitation of maximum field in the experimental setup. To look for possible exchange bias behavior we have recorded M-H loops under FC condition with a cooling field of H_{FC} = 3000 Oe. These field cooled M-H loops were recorded at several temperatures in the range of 25 K to 200 K *i.e.* for $T < T_N$. For measuring the isothermal M-H loops under FC condition, the sample was first cooled down through T_N under 3 kOe field before every measurement at a desired temperature.

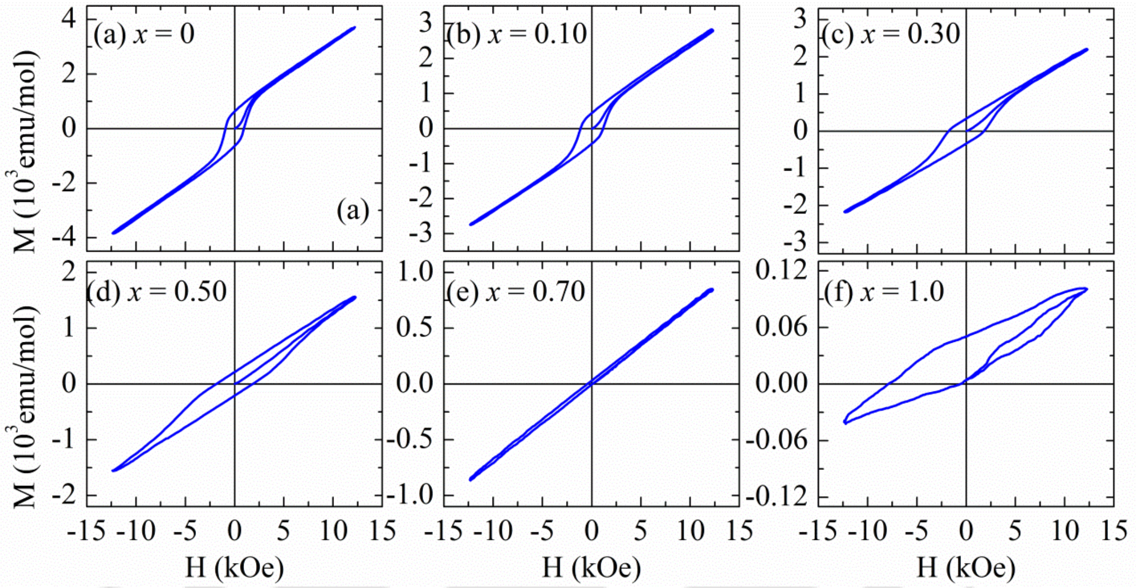

Figure 5.10: M-H loops recorded at $T = 25$ K under zero field condition (ZFC) for $x = 0$ – 1.0 samples.

Typical M-H loops (expanded scale), under FC condition (H = 3000 Oe), recorded at a few selected temperatures for $x = 0$ and 0.10 are shown in Fig. 5.11 while for $x = 0.30$ and $x = 0.50$ samples are shown in Fig. 5.12. The asymmetrical behavior of the measured M-H loops hints about the presence of exchange bias behavior. The $M – H$ loops are found to shift towards positive field axis at lower temperature ($T < T_{comp}$) and negative field axis at higher temperature ($T > T_{comp}$) suggesting the presence of both positive and negative EB in the system and their tunability with temperature. Quantitatively the exchange bias fields were determined using the relation $H_{EB} = (H_+ + H_-)/2$, where H_+ and H_- stand for positive and negative coercive fields, respectively. The effective coercive field H_C^{eff} was obtained using the relation $H_C^{eff} = (H_+ - H_-)/2$.

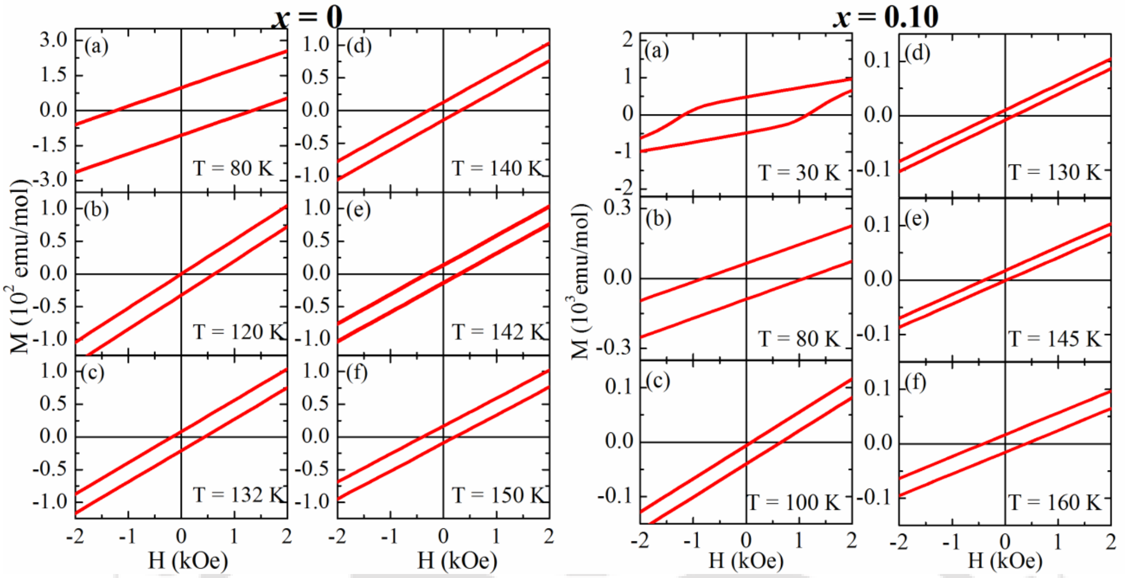

Figure 5.11: (a) – (f) Enlarged view of *M-H* loops in the vicinity of coercive fields measured under the field cooled condition for H = 3 kOe at different temperatures for x = 0 and x = 0.10 samples.

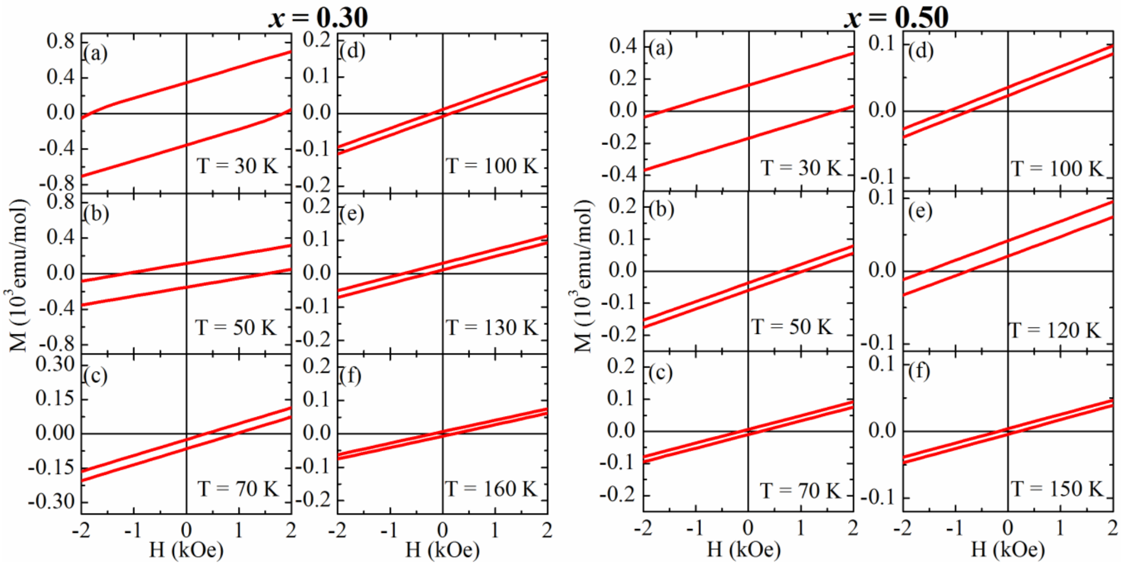

Figure 5.12: (a) – (f) Enlarged view of *M-H* loops in the vicinity of coercive fields measured under the field cooled condition for H = 3 kOe at different temperatures for x = 0.30 and x = 0.50 samples.

The temperature dependence of H_{EB} and H_C^{eff} obtained from isothermal magnetization measurements under FC conditions for x = 0, 0.10, 0.30 and 0.50 samples are shown in Fig. 5.13 (a & b). For all samples, the H_{EB} field is found to be negative in the temperature range of $T_{comp} < T < T_N$ and its magnitude increases as the temperature falls below T_N and attains a maximum negative value and then falls towards zero as T approaches T_{comp}. For further decrease in temperature ($T < T_{comp}$), the H_{EB} increase towards a maximum positive value followed by sharp fall towards zero. As can be seen from the Fig. 5.13(a), the magnitude of both positive and negative peak of H_{EB}, systematically increases with increase in x. The largest positive value of H_{EB} = 836 Oe and negative value of H_{EB} = -1167 Oe are obtained for x = 0.50 sample at T = 50 K and 120 K respectively. The temperature dependence of H_C^{eff} plots for x = 0 – 0.50 (Fig. 5.13(b)) samples show two peaks on either side of the T_{comp} with a minimum value at $T = T_{comp}$.

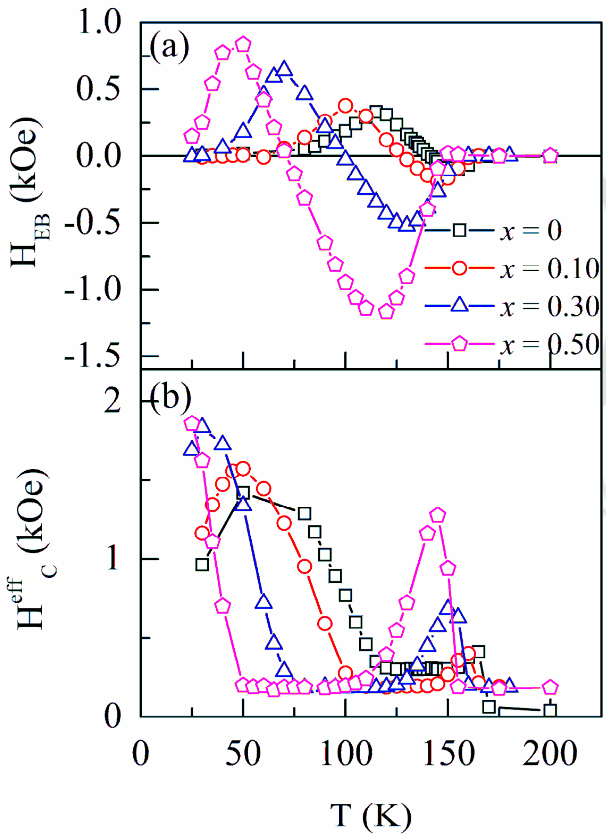

Figure 5.13: The temperature dependence of (a) exchange bias field, H_{EB} (upper panel) and (b) effective coercive field, H_C^{eff} (lower panel) for Gd$_{1-x}$Y$_x$CrO$_3$ samples with x = 0, x = 0.10, x = 0.30 and x = 0.50 samples measured under a cooling field of H = 3 kOe.

Such a reversal in the sign of H_{EB} across the T_{comp} along with the signature of two peaks of H_C^{eff} are reported in intermetallic alloys $Sm_{0.98}Gd_{0.02}Al_2$ and $Nd_{0.75}Ho_{0.25}Al_2$ [55,157], orthochromites $LaCr_{0.85}Mn_{0.15}CrO_3$ [94] and $TmCrO_3$ [158]. Yoshii *et al.* have studied EB in a similar orthochromite, $La_{1-x}Pr_xCrO_3$ [96] where they have reported a positive H_{EB} for $T < T_{comp}$ for H_{FC} = 3 kOe which is consistent with the present result. In a recent report on another isostructural orthochromite $Dy_{1-x}Nd_xCrO_3$ [159], only negative H_{EB} is observed which does not change its sign either with the change in the temperature or with the external cooling field.

The samples $x = 0 - 0.50$ exhibit the temperature driven MR due to competition between M_{Cr} and M_{Gd} and the state of magnetization at any temperature T is determined from the dominance of one moment over the other as the temperature is varied. Thus, the observed sign reversal of H_{EB} with change in temperature for $x = 0 - 0.50$ samples, can be explained by considering the competition between the FM component of Cr^{3+} moment (M_{Cr}) arising from the canting with that of the paramagnetic moment of Gd^{3+} ions (M_{Gd}) under the influence of negative internal field, H_I. The sign reversal of H_{EB} is due to the dominance of one of the above moments over the other as the temperature is decreased from T_N. As mentioned earlier in the text that in the temperature range of $T_{comp} < T < T_N$ the strength of M_{Cr} dominates over the paramagnetic moment of M_{Gd} and their antiparallel alignment results in a net positive magnetization along the direction of the applied field, H. As a result, an additional negative field is required to bring the magnetization to zero, which effectively shifts the loop to the negative side of field axis giving rise to negative EB. While in the temperature of $T < T_{comp}$, the strength of the PM moment M_{Gd} which lies opposite to H (at low fields) gets enhanced with decrease in temperature and exceeds the M_{Cr} resulting a net negative moment opposite to the direction of applied field H. This requires a larger positive coercive field during demagnetization to reverse the direction of magnetization which results a shift in the M-H loop towards the positive field axis giving positive exchange bias. At $T \sim T_{comp}$ the two competing moments M_{Cr} and M_{Gd} become equal and opposite resulting into zero magnetization which leads to H_{EB} and H_C^{eff} approaching close to zero.

5.2 Conclusions

The effect of non magnetic Y^{3+} ion substitution at the Gd site of $GdCrO_3$ is studied in this chapter.

Polycrystalline samples of $Gd_{1-x}Y_xCrO_3$ (x = 0.0 – 1.0) were prepared using the sol-gel method. Phase purity of the prepared samples was confirmed from the XRD patterns and the samples are found to crystallize in orthorhombic symmetry. The lattice parameters obtained from the Rietveld refinement are found to decrease with increase in doping concentration. The temperature dependence of magnetization reveals a systematic fall in AFM transition temperature (T_N) from 174 K for x = 0 to 142 K for x = 1.0 as a result of weakening of the superexchange interaction. Interesting temperature induced magnetization reversal is observed in the parent as well as in Y substituted samples upto x = 0.70 and the compensation temperature is found to decrease from 136 K for x = 0 to 42 K for x = 0.70. Tunable exchange bias is observed which changes its polarity across the magnetic compensation temperature. The origin of magnetization reversal and tunable exchange bias is explained on the basis of competition between the weak FM moment of Cr^{3+} ions and the paramagnetic moment of Gd^{3+} ions under the influence of negative internal field (H_I) from AFM ordered Cr^{3+} ions. Bipolar switching of magnetization is demonstrated by just changing the magnitude of the magnetic field but keeping the direction of the magnetic fixed.

Chapter 6

Conclusions

This chapter provides the summary of conclusions drawn from the analysis of structural and magnetic properties of transition elements (Mn and Fe) and Y substituted $SmCrO_3$ and $GdCrO_3$ series.

Single phase samples of Mn substituted $SmCrO_3$ *i.e.* $SmCr_{1-x}Mn_xO_3$ ($x = 0.0 – 0.50$) have been prepared successfully using the standard sol-gel route and the samples are found to crystallize in orthorhombic structure with *Pbnm* space group. The lattice parameters and volume of the unit cell increase with increase in Mn concentration and it is ascribed to the replacement of smaller Cr^{3+} ions by larger Mn^{3+} ions. Similarly, the Fe substituted $SmCrO_3$ have also been prepared in single phase form and they are also found to crystallize in orthorhombic structure with *Pbnm* space group.

The temperature dependence of magnetization of $SmCr_{1-x}Mn_xO_3$ samples show AFM transitions upto $x = 0.40$ and the transition temperature (T_N) decreases from 196 K for $x = 0$ to 75 K for $x = 0.40$ samples. Ferromagnetic like behavior is observed for $x = 0.50$ sample with $T_C = 70$ K due to the possible presence of Cr^{3+} - O^{2-} - Mn^{3+} and Mn^{3+} - O^{2-} - Mn^{4+} networks. A low temperature spin reorientation transition around 40 K is observed for $x = 0 – 0.30$ samples. In addition, some of the above samples exhibit interesting temperature induced magnetization reversal with magnetic compensation temperature (T_{comp}) increasing from 51 K for $x = 0.10$ to 126 K for $x = 0.30$. In order to further understand the magnetization reversal behavior, the samples with $x = 0.10$, 0.15, 0.20 and 0.30 of $SmCr_{1-x}Mn_xO_3$ series were taken up for the detailed *M-T* measurements by varying the cooling field from 100 Oe to 2000 Oe. As the cooling field is increased, the entire *M-T* curves are found to shift towards the positive magnetization as a result of enhancement in the FM component of canted Cr^{3+} ions. The origin of magnetization reversal is explained on the basis of competition between the FM component of canted Cr^{3+} ions and the paramagnetic moments of Mn^{3+} ions and magnetic Sm^{3+} ions under the influence of negative internal field arising from the antiferromagnetically ordered Cr^{3+} ions. The negative magnetization was quantitatively analyzed by fitting the measured FC magnetization data to the relation, $M = M_{Cr} + \frac{C(H+H_I)}{(T-\theta_C)}$, where M_{Cr} represents the canted FM component of Cr^{3+} ions and H_I is the internal field due to AFM ordered Cr^{3+} ions and C and θ_C represent the Curie constant and Curie temperature respectively.

The M-H loops of $x = 0.10$ sample measured at different temperatures under FC condition ($H = 5000$ Oe) show the tunable positive and negative exchange bias fields with its sign reversal in the vicinity of magnetic compensation temperature and the exchange bias field (H_{EB}) is found to vary from -0.45 kOe to +1.85 kOe with change in temperature. The presence of EB behavior is due to the competition between the FM component of canted Cr^{3+} ions and the PM moment of Sm^{3+} ions and doped Mn^{3+} ions under the influence of negative internal field. Bora *et al.* [74] have reported similar tunable EB behavior across the T_{comp} in isostructural orthochromite such as $NdCr_{1-x}Mn_xO_3$ and the reported H_{EB} in this compound varies between -1.6 kOe and + 0.39 kOe which is comparable to the value obtained in the present sample. The maximum value of H_{EB} observed in the present sample is comparable to that of reported in $NdMnO_3$ and $La_{0.15}Pr_{0.85}CrO_3$ compounds [85,96].

In Fe substituted $SmCrO_3$ series *i.e.* $SmCr_{1-x}Fe_xO_3$ ($x = 0$ - 0.50) all samples show AFM transition and the transition temperature (T_N) initially decreases upto $x = 0.20$ and for further increase in x, the T_N value increases due to the establishment of Fe^{3+} - O^{2-} - Fe^{3+} networks. The samples with $x = 0$ to $x = 0.20$ show a low temperature spin reorientation transition around $T = 40$ K due to the change in the magnetic spin configuration of Cr^{3+} ions. Temperature induced magnetization reversal with two compensation temperature is observed during FC mode for $x = 0.10$ and 0.15 samples. The T_{comp1} value is found to increase from 75 K for $x = 0.10$ to 148 K for $x = 0.15$ sample which are higher compared to those of Mn substituted samples. The origin of MR is ascribed to the different temperature dependence of the weak FM component of canted Cr^{3+} ions and the PM component of Sm^{3+} ions and doped Fe^{3+} ions and their competition under the influence of negative internal field as the temperature is varied.

Exchange bias behavior under FC mode ($H = 5000$ Oe) is observed for $x = 0.10$ sample and the exchange bias field (H_{EB}) also undergoes sign reversal twice in the vicinity of two compensation temperatures (T_{comp1} and T_{comp2}). The observed value of H_{EB} could be tuned between 2.25 kOe and -4.94 kOe as a function of measuring temperature. The presence of EB and its sign reversal across the compensation temperature is explained in terms of competition between the FM component of canted Cr^{3+} ions and PM component of Sm^{3+} ions and substituted Fe^{3+} ions and the change in domination of one component over the other as the temperature is varied. The maximum value of H_{EB} observed in the present sample is comparable to those of reported in $La_{0.80}Ce_{0.20}CrO_3$ and $NdCr_{1-x}Fe_xO_3$ compounds which also exhibit similar tunable EB behavior [16,73]. Bipolar switching of magnetization has been demonstrated for $x = 0.10$ and $x = 0.15$ samples similar to that of Mn substituted samples.

The substitution of both Mn and Fe at Cr site of $SmCrO_3$ leads to magnetization reversal behavior. For comparison, if we take same concentration of both substitutions, say $x = 0.10$ and $x = 0.15$, the Fe substitution exhibits higher T_{comp} value compared to Mn substitution and it is due to larger paramagnetic contribution from Fe^{3+} ion (5.9 μ_B) than that of Mn^{3+} ion (4.9 μ_B). This confirms that the observed magnetization reversals are in accordance with the paramagnetic model. Sign reversal of magnetization for Mn substitution is observed upto $x = 0.30$ sample whereas in Fe substitution for $x \geq 0.20$ samples no sign reversal is observed due to possible formation of AFM Fe^{3+} - O^{2-} - Fe^{3+} networks.

Single phase polycrystalline samples of $GdCr_{1-x}Mn_xO_3$ were prepared using sol-gel method. The refinement of the room temperature XRD patterns suggests that all samples exhibit orthorhombic structure with *Pbnm* space group. The lattice parameters *a, b* and volume of the unit cell increases while the *c* value decreases with increase in Mn concentration. All samples exhibit AFM transition and the transition temperature (T_N) is found to decrease from 174 K ($x = 0$) to 91 K ($x = 0.50$). The FC magnetization plot of $x = 0$ 0.05, 0.40 and $x = 0.50$ samples show the temperature induced magnetization reversal behavior with T_{comp} of 136 K, 139 K, 29 K and 27 K respectively. Tunable EB behavior with a sign reversal of H_{EB} across the T_{comp} is observed in $x = 0$ and 0.05 samples under the FC condition ($H = 3000$ Oe) with a maximum H_{EB} of 0.35 kOe and 1.6 kOe respectively. The observed temperature induced MR in $x = 0$ and $x = 0.05$ samples is explained by considering the competition between the weak FM component of Cr^{3+} ions and the PM component of Gd^{3+} ions and substituted Mn^{3+} ions, each of them having different temperature dependences, under a negative internal field. The occurrence of EB and its sign reversal across the T_{comp} in $x = 0$ and 0.05 samples is attributed to the competition between the above two magnetic moments (M_{Cr} and PM moment) and their different temperature dependences. A tunable positive and negative EB field across the T_{comp} is also observed for $x = 0.50$ sample. Magnetization reversal in samples with $x = 0.40$ and $x = 0.50$ and the tunable EB field in $x = 0.50$ is attributed to the competing canted AFM interaction in $Cr^{3+}– O^{2-}– Cr^{3+}$ networks, collinear AFM interaction in $Mn^{3+}– O^{2-} – Mn^{3+}$ networks and the PM moments of host Gd^{3+} ions and some of the Mn^{3+} ions. Bipolar switching of magnetization is demonstrated for $x = 0$ and 0.05 samples at a fixed temperature T ($< T_{comp}$) by varying the magnitude of applied magnetic field in same direction.

Polycrystalline samples of $GdCr_{1-x}Fe_xO_3$ ($x = 0 – 0.50$) are also found to crystallize in orthorhombic crystal structure with *Pbnm* space group. In this case all the lattice parameters are found to increase systematically with increase in Fe concentration. Raman spectra at room temperature show the presence of an oxygen breathing mode (A_g) in samples containing both Fe^{3+} and Cr^{3+} ions due to possible charge transfer mechanism between both the ions. Similar feature is also observed in compounds like $LaFe_{1-x}Cr_xO_3$ and $HoFe_{1-x}Cr_xO_3$ [146,147]. All samples show antiferromagnetic transition with considerable weak FM due to canting of Cr^{3+} moments. The transition temperature initially decreases from 172 K ($x = 0$) to 161 K ($x = 0.20$) and then it increases from 178 K ($x = 0.30$) to 260 K ($x = 0.50$) due to the formation of considerable $Fe^{3+}– O^{2-}– Fe^{3+}$ networks. Parent compound ($x = 0$) exhibits the temperature induce MR behavior which is completely quenched by Fe substitution, even for 5 at% due to the enhancement in the weak FM component of canted Cr^{3+} ions whereas 5 at% Mn substitution shows the magnetization reversal behavior. Unlike Mn substitution, a magnetic compensation behavior without any magnetization reversal is observed at T_{comp} = 125 K for Fe substitution with $x = 0.40$ which is ascribed to the presence of a predominant collinear antiferromagnetism in $Fe^{3+}– O^{2-}– Fe^{3+}$ networks which suppress the weak FM component. The temperature dependence of magnetization for $x = 0.50$ sample is consistent with the previous report by Yin *et al.* on $RFe_{0.50}Cr_{0.50}O_3$ (R = Gd) which shows the AFM ordering around 250 K [125]. The inverse susceptibility data of $x = 0$ to 0.40 samples in the paramagnetic region could be analyzed in terms of Curie-Weiss law and the estimated values of μ^{exp}_{eff} are found to be smaller compared to their corresponding theoretical values due to the presence of possible short range AFM $Cr^{3+}– O^{2-}– Cr^{3+}$ / $Fe^{3+}– O^{2-}– Fe^{3+}$ networks in the paramagnetic region.

Complex impedance spectra measured at different temperatures above the room temperature show the presence of non-Debye type thermally activated relaxation of process. The complex impedance plot shows that both grains and grain boundaries contribute to the conduction process. The ac conductivity data was analyzed based on the Jonscher's power law. The relaxation time of charge carriers and dc conductivity follow the Arrhenius law with comparable activation energy.

Single phase samples of $Gd_{1-x}Y_xCrO_3$ ($x = 0 – 1.0$) were prepared using the sol-gel method and the prepared samples are found to crystallize in *Pbnm* space group *i.e.* with orthorhombic structure. A decrease in lattice parameters and volume of the unit cell is observed upon Y substitution due to replacement of the larger Gd^{3+} ions by smaller Y^{3+} ions. The Raman spectra measured at room temperature show a systematic shift in the various Raman modes towards higher wave number because of difference in the mass and radius of the rare earth ion as a result of Y substitution for Gd in the pure $GdCrO_3$ sample.

A systematic fall in the AFM transition temperature is observed with increase in Y concentration as a result of weakening of the superexchange networks. Interesting temperature induced magnetization reversal is observed in the FC mode upto $x = 0.70$ samples. The compensation temperature decreases from 136 K for $x = 0$ to 42 K for $x = 0.70$ due to reduction in the net PM moment (M_{Gd}) and enhancement in the spin canting of Cr^{3+} ions as a result of the substitution of non magnetic Y^{3+} ion. The magnitude of negative internal field is found to decrease from 1.6 kOe ($x = 0$) to 1.3 kOe ($x = 0.70$) which is ascribed to the weakening of Cr^{3+} - O^{2-} - Cr^{3+} networks due to increase in lattice distortion as a result of substitution of Y^{3+} ions. Bipolar switching of magnetization is demonstrated for $x = 0$ to 0.50 samples by just changing the magnitude of the positive magnetic field keeping its direction fixed. Tunable exchange bias behavior as a function of temperature is observed for $x = 0$ to 0.50 samples and the exchange bias field changes it polarity across the T_{comp}. The occurrence of the sign reversal of magnetization and exchange bias is explained by considering the different temperature dependence of FM component of canted Cr^{3+} ions and the PM moment of Gd^{3+} ions and their competition under the influence of negative internal field arising from AFM ordered Cr^{3+} ions. Similar sign reversal of both magnetization and EB is reported in isostructural compounds like $La_{0.20}Ce_{0.80}CrO_3$, $La_{0.15}Pr_{0.85}CrO_3$ and $TmCrO_3$ with comparable value of exchange bias field (H_{EB}) [16,96,158]**.** However the sign of H_{EB} remains unchanged across T_{comp} in $La_{0.15}Pr_{0.85}CrO_3$ for H = 3000 Oe. In another single phase orthochromite $Dy_{1-x}Nd_xCrO_3$, having two magnetic rare earth ions at the A site, only negative exchange bias with a maximum H_{EB} ~ 2.5 kOe is observed and it doesn't show any reversal in magnetization [159].

Thus, in the present thesis work, magnetic properties of Mn and Fe substituted $SmCrO_3$ and $GdCrO_3$ series along with a non magnetic element Y substituted $GdCrO_3$ series have been studied. It is found that the substitution of Mn and Fe for Cr in $SmCrO_3$ leads to interesting temperature induced magnetization reversal and tunable exchange bias behavior. In case of $GdCrO_3$ series sign reversal of magnetization and exchange bias is observed only for Mn substitution while such behaviors are not observed for Fe substitution. The observed magnetic data are analyzed quantitatively by taking the help of existing theoretical models.

Future Scope of Studies

The compounds prepared for the present thesis work could be taken up for further studies and development of other physical properties and some of them are listed below.

- Study of possible ferroelectric properties and its coupling with the magnetization *i.e.* multiferroic properties which would enhance their multifunctional applications.
- $RCrO_3$ are known to show large magnetocaloric effect thus, study of the magnetocaloric effect, especially in Gd based orthochromites would explore the potential applications of these materials.
- Study of role of the particle size variation on the magnetic properties like magnetization reversal and exchange bias.
- Possibility of magnetization reversal and exchange bias in thin film form of the samples showing these behaviors can also be looked for to study the effect of lattice strain on these properties.
- Temperature dependent neutron powder diffraction studies under the ZFC and FC conditions in order to gain a better insight into the magnetic structure and origin of magnetic properties like spin reorientation and magnetization reversal.
- Study of temperature dependant electrical properties in the presence and absence of magnetic field to understand the electrical transport properties in these compounds.

- Study of the exchange bias behavior and its dependence on the cooling field by extending the limit of the applied magnetic field (~ 1 – 5 T).

भारतीय प्रौद्योगिकी संस्थान गुवाहाटी
Indian Institute of Technology Guwahati

References

[1] M. N. Baibich, J. M. Broto, A. Fert, F. N. Van Dau, F. Petroff, P. Etienne, G. Creuzet, A. Friederich, and J. Chazelas, Phys. Rev. Lett. **61**, 2472 (1988).

[2] G. Binasch, P. Grünberg, F. Saurenbach, and W. Zinn, Phys. Rev. B **39**, 4828 (1989).

[3] A. Fert, P. Grünberg, A. Barthélémy, F. Petroff, and W. Zinn, J. Magn. Magn. Mater. **140–144**, 1 (1995).

[4] B. Dieny, V. S. Speriosu, S. S. P. Parkin, B. A. Gurney, D. R. Wilhoit, and D. Mauri, Phys. Rev. B **43**, 1297 (1991).

[5] J. C. S. Kools, IEEE Trans. Magn. **32**, 3165 (1996).

[6] T. Ching, R. E. Fontana, T. Lin, D. E. Heim, V. S. Speriosu, B. A. Gurney, M. L. Williams, C. Tsang, R. E. Fontana, T. Lin, D. E. Heim, V. S. Speriosu, B. A. Gurney, and M. L. Williams, IEEE Trans. Magn. **30**, 3801 (1994).

[7] A. Kumar and S. M. Yusuf, Phys. Rep. **556**, 1 (2015).

[8] D. I. Khomskii, J. Magn. Magn. Mater. **306**, 1 (2006).

[9] R. M. Hornreich, J. Magn. Magn. Mater. **7**, 280 (1978).

[10] B. Rajeswaran, D. I. Khomskii, A. K. Zvezdin, C. N. R. Rao, and A. Sundaresan, Phys. Rev. B **86**, 214409 (2012).

[11] J. R. Sahu, C. R. Serrao, N. Ray, U. V. Waghmare, and C. N. R. Rao, J. Mater. Chem. **17**, 42 (2007).

[12] A. H. Cooke, D. M. Martin, and M. R. Wells, J. Phys. C Solid State Phys. **7**, 3133 (1974).

[13] K. Yoshii, J. Solid State Chem. **159**, 204 (2001).

[14] K. Yoshii, A. Nakamura, Y. Ishii, and Y. Morii, J. Solid State Chem. **162**, 84 (2001).

[15] Y. Cao, S. Cao, W. Ren, Z. Feng, S. Yuan, B. Kang, B. Lu, and J. Zhang, Appl. Phys. Lett. **104**, 232405 (2014).

[16] P. K. Manna, S. M. Yusuf, R. Shukla, and a. K. Tyagi, Appl. Phys. Lett. **96**, 242508 (2010).

[17] L. H. Yin, J. Yang, X. C. Kan, W. H. Song, J. M. Dai, and Y. P. Sun, J. Appl. Phys. **117**, 133901 (2015).

[18] J. Nogués and I. K. Schuller, J. Magn. Magn. Mater. **192**, 203 (1999).

[19] I. L. Prejbeanu, M. Kerekes, R. C. Sousa, H. Sibuet, O. Redon, B. Dieny, and J. P.

Nozières, J. Phys. Condens. Matter **19**, 165218 (2007).

[20] K. Momma and F. Izumi, J. Appl. Crystallogr. **44**, 1272 (2011).

[21] V. M. Goldschmidt, Naturwissenschaften **14**, 477 (1926).

[22] M. Aparnadevi and R. Mahendiran, J. Appl. Phys. **113**, 013911 (2013).

[23] A. K. Kundu, *Magnetic Perovskites* (Springer India, New Delhi, 2016).

[24] Y. Du, Z. X. Cheng, X.-L. Wang, and S. X. Dou, J. Appl. Phys. **108**, 093914 (2010).

[25] S. Blundell, *Magnetism in Condensed Matter* (Oxford University Press, 2001).

[26] Y. Tokura and N. Nagosa, Science (80-.). **288**, 462 (2000).

[27] M. D. Sturge, in (Academic Press, 1968), pp. 91–211.

[28] B. D. Culity and C. D. Graham, *Introduction to Magnetic Materials*, 2nd Editio (IEEE Press, New Jersey, 2009).

[29] H. A. Kramers, Physica **1**, 182 (1934).

[30] J. B. Goodenough, Reports Prog. Phys. **67**, 1915 (2004).

[31] C. Zener, Phys. Rev. **81**, 440 (1951).

[32] P. W. Anderson and H. Hasegawa, Phys. Rev. **100**, 675 (1955).

[33] I. E. Dzyloshinskii, **5**, 1259 (1957).

[34] T. Moriya, Phys. Rev. Lett. **4**, 228 (1960).

[35] T. Moriya, Phys. Rev. **120**, 91 (1960).

[36] A. H. Morrish, *The Physical Principles of Magnetism* (IEEE, 2001).

[37] A. J. Steele, *Quantum Magnetism Probed with Muon-Spin Relaxation* (University of Oxford, 2011).

[38] N. A. Spaldin, *Magnetic Materials* (Cambridge University Press, Cambridge, 2010).

[39] W. H. Meiklejohn and C. P. Bean, Phys. Rev. **102**, 1413 (1956).

[40] L. Néel, Ann. Phys. Paris **3**, 137 (1948).

[41] H. Adachi and H. Ino, Nature **401**, 148 (1999).

[42] R. Medapalli, I. Razdolski, M. Savoini, A. R. Khorsand, A. M. Kalashnikova, A. Tsukamoto, A. Itoh, A. Kirilyuk, A. V. Kimel, and T. Rasing, Eur. Phys. J. B **86**, 183 (2013).

[43] H. Young Jun, K. Jun Sig, S. In-Bo, and K. Chul Sung, IEEE Trans. Magn. **40**, 2808 (2004).

[44] R. Pauthenet, J. Appl. Phys. **29**, 253 (1958).

[45] N. Menyuk, K. Dwight, and D. G. Wickham, Phys. Rev. Lett. **4**, 119 (1960).

[46] M. Abe, M. Kawachi, and S. Nomura, J. Phys. Soc. Japan **31**, 940 (1971).

[47] R. Padam, S. Pandya, S. Ravi, A. K. Nigam, S. Ramakrishnan, A. K. Grover, and D. Pal, Appl. Phys. Lett. **102**, 112412 (2013).

[48] J. Barman, P. D. Babu, and S. Ravi, J. Magn. Magn. Mater. **418**, 300 (2016).

[49] Z. Yang, S. Tan, Y. Zhang, Y. Zhaorong, T. Shun, and Z. Yuheng, J. Phys. Condens. Matter **15**, 7411 (2003).

[50] I. J. Park, K. U. Kang, and C. S. Kim, IEEE Trans. Magn. **42**, 2882 (2006).

[51] A. Kumar, S. M. Yusuf, L. Keller, and J. V Yakhmi, Phys. Rev. Lett. **101**, 207206 (2008).

[52] S. M. Yusuf, A. Kumar, and J. V Yakhmi, J. Phys.Conf. Ser. **200**, 22073 (2010).

[53] X. H. Chen, K. Q. Wang, P. H. Hor, Y. Y. Xue, and C. W. Chu, Phys. Rev. B **72**, 054436 (2005).

[54] J. W. Taylor, J. a. Duffy, a. M. Bebb, M. R. Lees, L. Bouchenoire, S. D. Brown, and M. J. Cooper, Phys. Rev. B **66**, 161319 (2002).

[55] P. D. Kulkarni, A. Thamizhavel, V. C. Rakhecha, A. K. Nigam, P. L. Paulose, S. Ramakrishnan, and A. K. Grover, EPL **86**, 47003 (2009).

[56] P. Kumar, R. Kumar, S. Pandey, K. G. Suresh, and A. K. Nigam, Phys. B Condens. Matter **448**, 6 (2014).

[57] Z.-P. Li, J. Eisenmenger, C. W. Miller, and I. K. Schuller, Phys. Rev. Lett. **96**, 137201 (2006).

[58] P. Chaudhari, J. J. Cuomo, and R. J. Gambino, Appl. Phys. Lett. **22**, 337 (1973).

[59] S. Demirtas, M. R. Hossu, R. E. Camley, H. C. Mireles, and A. R. Koymen, Phys. Rev. B **72**, 184433 (2005).

[60] Y. Ren, T. T. M. Palstra, D. I. Khomskii, A. A. Nugroho, A. A. Menovsky, and G. A. Sawatzky, Phys. Rev. B **62**, 6577 (2000).

[61] A. V Mahajan, D. C. Johnston, D. R. Torgeson, and F. Borsa, Phys. Rev. B **46**, 10966 (1992).

[62] H. C. Nguyen and J. B. Goodenough, Phys. Rev. B **52**, 324 (1995).

[63] Y. Kimishima, Y. Ichiyanagi, K. Shimizu, and T. Mizuno, J. Magn. Magn. Mater. **210**, 244 (2000).

[64] Y. Kimishima, M. Uehara, and T. Saitoh, Solid State Commun. **133**, 559 (2005).

[65] L. D. Tung, M. R. Lees, G. Balakrishnan, and D. McK. Paul, Phys. Rev. B **75**, 104404 (2007).

[66] P. Mandal, A. Sundaresan, C. N. R. Rao, A. Iyo, P. M. Shirage, Y. Tanaka, C. Simon, V. Pralong, O. I. Lebedev, V. Caignaert, and B. Raveau, Phys. Rev. B **82**, 100416 (2010).

[67] J. Hemberger, S. Lobina, H.-A. Krug von Nidda, N. Tristan, V. Y. Ivanov, A. A. Mukhin, A. M. Balbashov, and A. Loidl, Phys. Rev. B **70**, 024414 (2004).

[68] J.-S. Jung, A. Iyama, H. Nakamura, M. Mizumaki, N. Kawamura, Y. Wakabayashi, and T. Kimura, Phys. Rev. B **82**, 212403 (2010).

[69] C. Moure and O. Peña, J. Magn. Magn. Mater. **337–338**, 1 (2013).

[70] K. Yoshii, Mater. Res. Bull. **47**, 3243 (2012).

[71] Y. Su, J. Zhang, Z. Feng, L. Li, B. Li, Y. Zhou, Z. Chen, and S. Cao, J. Appl. Phys. **108**, 13905 (2010).

[72] P. Gupta, R. Bhargava, P. Poddar, G. Preeti, B. Richa, P. Pankaj, P. Gupta, R. Bhargava, and P. Poddar, J. Phys. D. Appl. Phys. **48**, 025004 (2015).

[73] T. Bora and S. Ravi, J. Magn. Magn. Mater. **386**, 85 (2015).

[74] T. Bora and S. Ravi, J. Appl. Phys. **116**, 063901 (2014).

[75] R. L. Stamps, J. Phys. D Appl. Phys. **33**, R247 (2000).

[76] A. E. Berkowitz and K. Takano, J. Magn. Magn. Mater. **200**, 552 (1999).

[77] P. K. Manna and S. M. Yusuf, Phys. Rep. **535**, 61 (2014).

[78] S. Giri, M. Patra, and S. Majumdar, J. Phys. Condens. Matter **23**, 073201 (2011).

[79] S. Chandra, N. A. Frey Huls, M. H. Phan, S. Srinath, M. A. Garcia, Y. Lee, C. Wang, S. Sun, Ò. Iglesias, and H. Srikanth, Nanotechnology **25**, 055702 (2014).

[80] H. Singh, T. Chakraborty, K. Srikanth, R. Chandra, C. Mitra, and U. Kumar, Phys. B **448**, 77 (2014).

[81] C. Zhu, Z. Tian, L. G. Wang, and S. Yuan, J. Magn. Magn. Mater. **393**, 116 (2015).

[82] J. Barman and S. Ravi, Solid State Commun. **201**, 59 (2015).

[83] S. K. Giri, S. M. Yusuf, M. D. Mukadam, and T. K. Nath, J. Appl. Phys. **115**, 093906 (2014).

[84] S. K. Giri and T. K. Nath, J. Nanosci. Nanotechnol. **14**, 1209 (2014).

[85] F. Hong, Z. Cheng, J. Wang, X. Wang, and S. Dou, Appl. Phys. Lett. **101**, 102411 (2012).

[86] M. Patra, M. Thakur, S. Majumdar, and S. Giri, J. Phys. Condens. Matter **21**, 236004 (2009).

[87] Y. Tang, Y. Sun, and Z. Cheng, J. Appl. Phys. **100**, 023914 (2006).

[88] P. Gupta and P. Poddar, Inorg. Chem. **54**, 9509 (2015).

[89] R. Pradheesh, H. S. Nair, V. Sankaranarayanan, and K. Sethupathi, Appl. Phys. Lett. **101**, 142401 (2012).

[90] R. P. Singh, C. V. Tomy, and A. K. Grover, Appl. Phys. Lett. **97**, 182505 (2010).

[91] M. Ali, P. Adie, C. H. Marrows, D. Greig, B. J. Hickey, and R. L. Stamps, Nat. Mater. **6**, 70 (2007).

[92] J. Nogués, D. Lederman, T. J. Moran, and I. K. Schuller, Phys. Rev. Lett. **76**, 4624 (1996).

[93] D. J. Webb, A. F. Marshall, A. M. Toxen, T. H. Geballe, and R. M. White, IEEE Trans. Magn. **24**, 2013 (1988).

[94] T. Bora and S. Ravi, J. Appl. Phys. **114**, 183902 (2013).

[95] T. Bora and S. Ravi, J. Magn. Magn. Mater. **358–359**, 208 (2014).

[96] K. Yoshii, Appl. Phys. Lett. **99**, 142501 (2011).

[97] J. R. Barsoukov, E, Macdonald, *Impedance Spectroscopy Theory, Experiment, and Applications*, 2nd Editio (John Wiley & Sons, Inc., Hoboken, NJ, USA, 2010).

[98] A. K. Jonscher, Nature **267**, 673 (1977).

[99] A. K. Jonscher, J. Phys. D. Appl. Phys. **32**, R57 (1999).

[100] E. F. Bertaut, G. Bassi, G. Buisson, P. Burlet, J. Chappert, A. Delapalme, J. Mareschal, G. Roult, R. Aleonard, R. Pauthenet, and J. P. Rebouillat, J. Appl. Phys. **37**, 1038 (1966).

[101] Z. X. Cheng, X. L. Wang, S. X. Dou, H. Kimura, and K. Ozawa, J. Appl. Phys. **107**, 09D905 (2010).

[102] L. H. Yin, J. Yang, R. R. Zhang, J. M. Dai, W. H. Song, and Y. P. Sun, Appl. Phys. Lett. **104**, 032904 (2014).

[103] B. Rajeswaran, P. Mandal, R. Saha, E. Suard, A. Sundaresan, and C. N. R. Rao, Chem. Mater. **24**, 3591 (2012).

[104] P. Gupta and P. Poddar, RSC Adv. **5**, 10094 (2015).

[105] A. Jaiswal, R. Das, K. Vivekanand, T. Maity, P. M. Abraham, S. Adyanthaya, and P. Poddar, J. Appl. Phys. **107**, 013912 (2010).

[106] S. Yin, V. Sharma, A. McDannald, F. A. Reboredo, and M. Jain, RSC Adv. **6**, 9475 (2016).

[107] A. L. Linsebigler, G. Lu, and J. T. Yates, Chem. Rev. **95**, 735 (1995).

[108] A. McDannald, L. Kuna, and M. Jain, J. Appl. Phys. **114**, 113904 (2013).

[109] S. Yin and M. Jain, J. Appl. Phys. **120**, 043906 (2016).

[110] V. A. Khomchenko, I. O. Troyanchuk, R. Szymczak, and H. Szymczak, J. Mater. Sci. **43**, 5662 (2008).

[111] N. Sharma, B. K. Srivastava, A. Krishnamurthy, and A. K. Nigam, J. Alloys Compd. **545**, 50 (2012).

[112] A. K. Azad, A. Mellergard, S. G. Eriksson, S. A. Ivanov, S. M. Yunus, F. Lindberg, G. Svensson, and R. Mathieu, Mater. Res. Bull. **40**, 1633 (2005).

[113] T. Bora and S. Ravi, J. Appl. Phys. **114**, 033906 (2013).

[114] J. Mao, Y. Sui, X. Zhang, X. Wang, Y. Su, Z. Liu, Y. Wang, R. Zhu, Y. Wang, W. Liu, and X. Liu, Solid State Commun. **151**, 1982 (2011).

[115] J. Mao, Y. Sui, X. Zhang, Y. Su, X. Wang, Z. Liu, Y. Y. Wang, R. Zhu, Y. Y. Wang, W. Liu, and J. Tang, Appl. Phys. Lett. **98**, 192510 (2011).

[116] G. Gorodetsky, R. M. Hornreich, S. Shaft, B. Sharon, a. Shaulov, and B. M. Wanklyn, Phys. Rev. B **16**, 515 (1977).

[117] P. Gupta and P. Poddar, RSC Adv. **6**, 82014 (2016).

[118] M. Tripathi, R. J. Choudhary, and D. M. Phase, RSC Adv. **6**, 90255 (2016).

[119] X. L. Qian, D. M. Deng, Y. Jin, B. Lu, S. X. Cao, and J. C. Zhang, J. Appl. Phys. **115**, 193902 (2014).

[120] X.-L. Qian, J. Kang, B. Lu, S.-X. Cao, and J.-C. Zhang, RSC Adv. **6**, 10677 (2016).

[121] Y. Fang, S.-M. Yan, Y.-Y. Gong, W.-L. Zhu, Q.-Q. Cao, D.-H. Wang, and Y.-W. Du, Chinese Phys. B **23**, 127502 (2014).

[122] S. Huang, L. R. Shi, Z. M. Tian, H. G. Sun, and S. L. Yuan, J. Magn. Magn. Mater. **394**, 77 (2015).

[123] N. Sharma, B. K. Srivastava, A. Krishnamurthy, and A. K. Nigam, Solid State Sci. **12**,

1464 (2010).

[124] S. Biswas and S. Pal, Ceram. Int. **41**, 14712 (2015).

[125] L. H. Yin, J. Yang, P. Tong, X. Luo, W. H. Song, J. M. Dai, X. B. Zhu, and Y. P. Sun, Appl. Phys. Lett. **110**, 192904 (2017).

[126] J. Rodríguez-Carvajal, Phys. B Condens. Matter **192**, 55 (1993).

[127] R. A. Young, *"The Rietveld Method"* (Oxford University, New York, 1996).

[128] S. Foner, Rev. Sci. Instr. **30**, 548 (1959).

[129] A. Ghosh, K. Dey, M. Chakraborty, S. Majumdar, and S. Giri, EPL (Europhysics Lett. **107**, 47012 (2014).

[130] S. Huang, G. Zerihun, Z. Tian, S. Yuan, G. Gong, C. Yin, and L. Wang, Ceram. Int. **40**, 13937 (2014).

[131] T. Bora, P. Saravanan, and S. Ravi, J. Supercond. Nov. Magn. **26**, 1645 (2013).

[132] K. Yoshii and A. Nakamura, J. Solid State Chem. **155**, 447 (2000).

[133] J. Barman and S. Ravi, J. Magn. Magn. Mater. **426**, 82 (2017).

[134] J. Barman, T. Bora, and S. Ravi, J. Magn. Magn. Mater. **385**, 93 (2015).

[135] A. A. Belik, Inorg. Chem. **52**, 2015 (2013).

[136] P. Mandal, C. R. Serrao, E. Suard, V. Caignaert, B. Raveau, A. Sundaresan, and C. N. R. Rao, J. Solid State Chem. **197**, 408 (2013).

[137] M. EibschUtz, L. Holmes, J. P. Maita, and L. G. Van Uitert, Solid State Commun. **8**, 1815 (1970).

[138] L. Wang, S. W. Wang, X. Zhang, L. L. Zhang, R. Yao, and G. H. Rao, J. Alloys Compd. **662**, 268 (2016).

[139] P. D. Kulkarni, S. Venkatesh, A. Thamizhavel, V. C. Rakhecha, S. Ramakrishnan, and A. K. Grover, IEEE Trans. Magn. **45**, 2902 (2009).

[140] C. N. R. Rao, G V Subba, Wanklyn, B. M, Rao, Int. J. Phys. Chem. Solids **32**, 345 (1971).

[141] M. N. Iliev, M. V Abrashev, H.-G. Lee, V. N. Popov, Y. Y. Sun, C. Thomsen, R. L. Meng, and C. W. Chu, Phys. Rev. B **57**, 2872 (1998).

[142] M. C. Weber, J. Kreisel, P. A. Thomas, M. Newton, K. Sardar, and R. I. Walton, Phys. Rev. B **85**, 054303 (2012).

[143] A. P. Blessington Selvadurai, V. Pazhanivelu, C. Jagadeeshwaran, R. Murugaraj, I.

Panneer Muthuselvam, and F. C. Chou, J. Alloys Compd. **646**, 924 (2015).

[144] S. Venugopalan, M. Dutta, A. K. Ramdas, and J. P. Remeika, Phys. Rev. B **31**, 1490 (1985).

[145] G. Kotnana, V. G. Sathe, and S. Narayana Jammalamadaka, J. Raman Spectrosc. 764 (2018).

[146] J. Andreasson, J. Holmlund, C. S. Knee, M. Käll, L. Börjesson, S. Naler, J. Bäckström, M. Rübhausen, A. K. Azad, and S.-G. Eriksson, Phys. Rev. B **75**, 104302 (2007).

[147] G. Kotnana and S. N. Jammalamadaka, J. Appl. Phys. **118**, 124101 (2015).

[148] Aakansha, B. Deka, S. Ravi, and D. Pamu, Ceram. Int. **43**, 10468 (2017).

[149] B. Deka and S. Ravi, J. Alloys Compd. **720**, 589 (2017).

[150] N. Ortega, A. Kumar, P. Bhattacharya, S. B. Majumder, and R. S. Katiyar, Phys. Rev. B **77**, 014111 (2008).

[151] P. Margareta, A. Slobotka, M. Marjan, and D. Sandra, J. Am. Ceram. Soc. **97**, 3864 (2014).

[152] G. Li, Z. Chen, X. Sun, L. Liu, L. Fang, and B. Elouadi, Mater. Res. Bull. **65**, 260 (2015).

[153] C. Verdier, F. D. Morrison, D. C. Lupascu, and J. F. Scott, J. Appl. Phys. **97**, 024107 (2005).

[154] R. Kamel, A. Tozri, E. Dhahri, E. K. Hlil, and L. Bessais, J. Magn. Magn. Mater. **426**, 757 (2017).

[155] O. Peña, A. B. Antunes, G. Martínez, V. Gil, and C. Moure, J. Magn. Magn. Mater. **310**, 159 (2007).

[156] F. Hong, Z. Cheng, and X. Wang, Appl. Phys. Lett. **99**, 192503 (2011).

[157] S. Venkatesh, U. Vaidya, V. C. Rakhecha, S. Ramakrishnan, and A. K. Grover, J. Phys. Condens. Matter **22**, 496002 (2010).

[158] L. Wang, G. H. Rao, X. Zhang, L. L. Zhang, S. W. Wang, and Q. R. Yao, Ceram. Int. **42**, 10171 (2016).

[159] A. McDannald, C. R. dela Cruz, M. S. Seehra, and M. Jain, Phys. Rev. B **93**, 184430 (2016).

Publications/Communications in International Journals

From Thesis Work:

1. **Bibhuti B. Dash** and S. Ravi, *"Structural, magnetic and electrical properties of Fe substituted* $GdCrO_3$*"*, **Solid State Sciences**, **83** (2018) 192-200.

2. **Bibhuti B. Dash** and S. Ravi, *"Magnetization reversal and exchange bias study in bulk* $Gd_{1-x}Y_xCrO_3$ $(x = 0 - 1.0)$*"*, **Journal of Magnetism and Magnetic Materials**, **461** (2018) 91-99

3. **Bibhuti B. Dash** and S. Ravi, *"Effect of Yttrium substitution on the structural and magnetic properties of* $GdCrO_3$*"*, **Journal of Magnetism and Magnetic Materials**, **448** (2018) 355-359.

4. **Bibhuti B. Dash** and S. Ravi, "*Magnetization reversal and tunable exchange bias in* $GdCr_{1-x}Mn_xO_3$ $(x = 0 - 0.50)$*"*, **Journal of Magnetism and Magnetic Materials**, **429** (2017) 281-286.

5. **Bibhuti B. Dash** and S. Ravi, *"Sign reversal of magnetization in Mn substituted* $SmCrO_3$*"*, **Journal of Magnetism and Magnetic Materials**, **405** (2016) 209-213.

Outside Thesis Work:

1. T. R. Gopalarao, **Bibhuti B. Dash** and S. Ravi, *"Magnetic and electrical transport properties of* $La_{0.7}Sr_{0.3}MnO_3$ */*$LaFeO_3$ *bilayer thin films"*, **Journal of Magnetism and Magnetic Materials**, **441** (2017) 531-536.

Papers presented in International and National Conferences:

1. **Bibhuti B. Dash** and S. Ravi, *"Magnetic characterization of orthochromites by using the vibrating sample magnetometer"*, **International Conference on Sophisticated Instruments in Modern Research (ICSIMR 2017), IIT Guwahati, Assam, India.**

2. **Bibhuti B. Dash** and S. Ravi, *"Sign reversal of magnetization and tunable exchange bias in* $GdCr_{1-x}Mn_xO_3$ *(x = 0 – 0.50)"*, **National Conference in Advances in Material Science (AMS 2017), Gauhati University, Assam, India.**

3. **Bibhuti B. Dash** and S. Ravi, *"Magnetization reversal in* $SmCr_{0.85}Mn_{0.15}O_3$*"*, **Second International Conference on Material Science (ICMS 2017), Tripura Central University, Tripura, India.**

4. **Bibhuti B. Dash** and S. Ravi, *"Effect of Y substitution on structural and magnetic properties of* $GdCrO_3$*"*, **International Conference on magnetism and magnetic Materials (ICMAGMA 2017), DMRL, Hyderabad, India.**

5. **Bibhuti B. Dash** and S. Ravi, *"Sign reversal of magnetization in Mn substituted* $SmCrO_3$*"*, **International Conference on magnetism and magnetic Materials (ICMAGMA 2015), VIT University, Vellore, Tamil Nadu, India.**